Title
Vorticity-based modeling of stratified flows

Permalink
https://escholarship.org/uc/item/637909vg

Author
Khodkar, Mohammad Amin

Publication Date
2017

Peer reviewed|Thesis/dissertation

University of California
Santa Barbara

Vorticity-based modeling of stratified flows

A dissertation submitted in partial satisfaction
of the requirements for the degree

Doctor of Philosophy
in
Mechanical Engineering

by

Mohammad Amin Khodkar

Committee in charge:

Professor Eckart Meiburg, Chair
Professor Paolo Luzzatto-Fegiz
Professor Sumita Pennathur
Professor Libe Washburn

September 2017

The Dissertation of Mohammad Amin Khodkar is approved.

Professor Paolo Luzzatto-Fegiz

Professor Sumita Pennathur

Professor Libe Washburn

Professor Eckart Meiburg, Committee Chair

September 2017

Vorticity-based modeling of stratified flows

To the beautiful soul of Fatemeh and to the mighty heart of Mansoor, and to all who believe truth is the antidote to all sufferings.

Acknowledgements

Curriculum Vitæ
Mohammad Amin Khodkar

Education

2013	B.Sc. in Mechanical Engineering, University of Tehran, Tehran.
2017	Ph.D. in Mechanical Engineering (expected), University of California, Santa Barbara.

Work Experience

2014-2017	Graduate Student Researcher, Computational Fluid Dynamics Laboratory, Department of Mechanical Engineering, University of California at Santa Barbara.
2014-2017	Teaching Assistant, Computational Fluid Dynamics Laboratory, Department of Mechanical Engineering, University of California at Santa Barbara.

Journal Publications

M. A. Khodkar, M. M. Nasr-Azadani and E. Meiburg, (2016), "Intrusive gravity currents propagating into two-layer stratified ambients: Vorticity modeling", *Physical Review Fluids*, 1 (4), 044302.

M. A. Khodkar, M. M. Nasr-Azadani and E. Meiburg, (2017), "Partial-depth lock-release flows", *Physical Review Fluids*, 2 (6), 064802.

M. A. Khodkar, M. M. Nasr-Azadani and E. Meiburg, (2017), "Gravity currents propagating into two-layer stratified fluids: Vorticity-based models", submitted to *Journal of Fluid Mechanics*.

M. A. Khodkar, K. El Allam and E. Meiburg, (2017), "Intrusions propagating into linearly stratified ambients", submitted to *Journal of Fluid Mechanics*.

Awards

UC Santa Barbara Mechanical Engineering Department Fellowship (Fall 2017, Summer 2015 and Summer 2017).

Abstract

Vorticity-based modeling of stratified flows

by

Mohammad Amin Khodkar

Within the present investigation, the broad span of applications of the vorticity-based modeling concept for stratified flows, based on the simultaneous use of horizontal and vertical momenta equations in the form of vorticity balance principle, is studied in detail. Towards this objective, this approach, originally introduced by Borden and Meiburg [Z. Borden and E. Meiburg, Phys. Fluids **25 (10)**, 101301 (2013); Z. Borden and E. Meiburg, J. Fluid Mech. **726**, R1 (2013)], for gravity currents propagating into unstratified ambients and internal bores traveling at the interface of two-layer fluids, respectively, is extended to various well known stratified flow problems, in the following. These flows normally involve several fronts which can be analyzed according to the quasisteady conservation laws of mass and momentum by appropriate shift in the reference frame, or possibly unsteady sections for which the flow cannot be rendered quasisteady by any finite number of changes in the reference frames. The analyses of various flow components are then superimposed and matched to obtain the whole flow field. It is also demonstrated that under certain conditions the propagation of gravity currents (or intrusions) can lead to the formation of interfacial perturbations in the form of rarefaction waves or internal bores, which are a source of unsteadiness, and can substantially impact the flow dynamics as well as its energy budget.

Enforcing the conservation laws for horizontal and vertical momenta concurrently, enables us to avoid employing energy-based closure assumptions invoked by previous peer models. Consequently, the assessment of flow energetics becomes plausible, which can be

utilized to investigate the validity of the energy-related arguments made by other authors. Furthermore, the predictions of the current study obtained by detailed parametric studies are compared to the results of our two-dimensional direct numerical simulations as well as the theoretical and experimental findings of earlier investigations, where very good agreement is observed with regard to all flow properties.

Contents

Chapter 1

Introduction

Gravity currents represent a special class of predominantly horizontal flows that form due to hydrostatic pressure differences resulted by density gradients in a gravitational field [1–4]. They comprise a broad range of atmospheric and oceanic phenomena, such as turbidity currents, powder snow avalanches and thunderstorm outflows [3–7]. Gravity currents can be heavier or lighter than the ambient fluids, and respectively, travel along the bottom or top boundaries, or they can propagate horizontally at intermediate depths, when their densities fall in between the minimum and maximum density of the ambient. The latter cases, namely, *intrusions* or *intrusive gravity currents*, occur in a variety of atmospheric and oceanic situations, and have been vastly studied theoretically, experimentally and numerically by previous investigators [8–16].

The development of simplified models for predicting the front velocity of such currents has a long history, dating back to the pioneering work of von Kármán three quarters of a century ago [17], as well as subsequent investigations by [1, 8, 14, 15, 18]. As a common feature, all of the above models are based on the integral laws for the conservation of mass of the different fluids, and typically the conservation of overall horizontal momentum. An energy-related empirical argument is then employed along a certain streamline in order to quantify the head loss across the gravity current front, so that a closed system of algebraic equations is obtained. The key difference among the individual models lies in
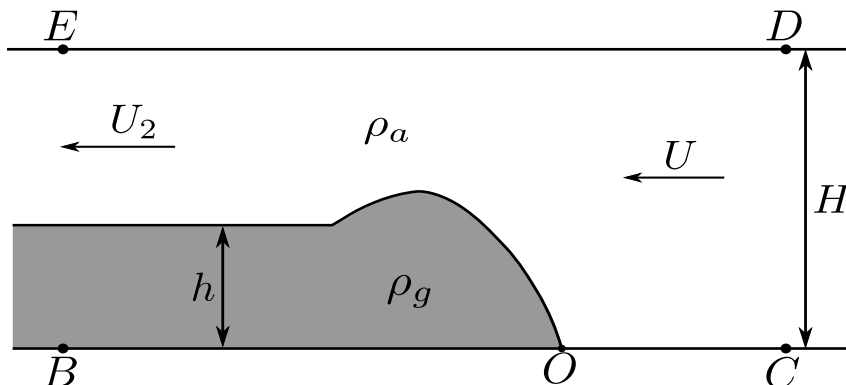
Figure 1.1: Schematic of a gravity current of thickness h propagating with velocity U into a channel of depth H, in a reference frame moving with the current front.

where this energy argument is invoked.

More recently, an alternative approach for modeling Boussinesq gravity currents was proposed by [19], cf. Fig. 1.1. Starting from the Euler equations for the conservation of horizontal and vertical momenta, the authors eliminate the pressure variable by focusing on the vorticity form of the Euler equation, thereby avoiding the need for a head loss closure assumption. They furthermore assume that the flow is steady in the reference frame moving with the current front, and that the gravity current fluid is at rest in this reference frame. In integral form, the authors thus obtain for the control volume $BCDE$

$$\oint \omega \mathbf{u} \cdot \mathbf{n} \, \mathrm{d}S = \iint -g' \frac{\partial \rho^*}{\partial x} \, \mathrm{d}A \,, \tag{1.1}$$

where ω and $\mathbf{u}$ represent the vorticity normal to the plane and the velocity vector, respectively, and g' is the reduced gravity defined as $g(\rho_g - \rho_a)/\rho_a$. ρ^* denotes the dimensionless density $(\rho - \rho_a)/(\rho_g - \rho_a)$. $\mathrm{d}A$, $\mathrm{d}S$ and $\mathbf{n}$ indicate a differential area within the control volume, a differential length along the boundaries of the control volume, and the unit outer normal vector to the control volume boundaries. The equation hence states that for a steady solution to exist, the rate at which vorticity is being convected

out of the control volume across boundary BE has to equal the rate at which it is being generated within the control volume by baroclinic production. The vorticity outflux can be evaluated as the vortex sheet strength U_2 times its principal velocity $U_2/2$ [20]. Thus the integral form of the inviscid vorticity conservation equation immediately leads to

$$\frac{1}{2}U_2^2 = g'h \,. \tag{1.2}$$

When combined with the mass conservation equation for the ambient stream

$$UH = U_2(H - h) \,, \tag{1.3}$$

we thus obtain the gravity current velocity as

$$\frac{U}{\sqrt{g'H}} = \sqrt{2\alpha}(1 - \alpha) \,, \tag{1.4}$$

where $\alpha = h/H$. This vorticity-based approach yields results that are different from, but quantitatively similar to those obtained with the model of [1]

$$\frac{U}{\sqrt{g'H}} = \sqrt{\frac{2 - \alpha}{1 + \alpha}(1 - \alpha)\alpha} \,. \tag{1.5}$$

In spite of their quantitatively similar predictions, there exist a few subtle differences between the models of [1] and [19], on which we briefly comment in the following.

1.1 Remarks on the commonalities and differences of Benjamin's and the vorticity model

Both [1] and [19] aim to establish relationships between the flow properties far up- and downstream of the gravity current front, by invoking *integral* conservation laws. Towards this end, both models make certain assumptions such as steady, uniform parallel flow far up- and downstream, slip top and bottom walls, a current that is at rest in the moving reference frame, and a sharp interface. These are, of course, simplifications of the true experimental situation, which is typically unsteady, dissipative and with a diffusive interface. Both models satisfy the integral form of the continuity equation for the ambient fluid, and both models satisfy the integral conservation equation for horizontal momentum, without viscous forces along the top and bottom walls. Up to this point, the models are identical.

The difference arises in how a third equation is obtained. [1] accomplishes this by employing Bernoulli's equation along the streamline upstream of the stagnation point, meaning that a *local* form of the inviscid horizontal momentum equation is employed simultaneously with the *integral* form of the horizontal momentum equation. By evaluating Bernoulli's equation along the upper wall, it is then shown that a head loss exists, unless $h/H = 0.5$. While the model assumes hydrostatic pressure profiles far up- and downstream of the gravity current front, it makes no attempt to incorporate the conservation of vertical momentum across the gravity current front, where the flow is nonhydrostatic as the ambient fluid is accelerated upwards near the front and subsequently turned back into the horizontal direction by the upper wall, with implications for the pressure profile along this wall.

The vorticity model takes a different approach in order to obtain a third equation. It incorporates the principle of vertical momentum conservation by writing the integral

form of the inviscid vorticity conservation equation between the up- and downstream boundaries, as discussed above. By combining this integral vorticity equation with the integral continuity equation we are able to determine the front velocity of the gravity current *without any knowledge of the pressure field.* This finding is consistent with the well known fact that in two-dimensional numerical simulations, the gravity current velocity can be determined from the streamfunction-vorticity form of the Navier-Stokes equations, without solving for the pressure [21]. The observation that the front velocity is solely a function of the conservation of mass and vorticity demonstrates the importance of incorporating vertical momentum conservation into the derivation. Once the front and ambient velocities have been determined from the integral conservation laws for mass and vorticity alone, the vorticity model evaluates the pressure variable directly from the integral conservation relation for horizontal momentum, without invoking Bernoulli's equation anywhere in the flow. We note that by employing the integral form of the inviscid vorticity equation, the vorticity model neglects the diffusive spreading of the interfacial vortex sheet, as well as any diffusive flux of vorticity across the top and bottom walls. For gravity currents propagating into shear, [22] compared DNS results for the traditional slip condition along the walls $\frac{\partial u}{\partial y} = 0$ with those for a no-flux condition $\frac{\partial^2 u}{\partial y^2} = 0$, and found the differences to be negligible.

An interesting observation was made by an anonymous referee: If one were to integrate Bernoulli's equation around the closed curve *BOCDEB*, assuming hydrostatic pressure along the in- and out flow boundaries, one recovers equation (1.2). However, this does *not* imply that the vorticity model effectively employs Bernoulli's equation. Rather, it merely reflects the fact that the front and ambient velocities can be evaluated without any knowledge of the pressure field, and that they do not uniquely determine the pressure field, so that different pressure fields can be constructed that are compatible with these given front and ambient velocities. For example, if identical headlosses exist

along the upper and lower walls, one still recovers equation (1.2). Hence, the correct way of evaluating the pressure is not from Bernoulli's law, but from the integral horizontal momentum equation for the entire control volume. It is easily shown by substitution that the pressure values obtained from integrating Bernoulli's law violate the integral conservation equation for horizontal momentum, except for the case of $h/H = 0.5$.

We can hence summarize the key commonalities and differences between the models by [1] and [19] as follows: The vorticity model is based on the three integral conservation laws for (i) mass of the ambient fluid, (ii) horizontal momentum, and (iii) vorticity. It does not apply Bernoulli's law anywhere, either explicitly or implicitly. The model of [1], on the other hand, is based on (i) the integral form of the continuity equation for the ambient fluid, (ii) the integral conservation law for horizontal momentum, and (iii) Bernoulli's equation along the stagnation point streamline. As mentioned above, despite these subtle differences, the quantitative predictions by the two models are quite close to each other, and they can be viewed as somewhat different approximations to the true experimental situation.

In the following, we extend the vorticity-based modeling approach introduced by [19] and [25] to the gravity currents and intrusions propagating into various background ambients, each of which may include different steady and unsteady sections. Chapter 2 studies intrusions traveling into two-layer statified ambients, while it investigates the possibility of formation of internal bores, which can substantially influence the dynamics of the flow. It also analyzes the energy budget of the flow, and evaluates the rate of conversion of energy between different flow compartments. Chapter 3 applies the vorticity modeling concept to flows which cannot be rendered quasisteady by any appropriate shift of the reference frame, owing to the existence of rarefaction waves. In chapter 4, the propagation of gravity currents into two-layer fluids is investigated, whereas the presence of stratification adds to the complexity of the flow, as it can lead to the emergence

of upstream disturbances in the form of expansion wave or internal bore leading an expansion wave. In chapter 5, we develop a vorticity model for intrusive gravity currents propagating into linear stratifications. This model relies on a second-order PDE suggested by [48] for the vertical displacement of the streamline between the up- and downstream flows, as a function of its vertical inflow location. In all the chapters, the predictions of the present study are compared to the corresponding DNS results as well as the theoretical and experimental data of previous works. Finally, chapter 6 presents the summary of all the findings, gives some concluding remarks, and describes the outlook of this model.

Chapter 2

Intrusive gravity currents into two-layer stratified ambients

Intrusions are conventionally produced in the laboratoy via a *lock-release* or *lock-exchange* procedure. The simplified configuration of such procedure is shown in Fig. 2.1. Here, ρ_c denotes the intermediate density of the intrusion fluid, while the densities of the lower and upper ambient layers are given by ρ_l and ρ_u, respectively. Upon removal of the gate, the intrusion develops and propagates to the right along the horizontal interface. Simultaneously, return flows evolve along the top and bottom walls in the form of left-propagating gravity currents.

The rich history of research into the dynamics of intrusions dates back at least to the investigations by [8] and [9], who studied intrusions propagating along sharp, thin interfaces. [8] explore both bottom and interfacial currents propagating into two-layer stratified ambients. In a reference frame moving with the intrusion front, they consider the intrusion fluid to be at rest, consistent with the pioneering work of [1] who analyzed gravity currents moving into a uniform fluid. Furthermore, they assume that the interface ahead of the intrusion remains undisturbed. The authors enforce the conservation of mass in each of the two ambient layers, as well as the conservation of overall horizontal momentum. In addition, they assume that energy is conserved, so that Bernoulli's equa-
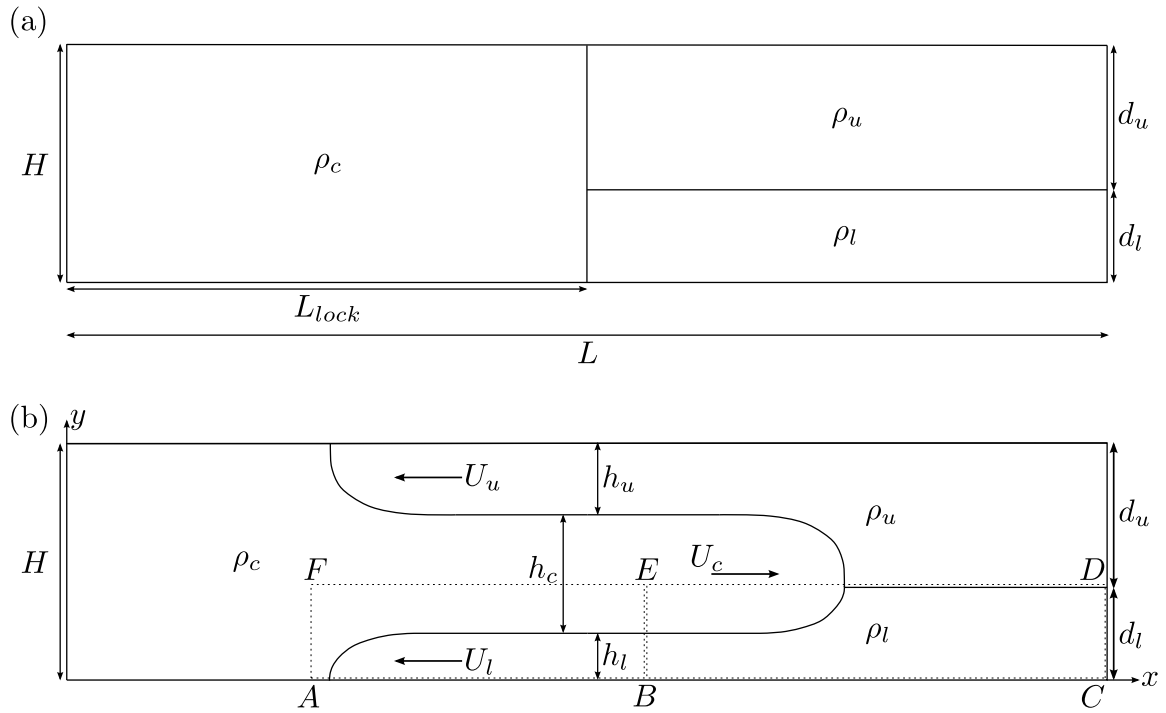
Figure 2.1: Schematic of an intrusion current generated by a lock-release process: Upon removal of the gate, an intrusion of intermediate density ρ_c forms and propagates to the right along the horizontal interface separating heavy fluid of density ρ_l from light fluid of density ρ_u. Concurrently, left-propagating light and dense gravity currents emerge along the upper and lower walls, respectively. The dotted lines indicate the control volumes for which mass and vorticity conservation equations will be formulated below.

tion holds along each of the three interface segments. When solving the resulting system
of equations for the ambient layer depths, the authors find that for a range of initial layer
depths and fluid densities, the solution is nonunique, so that an additional criterion is
required to determine which solution will be seen in the experiment. Based on earlier
studies of dissipative currents, the authors hypothesize that the energy-conserving theo-
retical solution that maximizes the volumetric flow rate is the one that will be observed
experimentally. In this way, they obtain good agreement with corresponding experiments
in terms of the intrusion front velocity. We note, however, that these experiments con-
sider only symmetric intrusions, for which the interface ahead of the intrusion remains
undisturbed. Interestingly, the theoretical arguments developed by [8] are not limited to
Boussinesq flows, but hold for arbitrary density ratios.

[9] carry out experiments for the doubly symmetric configuration, in which the am-
bient layers have equal depths and the intrusion density is the average of the ambient
densities. They focus especially on the influence of the thickness of the interface ahead
of the intrusion. [10] extend this line of research to particle-driven intrusions, for which
they compare experimental observations with predictions by theoretical models that ac-
count for the effect of sedimentation. Further experiments on intrusive gravity currents
by [11] provide information on the detailed structure of the flow. The authors find that
an approximately energy-conserving intrusion head is followed by a wake region, which
is characterized by large billows that result in significant mixing and dissipation. In the
tail region, by contrast, little mixing occurs and the velocity is approximately uniform.
The issues of mixing and entrainment are studied further by [23] for situations in which
successive intrusions propagate into a stratified ambient, so that the interfacial region
gradually widens. The formation of internal and solitary waves in such configurations is
investigated by [12]. A first highly resolved computational investigation into the dynam-
ics of intrusions by [24] reproduces many of the experimentally observed features and

allows for a detailed evaluation of the various components of the energy budget.

[13] simplify the theoretical approach of [8] for situations in which the density con-
trasts among the various fluids are small, so that the Boussinesq assumption can be
invoked. They define the dimensionless parameters Δ

$$\Delta = \frac{d_u - d_l}{H},\tag{2.1}$$

which represents the relative difference in the ambient layer thicknesses, cf. Fig. 2.1, as
well as ϵ

$$\epsilon = \frac{\rho_c - \bar{\rho}}{\rho_l - \rho_u},\tag{2.2}$$

which indicates the deviation of the intrusion density from the so-called equilibrium
density $\bar{\rho} = \frac{\rho_l h_l + \rho_u h_u}{H}$. The case of $\epsilon = 0$ corresponds to the situation in which the
intrusion density equals the depth-weighted mean density of the two ambient layers. The
authors point out that for both the doubly symmetric case with $\Delta = \epsilon = 0$ and the
simple symmetric case, also referred to as the equilibrium case, with $\Delta \neq 0$ and $\epsilon = 0$
the interface ahead of the intrusion remains flat. On the other hand, when $\epsilon \neq 0$, a
leading wave forms along the interface ahead of the intrusion front. This leading wave
affects the energy budget of the flow, so that the discrepancy between predictions by
the original, energy-conserving theory and experimental observations widens. For small,
nonvanishing values of ϵ, [13] conduct a perturbation analysis which results in improved
agreement with experimental data.

[14] further investigate both symmetric and nonsymmetric intrusions. They confirm
the finding by [13] that the interface ahead of the intrusion remains undisturbed for $\epsilon = 0$.
In addition, based on the assumption that all of the initially available potential energy
is converted into kinetic energy, they find that for $\epsilon = 0$ the intrusion velocity has a

minimum, and that for $\Delta = 0$ the speed of the intrusion does not depend on its density. The leading wave traveling ahead of the intrusion extracts relatively little energy from the flow, as will also be discussed in section 2.5. Consequently, [14] still yields acceptable results even far from the equilibrium condition.

[15] develop a theoretical model that accounts for the influence of the upstream leading wave in nonequilibrium intrusion flows. They accomplish this by coupling the mass and streamwise momentum conservation equations for the steady-state flow in the vicinity of the intrusion front to the two-layer shallow water equations for the propagating upstream interfacial wave. This approach, which requires an empirical assumption regarding the wave amplitude, allows them to predict the velocity of nonequilibrium intrusions and to obtain good agreement with experimental observations.

A common theme in the above investigations is the central role of energy considerations. In addition to imposing the conservation of mass and horizontal momentum, existing theoretical models commonly assume either the validity of Bernoulli's equation along certain streamlines, or the conversion of the entire initially available potential energy into kinetic energy. As described in chapter 1, the alternative vorticity-based approach of [19] and [25] for modeling stratified flows, is based on enforcing the conservation of vertical momentum in addition to mass and horizontal momentum, rather than an energy argument. In this way, energy is free to dissipate at a rate dictated by the conservation of mass, horizontal and vertical momenta, consistent with the principles governing incompressible flow. For many models of stratified flows the conservation of vertical momentum can be enforced via the vorticity equation, which typically gives rise to algebraic relationships along individual interfaces between fluids of different densities. In this way, [19] and [25] are able to develop a new class of models for gravity currents and internal bores that yield better agreement with high-resolution, Direct Numerical Simulations (DNS) than earlier models. As pointed out by the authors, these vorticity-

based models enable us to analyze the energy budget of the flows *a posteriori*, after the flow configuration has been determined, so that the rate of energy dissipation can be evaluated explicitly, rather than be assumed *a priori*.

Within the present investigation, we will apply the inviscid vorticity-based modeling approach to both equilibrium and nonequilibrium intrusions in the Boussinesq limit, while the leading wave propagating ahead of the intrusion is treated as a bore. This will allow us to obtain predictions for the intrusion velocity, for the amplitude and propagation velocity of the bore, as well as for the thicknesses and propagation velocities of the ambient counterflows, without the need for empirical, energy-based closure assumptions. We will compare these predictions both to earlier models by other authors, as well as to new, two-dimensional direct numerical simulation Navier-Stokes results, and we will analyze the energetics of the flow fields. This chapter is organized as follows: In sections 2.1 and 2.2, we develop closed theoretical models for symmetric and nonsymmetric intrusions, based on the conservation of mass and vorticity only and without invoking any energy-related arguments. Section 2.3 describes the setup of the corresponding DNS simulations. Section 2.4 discusses the model predictions for various flow properties, including the velocities and thicknesses of all currents and the height and speed of the leading bore. It also compares these predictions to DNS results, and to earlier theoretical and experimental findings by other authors. In section 2.5 we analyze the energy budget of the flow, in order to assess the assumptions underlying earlier models. The influence of the Re and Pe-values in the DNS simulations is discussed in section 2.6. Section 2.7 summarizes the findings and presents the main conclusions.

2.1   Symmetric intrusions

We return to Fig. 2.1 for a full description of the physical problem under considera-
tion. A tank of length L and height H is divided into two compartments by means of a
vertical gate. The right compartment is initially filled up to height d_l with heavy fluid of
density ρ_l. A lighter fluid layer of density ρ_u and thickness d_u is placed above this dense
fluid. The left compartment (the 'lock') of length L_{lock} contains fluid of intermediate
density ρ_c, so that $\rho_u < \rho_c < \rho_l$.

Upon removal of the gate, the intermediate density fluid forms a right-propagating
intrusion of velocity U_c. Simultaneously, two left-propagating gravity currents emerge
along the top and bottom walls: a light one of density ρ_u and height h_u, and a heavy
one of density ρ_l and height h_l. If these two left-propagating currents have identical
front velocities $U_l = U_u$, we refer to the intrusion as symmetric or equilibrium, other-
wise it is called nonequilibrium or nonsymmetric [[13–15]]. For symmetric intrusions, no
fluid crosses the line $y = d_l$, which represents a streamline for all times. [13] observe
experimentally that symmetric intrusions form when

$$\rho_c = \frac{\rho_l d_l + \rho_u d_u}{H} \, . \tag{2.3}$$

[15] demonstrate that this relation is equivalent to what they term the 'neutral buoyancy
condition'

$$g'_u d_u = g'_l d_l \, , \tag{2.4}$$

where $g'_l = g(\rho_l - \rho_c)/\rho_c$ and $g'_u = g(\rho_c - \rho_u)/\rho_c$. They relate this neutral bouyancy
condition to the formation of two left-propagating gravity currents with identical front
velocities. For the special situation of $d_l = H/2$ and $\rho_c = (\rho_l + \rho_u)/2$, the flow is geo-
metrically symmetric with regard to $y = H/2$, and the top and bottom gravity currents

have thicknesses of $H/4$ [9, 10, 12, 13].

The symmetric intrusion case is characterized by the five unknowns U_c, U_l, U_u, h_l and h_u. Since $y = d_l$ represents a streamline, we can solve separately for the flows below and above this line. For the lower part of the tank, the three unknowns U_c, U_l and h_l are governed by the mass conservation equation within the control volume $BCDE$ (Fig. 2.1) in the reference frame moving with the front of the interfacial current

$$U_c d_l = (U_l + U_c)h_l \,, \tag{2.5}$$

as well as two vorticity conservation equations for the two fronts, while we assume the flow is inviscid, Boussinesq and quasisteady [19, 25]. In the reference frame of the interfacial gravity current, we obtain for the control volume $BCDE$

$$g'_l(d_l - h_l) = \frac{1}{2}(U_l + U_c)^2 \,, \tag{2.6}$$

and in the reference frame of the bottom current, the conservation of vorticity in control volume $ABEF$ yields

$$g'_l h_l = \frac{1}{2}(U_l + U_c)^2 \,. \tag{2.7}$$

Solving these three equations results in

$$h_l = \frac{d_l}{2} \,, \tag{2.8}$$

$$U_c = U_l = \frac{1}{2}\sqrt{g'_l d_l} \,. \tag{2.9}$$

Corresponding considerations for the region above $y = d_l$ yield

$$h_u = \frac{d_u}{2}, \tag{2.10}$$

$$U_c = U_u = \frac{1}{2}\sqrt{g'_u d_u}. \tag{2.11}$$

This demonstrates that the condition (2.4) formulated by [15] for the formation of symmetric intrusions can be derived from the conservation of mass and momentum alone.

At this point, it is useful to introduce characteristic scales for length $(x_{ref} = H)$, velocity $(U_{ref} = \sqrt{g'H})$ and density difference $(\rho_l - \rho_u)$, where $g' = (\rho_l - \rho_u)/\rho_c$, so that we can define dimensionless variables of the form

$$x^* = \frac{x}{H}, \tag{2.12}$$

$$U^* = \frac{U}{\sqrt{g'H}}, \tag{2.13}$$

$$\rho^* = \frac{\rho - \rho_u}{\rho_l - \rho_u}. \tag{2.14}$$

In this way, the dimensionless solution for the case of a symmetric intrusion takes the form

$$h_l^* = \frac{d_l^*}{2}, \tag{2.15}$$

$$h_u^* = \frac{d_u^*}{2}, \tag{2.16}$$

$$U_c^* = U_l^* = U_u^* = \frac{1}{2}\sqrt{(1 - \rho_c^*)d_l^*}. \tag{2.17}$$

Furthermore, equation (2.3) in dimensionless form yields $\rho_c^* = d_l^*$. Hence, for symmetric intrusions the dimensionless interface height equals the dimensionless intrusion density.

Consequently, we can rewrite equation (2.17) equivalently as

$$U_c^* = U_l^* = U_u^* = \frac{1}{2}\sqrt{\rho_c^* d_u^*} = \frac{1}{2}\sqrt{d_l^* d_u^*}. \tag{2.18}$$

Since for the symmetric case the left-propagating gravity currents as well as the intrusion are effectively half-depth currents in the sense of [1], it follows that they conserve energy. Hence it is not surprising that for symmetric intrusions the present results agree with those of earlier investigations by [8], [13], [14] and [15], all of whom had invoked energy conservation arguments. These theoretical solutions will be compared to experimental and DNS simulation data in section 2.4.

2.2 Nonsymmetric intrusions with upstream leading bore

When the symmetry condition (2.4) is not satisfied, the left-propagating gravity currents along the upper and lower walls will exhibit different front velocities. In the following, we will discuss and compare two different models for the resulting nonequilibrium intrusion. Model 1, depicted in Fig. 2.2, is inspired by the experiments of [13], which demonstrate the presence of a leading wave propagating ahead of the interfacial gravity current. In the following, we will model this leading wave as a bore. The alternative model 2, shown in Fig. 2.3, is based on simulation results from the present study to be discussed below. It differs from model 1 in that it also allows for the existence of an internal bore on the faster of the two left-propagating gravity currents, at the same streamwise location as the front of the slower gravity current. We will discuss the significance of including this left-propagating bore, later in section 2.4.

In contrast to the five unknowns that fully describe the symmetric problem, nonsym-
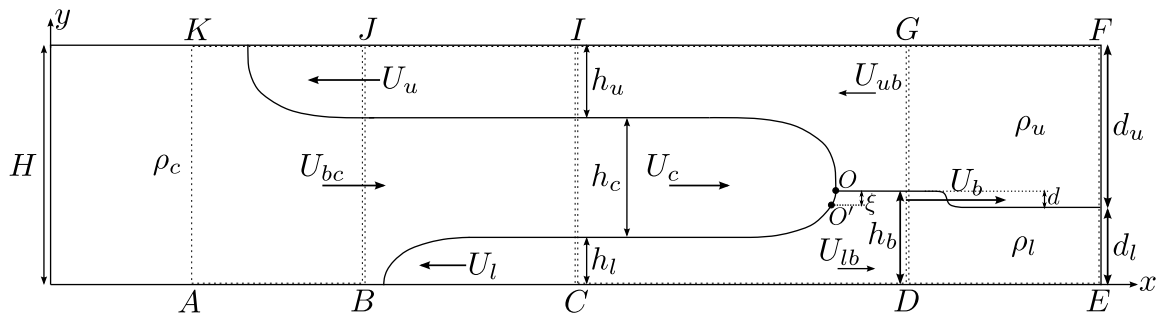
Figure 2.2: Schematic of a nonsymmetric or nonequilibrium intrusion with $(\rho_c - \rho_u)/(\rho_l - \rho_u) > d_l/H$. A leading bore travels along the interface ahead of the intrusion, with a larger velocity than the intrusion itself. The dotted lines indicate the control volumes for which mass and vorticity conservation equations will be formulated below. We refer to this model as 'model 1' in the text.

metric intrusions give rise to several additional unknown variables. For the leading bore, these involve the wave speed U_b and the interface height h_b downstream of the wave, as well as the downstream upper and lower layer velocities U_{lb} and U_{ub}. In addition, we need to solve for the intrusion velocity U_{bc} in the region between the gravity current fronts, so that model 1 is characterized by a total of ten unknown quantities. Hence, ten independent conservation equations are required for a full description. Model 2 results in two additional unknowns, *viz.* U'_u and h'_u, compared to model 1.

Corresponding to our earlier analysis of the symmetric case, we can formulate the equations for the nonsymmetric case by considering the conservation of mass and vorticity in various control volumes. We begin by focusing on control volume $DEFG$, in the reference frame moving with the leading bore. It is worth-mentioning that however we model this interfacial disturbance propagating ahead of the intrusive gravity current as a bore, some previous studies such as [15] have treated that as a nonlinear wave. Our assumption means, we suppose this instability travels with a constant speed and the ambient interface after it will find a constant height. This is also another simplification, because some undulations will emerge along the interface, right after this instability.

Figure 2.3: Alternative model for a nonequilibrium intrusion with $(\rho_c - \rho_u)/(\rho_l - \rho_u) > d_l/H$. Here, in addition to leading bore ahead of interfacial gravity current, the faster propagating gravity current along the upper wall exhibits a bore at the same streamwise location as the front of the slower gravity current along the lower wall. The dotted lines indicate the control volumes for which mass and vorticity conservation equations will be formulated below. We refer to this model as 'model 2' in the text.

Regardless, these assumptions look reasonable and yield acceptable results as shown in sections 2.3 and 2.4. Mass conservation for the upper and lower layers, and vorticity conservation along the interface, give

$$U_b d_l = (U_b - U_{lb})h_b, \tag{2.19}$$

$$U_b d_u = (U_b + U_{ub})(H - h_b), \tag{2.20}$$

$$g'(h_b - d_l) = \left(U_b + \frac{U_{ub} - U_{lb}}{2}\right)(U_{lb} + U_{ub}). \tag{2.21}$$

Equations (2.19) to (2.21) can be applied to both models 1 and 2, without any modifications. Next, we focus on control volume $CDGI$ for model 1 shown in Fig. 2.2, in the reference frame moving with the intrusion. The two continuity equations for the upper and lower layer can be written in straightforward fashion as

$$(U_c - U_{lb})h_b = (U_c + U_l)h_l, \tag{2.22}$$

$$(U_c + U_{ub})(H - h_b) = (U_c + U_u)h_u. \tag{2.23}$$

Formulating separate vorticity conservation equations along the upper and lower interface branches requires some additional thought, as we need to determine how the vorticity inflow from the upstream of cross-section GD in Fig. 2.2 and 2.3, $\left(U_c + \frac{U_{ub} - U_{lb}}{2}\right)(U_{ub} + U_{lb})$, is divided up among these two interface branches separating ambient fluids. In this context, a thought experiment is instructive: Imagine that in the initial configuration the upper and lower fluid layers in the right compartment are separated by an infinitesimally thin layer of fluid with density ρ_c, so that there are effectively two separate interfaces connecting the left-propagating gravity current fronts to the upstream of leading bore. It is straightforward to write down the individual vorticity conservation equations for these two separate interfaces. By letting the thickness of this initial, intermediate fluid layer in the right compartment go to zero, we obtain

$$-g_l'(h_b - h_l) + \frac{g_l'}{g'}\left(U_c + \frac{U_{ub} - U_{lb}}{2}\right)(U_{ub} + U_{lb}) = -\frac{1}{2}(U_l + U_c)^2, \quad (2.24)$$

$$g_u'(H - h_b - h_u) + \frac{g_u'}{g'}\left(U_c + \frac{U_{ub} - U_{lb}}{2}\right)(U_{ub} + U_{lb}) = \frac{1}{2}(U_u + U_c)^2. \quad (2.25)$$

The corresponding equations for model 2 take the form

$$(U_c - U_{lb})h_b = (U_c + U_l)h_l, \quad (2.26)$$

$$(U_c + U_{ub})(H - h_b) = (U_c + U_u')h_u', \quad (2.27)$$

$$-g_l'(h_b - h_l) + \frac{g_l'}{g'}\left(U_c + \frac{U_{ub} - U_{lb}}{2}\right)(U_{ub} + U_{lb}) = -\frac{1}{2}(U_l + U_c)^2, \quad (2.28)$$

$$g_u'(H - h_b - h_u') + \frac{g_u'}{g'}\left(U_c + \frac{U_{ub} - U_{lb}}{2}\right)(U_{ub} + U_{lb}) = \frac{1}{2}(U_u' + U_c)^2. \quad (2.29)$$

Control volume $BCIJ$, in the reference frame moving with the lower gravity current

front, provides the vorticity equation

$$g_l' h_l = \frac{1}{2}(U_l + U_c)^2 \,. \tag{2.30}$$

For model 2, it gives rise to the additional equations for the conservation of mass and vorticity for the internal bore of the faster current

$$(U_{bc} + U_l)(H - h_u) = (U_c + U_l)(H - h_l - h_u') \,, \tag{2.31}$$

$$g_u'(h_u' - h_u) + \left(U_l + \frac{U_{bc} - U_u}{2}\right)(U_u + U_{bc}) = \left(U_l + \frac{U_c - U_u'}{2}\right)(U_u' + U_c) \,. \tag{2.32}$$

The simulation results to be discussed below indicate that the internal bore of the faster gravity current is located at the same streamwise location as the front of the slower current, so that

$$U_l = U_w \,. \tag{2.33}$$

The final two equations are obtained for control volume $ABJK$, by formulating the conservation of mass and vorticity in the reference frame of the upper gravity current front

$$U_u H = (U_{bc} + U_u)(H - h_u) \,, \tag{2.34}$$

$$g_u' h_u = \frac{1}{2}(U_u + U_{bc})^2 \,. \tag{2.35}$$

Model 1 is completely described by equations (2.19) to (2.25), in addition to (2.30), (2.34) and (2.35). Model 2, on the other hand, is governed by equations (2.19) to (2.21), along with (2.26) to (2.35). Note that these respective systems of algebraic equations are closed, so that they do not require any closure assumptions. Specifically, they were derived without any considerations of energy arguments. While analytical solutions for these

systems of nonlinear algebraic equations cannot be obtained under general conditions, they can be solved numerically in straightforward fashion via using a bisection root solver. The solutions, rendered dimensionless according to (2.12) to (2.14), will be discussed in the following. We remark that the numerical solution procedure gave no indication of multiple solutions anywhere in the parameter regime for models 1 and 2. This is in contrast to the models employed in the earlier investigations by [8] and [13], which had obtained nonunique solutions for a range of interface heights and intrusion densities.

2.3   DNS simulations

In order to assess the validity and predictive capability of the above models, we will present comparisons with earlier models of [8], [14] and [15], as well as with direct numerical simulations of the unsteady two-dimensional Navier-Stokes equations in the Boussinesq limit. These simulations were conducted with our code TURBINS, which has been described and validated in detail by [26] and [27]. TURBINS is a finite-difference solver based on a fractional step projection method, along with TVD-RK3 time integration. It solves the dimensionless conservation equations for mass, momentum and density

$$\nabla\cdot\mathbf{u}^* \;=\; 0\,, \tag{2.36}$$

$$\frac{\partial\mathbf{u}^*}{\partial t^*} + \mathbf{u}^*\cdot\nabla\mathbf{u}^* \;=\; -\nabla p^* + \frac{1}{Re}\nabla^2\mathbf{u}^* + \rho^*\mathbf{e}^g\,, \tag{2.37}$$

$$\frac{\partial\rho^*}{\partial t^*} + \mathbf{u}^*\cdot\nabla\rho^* \;=\; \frac{1}{Pe}\nabla^2\rho^*\,, \tag{2.38}$$

where $\mathbf{e}^g$ represents the unit vector in the direction of gravity and t^* is defined as t/t_{ref}, where $t_{ref} = H/\sqrt{g'H}$. The dimensionless parameters in the form of a Reynolds number

22

Re and a Péclet number Pe are defined as

$$Re = \frac{u_b H}{\nu}, \qquad (2.39)$$

$$Pe = \frac{u_b H}{D}. \qquad (2.40)$$

As stated earlier, the buoyancy velocity u_b is given by $\sqrt{g'H}$, with the channel height H representing the characteristic length scale. ν and D indicate the kinematic viscosity and the diffusivity of the density field, respectively. We apply free slip conditions for the velocity, along with vanishing normal flux conditions for the density field, along all solid boundaries. The Reynolds and Péclet numbers are set to 12,000 and 30,000 in the simulations, unless stated otherwise. These fairly high Re and Pe numbers result in a relatively minor influence of viscosity and diffusion on the current velocities and heights. The fluid is at rest initially, with the density field specified according to Fig. 2.1 as

$$\rho^* = \begin{cases} \rho_c^* & \text{if } x^* \leq L_{lock}, \\ 1 & \text{if } x^* > L_{lock} \text{ and } y^* \leq d_l^*, \\ 0 & \text{otherwise}. \end{cases} \qquad (2.41)$$

The computational domain has a dimensionless length of 60 and a height of 1, and the lock length is set to 30. The computational grid has a uniform spacing of $\Delta x^* = 0.01$ and $\Delta y^* = 0.005$, which is sufficiently fine not to influence the simulation results.

Figure 2.4 shows the evolution of the doubly symmetric case with $d_l = H/2$ and $\rho_c = (\rho_l + \rho_u)/2$. The left-propagating gravity currents along the upper and lower walls and the right-propagating intrusion all have identical front velocities. For comparison, Fig. 2.5 presents the case of an equilibrium intrusion with $\rho_c^* = d_l^* = 0.3$. The slightly different
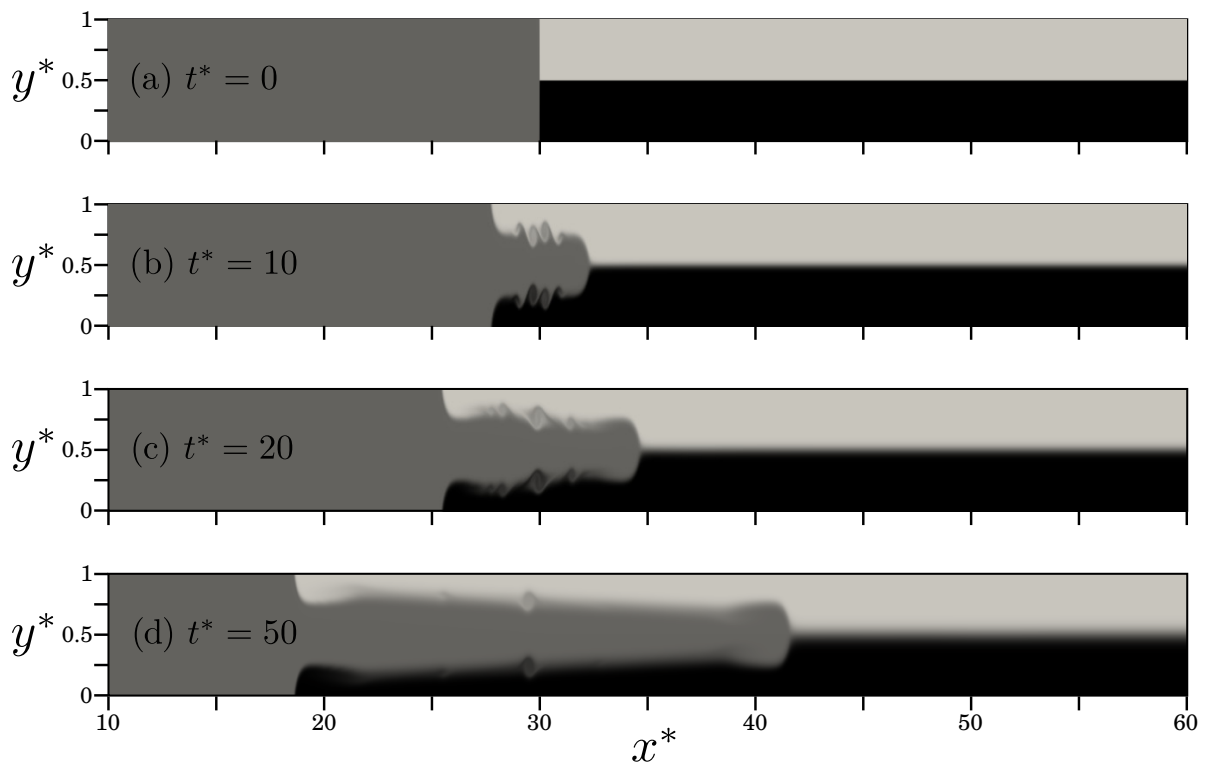
Figure 2.4: Evolution of the density field for a doubly symmetric intrusion starting from rest. In dimensionless form, the initial conditions of the problem are $\rho_c^* = d_l^* = 0.5$. The density field varies from $\rho^* = 0$ (light gray) to $\rho^* = 1$ (black).
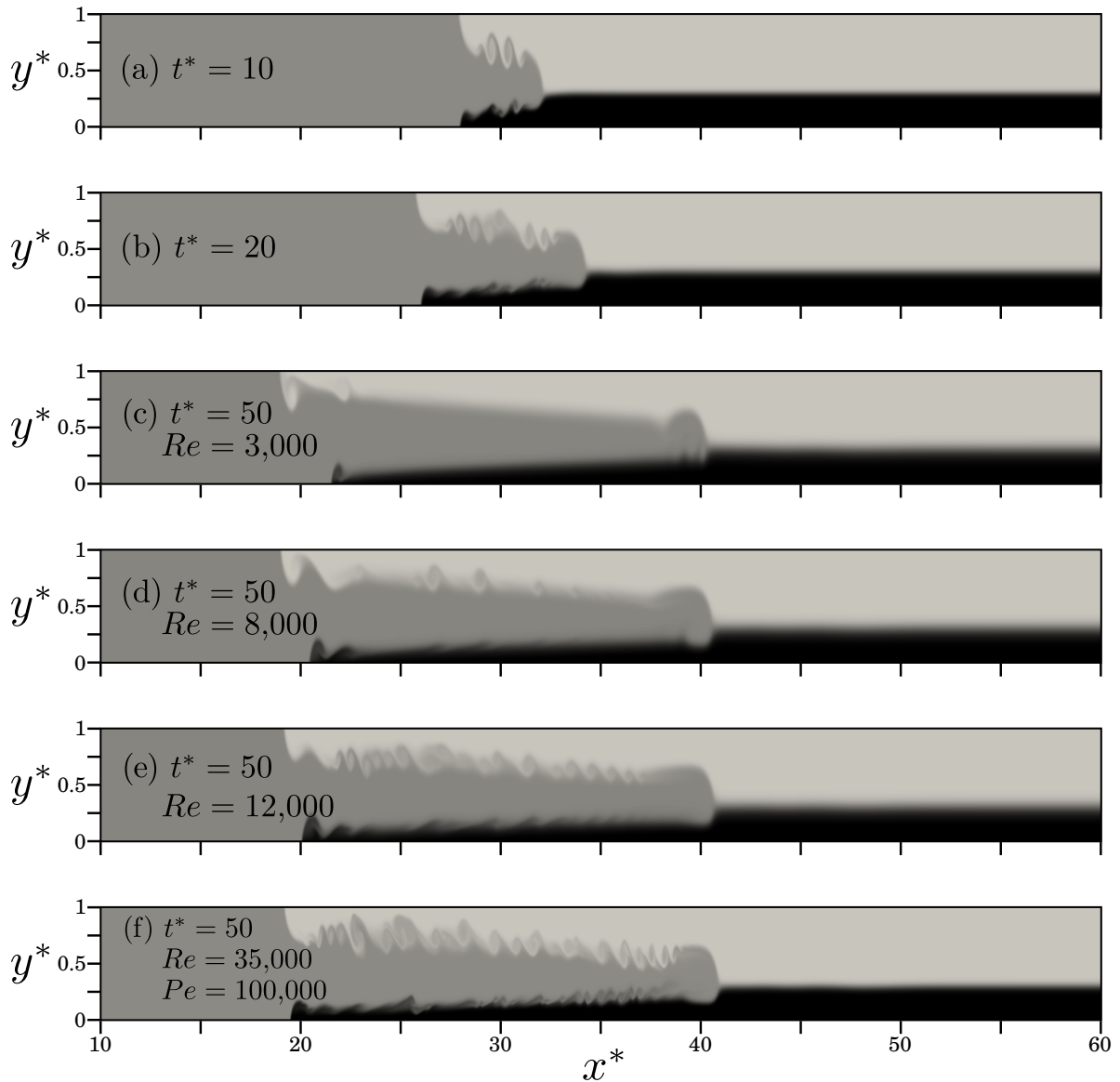
Figure 2.5: Evolution of an equilibrium intrusion for $\rho_c^* = d_l^* = 0.3$. While the inviscid model predicts that the left-propagating gravity currents should have identical front velocities, the viscous simulation yields slightly different front speeds. For increasing Reynolds numbers, however, these front velocities are increasingly close to each other. As predicted by the model, the interface ahead of the intrusion remains undisturbed.

front velocities of the two left-propagating gravity currents are a consequence of the finite Reynolds number in the simulation, which implies that the top and bottom currents effectively have different Reynolds numbers based on their individual heights. This is confirmed by the simulation results for $Re = 3,000$, $8,000$ and $12,000$ shown in frames c, d and e of Fig. 2.5, which indicate that the front velocities of the left-propagating currents approach each other as the Reynolds number is increased. Frame f demonstrates an extreme case with $Re = 35,000$ and $Pe = 100,000$, for which the difference in the front velocities of the left-propagating currents has become quite small. This simulation was carried out with a resolution two times finer in the horizontal direction and three times finer in the vertical direction. In spite of the symmetry-breaking due to these slightly different front velocities, we recognize that the right-propagating intrusion does not give rise to a leading bore along the horizontal interface.

Figure 2.6 illustrates the case of a nonequilibrium intrusion for $\rho_c^* = 0.5$ and $d_l^* = 0.3$. In this case, the front velocities of the left-propagating gravity currents along the top and bottom walls differ substantially. Along the horizontal interface separating the dense from the light fluid, the advancing intrusion causes the formation of an undular bore that propagates significantly faster than the intrusion itself. In addition, closer inspection of the upper gravity current at time $t^* = 50$ reveals the existence of a bore near the streamwise location of the lower current front, consistent with the sketch of model 2 in Fig. 2.3 above. Additional simulations for a broad range of ρ_c^* and d_l^* (not shown) confirm this observation. These DNS results are fully consistent with the earlier experimental observations of [9], [10], [12], [13] and [14].

In order to obtain accurate values for the front velocities of all currents, we mark the fluid corresponding to each current by means of a passive scalar ('dye'), which is tracked in the simulation as a separate concentration field, with the same Pe-value as the density field. We can then define the front position x_f^* as the location where the local
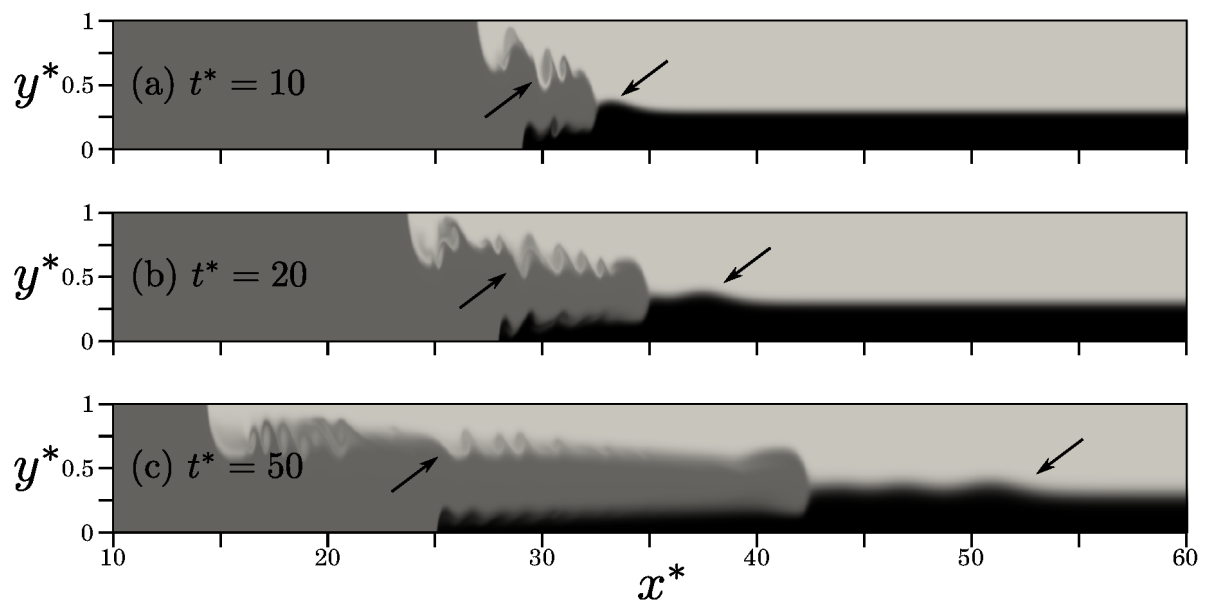
Figure 2.6: Evolution of a nonsymmetric intrusion for $\rho_c^* = 0.5$ and $d_l^* = 0.3$. For this nonequilibrium case, the left-propagating currents have different front velocities, and two internal waves form: one propagates to the right ahead of the interfacial gravity current, and the other one travels along the interface of the faster left-propagating gravity current, at the same streamwise location as the front of the slower current. The locations of these internal waves are indicated by arrows in the figure.
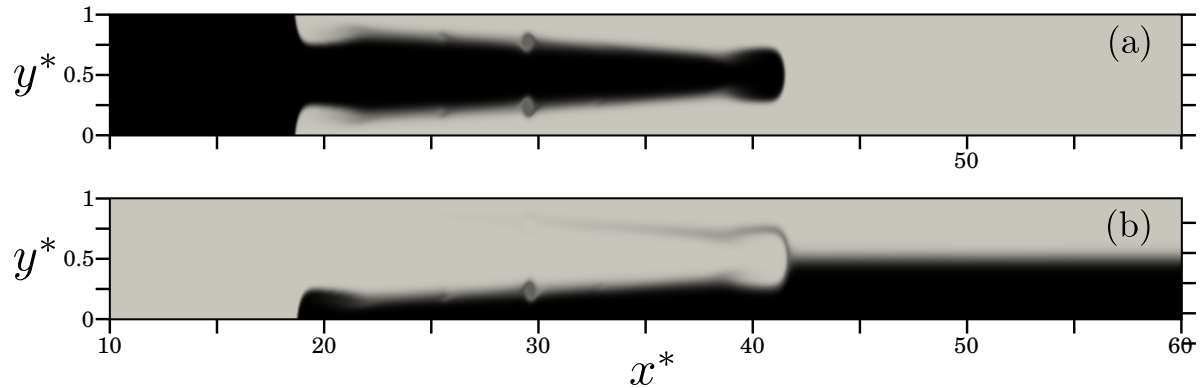
Figure 2.7: By marking the fluid of each current with dye, we can evaluate the current heights and velocities, as described in detail in the text.

dimensionless current height computed as

$$\eta^*(x^*, t^*) \;=\; \int_0^1 c_d^*(x^*, y^*, t^*) \; \mathrm{d}y^* \,. \tag{2.42}$$

first exceeds a value of 0.01. Here c_d^* denotes the dimensionless dye concentration, and η^* indicates the local height of a current. Figure 2.7 provides examples for tracking the intrusion and lower gravity current fluids, respectively.

Figure 2.8 shows the front locations as functions of time, for the symmetric and nonsymmetric intrusions of Figs. 2.4 to 2.6. After an initial transient, each current propagates with a quasisteady velocity, in spite of continuously evolving interfacial instabilities and mixing. The straight line segments indicate the respective quasisteady front velocities, obtained by linear fits of the DNS results.

The quasisteady heights of the left-propagating currents are obtained as follows. For the slower one, we determine the effective height h^* by evaluating

$$h^* = \frac{\int_{x_f^*}^{L_{lock}^*} \eta^*(x^*, t_s^*) \; \mathrm{d}x^*}{L_{lock}^* - x_f^*} \,. \tag{2.43}$$
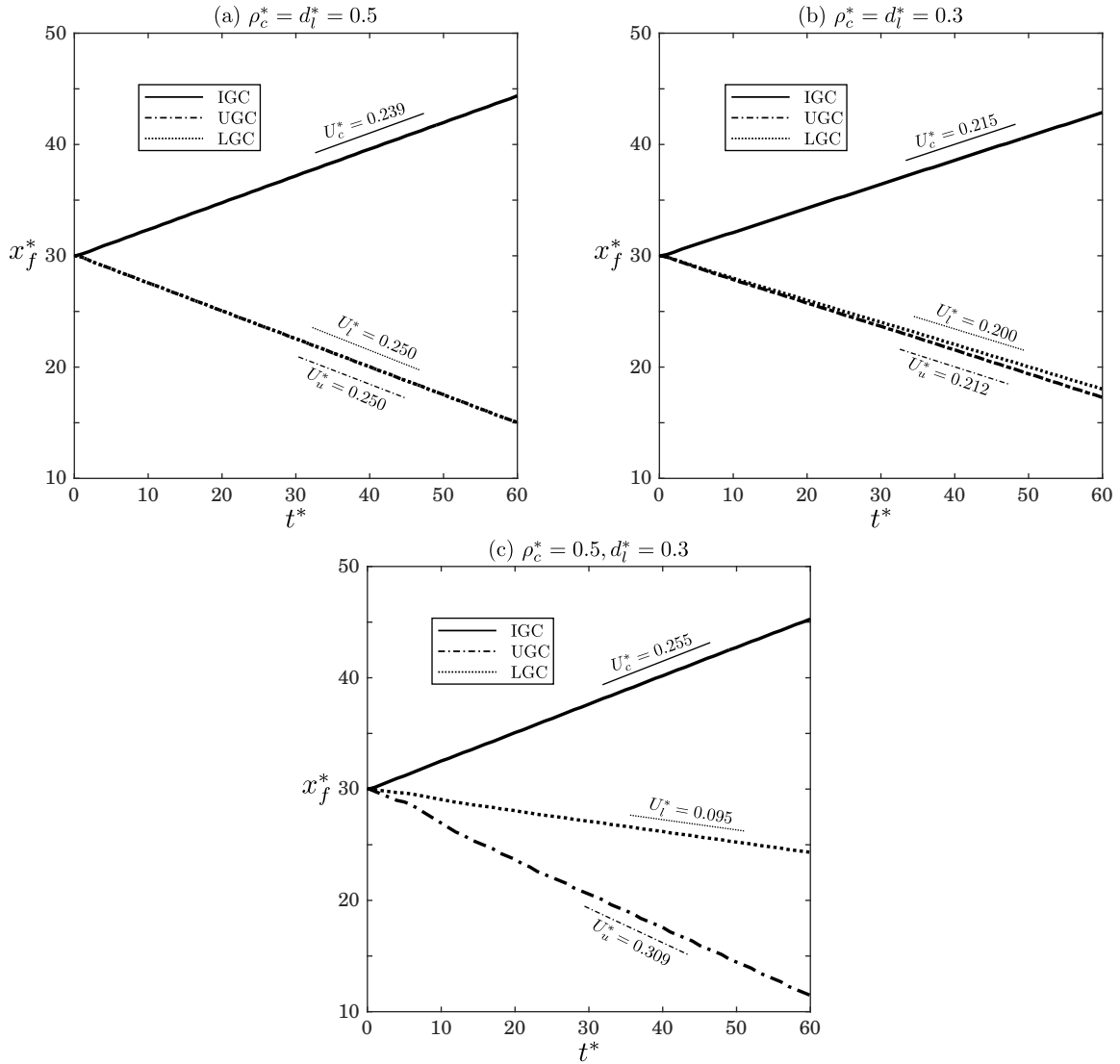
28

Figure 2.8: Simulation results for the front locations as functions of time, for the flows shown in Figs. 2.4 to 2.6. Here, IGC stands for Interfacial Gravity Current, while UGC and LGC denote Upper Gravity Current and Lower Gravity Current, respectively. The straight line segments represent the quasisteady front velocities, obtained by linear fits of the DNS results.
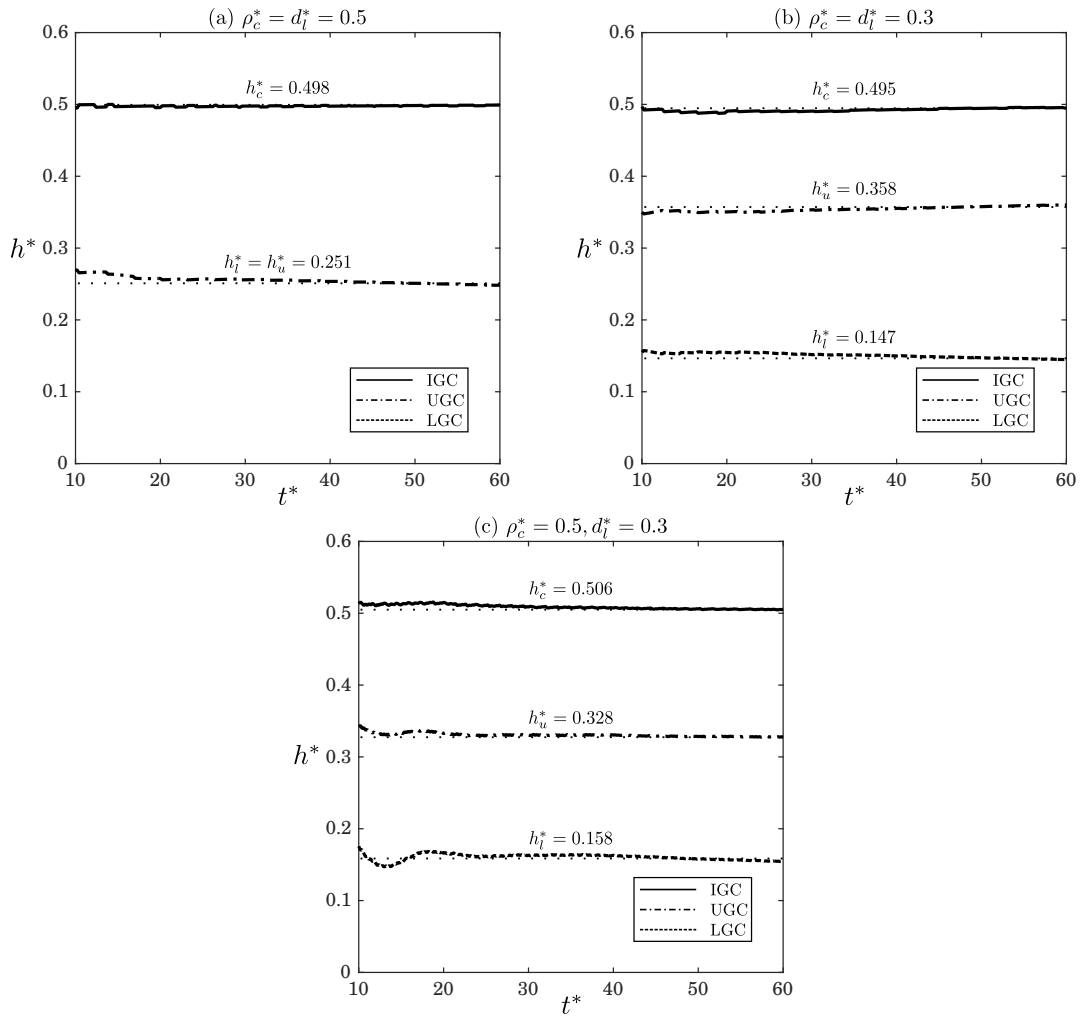
Figure 2.9: Effective current heights h_l^* and h_u^* as functions of time, for the flows shown in Figs. 2.4 to 2.6. The solid and dash-dotted lines indicate the instantaneous heights of the lower and upper gravity currents, respectively. The dotted horizontal lines indicate the quasisteady values evaluated at $t^* = 50$.
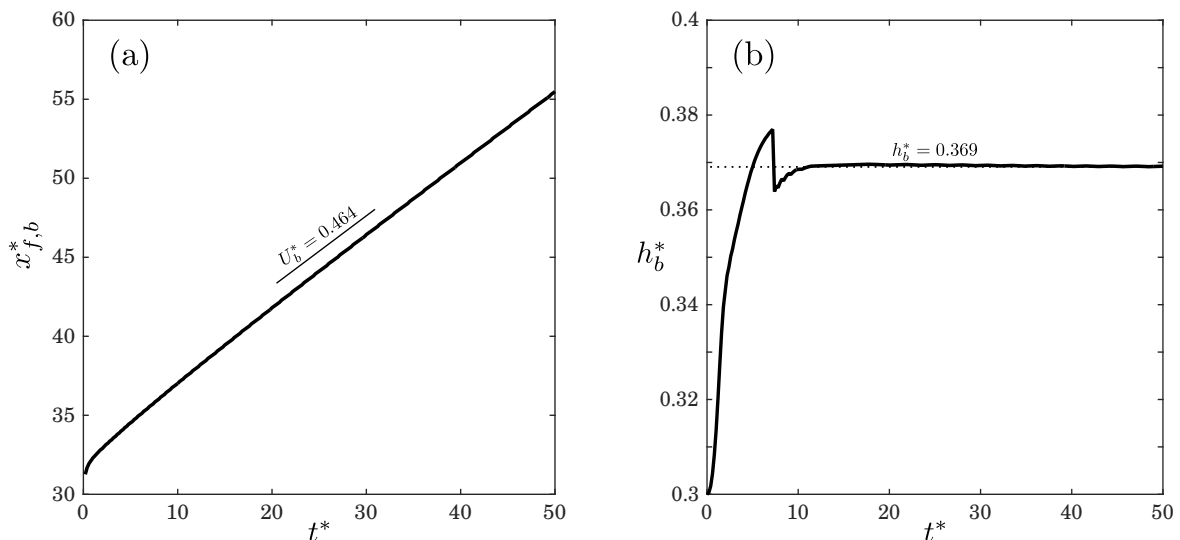
Figure 2.10: Variation of the (a) front location, and (b) height of the right-propagating internal bore as a function of time, for the nonsymmetric intrusion shown in Fig. 2.6.

where x_f^* indicates the front location of slower left-propagating current and t_s^* is chosen sufficiently large to ensure that the solution is quasisteady. For the faster moving gravity current, we determine the effective height correspondingly by integrating over the x-interval from the front of the faster moving current to the front of the slower moving current, and finally, the interfacial gravity current height can be computed by taking the integration over the x-interval from L_{lock}^* to the front of this current. Figure 2.9 demonstrates that these effective current heights indeed approach quasisteady values. In order to compare the DNS simulation results with predictions by the vorticity model, we employ the current heights at time $t_s^* = 50$, when they have reached quasisteady values.

The velocity U_b^* and height h_b^* of the right-propagating bore are evaluated as follows. As the bore propagates along the interface, it deflects this interface upward or downward, thereby causing a rapid change in $\partial\rho^*/\partial x^*$ along $y^* = d_l^*$. By starting at the right wall and sweeping leftward along $y^* = d_l^*$, we identify the x-location where $\partial\rho^*/\partial x^*$ first exceeds 0.01, and take this as the location of the bore. Figure 2.10a shows the front

location of the bore as a function of time, for the nonsymmetric case of Fig. 2.6. After a brief initial transient, we observe that the bore propagates with a constant velocity. It also validates that assuming a constant velocity for this instability and treating it like a bore, is in accordance with the simulations.

From equation (2.42) we can evaluate the local interface height η_b^* as function of time. We can then define the effective bore height h_b^* as the average height of the interface over the x-interval from the bore front location $x_{f,c}^*$ to the interfacial gravity current nose $x_{f,b}^*$

$$h_b^* = \frac{\int_{x_{f,c}^*}^{x_{f,b}^*} \eta_b^*(x^*, t_s^*) \, \mathrm{d}x^*}{x_{f,b}^* - x_{f,c}^*} \,. \tag{2.44}$$

where we take $t_s^* = 50$ to ensure a quasisteady result, as indicated by Fig. 2.10b. Regardless of the undular nature of this bore, the average height of the interface behind the bore reaches a constant value. The deflection in the interface height can be evaluated as

$$d^* = |h_b^* - d_l^*| \,. \tag{2.45}$$

2.4   Discussion of results

In the following, we will discuss DNS simulation results and compare them with predictions by the vorticity model and by earlier models of other authors, as well as with earlier experimental observations. For the equilibrium intrusion case, where $\rho_c^* = d_l^*$, the vorticity model predictions are based on the symmetric configuration of Fig. 2.1, while for nonequilibrium cases we employ the model 2 configuration, depicted by Fig. 2.3. We will also compare model 2 with model 1 at the end of this section. We note that in the limit of $d_l^* \to \rho_c^*$, the predictions for the nonsymmetric case smoothly approach those of the symmetric case for all physical variables. To discuss the physical results,
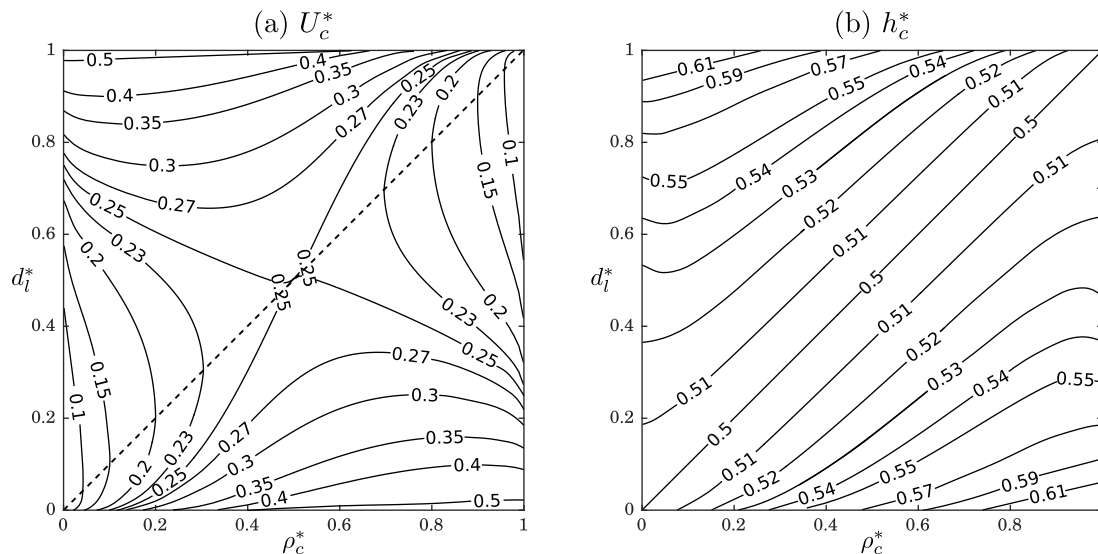
Figure 2.11: Phase-space diagram for (a) the intrusion velocity U_c^*, and (b) the intrusion thickness h_c^*. Equilibrium intrusions form along the diagonal $d_l^* = \rho_c^*$. For a given ρ_c^*, the minimum velocity is seen to occur for the equilibrium intrusion, located on the dashed diagonal line.

we employ phase-space plots in the ρ_c^*, d_l^*,-plane. Figure 2.11a shows vorticity model predictions for the intrusion velocity U_c^*. For the case of a doubly symmetric intrusion with $\rho_c^* = d_l^* = 0.5$, the model predicts $U_c^* = 0.25$, which is consistent with the earlier results of [1] and [19] for energy-conserving currents, when rescaled for half the tank height. For the limiting cases of ($\rho_c^* = 0$, $d_l^* = 1$) and ($\rho_c^* = 1$, $d_l^* = 0$) the model predicts front velocities near one half, but not exactly equal to one half. As we will see below, this reflects the fact that as $d_l^* \to 0$ or 1, the bore height does not approach zero. In other words, the limits of $d_l^* \to 0$ and 1 are singular, in the sense that the flow does not reduce to the case of a full-depth lock-release gravity in a smooth fashion. We remark that the doubly symmetric case represents a point of symmetry for the figure, so that an intrusion with (ρ_c^*, d_l^*) has the same velocity as one with ($1 - \rho_c^*$, $1 - d_l^*$). Recall that [14] found that for a fixed value of d_l^* the intrusion speed does not depend on the intrusion density. The vorticity model shows that in the range $0.2 < \rho_c^* < 0.8$ the
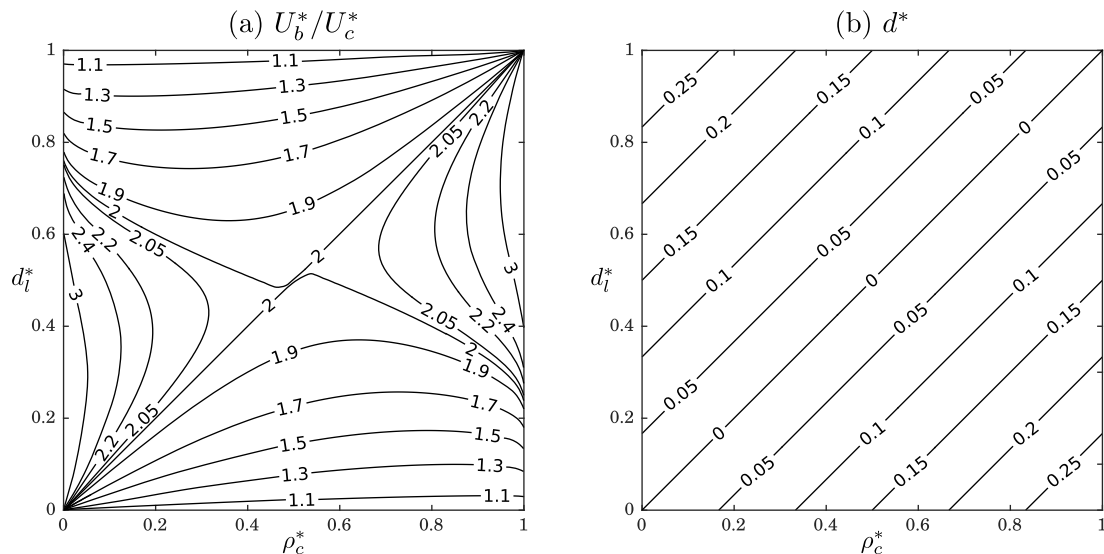
Figure 2.12: (a) Phase-space diagram for the ratio of the leading bore speed to the intrusion speed U_b^*/U_c^*. For equilibrium intrusions $U_b^*/U_c^* = 2$, consistent with the value for linear long waves. (b) Phase-space diagram for the interfacial deflection d^* due to the leading bore. d^*, defined by equation (2.45), varies linearly with the magnitude of difference between ρ_c^* and d_l^*.

intrusion velocity indeed varies only weakly with the density. However, for very small or large intrusion densities, the intrusion speed depends more strongly on its density. [14] had furthermore observed that for a fixed intrusion density, the equilibrium configuration has the minimum propagation velocity. This is confirmed by the contours of Fig. 2.11a, which have their extrema along the main diagonal. Figure 2.11b shows corresponding results for the intrusion thickness h_c^*. Along the main diagonal $\rho_c^* = d_l^*$, we find that h_c^* has a constant value of 0.5, which is consistent with the observation that for $\rho_c^* = d_l^*$ we obtain energy-conserving equilibrium intrusions. Away from the diagonal the intrusion thickness increases, which suggests that it is gaining energy. We will return to this point in section 2.5.

Figure 2.12a shows the phase-plane diagram for the ratio U_b^*/U_c^* of the bore velocity to the intrusion velocity, while 2.12b presents corresponding results for the bore height. The

bore height is seen to vanish along the diagonal $\rho_c^* = d_l^*$, consistent with the formation of equilibrium intrusions. As mentioned above, in the limits of $d_l^* \to 0$ or 1, the bore height does not approach zero, so that the flow does not reduce to a full-depth lock-exchange gravity current in a smooth fashion.

As pointed out by [13] and [15], in the limit of vanishing height bores travel with the speed of long waves, so that $U_b^*/U_c^* \to 2$. This is confirmed by Fig. 2.12a. Furthermore, in the limits of $d_l^* \to 0$ or 1, U_b^*/U_c^* barely exceeds one, so that the intrusion moves almost as fast as the leading bore. We note that all contours in Fig. 2.12b are parallel to the main diagonal and equidistant, which suggests that the bore height depends only on the difference between ρ_c^* and d_l^*, and this dependence is linear, as will be demonstrated more clearly, later in Fig. 2.17. This is consistent with earlier observations by [14] and [15]. We note that for the relation $d^* = \Lambda(\rho_c^* - d_l^*)$ the current model predicts approximately the same value of Λ as those of the two earlier investigations, which corroborates the assumptions made in those studies.

Figure 2.13 displays phase-plane results for the velocities and thicknesses of the left-propagating upper and lower gravity currents. For increasing ρ_c^* and decreasing d_l^* the bottom-propagating gravity current slows down, due to a decrease in its available potential energy. In fact, for large values of ρ_c^* and small values of d_l^* the bottom current can have a negative front velocity, so that it travels to the right. Corresponding results are obtained for the top current. Note that for $d_l^* \approx 1$ and small ρ_c^* the vorticity model predicts values of the lower gravity current velocity $U_l^* > 0.8$. This is much larger than the value of one half for a full-depth lock-exchange gravity current, which again indicates that the limits of $d_l^* \to 0$ and 1 are singular. This singularity may be a consequence of treating the interfacial disturbance as a bore, which may no longer be valid as we approach these limits. It furthermore suggests that in this limit the lower gravity current in the intrusion configuration is gaining energy. We will return to this issue below.
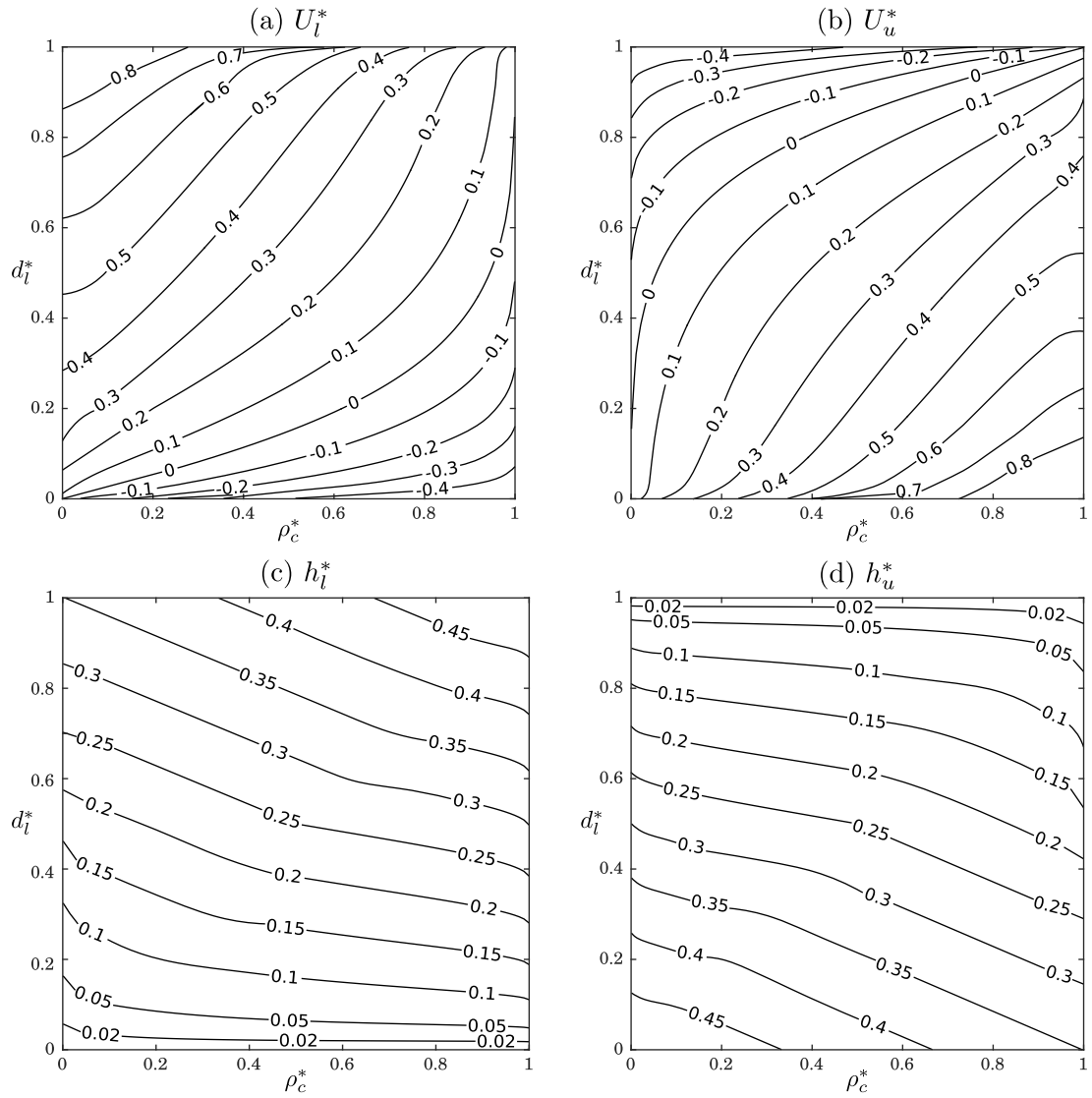
Figure 2.13: Phase-space diagram for the the velocities (U_l^*, U_u^*) and heights (h_l^*, h_u^*) of the lower and upper gravity currents. A discussion of the results is provided in the text.

The behavior of the gravity current height contours is interesting as well. As demonstrated by Figs. 2.13c and 2.13d, for a constant intrusion density, the isolines are approximately equidistant over a large range of d_l^* which suggests a nearly linear variation of h_l^* and h_u^* with d_l^*. Again, the limit of $d_l^* \to 1$ is informative. For ρ_c^*-values near one, the flow is near equilibrium, so that no sizeable bore forms and the upper ambient layer becomes dynamically unimportant. Hence the flow becomes similar to a traditional full-depth lock-exchange problem with current depths near one half, although much smaller front velocities. On the other hand, for $d_l^* \to 1$ but ρ_c^* near zero, a large bore forms in the upper ambient layer and the lower gravity current thickness is reduced to about 0.35. We note that this problem has an inherent symmetry as a result of the Boussinesq approximation, in that there is an equivalence between intrusions with ρ_c^* and d_l^* on one hand, and those with $1 - \rho_c^*$ and $1 - d_l^*$ on the other. Consequently, the following expressions hold

$$U_c^*(\rho_c^*, d_l^*) = U_c^*(1 - \rho_c^*, 1 - d_l^*), \qquad (2.46)$$

$$U_l^*(\rho_c^*, d_l^*) = U_u^*(1 - \rho_c^*, 1 - d_l^*), \qquad (2.47)$$

$$h_l^*(\rho_c^*, d_l^*) = h_u^*(1 - \rho_c^*, 1 - d_l^*). \qquad (2.48)$$

For the intrusion velocity, Fig. 2.14 compares vorticity model predictions with current DNS simulation results, as well as with earlier experimental data and model predictions by other authors. Within the present investigation, we conducted simulations for $d_l^* = 0.1, 0.2...0.9$, as well as for the ρ_c^*-values of 0.25, 0.5 and 0.61, in order to be able to compare with the earlier theoretical and experimental investigations of [14] and [15]. The figure shows that the vorticity model predictions are close to those of the earlier models by [14] and [15], and over a substantial range of d_l^* fall in between these two models. Within
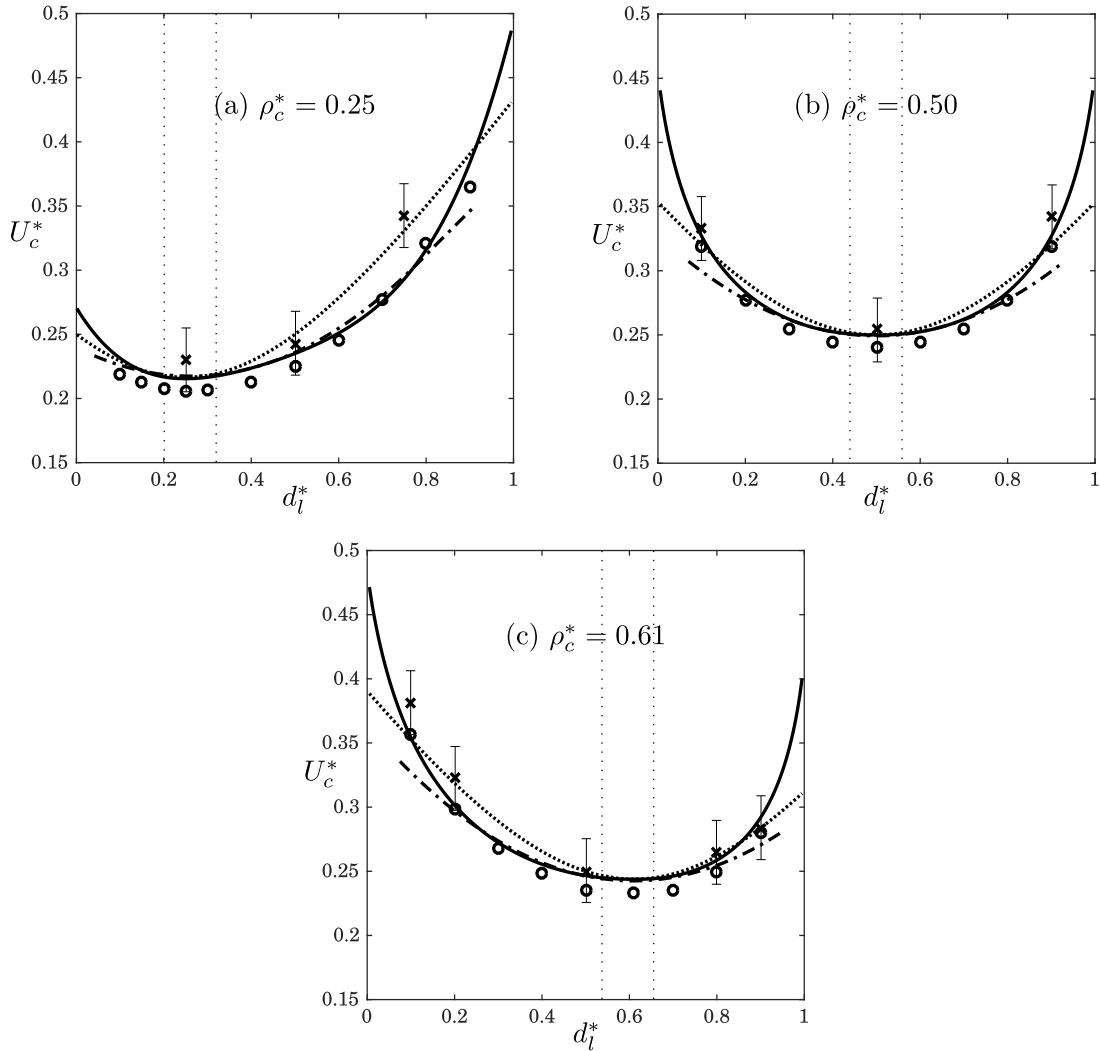
Figure 2.14: The interfacial gravity current speed U_c^* as a function of the interface height d_l^*, for (a) $\rho_c^* = 0.25$, (b) $\rho_c^* = 0.50$, and (c) $\rho_c^* = 0.61$. Solid lines represent the present vorticity model predictions, dotted lines show the results of global energy-conserving model proposed by [14], dash-dot lines indicate the intrusion speed given by [15], and discrete circles and crosses represent the present DNS results and the experimental data of [14], respectively. The vertical dotted lines demonstrate the range of validity of the investigation by [8]. Within this range, their results (not shown here) agree closely with all other theoretical, numerical and experimental data.

its narrow range of validity between the vertical dotted lines, the model of [8] yields predictions in very close agreement with those of the other models, so that we do not show them in this figure. All four models predict that the minimum propagation velocity occurs at equilibrium conditions, which is consistent with the experimental observations of [14] and the present simulation results. Due to the finite Re-values employed in the DNS simulations, the DNS front velocity data generally fall slightly below the vorticity model predictions, as will be discussed in further detail below.

Figure 2.15 compares vorticity model predictions with DNS results for the intrusion thickness as a function of the interface height. For all three ρ_c^*-values, h_c^* reaches a minimum value of 0.5 for the equilibrium case. Away from the equilibrium point, the intrusion thickens. We will discuss this observation from an energy perspective in section 2.5.

The DNS simulations show that the bore propagates with an approximately constant velocity. Figure 2.16 presents vorticity model predictions and simulation data for the ratio of the bore velocity to the intrusion velocity U_b^*/U_c^*, as a function of d_l^* and ρ_c^*. As explained by [15], in the limiting case where the bore height $d^* \to 0$, U_b^* approaches the linear long wave speed $\sqrt{d_l^* d_u^*}$. Hence, for near-equilibrium intrusions we expect that $U_b^*/U_c^* \to 2$, which is confirmed by the vorticity model predictions and DNS results.

Figure 2.17 shows the dimensionless bore amplitude d^* as a function of the interface height d_l^* for the same three ρ_c^*-values. Due to the undular nature of this leading bore, d^* is evaluated as a spatial average of the interface height. The present vorticity model predictions are seen to be in close agreement with the results of [15]. Specifically, both models exhibit a linear dependence of the bore height on $|\rho_c^* - d_l^*|$. Hence the vorticity model provides theoretical support for the empirical assumptions underlying equation (4.16) of [15]. Figure 2.18 demonstrates that both model predictions are consistent with corresponding DNS results.
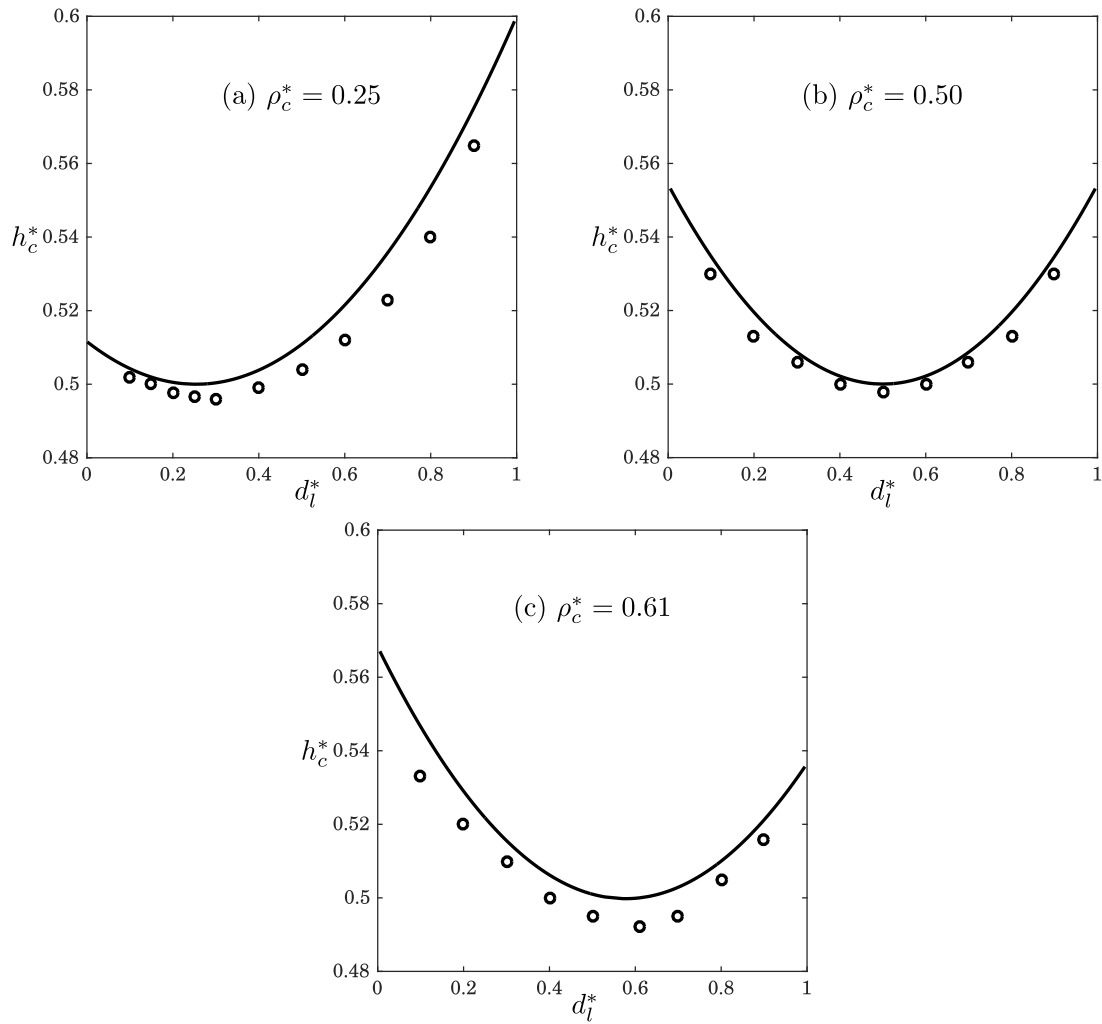
Figure 2.15: The interfacial gravity current thickness h_c^* as a function of the interface height d_l^*, for (a) $\rho_c^* = 0.25$, (b) $\rho_c^* = 0.50$, and (c) $\rho_c^* = 0.61$. Solid lines indicate predictions by the present vorticity model, while discrete circles represent the present DNS results.
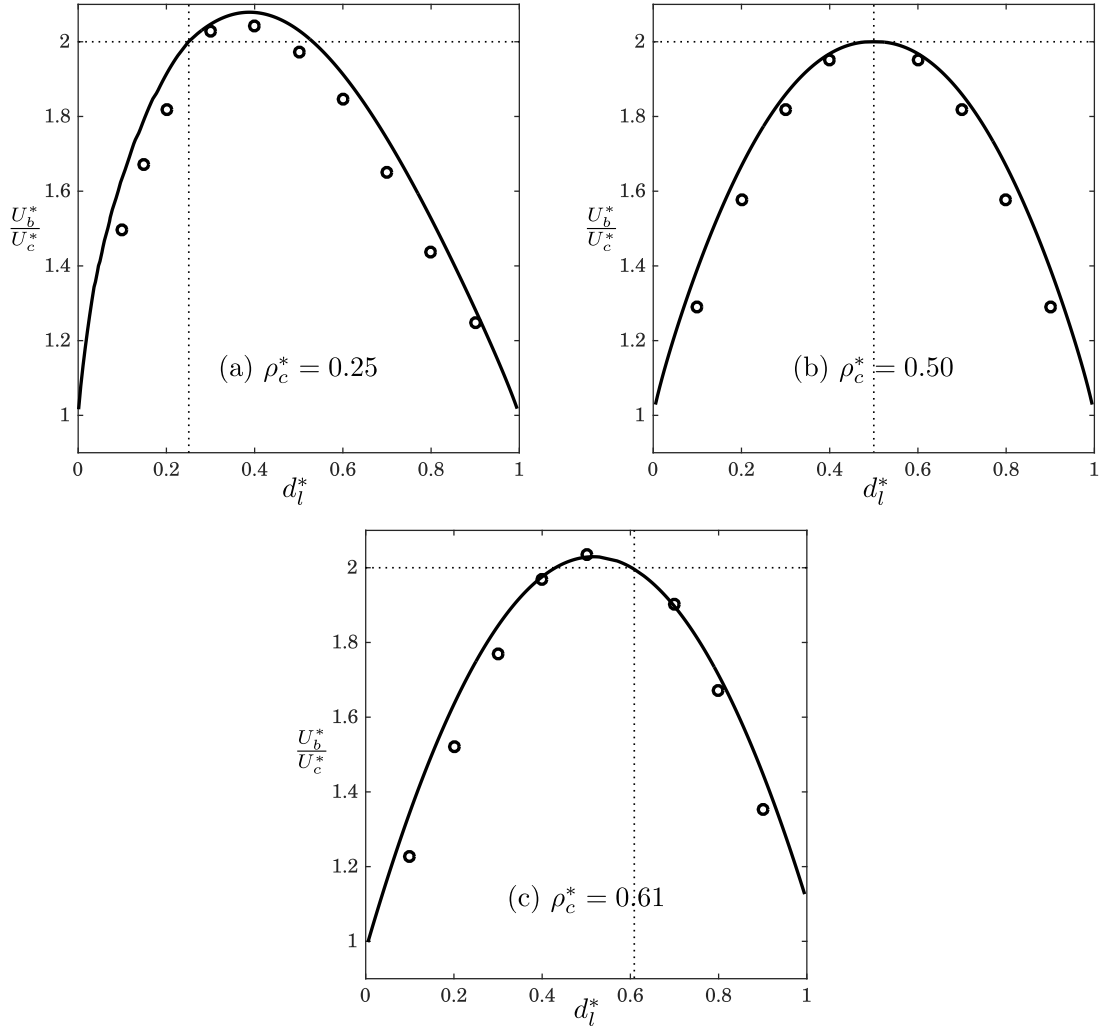
Figure 2.16: Variation of the ratio of leading bore speed to intrusion speed U_b^*/U_c^* with interface height d_l^*, for (a) $\rho_c^* = 0.25$, (b) $\rho_c^* = 0.50$, and (c) $\rho_c^* = 0.61$. Solid lines represent the present vorticity model predictions, while discrete circles indicate the present DNS results. The dotted lines show that for $d_l^* = \rho_c^*$ the model predicts $U_b^*/U_c^* = 2$, as expected for linear waves.
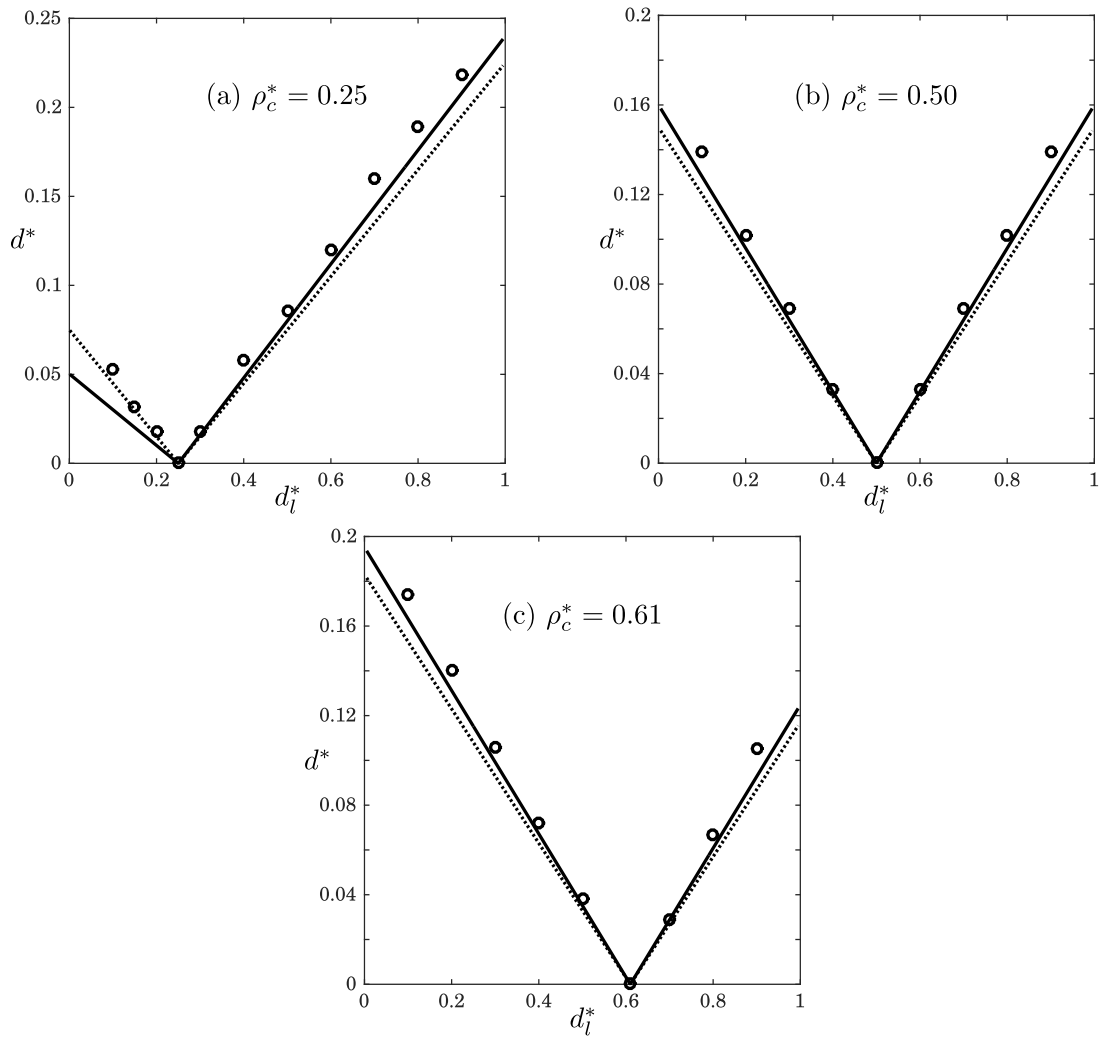
Figure 2.17: Variation of the amplitude d^* of the right-propagating internal bore with the interface height d_l^*, for (a) $\rho_c^* = 0.25$, (b) $\rho_c^* = 0.50$, and (c) $\rho_c^* = 0.61$. The solid lines represent the present vorticity model predictions, the dotted lines show results of [15], and the discrete circles indicate the present DNS results.
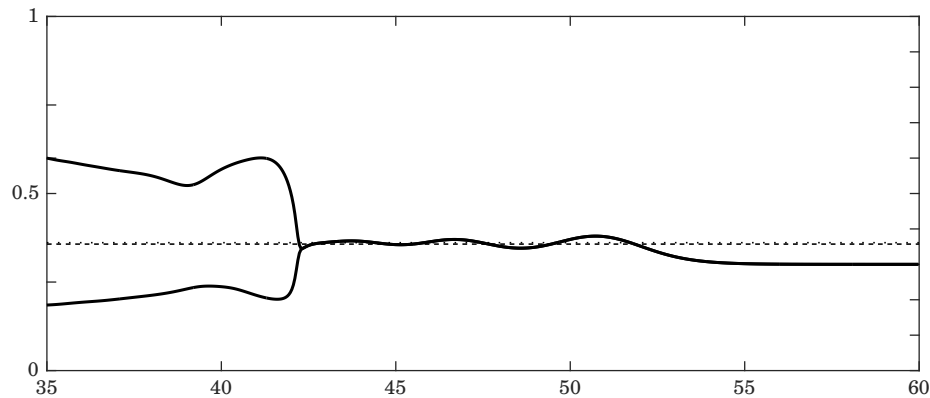
Figure 2.18: Comparison between the present DNS results and model predictions for the bore height, i.e., the height of the interface between the intrusion front and the leading bore. The dashed and dotted horizontal lines, which are nearly identical, indicate the predictions by the present vorticity model and that of [15] for h_b^*, respectively. The DNS results (solid line) represent the interface location from the nonequilibrium simulation in Fig. 2.6 at $t^* = 50$, for $\rho_c^* = 0.5$ and $d_l^* = 0.3$. The bore is undular in nature, and the DNS interface height fluctuates around an average value that is closely approximated by the dashed and dotted horizontal lines. We take this as indication of good agreement between the model predictions and the simulation results.

For the propagation velocities of the upper and lower gravity currents, Fig. 2.19 compares the vorticity model predictions to the DNS results. Again, good overall agreement is observed. The velocity of each gravity current is a function of its available potential energy, which scales with the square of the layer height multiplied by its density difference relative to the intrusion fluid. Both the model predictions and the DNS results confirm that under equilibrium conditions ($\rho_c^* = d_l^*$) the gravity currents have identical front velocities. When $d_l^* < \rho_c^*$, the lower gravity current has less available energy than the upper one, so that it travels more slowly. As d_l^* increases, the lower gravity current speeds up while the upper one slows down, until for $d_l^* = \rho_c^*$ the two velocities become equal to each other. Beyond this point, the lower gravity current propagates faster than the upper one.

We now proceed to discuss results for the quasisteady current heights. Figure 2.20
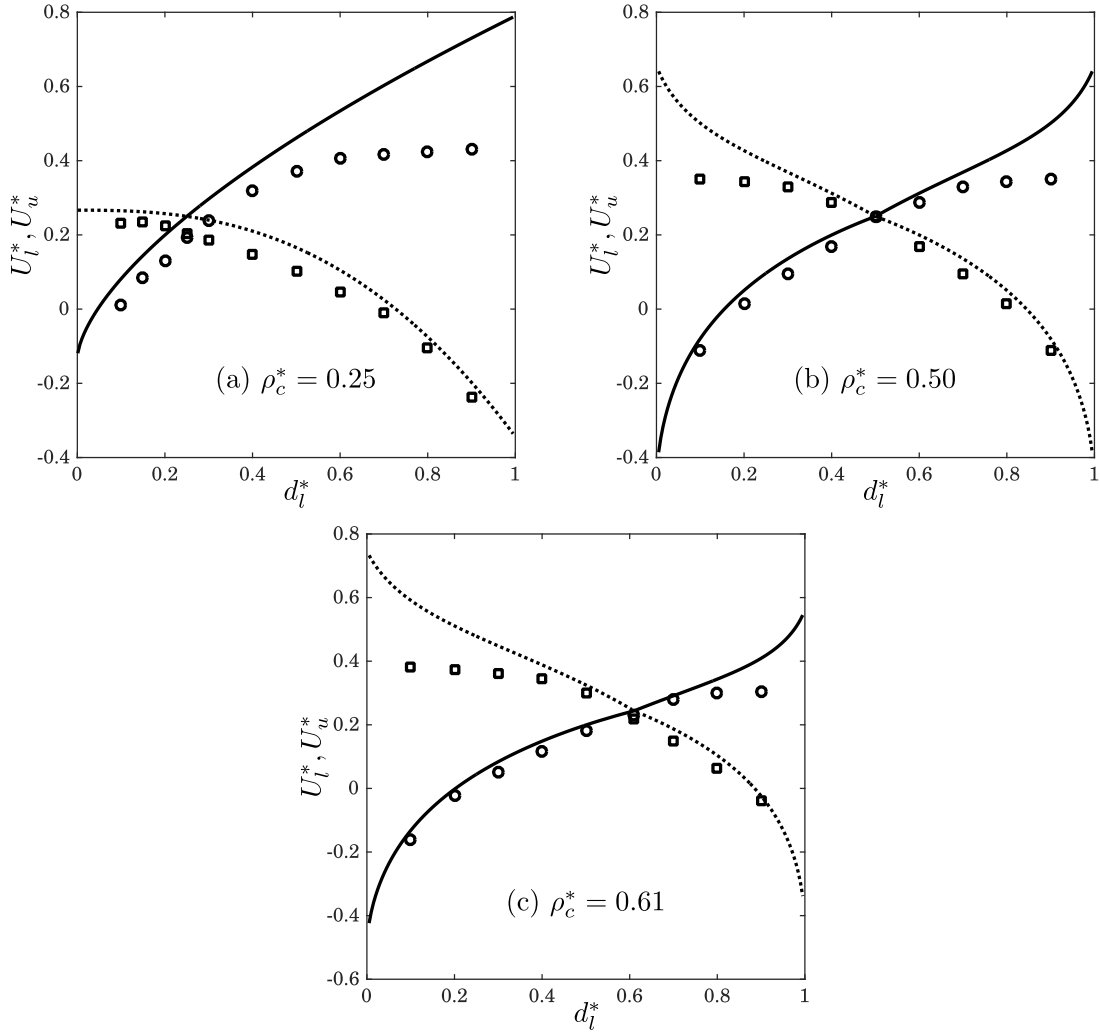
Figure 2.19: Front velocities U_l^* and U_u^* of the left-propagating lower and upper gravity currents, as functions of the interface height d_l^*, for (a) $\rho_c^* = 0.25$, (b) $\rho_c^* = 0.50$, and (c) $\rho_c^* = 0.61$. In this figure, solid and dotted lines represent model-predicted values of lower and upper gravity currents, respectively, while discrete circles and squares are the respective simulation speeds of these two gravity currents.

compares the DNS values for the lower and upper current heights with the corresponding vorticity model predictions. Again, good agreement between the model predictions and the simulation results is observed over the entire range of d_l^*, for all three values of ρ_c^*. Moreover, as demonstrated by this figure, h_l^* and h_u^* vary nearly linearly with the interface height, especially far from $d_l^* = 0$ or $d_l^* = 1$. The slopes of the curves are close to 0.5 (and -0.5 for h_u^*), for all values of ρ_c^*. Recall that for equilibrium intrusions we had found $h_l^* = d_l^*/2$ and $h_u^* = d_u^*/2$.

For $\rho_c^* = 0.5$ and the entire range of d_l^*, Fig. 2.21 compares predictions by the simplified model 1 (Fig. 2.2) with those of the more complete model 2 (Fig. 2.3), which accounts for the bore in the faster moving gravity current. We observe that the predictions by the two different models are close to each other, and to the simulation results, for the intrusion velocity, the gravity current heights, and the ratio of the right-propagating bore velocity to the intrusion velocity. On the other hand, for the velocity of the faster left-propagating current, which accounts for the key difference between the two models, the two model predictions deviate substantially from each other, and the more comprehensive model 2 yields closer agreement with the DNS simulation results.

2.5   Energy discussion

All of the above information about the flow was gained without any consideration of energy arguments. This is in contrast to all earlier analyses of intrusion current models, which had invoked energy-related assumptions in certain parts of the flow field. Consequently, we can now investigate the energy balance along certain streamlines and in specific control volumes a *posteriori*, in order to obtain insight into the validity of the assumptions underlying earlier models. Toward this objective, we analyze the headloss along the bottom and top of the tank, denoted by Δ_l and Δ_u, from D to C and G to I,
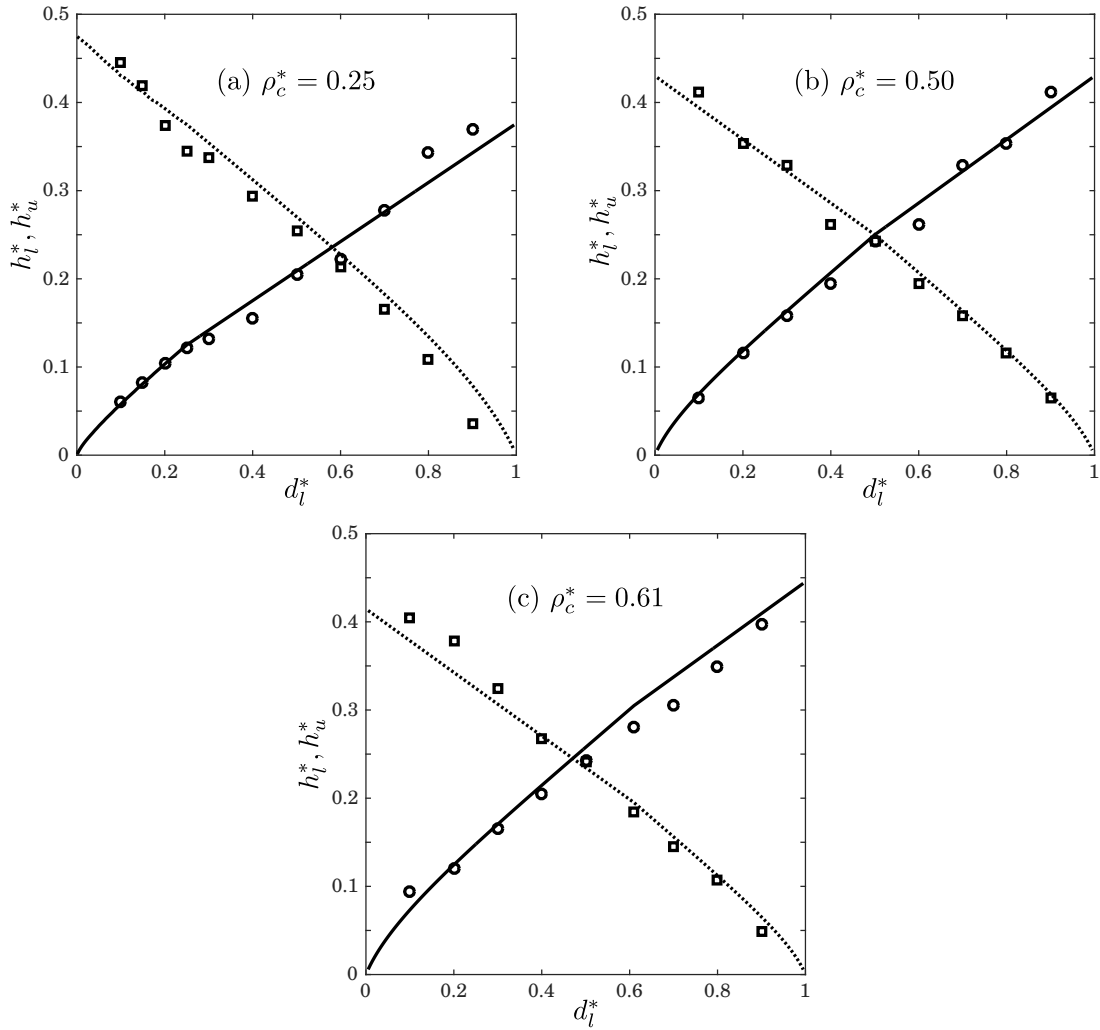
Figure 2.20: Thicknesses h_l^* and h_u^* of the lower and upper and gravity currents, as functions of the interface height d_l^*, for (a) $\rho_c^* = 0.25$, (b) $\rho_c^* = 0.50$, and (c) $\rho_c^* = 0.61$. Solid and dotted lines represent the present vorticity model predictions for the lower and upper gravity currents, respectively. Discrete circles and squares indicate the corresponding DNS results. All of the DNS results were evaluated at $t_s^* = 50$.
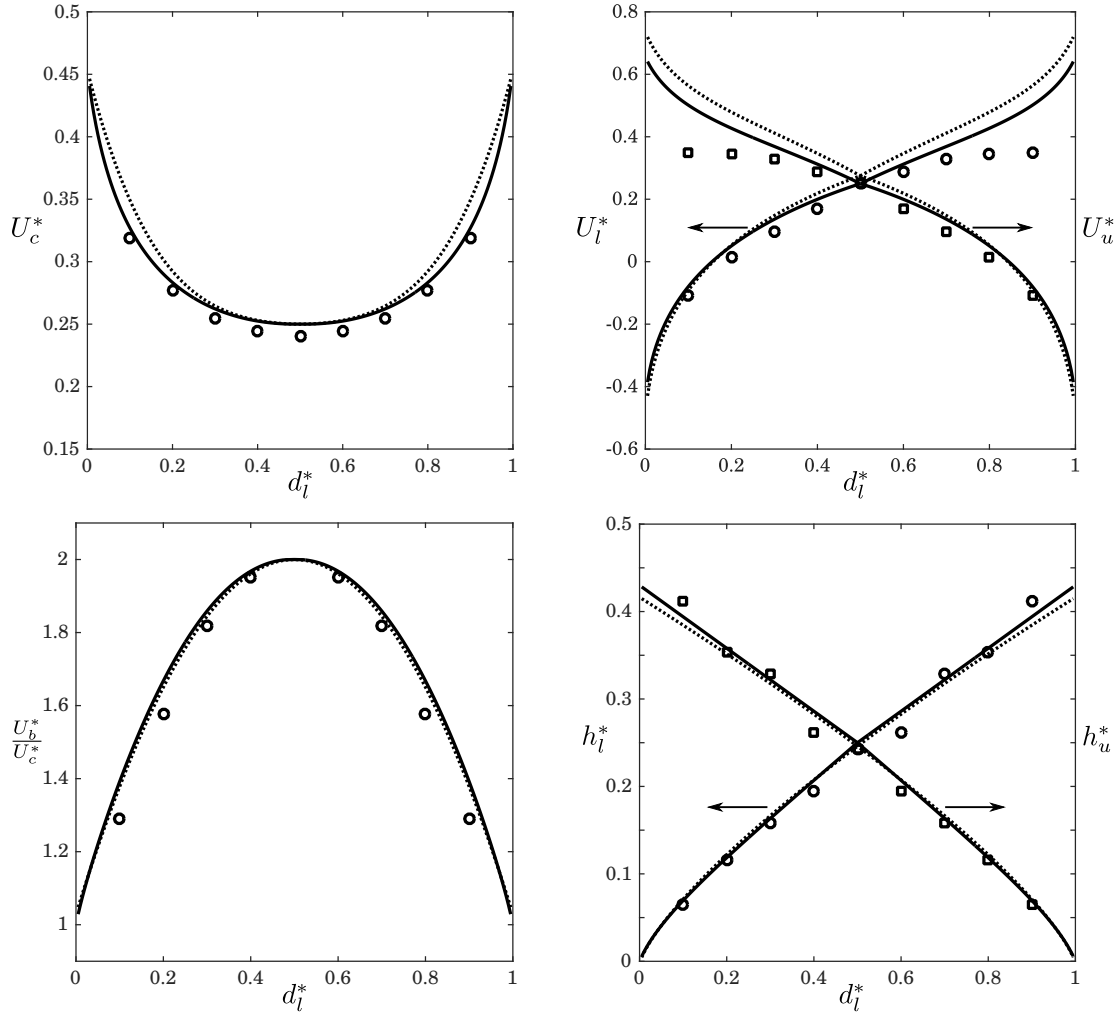
Figure 2.21: Comparison of the predictions by the two nonsymmetric intrusion models proposed in section 2.2 for the intrusion speed U_c^*, the lower and upper gravity currents speeds U_l^* and U_u^*, the ratio of leading bore speed to intrusion speed $\frac{U_b^*}{U_c^*}$, and the lower and upper gravity currents heights h_l^* and h_u^*. Solid lines indicate the results predicted by model 2, while dotted lines represent the results obtained by the simplified model 1. Discrete circles and squares show the numerical results. For all graphs, $\rho_c^* = 0.5$.

in the control volume $CDGI$ and in the reference frame of the interfacial gravity current, shown in Fig. 2.3. We furthermore calculate the headloss inside the intrusion, indicated by Δ_c, from B' to C', along the streamline passing through these two points in the control volume of $BCIJ$. We consider the following modified Bernoulli equations in which we allow for an energy loss or gain to occur

$$p_G + \frac{1}{2}\rho_{ref}(U_c + U_{ub})^2 \;=\; p_I + \frac{1}{2}\rho_{ref}(U_c + U_u')^2 + \Delta_u \,, \tag{2.49}$$

$$p_D + \frac{1}{2}\rho_{ref}(U_c - U_{lb})^2 \;=\; p_C + \frac{1}{2}\rho_{ref}(U_c + U_l)^2 + \Delta_l \,, \tag{2.50}$$

$$p_{B'} + \frac{1}{2}\rho_{ref}(U_l + U_{bc})^2 \;=\; p_{C'} + \frac{1}{2}\rho_{ref}(U_l + U_c)^2 + \Delta_c \,. \tag{2.51}$$

Here $p_{()}$ denotes the pressure at the corresponding location. In equations (2.49) - (2.51), the velocities are known from the earlier analysis presented in sections 2.1 and 2.2. The required pressure differences, in the absence of viscous forces along the top and bottom boundaries, can readily be obtained from the horizontal momentum conservation equations for the respective control volumes, which have the general form

$$\int (p_i + \rho_{ref}U_i^2)\,\mathrm{d}y = \int (p_o + \rho_{ref}U_o^2)\,\mathrm{d}y\,, \tag{2.52}$$

where $\rho_{ref} = \rho_c$, consistent with the Boussinesq approximation, and i and o indicate inlet and outlet, respectively. By assuming that the pressure is hydrostatic at the in- and outflow boundaries of the respective control volumes, i.e., far from any front so that the flow is locally unidirectional, we obtain the following dimensionless expressions for the corresponding pressure drops

$$p_G^* - p_I^* = \frac{\left(U_c^* + U_u'^*\right)^2 h_u'^* - \left(U_c^* + U_{ub}^*\right)^2 \left(1 - h_b^*\right) + \frac{1}{2}\rho_c^*\left(1 - h_b^* - h_u'^*\right)^2}{1 - h_b^*},(2.53)$$

$$p_D^* - p_C^* = \frac{\left(U_c^* + U_l^*\right)^2 h_l^* - \left(U_c^* - U_{lb}^*\right)^2 h_b^* + \frac{1}{2}\left(1 - \rho_c^*\right)\left(h_b^* - h_l^*\right)^2}{h_b^*},\qquad(2.54)$$

$$p_{B'}^* - p_{C'}^* = \frac{\left(U_c^* + U_l^*\right)^2 \left(h_b^* - h_l^*\right) - \left(U_{bc}^* + U_l^*\right)^2 h_b^* + \frac{1}{2}(1 - \rho_c^*)h_l^{*2}}{h_b^*}.\qquad(2.55)$$

We note that pressure and headloss are nondimensionalized by $p_{ref} = \Delta_{ref} = \rho_c g' H$. All other variables are scaled according to equations (2.12) - (2.14). By substituting equations (2.53) - (2.55) into equations (2.49) - (2.51), we obtain the desired headlosses, as shown in the phase space diagrams of Fig. 2.22. The figure confirms that all headlosses vanish for $\rho_c^* = d_l^*$, i.e. for equilibrium intrusions. For all other situations, the headloss terms are nonzero for all three currents. Furthermore, the headloss contours again reflect the symmetry properties observed in the earlier analysis, so that

$$\Delta_c^*(\rho_c^*, d_l^*) = \Delta_c^*(1 - \rho_c^*, 1 - d_l^*),\qquad(2.56)$$

$$\Delta_l^*(\rho_c^*, d_l^*) = \Delta_u^*(1 - \rho_c^*, 1 - d_l^*).\qquad(2.57)$$

Interestingly, we find that all nonequilibrium intrusions experience an energy *gain*. This is consistent with our ealier findings, shown in Figs. 2.15 and 2.11b, that $h_c^* > 0.5$ for all nonequilibrium intrusions. Furthermore the figure indicates that the left-propagating gravity currents can also gain energy for certain parameter ranges. The lower gravity current gains energy when $d_l^* > \rho_c^*$, while the upper gravity current experiences an energy gain when $d_l^* < \rho_c^*$. We expect that an energy gain of the lower current should result in an effective thickness of this current larger than one half, i.e., $h_l^*/h_b^* > 0.5$. This is
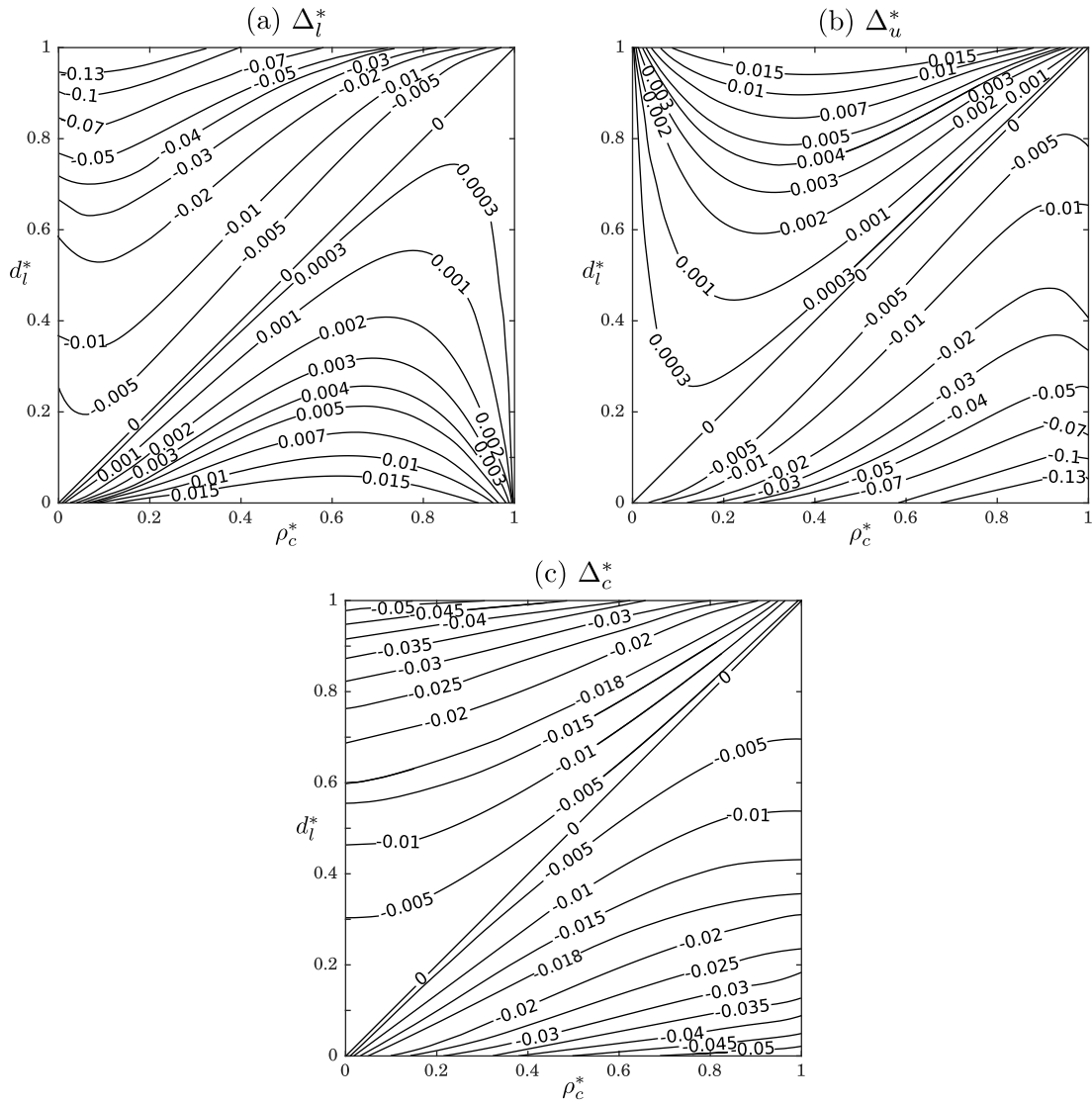
Figure 2.22: Phase-space diagram for headloss along the bottom (Δ_l^*), top (Δ_u^*) and the centerline of intrusion (Δ_c^*), computed as functions of ρ_c^* and d_l^*.
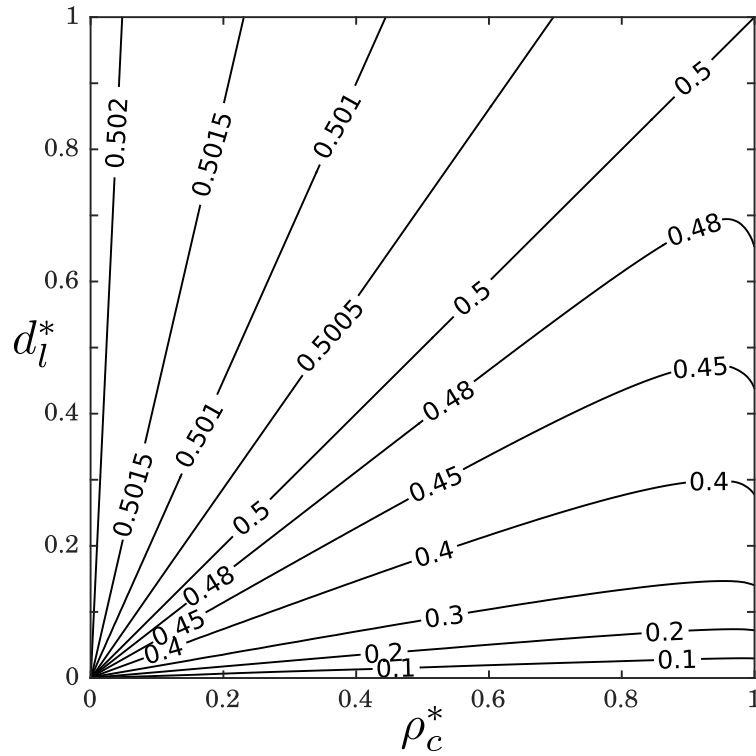
Figure 2.23: Phase-space diagram for the ratio of the lower gravity current thickness h_l^* to the lower ambient current thickness h_b^* upstream of the intrusion. In the region where $d_l^* > \rho_c^*$, i.e., where the lower gravity current gains energy, this ratio exceeds one half.

confirmed by Fig. 2.23.

We now focus on the conversion of potential energy (PE) to kinetic energy (KE). Initially, when the fluid is at rest, all of the mechanical energy is in the form of PE. In the absence of any mixing, the theoretically lowest level of PE that can be achieved by the system corresponds to the state in which the dense, intermediate and light fluids are arranged on top of each other in horizontal layers of thicknesses $(1 - \alpha)d_l$, αH and $(1 - \alpha)(H - d_l)$, respectively, where α denotes the geometric ratio of L_{lock}/L. We can compute the PE per unit width of the intial state, and of the final state of lowest energy,

with respect to the bottom wall as

$$E_{p,i} = \frac{1}{2}gL\Big[\alpha\rho_c H^2 + (1-\alpha)\big((\rho_l - \rho_u)d_l^2 + \rho_u H^2\big)\Big], \tag{2.58}$$

$$E_{p,f} = \frac{1}{2}gL\Big[(\rho_l - \rho_c)\big((1-\alpha)d_l\big)^2 + (\rho_c - \rho_u)\big((1-\alpha)d_l + \alpha H\big)^2 + \rho_u H^2\Big]. \tag{2.59}$$

The Available Potential Energy (APE) per unit width represents the difference between these two states

$$APE = \frac{1}{2}gL_{lock}(1-\alpha)\big[d_l^2\rho_l + (H^2 - 2d_l H)\rho_c + (-H^2 + 2d_l H - d_l^2)\rho_u\big], \tag{2.60}$$

We nondimensionalize the energy per unit width by $\rho_{ref}U_{ref}^3 x_{ref}t_{ref}$, which can be simplified to $\rho_c g' H^3$. We thus obtain

$$APE^* = \frac{1}{2}\beta(1-\alpha)(d_l^{*2} - 2d_l^*\rho_c^* + \rho_c^*), \tag{2.61}$$

where β indicates the ratio of the lock length to the tank height. As expected, APE^* has a minimum with respect to d_l^* when $d_l^* = \rho_c^*$, which is consistent with our earlier observation that for a given value of ρ_c^* symmetric intrusions have the lowest propagation speed.

Once the gate is removed, PE is converted into KE. We can now employ the quasis-teady front velocities calculated above from arguments of mass and momentum conservation, in order to calculate the rates at which the PE and KE of the overall flow, or of the various control volumes within the flow, change with time. For the symmetric intrusion case shown in Fig. 2.1, we can consider the entire tank as our control volume and evaluate the rate of change in KE and PE of the whole flow field, caused by the propagation of gravity currents. By multiplying the rate at which the area of each current grows with

the kinetic energy per area, we obtain the respective rates at which KE of the individual currents grow

$$\dot{E}_{k,c} = \frac{1}{2}\rho_c(U_l + U_c)h_cU_c^2\,,\tag{2.62}$$

$$\dot{E}_{k,u} = \frac{1}{2}\rho_c(U_u + U_c)h_uU_u^2\,,\tag{2.63}$$

$$\dot{E}_{k,l} = \frac{1}{2}\rho_c(U_l + U_c)h_lU_l^2\,.\tag{2.64}$$

Here, $\dot{E}_{k,c}$, $\dot{E}_{k,u}$ and $\dot{E}_{k,l}$ refer to the kinetic energies of the interfacial gravity current, and of the left-propagating upper and lower currents, respectively. Note that as a result of the Boussinesq approximation, the density is taken as ρ_c for all currents. Nondimensionalizing the energy transfer rates by $\rho_{ref}U_{ref}^3x_{ref}$ yields

$$\dot{E}_{k,c}^* = \frac{1}{2}(U_l^* + U_c^*)h_c^*U_c^{*2}\,,\tag{2.65}$$

$$\dot{E}_{k,u}^* = \frac{1}{2}(U_u^* + U_c^*)h_u^*U_u^{*2}\,,\tag{2.66}$$

$$\dot{E}_{k,l}^* = \frac{1}{2}(U_l^* + U_c^*)h_l^*U_l^{*2}\,.\tag{2.67}$$

By summing up the above expressions, we obtain that the rate of growth of KE in the entire flow field equals U_c^{*3}.

The rate at which PE of the entire tank changes can similarly be obtained by evaluating the rates at which fluid of one density is replaced by fluid of another density, via the motion of the individual currents. We obtain

$$\dot{E}_{p,c} = \frac{1}{2}(\rho_c - \rho_l)g(d_l^2 - h_l^2)U_c + \frac{1}{2}(\rho_c - \rho_u)g\big[(h_c + h_l)^2 - d_l^2\big]U_c\,,\tag{2.68}$$

$$\dot{E}_{p,u} = \frac{1}{2}(\rho_u - \rho_c)g\big[H^2 - (H - h_u)^2\big]U_u\,,\tag{2.69}$$

$$\dot{E}_{p,l} = \frac{1}{2}(\rho_l - \rho_c)gh_l^2U_l\,.\tag{2.70}$$

Rendering these results dimensionless gives

$$\dot{E}_{p,c}^* = -\frac{1}{2}(1 - \rho_c^*)(d_l^{*2} - h_l^{*2})U_c^* + \frac{1}{2}\rho_c^*\big[(h_c^* + h_l^*)^2 - d_l^{*2}\big]U_c^*, \tag{2.71}$$

$$\dot{E}_{p,u}^* = -\frac{1}{2}\rho_c^*\big[1 - (1 - h_u^*)^2\big]U_u^*, \tag{2.72}$$

$$\dot{E}_{p,l}^* = \frac{1}{2}(1 - \rho_c^*)h_l^{*2}U_l^*. \tag{2.73}$$

Summing up expressions (2.71) to (2.73) yields that the flow field loses PE at the rate $-U_c^{*3}$, so that for symmetric intrusions indeed all of the lost potential energy is converted into kinetic energy. Alternatively, we can consider separately the control volumes above and below $y^* = d_l^*$, along the entire length of the tank. It is straightforward to show that the total energies inside each of these control volumes do not vary with time, which is consistent with our earlier observation that $\Delta_c^* = \Delta_l^* = \Delta_u^* = 0$ for symmetric intrusions.

In the following, we extend the analysis to nonsymmetric intrusions. We evaluate the rates at which PE and KE change for the intrusion and the lower and upper gravity currents, by focusing on the control volumes $BDGJ$, $B'D'GJ$ and $BDD'B'$ in the laboratory reference frame, as shown in Fig. 2.3. We obtain the rates of change of KE for the intrusion and the upper and lower currents as

$$\dot{E}_{k,c} = \frac{1}{2}\rho_c(U_l + U_c)h_c U_c^2 - \frac{1}{2}\rho_c U_l(H - h_u)U_{bc}^2, \tag{2.74}$$

$$\dot{E}_{k,u} = \frac{1}{2}\rho_c(U_l + U_c)h_u' U_u'^{\,2} - \frac{1}{2}\rho_c U_l h_u U_u^2 - \frac{1}{2}\rho_c U_c U_{ub}^2(H - h_b), \tag{2.75}$$

$$\dot{E}_{k,l} = \frac{1}{2}\rho_c(U_l + U_c)h_l U_l^2 - \frac{1}{2}\rho_c U_c h_b U_{lb}^2. \tag{2.76}$$

Rendering the above equations nondimensional yields

$$\dot{E}_{k,c}^* = \frac{1}{2}(U_l^* + U_c^*)h_c^* U_c^{*2} - \frac{1}{2}U_l^*(1 - h_u^*)U_{bc}^{*\,2}\,, \tag{2.77}$$

$$\dot{E}_{k,u}^* = \frac{1}{2}(U_l^* + U_c^*)h_u'^{\,*} U_u'^{*2} - \frac{1}{2}U_l^* h_u^* U_u^{*2} - \frac{1}{2}U_c^* U_{ub}^{*\,2}(1 - h_b^*)\,, \tag{2.78}$$

$$\dot{E}_{k,l}^* = \frac{1}{2}(U_l^* + U_c^*)h_l^* U_l^{*2} - \frac{1}{2}U_c^* h_b^* U_{lb}^{*2}\,. \tag{2.79}$$

By following the same approach as for symmetric intrusions, we find the rates of change of PE as a result of the current motion

$$\dot{E}_{p,c} = \frac{1}{2}(\rho_c - \rho_u)g\big[(h_l + h_c)^2 - h_b^2\big]U_c + \frac{1}{2}(\rho_c - \rho_l)g(h_b^2 - h_l^2)U_c\,, \tag{2.80}$$

$$\dot{E}_{p,u} = \frac{1}{2}(\rho_u - \rho_c)g\big[(H - h_u)^2 - (H - h_u')^2\big]U_l\,, \tag{2.81}$$

$$\dot{E}_{p,l} = \frac{1}{2}(\rho_l - \rho_c)gh_l^2 U_l\,. \tag{2.82}$$

In dimensionless form, equations (2.80) to (2.82) result in

$$\dot{E}_{p,c}^* = \frac{1}{2}\rho_c^*\big[(h_l^* + h_c^*)^2 - h_b^{*2}\big]U_c^* - \frac{1}{2}(1 - \rho_c^*)(h_b^{*2} - h_l^{*2})U_c^*\,, \tag{2.83}$$

$$\dot{E}_{p,u}^* = -\frac{1}{2}\rho_c^*\big[(1 - h_u^*)^2 - (1 - h_u'^{\,*})^2\big]U_l^*\,, \tag{2.84}$$

$$\dot{E}_{p,l}^* = \frac{1}{2}(1 - \rho_c^*)h_l^{*2} U_l^*\,. \tag{2.85}$$

By summing up the rates at which KE and PE of the various currents change within the control volume $BDGJ$, we obtain an expression for the net rate of change of mechanical energy within $BDGJ$, $\dot{E}_{BDGJ}^*$. Interestingly, $\dot{E}_{BDGJ}^*$ is always positive for any nonequal combimation of (ρ_c^*, d_l^*), cf. Fig. 2.24. Aditionally, we can analyze the energy fluxes

across the right and left boundaries into $BDGJ$ as

$$\dot{E}^*_{rs} = \frac{1}{2}(1 - h^*_b)U^{*}_{ub}{}^3 - \frac{1}{2}h^*_b U^{*3}_{lb}, \tag{2.86}$$

$$\dot{E}^*_{ls} = \frac{1}{2}(1 - h^*_u)U^{*}_{bc}{}^3 - \frac{1}{2}h^*_u U^{*3}_u. \tag{2.87}$$

Here, $\dot{E}^*_{rs}$ and $\dot{E}^*_{ls}$ represent the energy fluxes into $BDGJ$ from the right and left boundaries. The energy budgets for the control volumes $BDD'B'$ and $B'D'GJ$ can be evaluated correspondingly, and provide separate insight into the energetics of the control volumes encompassing the lower and upper gravity currents, cf. Fig. 2.24b and c.

We can assess the energetics associated with the leading bore by analyzing the rates of change of KE and PE in the control volume $DEFG$. In this way, we obtain

$$\dot{E}_{k,b} = \frac{1}{2}\rho_c U_b \left[U^2_{lb} h_b + U^2_{ub}(H - h_b) \right], \tag{2.88}$$

$$\dot{E}_{p,b} = \frac{1}{2}(\rho_l - \rho_u)g\left(h^2_b - d^2_l \right)U_b. \tag{2.89}$$

Nondimensionalizing equations (2.88) and (2.89) results in

$$\dot{E}^*_{k,b} = \frac{1}{2}U^*_b \left[U^{*}_{lb}{}^2 h^*_b + U^{*}_{ub}{}^2(1 - h^*_b) \right], \tag{2.90}$$

$$\dot{E}^*_{p,b} = \frac{1}{2}\left(h^{*2}_b - d^{*2}_l \right)U^*_b. \tag{2.91}$$

Adding these two expressions yields the rate $\dot{E}^*_b$ at which the total mechanical energy within control volume $DEFG$ increases, as the propagating bore sets both fluid layers in motion and also raises the center of gravity of the dense fluid. By subtracting $\dot{E}^*_b$ from the entering energy flux, we obtain the portion of this energy influx that is dissipated by the bore, $\Delta\dot{E}^*_b$, cf. Fig. 2.25a. We find that for the intrusions in the vicinity of the equilibrium condition, a small fraction of 0.01% of the entering energy flux is dissipated.

Far away from equilibrium, on the other hand, this fraction can exceed 2%.

A corresponding evaluation of the energy within control volume $ABJK$ yields

$$\dot{E}_{k,lw} = \frac{1}{2}\rho_c U_l\left[U_u^2 h_u + U_{bc}^2(H - h_u)\right],\tag{2.92}$$

$$\dot{E}_{p,lw} = \frac{1}{2}(\rho_u - \rho_c)g\left[H^2 - (H - h_u)^2\right]U_l,\tag{2.93}$$

which in dimensionless form reads

$$\dot{E}_{k,lw}^* = \frac{1}{2}U_l^*\left[U_u^{*2} h_u^* + U_{bc}^{*\,2}(1 - h_u^*)\right],\tag{2.94}$$

$$\dot{E}_{p,lw}^* = -\frac{1}{2}\rho_c^*\left[1 - (1 - h_u^*)^2\right]U_l^*.\tag{2.95}$$

The rate $\dot{E}_{p,ADGK}^*$ at which PE is released in control volume $ADGK$ can be obtained by summing up equations (2.83) - (2.85) and (2.95). The rate $\Delta\dot{E}_t^*$ at which mechanical energy inside $ADGK$ is dissipated is found by substracting from $\dot{E}_{p,ADGK}^*$ the rate at which KE of the various currents grows, as well as the rate at which energy is being transferred to the leading bore across the boundary DG

$$\Delta\dot{E}_t^* = \dot{E}_{p,ADGK}^* - \dot{E}_{k,c}^* - \dot{E}_{k,u}^* - \dot{E}_{k,l}^* + \dot{E}_{rs}^*.\tag{2.96}$$

Figure 2.25b displays the fraction of the released potential energy that is dissipated, $|\Delta\dot{E}_t^*/\dot{E}_{p,ADGK}^*|$. We find this fraction to be small for the entire range of ρ_c^* and d_l^*.

A further interesting question concerns the fraction of the potential energy released in $ADGK$ that is used to support the leading bore, i.e., the ratio $|\dot{E}_b^*/\dot{E}_{p,ADGK}^*|$. Figure 2.24 shows that for nearly symmetric conditions, the fraction of PE exctracted by the leading bore is on the order of a few percent. However, for strongly nonsymmetric cases it can reach up to 20%. This confirms that the assumption by [14], who neglected the effect
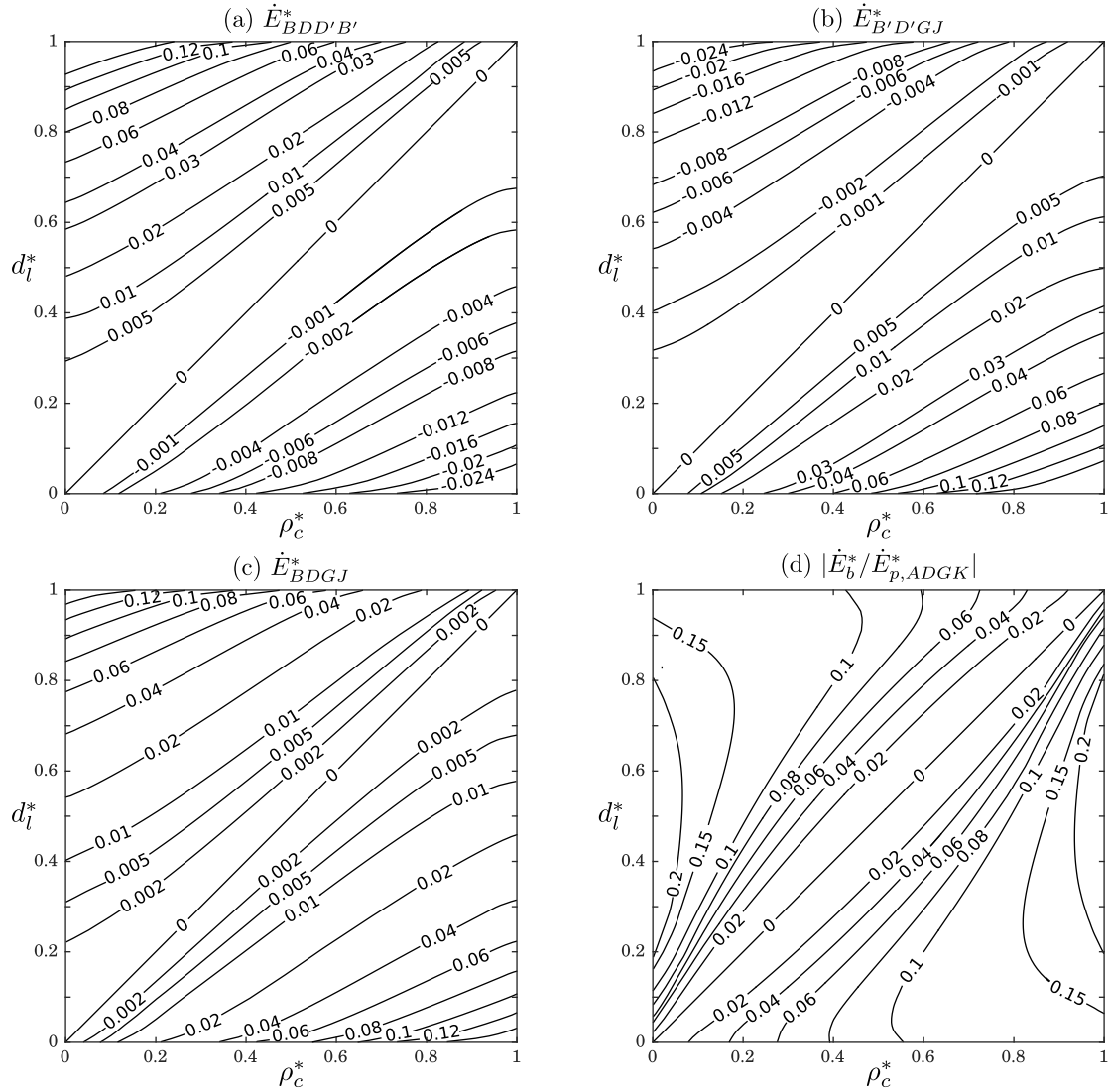
Figure 2.24: Phase-space diagrams for the rates at which the mechanical energy changes with time inside the various control volumes: a) $\dot{E}^*_{BDD'B'}$, b) $\dot{E}^*_{B'D'GJ}$, and c) $\dot{E}^*_{BDGJ}$. Frame d) indicates the fraction of the potential energy released in control volume $ADGK$ that goes into the leading bore.
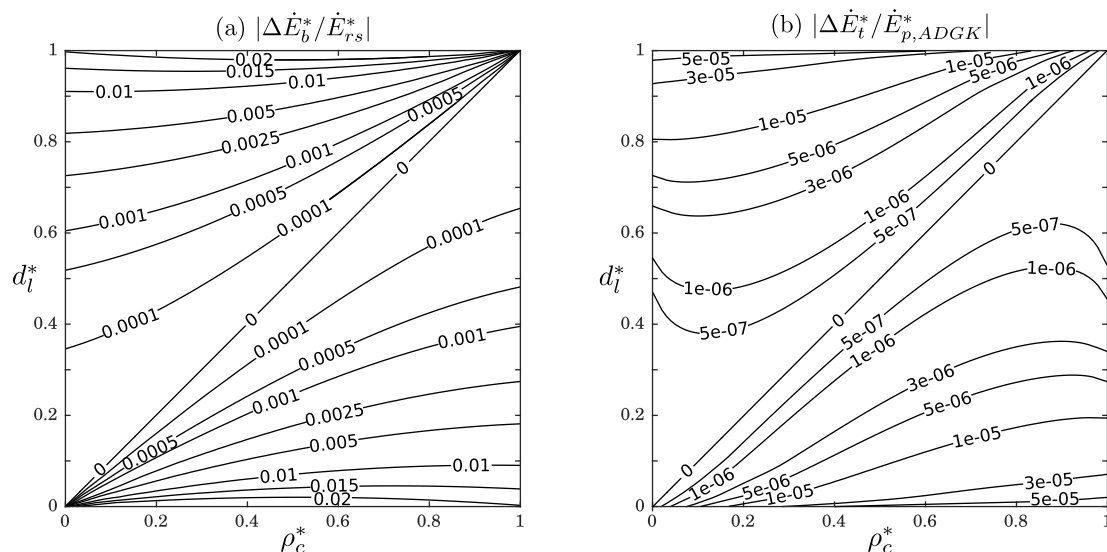
Figure 2.25: Phase-space diagrams for the dissipated fraction of (a) the convective energy flux into $DEFG$, $-\dot{E}_{rs}^*$, and (b) the released potential energy within control volume $ADGK$.

of the bore on the overall energetics of the flow, is most accurate for nearly symmetric intrusions.

2.6   Influence of Re and Pe

As described earlier, our DNS simulations employed finite values of the Reynolds and Péclet numbers. In light of the fact that earlier studies such as [21] had observed a certain dependence of the gravity current velocity on Re, it is hence of interest to investigate how the comparison between the DNS results and the inviscid vorticity model predictions is affected by changes in Re and Pe. Figure 2.26 provides information on this issue, for $\rho_c^* = 0.5$ and $0 < d_l^* < 1$. For the left graph, where we investigate the effect of the Reynolds number, Pe is held constant at 30,000 in all the simulations. For all parameter values, the intrusion velocity is seen to increase with Re, yielding closer agreement with the model predictions. For the right graph, where we focus on the influence of the Péclet
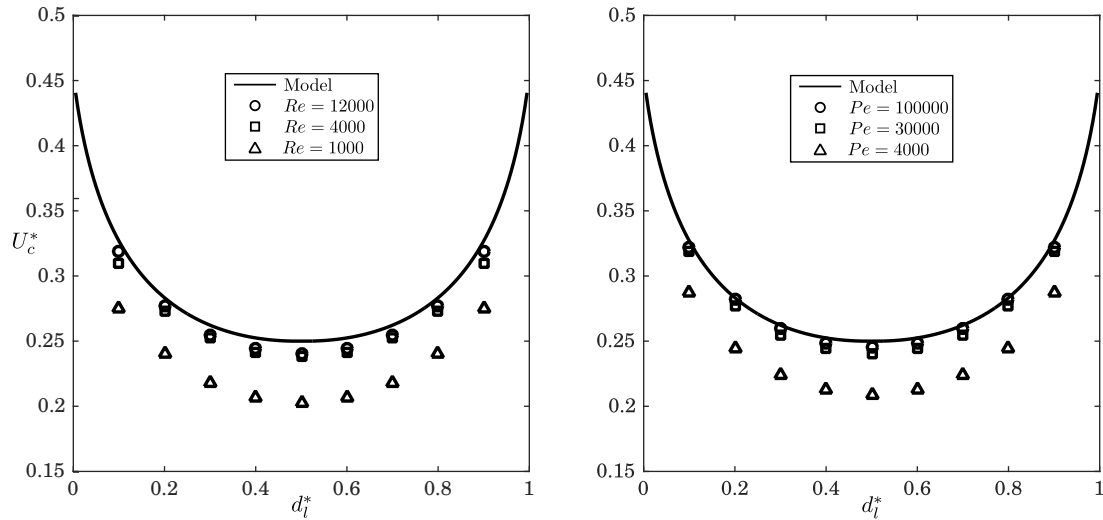
Figure 2.26: Influence of the Reynolds (left) and Péclet (right) numbers on the intrusion velocity. In the left graph $Pe = 30,000$, and in the right one $Re = 12,000$. The DNS results are seen to approach the vorticity model predictions as Re and Pe increase.

number, Re is held fixed at 12,000. The numerical intrusion speed uniformly approaches the vorticity model prediction as Pe is increased. When Re and Pe are above 4,000 and 30,000, respectively, the intrusion velocity no longer depends strongly on Re or Pe for intermediate values of d_l^*. However, for $d_l^* \approx 0$ or 1, the gravity currents developing along the upper or lower walls are quite thin, so that the DNS results remain more sensitive to changes in Re or Pe.

2.7   Summary

We have employed the laws of mass and momentum conservation to develop a closed model for intrusive gravity currents propagating along the interface of a two-layer stratified ambient. Based on the vorticity form of the momentum conservation principle, the model does not require any empirical closure assumptions. Using this model, we conduct a detailed parametric study in terms of the dimensionless intrusion density and the lower

layer height of the ambient, which reproduces the correct behavior for all known limits and confirms many previous experimental observations. Specifically, the present model demonstrates that the conservation of mass and momentum dictates the formation of equilibrium flows when the intrusion density equals the depth-weighted mean density of the two ambient layers, consistent with the obervations by [13]. These equilibrium intrusions are seen to correspond to classical energy-conserving gravity currents with a thickness of half the channel height.

The parametric study confirms that for a fixed intrusion density, the equilibrium configuration corresponds to the minimum propagation velocity, in agreement with the experimental observations of [14]. The model furthermore demonstrates that the limits of ($\rho_c^* = 0$, $d_l^* = 1$) and ($\rho_c^* = 1$, $d_l^* = 0$) are not smooth, in the sense that the height of the leading bore does not uniformly go to zero, so that the solution does not smoothly approach the case of a classical lock-exchange gravity current. The bore height smoothly approaches zero and its velocity reduces to that of a linear wave as the intrusion nears equilibrium conditions. In addition, the bore height is seen to vary linearly with $|\rho_c^* - d_l^*|$, consistent with earlier observations by [14] and [15]. An *a posteriori* energy analysis demonstrates that under nonequilibrium conditions the intrusion *gains* energy.

The predictions by the parametric study are furthermore compared to two-dimensional DNS results, and very good agreement is found with regard to all flow properties, including the propagation velocities of the intrusion and the gravity currents, their thickness, as well as the height and velocity of the leading bore.

Chapter 3

Partial-depth lock-release flows

As described in chapter 1, the work by [19] introduced the vorticity modeling approach for a gravity current front in an integral form, for a flow fields that can be rendered steady by shifting to a reference frame moving with the front. [16] subsequently extended this approach to unsteady flow fields composed of several fronts propagating at different velocities. They accomplished this by analyzing each front separately in a reference frame that renders it steady, and by then matching the solutions in the different reference frames.

Within the current chapter, we will extend the vorticity modeling approach to fully unsteady flows, i.e., to flow fields that cannot be constructed by superimposing and then matching a finite number of quasisteady components. In order to develop the modeling framework, we will focus on the canonical lock-release configuration, cf. Fig. 3.1. A tank of length L and height H is divided into two compartments: a rectangular lock with length L_{lock} and height H_{lock} initially contains the heavy fluid of density ρ_g, while the remainder of the space is occupied by the light ambient fluid of density ρ_a. Initially, these two immiscible fluids are separated by a gate. Upon removal of the gate, the heavy fluid forms a gravity current with velocity $u_{g,r}$ and height $h_{g,r}$ that travels towards the right along the bottom wall. This gravity current is connected to the lock fluid by a rarefaction or expansion wave of height $h(x,t)$, either directly, as in Fig. 3.1b or via a

bore, as in Fig. 3.1c. The left and right edges of this expansion wave travel with speeds u_l and u_r, respectively. Note that positive velocity values correspond to the directions of the arrows in Fig. 3.1. We aim to analyze the flow before the left edge of the rarefaction wave or the bore interact with the left wall. Within the rarefaction wave, the dense fluid has a velocity $u_g(h)$. Concurrently, the ambient forms a left-propagating return flow with velocity $u_{a,r}$ above the gravity current, and $u_a(h)$ above the rarefaction wave. The velocity $u(h)$ with which the interface location of height h moves horizontally, varies from $-u_l$ to u_r within the rarefaction wave. If the lock height H_{lock} equals the tank height H, we refer to the flow as a full-depth lock-release current, while for $H_{lock} \neq H$ we obtain a partial-depth lock-release flow.

Based on the two-layer shallow-water equations, [28] proposed a model for partial-depth lock-release flows that includes the rarefaction wave behind the gravity current. Since the shallow water equations cannot directly model the gravity current front, its effect is accounted for by an empirically modified front condition. For $H_{lock}/H \leq 0.5$, predictions by this model agree closely with experimental observations. While the shallow water model correctly predicts that a left-propagating bore forms for $H_{lock}/H > 0.5$, this bore is not accounted for in the model, so that the agreement between model and experiments deteriorates in this parameter range.

[18] propose a model that accounts for the entire flow fields, i.e., both for the rarefaction wave as well as for the right- and left-propagating fronts. They employ a control volume approach that conserves mass and horizontal momentum, and also enforces the unsteady Bernoulli equation along the top boundary. The authors furthermore assume the interface height to be uniform along the rarefaction wave, and to change abruptly from $h_{g,r}$ to H_{lock} at the left edge. In this way, they obtain for the gravity current speed
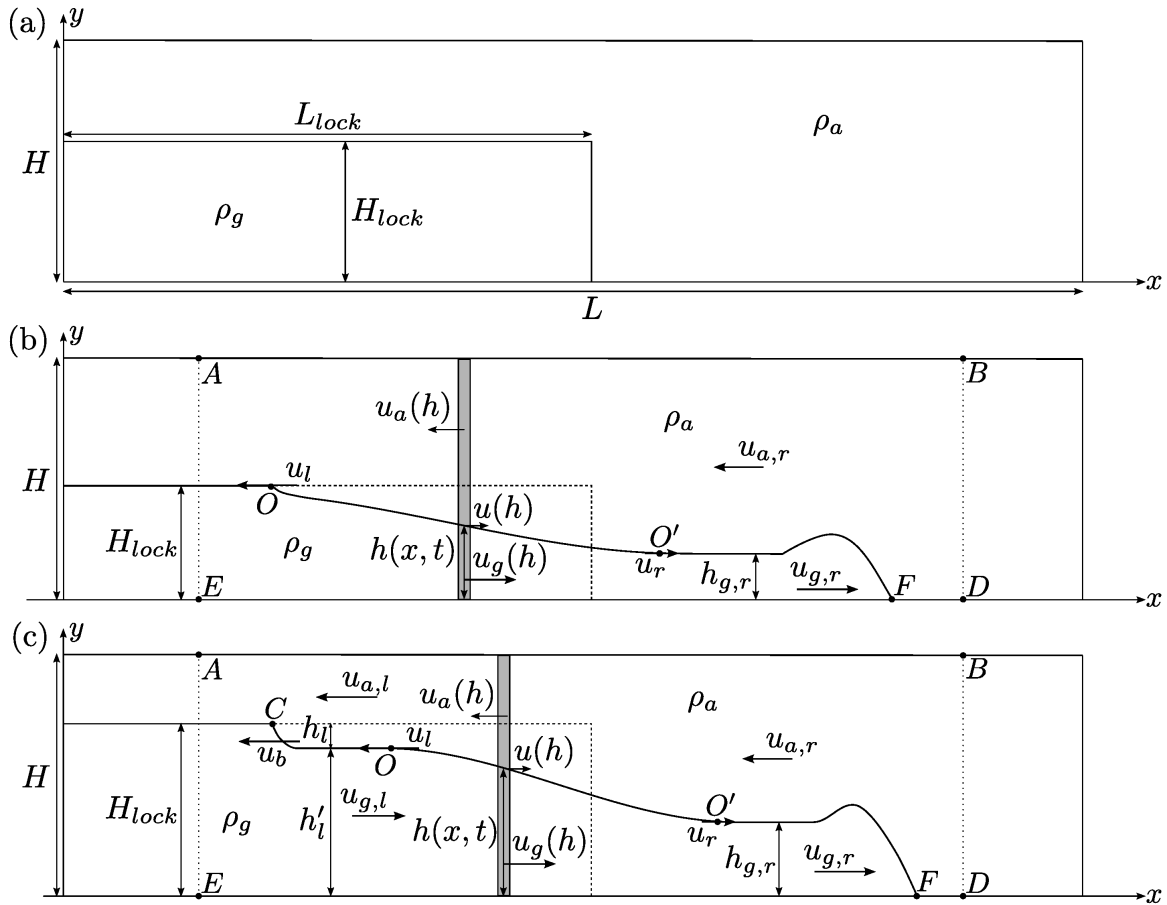
Figure 3.1: Schematic of a partial-depth lock-release flow. (a) Initially, the dense fluid is confined to a lock of length L_{lock} and height H_{lock}. (b) Upon removal of the gate, the heavy fluid of density ρ_g forms a gravity current with quasisteady propagation velocity $u_{g,r}$ and height $h_{g,r}$. The light ambient fluid of density ρ_a forms a return flow. For $H_{lock} < H/2$, the quasisteady gravity current is connected to the lock fluid by an unsteady expansion fan. (c) For $H_{lock} > H/2$, a quasisteady bore of height h_l and velocity u_b forms at the left edge of the expansion fan. The thin gray rectangles in (b) and (c) indicate the differential control volumes employed to derive the conservation laws.

in the Boussinesq limit

$$\frac{u_{g,r}}{\sqrt{g'H}} = \frac{1}{2}\sqrt{\frac{H_{lock}(2H - H_{lock})}{H^2}} \,. \tag{3.1}$$

The experiments by [18] furthermore confirm that it is possible for gravity currents with $h_{g,r}/H > 0.347$ to form, whereas [1] had suspected that such currents "would be difficult, if not impossible, to produce experimentally." The authors attribute this observation to the momentum and energy transfer between the rarefaction wave and the current front, which is not accounted for in Benjamin's model.

The present chapter proposes a differential vorticity-based approach for analyzing the entire unsteady flow field, including the gravity current, the rarefaction wave, and the internal bore. Section 3.1 constructs the vorticty-based model and obtains predictions for the speed and height of the gravity current, as well as for the velocities of the left and right edges of the expansion fan. Section 3.2 presents DNS simulations and compares them to the model predictions, as well as to theoretical and experimental findings of earlier studies. Section 3.3 describes an *a posteriori* analysis of the flow energetics, while section 3.4 summarizes the findings and gives some concluding remarks.

3.1 Theory

Within the region of the rarefaction wave, the flow is unsteady and varies spatially, so that it cannot be rendered quasisteady by a change of reference frame. Hence we need to establish the governing equations for a *differential* control volume in this region, as shown by the thin gray rectangles in Figs. 3.1b and 3.1c, rather than for an integral control volume as in the work of [19] and [25]. In order to formulate the governing system of equations for this differential control volume, we represent the rarefaction wave as a
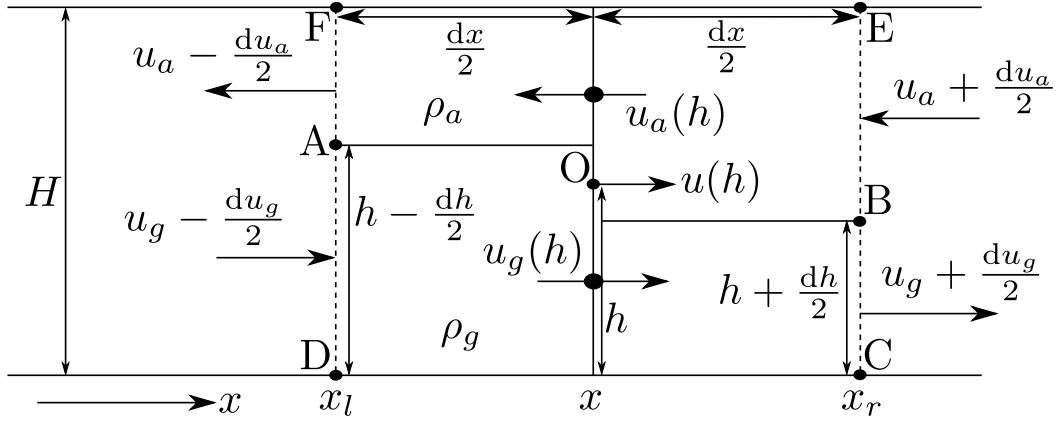
Figure 3.2: Magnified form of the differential control volume in Fig. 3.1. The entire control volume DCEF moves with the velocity $u(h)$ of the step-like variation in interface height at location O, so that the flow within the control volume is quasisteady. We assume locally uniform flow within each layer at the in- and outflow boundaries. Note that $\mathrm{d}h < 0$.

series of infinitesimal step-like variations in interface height of size $\mathrm{d}h$. A detailed view of this differential control volume is shown in Fig. 3.2. It contains the section over which the interface height varies from $(h - \mathrm{d}h/2)$ at the left boundary to $(h + \mathrm{d}h/2)$ at the right boundary, by means of a jump $\mathrm{d}h < 0$ at the center of the control volume. The entire control volume moves with the velocity $u(h)$ of the jump. We assume the fluids to be inviscid, and their density difference to be sufficiently small for the Boussinesq approximation to be valid. Furthermore, we consider the flow in each layer at the control volume boundaries to be purely horizontal, and independent of the vertical coordinate. With this assumption of locally unidirectional flow, we can write the mass conservation equations for the lower and upper layers, i.e. for the control volumes ABCD and ABEF, as

$$\left[\left(u_g - \frac{\mathrm{d}u_g}{2}\right) - u\right]\left(h - \frac{\mathrm{d}h}{2}\right) = \left[\left(u_g + \frac{\mathrm{d}u_g}{2}\right) - u\right]\left(h + \frac{\mathrm{d}h}{2}\right), \qquad (3.2)$$

$$\left[\left(u_a + \frac{\mathrm{d}u_a}{2}\right) + u\right]\left(H - h - \frac{\mathrm{d}h}{2}\right) = \left[\left(u_a - \frac{\mathrm{d}u_a}{2}\right) + u\right]\left(H - h + \frac{\mathrm{d}h}{2}\right). \quad (3.3)$$

By neglecting higher order terms, equations (3.2) and (3.3) simplify to

$$(u_g - u)\mathrm{d}h + h\mathrm{d}u_g = 0\,, \tag{3.4}$$

$$(u_a + u)\mathrm{d}h - (H - h)\mathrm{d}u_a = 0\,. \tag{3.5}$$

We now derive the conservation equation for the vorticity along the interfacial segment AB within the differential control volume DCEF in Fig. 3.2. Towards that end, we start from the integral form of the vorticity conservation law for inviscid, variable-density flow

$$\frac{\mathrm{d}}{\mathrm{d}t} \iint\limits_{\mathrm{DCEF}(t)} \omega\, \mathrm{d}A + \oint\limits_{\mathrm{CS}(t)} \omega \mathbf{V}_r \cdot \mathbf{n}\, \mathrm{d}S = - \iint\limits_{\mathrm{DCEF}(t)} g' \frac{\partial \rho^*}{\partial x}\, \mathrm{d}A\,. \tag{3.6}$$

Here $\mathrm{CS}(t)$ denotes the surface of the control volume DCEF, and $\mathbf{V}_r$ represents the velocity of the fluid relative to the moving control volume boundary.

The temporal rate of change of the circulation inside the control volume vanishes, because the control volume size and the interface shape within do not change over time

$$\frac{\mathrm{d}}{\mathrm{d}t} \iint\limits_{\mathrm{DCEF}(t)} \omega\, \mathrm{d}A = 0\,. \tag{3.7}$$

Next, the flux of vorticity crossing the surface of the control volume can be formulated as

$$\oint\limits_{\mathrm{CS}(t)} \omega \mathbf{V}_r \cdot \mathbf{n}\, \mathrm{d}S =$$

$$- \underbrace{\left[\left(u_a - \frac{\mathrm{d}u_a}{2}\right) + \left(u_g - \frac{\mathrm{d}u_g}{2}\right)\right]}_{\text{vortex sheet strength}} \times \underbrace{\frac{1}{2}\left[\left(u_g - \frac{\mathrm{d}u_g}{2}\right) - \left(u_a - \frac{\mathrm{d}u_a}{2}\right) - 2u\right]}_{\text{vortex sheet principal velocity}}$$

$$+ \left[\left(u_a + \frac{\mathrm{d}u_a}{2}\right) + \left(u_g + \frac{\mathrm{d}u_g}{2}\right)\right] \times \frac{1}{2}\left[\left(u_g + \frac{\mathrm{d}u_g}{2}\right) - \left(u_a + \frac{\mathrm{d}u_a}{2}\right) - 2u\right]\,.$$

$$\tag{3.8}$$

67

Simplifying equation (3.8) gives

$$\oint_{\text{CS}(t)} \omega \mathbf{V}_r \cdot \mathbf{n} \, \mathrm{d}S = \mathrm{d}u_g \left(u_g - u \right) - \mathrm{d}u_a \left(u_a + u \right) . \tag{3.9}$$

To evaluate the baroclinic vorticity generation term on the right hand side of equation (3.6), we remind ourselves that the interface is sharp, and that the dimensionless density $\rho^* = 1$ everwhere below the interface, and $\rho^* = 0$ everywhere above. Within the control volume DCEF, the interface consists of the two horizontal segments to the left and the right, and the vertical segment of length $\mathrm{d}h$ at the center. Consequently, the only location within the control volume where $\partial \rho^* / \partial x \neq 0$ is along this vertical interface segment of length $\mathrm{d}h$ adjacent to point O. Integration along any horizontal line that crosses this vertical interface segment gives $\int \partial \rho^* / \partial x \, \mathrm{d}x = -1$. Consequently, we obtain $\iint \partial \rho^* / \partial x \, \mathrm{d}A = -\mathrm{d}h$, which results in

$$\iint_{\text{DCEF}(t)} g' \frac{\partial \rho^*}{\partial x} \, \mathrm{d}A = -g' \mathrm{d}h , \tag{3.10}$$

where $\mathrm{d}h < 0$. Since $\partial \rho^* / \partial x \neq 0$ only along the vertical segment of the step, the horizontal interface segments do not contribute to the area integral, so that its value is independent of the horizontal extent of the interval $x_r - x_l$. By substituting equations (3.7), (3.9) and (3.10) into (3.6), we obtain

$$\mathrm{d}u_g \left(u - u_g \right) - \mathrm{d}u_a \left(u + u_a \right) = -g' \mathrm{d}h . \tag{3.11}$$

By combining the continuity equations (3.4) and (3.5) with the vorticity equation (3.11),

68

we obtain the system

$$\frac{\mathrm{d}u_g}{\mathrm{d}h} = -\frac{1}{h}\left(u_g - u\right), \tag{3.12}$$

$$\frac{\mathrm{d}u_a}{\mathrm{d}h} = \frac{1}{H-h}\left(u_a + u\right), \tag{3.13}$$

$$\frac{1}{h/H}\left(u - u_g\right)^2 + \frac{1}{1-h/H}\left(u + u_a\right)^2 = g'H. \tag{3.14}$$

Note that while the dense and light fluid velocities are governed by first order ODEs, the vorticity equation reduces to an algebraic relationship. We now choose the channel height H and buoyancy velocity $\sqrt{g'H}$ as reference scales to render equations (3.12) to (3.14) dimensionless

$$\frac{\mathrm{d}u_g^*}{\mathrm{d}h^*} = -\frac{1}{h^*}\left(u_g^* - u^*\right), \tag{3.15}$$

$$\frac{\mathrm{d}u_a^*}{\mathrm{d}h^*} = \frac{1}{1-h^*}\left(u_a^* + u^*\right), \tag{3.16}$$

$$1 = \frac{1}{h^*}\left(u^* - u_g^*\right)^2 + \frac{1}{1-h^*}\left(u^* + u_a^*\right)^2, \tag{3.17}$$

where the *-symbol refers to the dimensionless variables.

When the rarefaction wave is directly connected to the lock fluid, as shown in Fig. 3.1b, both fluids are at rest at the left edge of the rarefaction wave, so that

$$u_g^*(H_{lock}^*) = u_a^*(H_{lock}^*) = 0. \tag{3.18}$$

This provides the two required conditions at the left boundary for ODEs (3.15) and (3.16). Corresponding boundary conditions for the configuration with the left-propagating bore, shown in Fig. 3.1c, will be discussed in section 3.1.1. Equation (3.17) then gives for the

propagation velocity of the left edge of the expansion wave

$$u_l^* = -u^*(H_{lock}^*) = \sqrt{H_{lock}^*(1 - H_{lock}^*)}\,. \tag{3.19}$$

At the right edge O' of the expansion wave, the expansion fan flow has to match the gravity current, so that it needs to satisfy

$$u_g^*(h_{g,r}^*) = u_{g,r}^*\,, \tag{3.20}$$

$$u_a^*(h_{g,r}^*) = u_{a,r}^*\,. \tag{3.21}$$

The gravity current height $h_{g,r}^*$ is determined by the condition

$$h_{g,r}^* = \frac{1}{2}(u_{g,r}^* + u_{a,r}^*)^2\,, \tag{3.22}$$

which arises from the vorticity conservation principle for the gravity current front, cf. [19] and section 1.1 of the present work. Combining (3.20)-(3.22) yields the front condition

$$h_{g,r}^* = \frac{1}{2}\left[u_g^*(h_{g,r}^*) + u_a^*(h_{g,r}^*)\right]^2\,. \tag{3.23}$$

u_r^* can be evaluated by substituting the gravity current properties into the vortcity balance equation (3.17), which gives

$$u_r^* = (1 - h_{g,r}^*)u_g^*(h_{g,r}^*) - h_{g,r}^* u_a^*(h_{g,r}^*) - \sqrt{h_{g,r}^*(1 - h_{g,r}^*)\left\{1 - \left[u_g^*(h_{g,r}^*) + u_a^*(h_{g,r}^*)\right]^2\right\}}\,, \tag{3.24}$$

where $h_{g,r}^*$ can be calculated from equation (3.23).

The above system of equations (3.15)-(3.17), together with the boundary conditions

(3.18) and the front condition (3.23), thus completely determines the combined expansion fan and gravity current flow. This system can be solved numerically by integrating equations (3.15) and (3.16) from H^*_{lock} to the h^*-value that satisfies condition (3.23). We also update the interfacial velocity u^* from equation (3.17) in each integration step. The interface height at which we terminate the integration process is then the gravity current height. In this study, we employ the standard fourth-order Runge-Kutta scheme to carry out the integration.

Equations (3.15) to (3.17) can be recast in terms of a single ODE for $u_g^*(h^*)$. Towards this end, equations (3.15) and (3.16) are combined and integrated with respect to h^*, which results in

$$u_g^* h^* = u_a^* (1 - h^*) \,, \tag{3.25}$$

which simply states that the volume flux to the left above the interface has to equal the volume flux to the right below the interface. We can hence eliminate u_a^* from equation (3.17), so that we obtain for u^* as a function of h^* and u_g^*

$$u^* = \frac{1 - 2h^*}{1 - h^*} u_g^* \pm \sqrt{\frac{h^*}{1 - h^*}\left[(1 - h^*)^2 - u_g^{*2}\right]} \,. \tag{3.26}$$

Substituting equation (3.26) into (3.15) then yields

$$h^* \frac{\mathrm{d}u_g^*}{\mathrm{d}h^*} + \frac{h^*}{1 - h^*} u_g^* \pm \sqrt{\frac{h^*}{1 - h^*}\left[(1 - h^*)^2 - u_g^{*2}\right]} = 0 \,. \tag{3.27}$$

for the velocity of the dense fluid within the expansion fan as a function of the local interface height h^*. Interestingly, equation (3.27) is identical to the one obtained by [28] via a two-layer shallow-water analysis, as will be discussed below in further detail.

3.1.1   Formation of the left-propagating bore

The earlier investigations by [28] and [18] demonstrated that the expansion fan is not always directly connected to the lock fluid, as sketched in Fig. 3.1b. Rather, beyond a critical value of the lock height H_{lock} a bore or hydraulic drop forms that connects the left edge of the rarefaction wave to the stationary fluid in the lock, as shown in Fig. 3.1c. This is also confirmed by the DNS simulations to be discussed below. We now proceed to analyze the formation of the bore, and its interaction with the left edge of the expansion wave, based on the vorticity approach.

As long as the interfacial wave speed u^* varies monotonically with h^* throughout the expansion fan region, the slope of the fan's interface will decrease everywhere with time, so that a bore does not form. If, on the other hand, u^* reaches an extremum u^*_{min} for an intermediate value of h^*, the interfacial segment with this minimum velocity travels leftward faster than the left edge of the wave, and catches up with it. The interface hence steepens locally and a bore forms where the expansion fan meets the lock fluid, as sketched in Fig. 3.1c. This situation corresponds to the observation by [28] of a multivalued solution for the interfacial height when $H^*_{lock} > 0.5$. Now the boundary conditions at the left edge of the expansion fan take the form

$$u^*_g(h'^*_l) \;=\; u^*_{g,l}\,, \tag{3.28}$$

$$u^*_a(h'^*_l) \;=\; u^*_{a,l}\,. \tag{3.29}$$

In order to determine the value of H^*_{lock} at which the bore first appears, we need to determine the value of H^*_{lock} for which the u^*-profile first exhibits an extremum. Taking
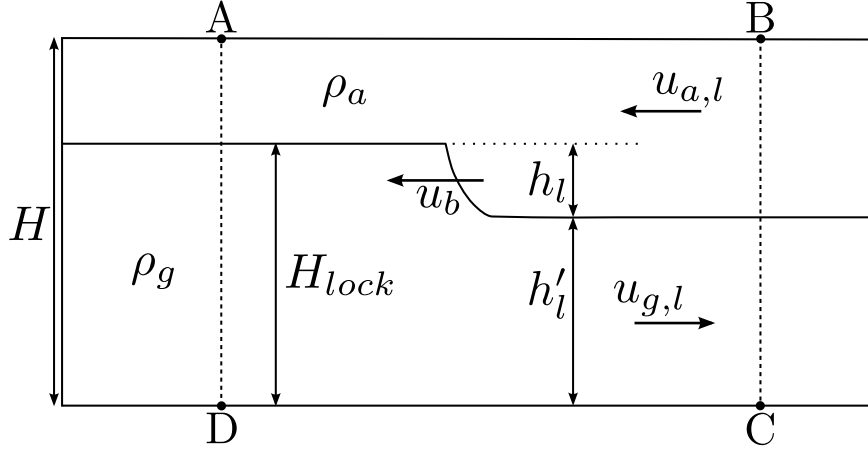
Figure 3.3: Schematic of the control volume around the hydraulic drop of configuration 3.1c.

the derivative of equation (3.17) with respect to h^* yields

$$\left[\frac{2(u^* - u_g^*)}{h^*} + \frac{2(u^* + u_a^*)}{1 - h^*}\right]\frac{\mathrm{d}u^*}{\mathrm{d}h^*} - \frac{3(u^* - u_g^*)^2}{h^{*2}} + \frac{3(u^* + u_a^*)^2}{(1 - h^*)^2} = 0\,, \tag{3.30}$$

where $\mathrm{d}u_g^*/\mathrm{d}h^*$ and $\mathrm{d}u_a^*/\mathrm{d}h^*$ have been replaced based on equations (3.15) and (3.16). A local minimum for the interfacial velocity ($\mathrm{d}u^*/\mathrm{d}h^* = 0$) exists when

$$\frac{u^* - u_g^*}{h^*} = \frac{u^* + u_a^*}{1 - h^*}\,. \tag{3.31}$$

As we will see in section 3.1.2, a u^*-minimum first appears for the largest value of h^*, i.e., at the left edge of the rarefaction wave (location O in Fig. 3.1b) where $u_g^* = u_a^* = 0$. For these conditions, equation (3.31) gives $H_{lock}^* = 0.5$, which agrees with the findings of [28].

For flows with bores we have to match the left edge of the expansion fan to the bore at the interface height h_l', cf. Fig. 3.1c. To obtain the velocities of the upper and lower fluid layers between the bore and the expansion fan, we first investigate the left-propagating bore in isolation from the rest of the flow, as sketched in Fig. 3.3. In the reference

frame moving with the bore, the continuity equations for both layers and the vorticity conservation equation for the control volume ABCD in Fig. 3.3 read

$$u_b^* H_{lock}^* \;=\; (u_b^* + u_{g,l}^*)h_l'^* \,, \tag{3.32}$$

$$u_b^*(1 - H_{lock}^*) \;=\; (u_b^* - u_{a,l}^*)(1 - h_l'^*) \,, \tag{3.33}$$

$$\frac{1}{2}(u_{g,l}^* + u_{a,l}^*)(2u_b^* \;+\; u_{a,l}^* - u_{g,l}^*) = h_l^* \,, \tag{3.34}$$

cf. [25]. If the interface height h_l' to the right of the bore is known, these equations fully determine the fluid and bore velocities. In order to understand how the flow selects this interface height, it is instructive to analyze the energetics of the bore region. Towards this end, we determine the pressure difference along the top wall $p_A - p_B$ from the horizontal momentum conservation equation for ABCD

$$\int_D^A \left[\rho_{ref} u_i(y)^2 + p_i(y)\right] \, \mathrm{d}y = \int_C^B \left[\rho_{ref} u_o(y)^2 + p_o(y)\right] \, \mathrm{d}y \,, \tag{3.35}$$

where $p_i(y)$ and $p_o(y)$ indicate the pressure functions from A to D and B to C, respectively. $u_i(y)$ and $u_o(y)$ represent the piecewise constant fluid velocities across the in- and outflow boundaries. The reference density is also $\rho_{ref} = \rho_a$. The pressure can be considered hydrostatic far up- and downstream of the bore, so that $p_i(y)$ and $p_o(y)$ take the form

$$p_i(y) = \begin{cases} p_A + \rho_a g(H - y) & y \geq H_{lock} \,, \\[2ex] p_A + \rho_a g(H - H_{lock}) + \rho_g g(H_{lock} - y) & y < H_{lock} \,. \end{cases} \tag{3.36}$$

$$
p_o(y) = \begin{cases}
p_\text{B} + \rho_a g(H - y) & y \geq h'_l\,, \\[2em]
p_\text{B} + \rho_a g(H - h'_l) + \rho_g g(h'_l - y) & y < h'_l\,.
\end{cases} \tag{3.37}
$$

Nondimensionalizing these relations and substituting them into equation (3.35) yields

$$
p_\text{A}^* - p_\text{B}^* = h'^*_l(u_b^* + u_{g,l}^*)^2 + (1 - h'^*_l)(u_b^* - u_{a,l}^*)^2 - u_b^{*2} - \frac{1}{2}\left(H_{lock}^{*2} - h'^{*2}_l\right), \tag{3.38}
$$

where the dimensional pressures have been divided by $\rho_a g' H$ to obtain the dimensionless ones. The rate of dissipation of energy $\Delta \dot{E}$ for the entire control volume, in the reference frame of the bore, can be calculated as

$$
\Delta \dot{E} = \int_\text{D}^\text{A} \left(\frac{1}{2}\rho_a u_i^2 + p_i + \rho_i g y\right) u_i \; \mathrm{d}y - \int_\text{C}^\text{B} \left(\frac{1}{2}\rho_a u_i^2 + p_o + \rho_o g y\right) u_o \; \mathrm{d}y\,, \tag{3.39}
$$

where ρ_i and ρ_o denote the fluid densities at the in- and outlet of ABCD. After nondimensionalization and simplification, equation (3.39) reads

$$
\begin{aligned}
\Delta \dot{E}^* \;=\;\; & (p_\text{A}^* - p_\text{B}^*)u_b^* + H_{lock}^*(H_{lock}^* - h'^*_l)u_b^* + \frac{1}{2}u_b^{*3} \\
& - \frac{1}{2}h'^*_l(u_b^* + u_{g,l}^*)^3 - \frac{1}{2}(1 - h'^*_l)(u_b^* - u_{a,l}^*)^3\,.
\end{aligned} \tag{3.40}
$$

Note that $\Delta \dot{E}$ has been scaled by $\rho_a g'^{\frac{3}{2}} H^{\frac{5}{2}}$ to be rendered dimensionless.

Figure 3.4 displays the net rate of energy loss $\Delta \dot{E}^*$ for the bore sketched in Fig. 3.3, as a function of h'^*_l and for several values of H_{lock}^*. The results show that, independent of the lock height, the interface height $h'^*_l = 0.5$ corresponds to energy-conserving flow. An interface height of less than half the channel height would require an energy gain, so that it cannot be physically realized. As we will see in the DNS simulations to be discussed below, for all lock heights the flow develops a nearly energy-conserving bore
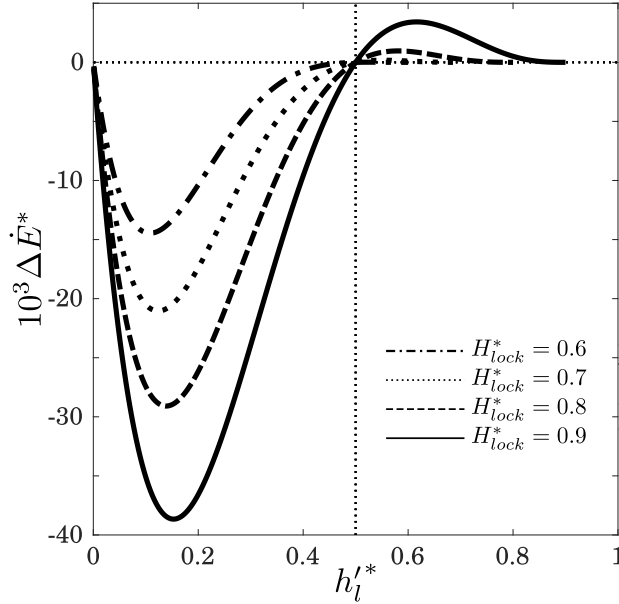
Figure 3.4: Variation of the rate of dissipation of energy $\Delta \dot{E}^*$ as a function of the interface height after the hydraulic drop $h_l'^*$, computed for an isolated bore traveling along the interface of a two-layer flow for various lock heights H_{lock}^*. For all lock heights, an interface height $h_l'^* = 0.5$ after the bore corresponds to energy-conserving flow.

with an interface height $h_l'^* \approx 0.5$, corresponding to the familiar observation of an energy-conserving half-depth current for a full-depth lock-release [1, 19].

Substituting $h_l'^* = 0.5$ into equations (3.32)-(3.34) then gives $u_b^* = 0.5$ and $u_{g,l}^* = u_{a,l}^* = H_{lock}^* - 0.5$. In section 3.2.1 we will compare these results to DNS simulations. These flow velocities $u_{g,l}^*$ and $u_{a,l}^*$ to the right of the bore can now serve as boundary conditions at the left edge of the expansion fan. Substitution into equation (3.17) yields the propagation velocity of the left edge of the rarefaction wave

$$u_l^* = \sqrt{H_{lock}^*(1 - H_{lock}^*)}. \tag{3.41}$$

This result is identical to equation (3.19), which represents the velocity of left edge of the expansion fan for configuration 3.1b without a bore. For any lock height $H_{lock}^* > 0.5$, we can now solve equations (3.15)-(3.17) in the interval $h_{g,r}^* \leq h^* \leq h_l'^* = 0.5$, subject to

these boundary conditions and the front condition (3.23).

3.1.2   Predictions by the vorticity-based model

We employ a standard fourth-order Runge-Kutta method to solve equations (3.15) and (3.16), along with the algebraic equation (3.17), for the configuration sketched in Fig. 3.1b. For now, we apply boundary conditions (3.18) at $h^* = H^*_{lock}$, and condition (3.23) at the front. The validity of the conditions (3.18) will then have to be established *a posteriori*, based on whether or not they result in a multivalued solution, as discussed in section 3.1.1. Figure 3.5a displays the dense and light fluid velocities as functions of the local interface height, for the specific lock height value $H^*_{lock} = 0.5$. The lower layer fluid continually speeds up from the lock towards the gravity current, while the upper layer velocity is seen to reach a local maximum close to where the expansion fan transitions to the gravity current.

Figure 3.5b shows the interfacial velocity u^* as a function of the interface height h^*, for several different lock heights. As we anticipated based on the analysis in section 3.1.1, for $H^*_{lock} = 0.4$ and 0.5 the interfacial velocity u^* increases monotonically from negative values at the lock to positive values in the vicinity of the gravity current, which indicates that the left edge of the expansion fan travels to the left, while its right edge travels to the right. For $H^*_{lock} = 0.6$, 0.8 and 0.9, on the other hand, we find that solutions based on the configuration shown in 3.1b, with boundary conditions (3.18), yield a local minimum for an intermediate interface height near the lock, which indicates that a left-propagating bore will form, so that boundary conditions (3.18) are invalid, and interfacial velocities below -0.5 will not emerge in the flow. Figure 3.5b confirms that a bore first appears for $H^*_{lock} = 0.5$, since for this value the slope of $u^*(h^*)$ first vanishes at the left edge of the expansion fan. These results are consistent with the analysis of section 3.1.1, and with
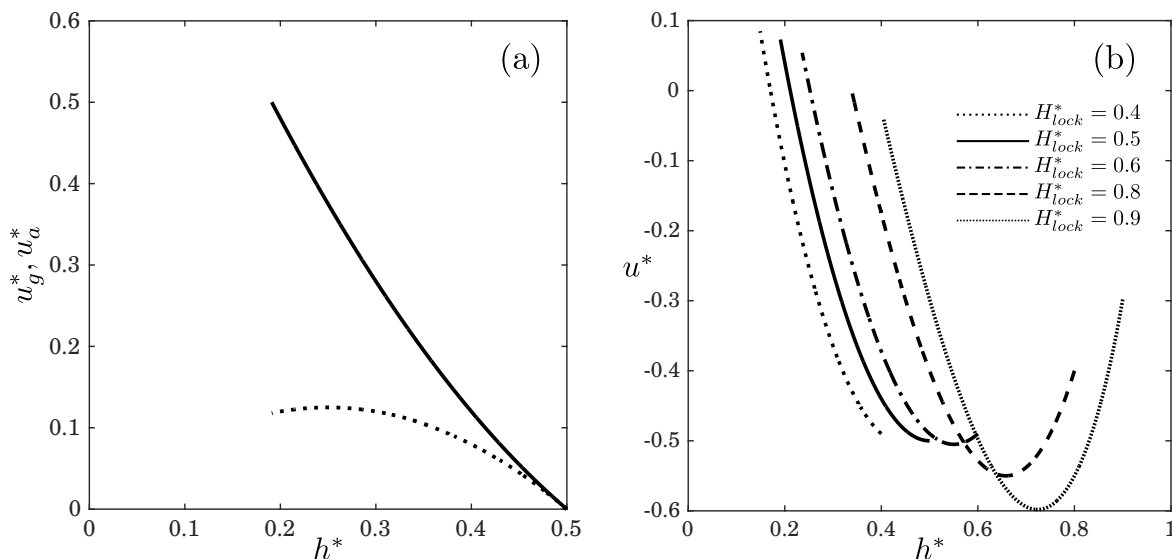
Figure 3.5: (a) Variation of the lower layer velocity u_g^* (solid line) and the upper layer velocity u_a^* (dotted line), as function of the local interface height h^*, for $H_{lock}^* = 0.5$. (b) Interfacial velocity u^* as function of h^* along the rarefaction wave, for various values of the lock height H_{lock}^*. These solutions were obtained based on the configuration of Fig. 3.1b, with boundary conditions (3.18).

the findings of [28].

The analysis in section 3.1.1, along with the observations of multivalued solutions for the interfacial velocity when $H_{lock}^* > 0.5$, suggests that in this regime boundary conditions (3.28) and (3.29) need to be enforced, which result in the interfacial velocities shown in Fig. 3.6. u^* now decreases monotonically with h^*, and the expansion fan is confined to the range $h_{g,r}^* \leq h^* \leq 0.5$.

3.1.3 A note on the relationship between the vorticity-based model and the two-layer shallow-water equations

[28] derive equation (3.27) from the two-layer shallow-water equations, after employing the method of characteristics. In the following, we will show that in the limit of locally unidirectional flow, and when the velocity does not vary across the thickness of
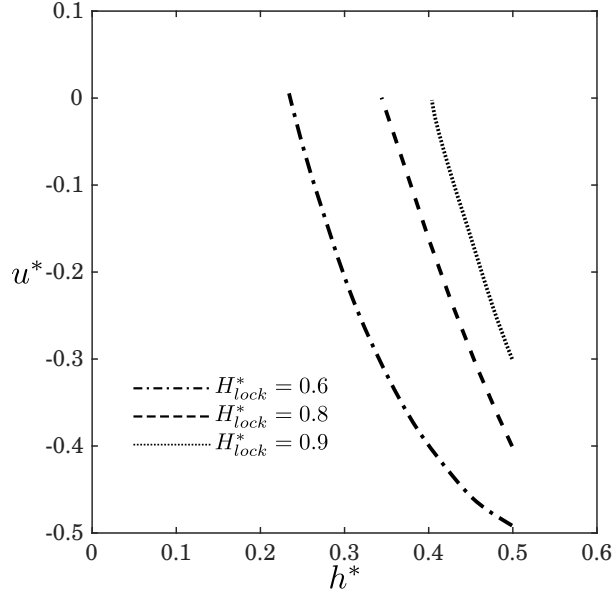
Figure 3.6: Variation of the interfacial velocity u^* as a function of h^* along the expansion fan, for various values of $H_{lock}^* > 0.5$. These solutions were obtained based on configuration 3.1c and boundary conditions (3.28) and (3.29). As discussed in the text, in these cases the left edge of the rarefaction wave is located at $h^* = h_l'^* = 0.5$ and the solution for u^* exists only for the range $h_{g,r}^* \leq h^* \leq 0.5$.

each layer, the vorticity model is consistent with the shallow-water equations. This discussion is merely intended to clarify the relationship between the two approaches, and to establish under what conditions they are equivalent to each other. The two-layer shallow water equations have clearly proved to be highly useful, and we do not mean to imply any shortcomings of this approach.

Figure 3.7 displays an arbitrary two-layer stratified flow, with the gray rectangular area indicating a fixed control volume of length Δx. For a two-dimensional inviscid flow in the Boussinesq approximation, the vorticity equation reads

$$\frac{\partial \omega}{\partial t} + \mathbf{u} \cdot \nabla \omega = -g' \frac{\partial \rho^*}{\partial x} \, . \tag{3.42}$$
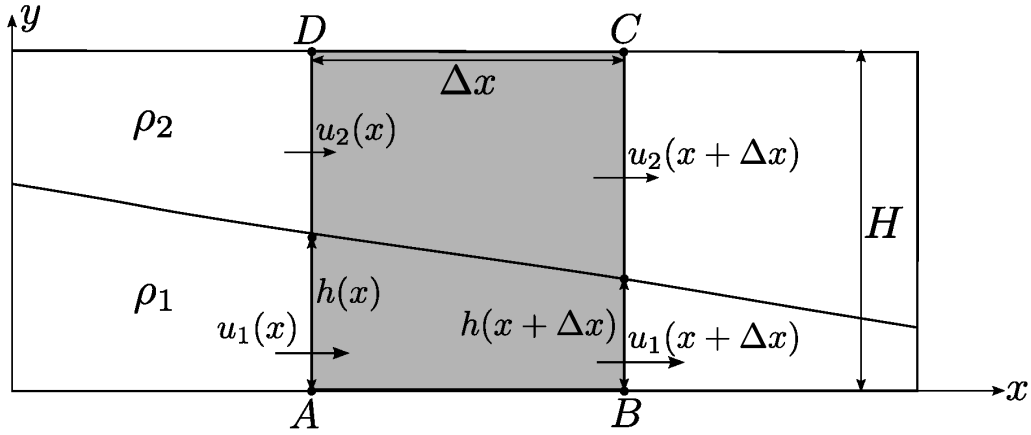
79

Figure 3.7: Control volume employed for the purpose of discussing the relationship be-tween the vorticity-based model and the shallow water equations, cf. the discussion in the text.

Integration over control volume $ABCD$ yields

$$\underbrace{\iint_{ABCD} \frac{\partial \omega}{\partial t} \, \mathrm{d}A}_{I_1} + \underbrace{\oint_{CS} \omega \mathbf{u} \cdot \mathbf{n} \, \mathrm{d}S}_{I_2} = \underbrace{\iint_{ABCD} -g' \frac{\partial \rho^*}{\partial x} \, \mathrm{d}A}_{I_3}, \qquad (3.43)$$

where CS denotes the surface of the control volume $ABCD$. We now consider the flow to be locally unidirectional at the in- and outflow boundaries, and assume that u_1 and u_2 do not vary with y. The integrals in equation (3.44) can then be evaluated individually. Integral I_1, which accounts for the temporal rate of change of vorticity within $ABCD$, yields

$$I_1 = \frac{\partial}{\partial t} \int_x^{x+\Delta x} \mathrm{d}x \int_0^H -\frac{\partial u}{\partial y} \, \mathrm{d}y = \frac{\partial}{\partial t} \int_x^{x+\Delta x} -(u_2 - u_1) \mathrm{d}x. \qquad (3.44)$$

I_2 accounts for the convective flux of vorticity into and out of the control volume, which can be obtained by multiplying the strength of the vortex sheet with its principal velocity.

80

Consequently,

$$I_2 = \frac{u_1^2(x + \Delta x) - u_1^2(x)}{2} - \frac{u_2^2(x + \Delta x) - u_2^2(x)}{2} \, . \tag{3.45}$$

Finally, the baroclinic vorticity generation can be evaluated as

$$
\begin{aligned}
I_3 &= \int_0^H \mathrm{d}y \int_x^{x+\Delta x} -g' \frac{\partial \rho^*}{\partial x} \mathrm{d}x = \int_0^H -g' \big[\rho^*(x + \Delta x) - \rho^*(x) \big] \mathrm{d}y \\
&= -g' \big[h(x + \Delta x) - h(x) \big] \, .
\end{aligned}
\tag{3.46}
$$

In the limit of $\Delta x \to 0$, we thus obtain

$$\frac{\partial u_2}{\partial t} - \frac{\partial u_1}{\partial t} + u_2 \frac{\partial u_2}{\partial x} - u_1 \frac{\partial u_1}{\partial x} = g' \frac{\partial h}{\partial x} \, . \tag{3.47}$$

This is identical to what one obtains in the Boussinesq limit from the shallow water equations when subtracting the lower layer momentum equation (3.3) from the upper layer one (3.4) in [28]. We thus conclude that, perhaps not unexpectedly, for locally unidirectional flow with constant velocity across the height of each layer, the vorticity-based model and shallow water theory are equivalent to each other. When the velocity is not approximately unidirectional, such as in the vicinity of a gravity current front or an internal bore, shallow water theory is no longer applicable, whereas vorticity-based models are still able to capture the physics correctly.

3.2   DNS results and comparisons

In the following, we compare predictions by the vorticity model with direct numerical simulation results, as well as with earlier experimental data and model predictions by other authors. The DNS data were obtained with our code TURBINS. As discussed in

chapter 2, TURBINS is a finite-difference solver based on a fractional step projection method, along with TVD-RK3 time integration. It solves the unsteady, incompressible Navier-Stokes equations in the Boussinesq limit

$$\nabla \cdot \mathbf{V}^* = 0 \,, \tag{3.48}$$

$$\frac{\partial \mathbf{V}^*}{\partial t^*} + \mathbf{V}^* \cdot \nabla \mathbf{V}^* = -\nabla p^* + \frac{1}{Re} \nabla^2 \mathbf{V}^* + \rho^* \mathbf{e}^g \,, \tag{3.49}$$

$$\frac{\partial \rho^*}{\partial t^*} + \mathbf{V}^* \cdot \nabla \rho^* = \frac{1}{Pe} \nabla^2 \rho^* \,, \tag{3.50}$$

where $\mathbf{V}^*$ and $\mathbf{e}^g$ represent the velocity vector and unit vector in the direction of gravity, respectively. The dimensionless time is defined as $t^* = t/\sqrt{H/g'}$. The governing dimensionless parameters have the form of a Reynolds number $Re = \sqrt{g'H_{lock}}H_{lock}/\nu$ and a Péclet number $Pe = \sqrt{g'H_{lock}}H_{lock}/D$. Here, ν indicates the kinematic viscosity and D denotes the diffusivity of the density field. We apply free-slip conditions for the velocity, along with vanishing normal flux conditions for the density field, along all solid boundaries. Re and Pe are set to 8,000 and 40,000 in the simulations, respectively, to minimize the effects of diffusion. Initially the fluids are at rest, and the density field is as sketched in Fig. 3.1a. The computational domain has the dimensionless size 70×1, and the lock length is set to 35. The domain is discretized uniformly with $\Delta x^* = 0.01$ and $\Delta y^* = 0.004$, which is sufficiently fine to yield converged results.

Figure 3.8 shows the temporal evolution of a partial lock-release flow for various values of the lock height H_{lock}^*. All values of H_{lock}^* give rise to a right-propagating gravity current ahead of a rarefaction wave. On the other hand, the left-propagating flow varies qualitatively with H_{lock}^*. For small values of H_{lock}^*, the rarefaction wave extends all the way to the lock fluid. For increasing lock heights, the front propagating into the lock fluid becomes steeper and bore-like, as seen in frames 3.8e and f. This observation is consistent with the earlier investigations of [28] and [18]. [28] state that this bore begins
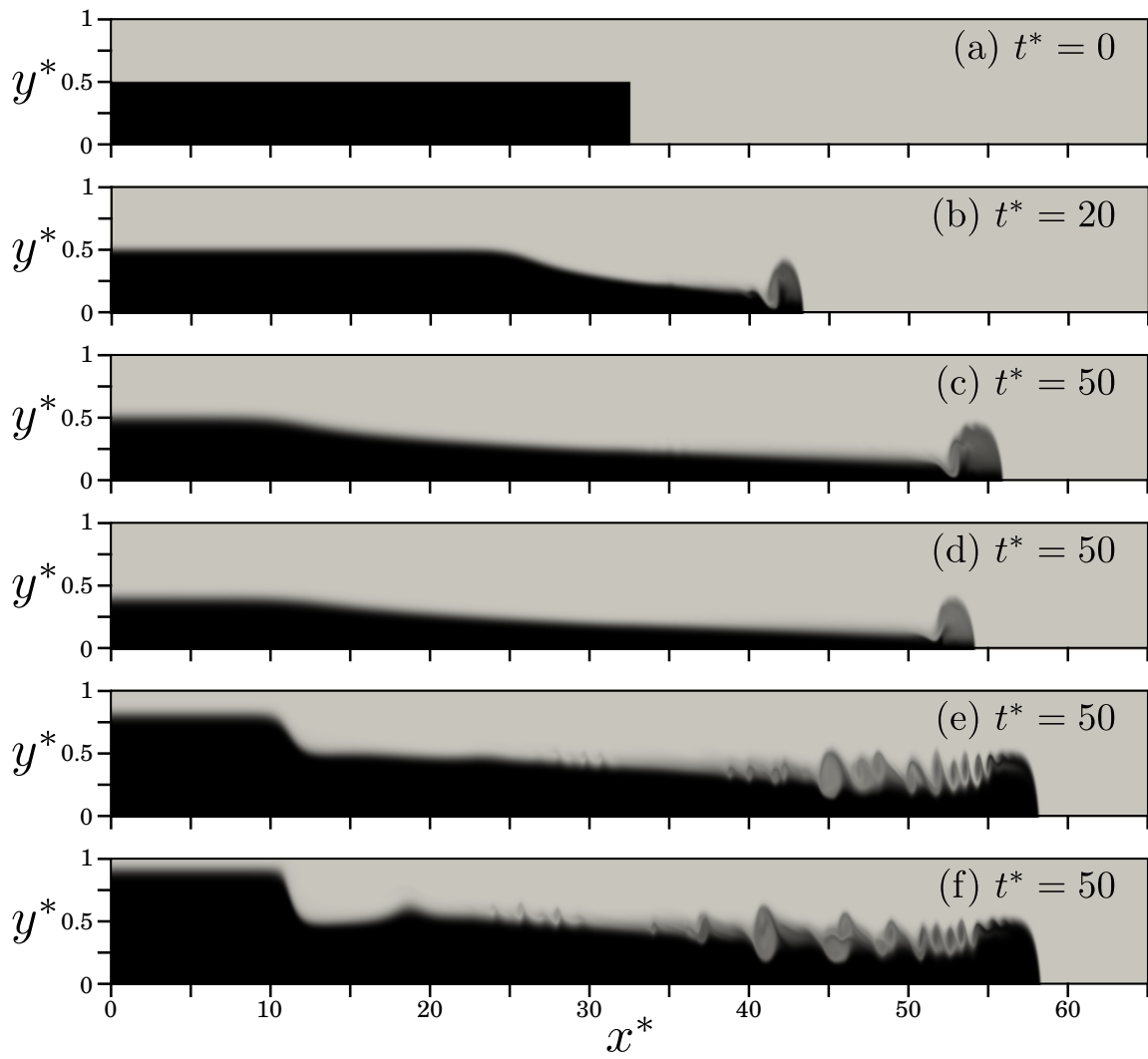
Figure 3.8: (a-c): Temporal evolution of the density field for a partial-depth lock-release flow with $H_{lock}^* = 0.5$. (d-f): Density field at $t^* = 50$ for $H_{lock}^* = 0.4$ (d), $H_{lock}^* = 0.8$ (e), and $H_{lock}^* = 0.9$ (f). The density field varies from $\rho^* = 0$ (light gray) to $\rho^* = 1$ (black).

to form experimentally when $H^*_{lock} \approx 0.7$, while their model predicts bore formation for $H^*_{lock} > 0.5$, in agreement with our analysis in section 3.1. They attribute this discrepancy to diffusive effects and interfacial mixing, both of which are neglected in their theory. [18] argue that the formation of the left-propagating bore starts when infinitesimal long waves travel faster than the left edge of the rarefaction wave, which is theoretically shown to occur for $H^*_{lock} > 2/3$.

To evaluate the front velocity of the gravity current in the DNS simulation, we track its front location $x^*_{g,r}$ with time. We define the local dimensionless interface height $\eta^*(x^*, t^*)$ as

$$\eta^*(x^*, t^*) = \int_0^1 \rho^*(x^*, y^*, t^*) \, \mathrm{d}y^* \,, \tag{3.51}$$

and determine $x^*_{g,r}$ as the rightmost location at which $\eta^* > 0.01$. The solid lines in Figs. 3.9a and 3.10a show that for $H^*_{lock} = 0.5$ and 0.8 the slope $\mathrm{d}x^*_{g,r}/\mathrm{d}t^*$ becomes constant after a brief initial transient, which indicates a quasisteady gravity current velocity.

Finding the horizontal location of the right edge x^*_r of the rarefaction wave as a function of time is slightly more complicated. Figure 3.11 shows that behind the gravity current head the interface height drops abruptly. For $H^*_{lock} \leq 0.5$, an extended interface segment of nearly constant height follows that can easily be identified. For $H^*_{lock} > 0.5$, on the other hand, the gravity current exhibits significant turbulence, so that its interface height fluctuates until it reaches the rarefaction wave. Within the rarefaction wave region, the interface height fluctuations are much reduced. Consequently, in order to identify x^*_r coming from the left, we search for the end of an extended region of at least three unit lengths over which $\partial \eta^*/\partial x^*$ does not change its sign. The data shown by the dotted lines in Fig. 3.9a and 3.10a indicate that this methodology is successful in identifying the right edge of the expansion fan and finding its propagation velocity, which is constant to a good approximation. We note that for $H^*_{lock} = 0.8$ the velocity of the right edge u^*_r is

Figure 3.9: DNS results for the temporal evolution of (a) the front location of the gravity current (solid line) and the location of the right edge of the rarefaction wave (dotted line), and (b) the location of the left edge of the wave, for $H^*_{lock} = 0.5$. The straight line segments represent the corresponding quasisteady velocities, obtained by linear fits of the DNS results.
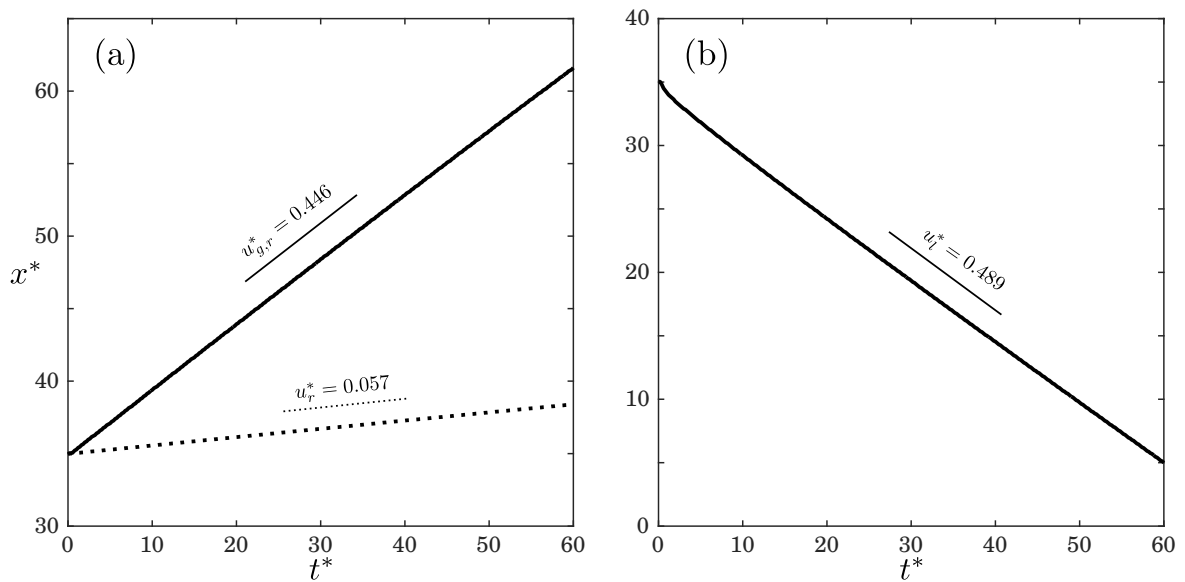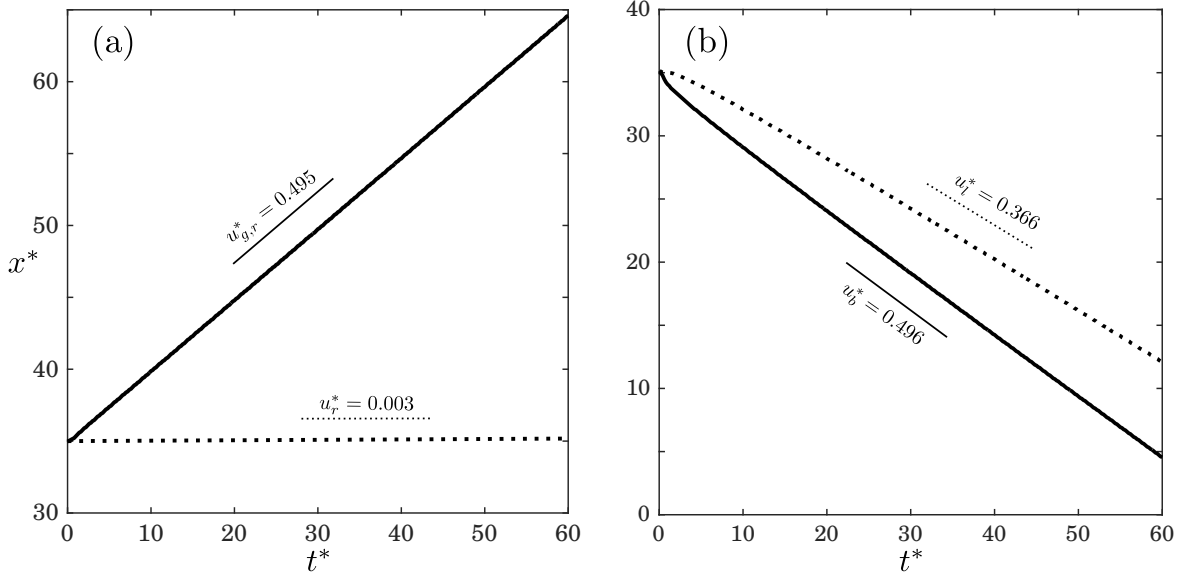
Figure 3.10: DNS results for the temporal evolution of (a) the front location of the gravity current (solid line) and the location of the right edge of the rarefaction wave (dotted line), and (b) the left edge of the bore (solid line) and of the rarefaction wave (dotted line), for $H_{lock}^* = 0.8$. The straight line segments represent the corresponding quasisteady velocities, obtained by linear fits of the DNS results.

substantially smaller as compared to $H_{lock}^* = 0.5$. These DNS data will be compared to model predictions in section 3.2.1.

After determining the locations of the gravity current front $x_{g,r}^*$ and the right edge of the rarefaction wave x_r^*, the gravity current height $h_{g,r}^*$, can be obtained as the average of η^* over the interval from x_r^* to $x_{g,r}^*$

$$h_{g,r}^* = \frac{\int_{x_r^*}^{x_{g,r}^*} \eta^*(x^*, t_s^*)\ \mathrm{d}x^*}{x_{g,r}^* - x_r^*}\ , \tag{3.52}$$

where t_s^* should be chosen sufficiently large, such that the gravity current height has become time-independent. Here, we take $t_s^* = 50$.

The left edge of the rarefaction wave is the location at which the interface height begins to decrease from its lock value H_{lock}^*. Hence, its location x_l^* can be obtained as
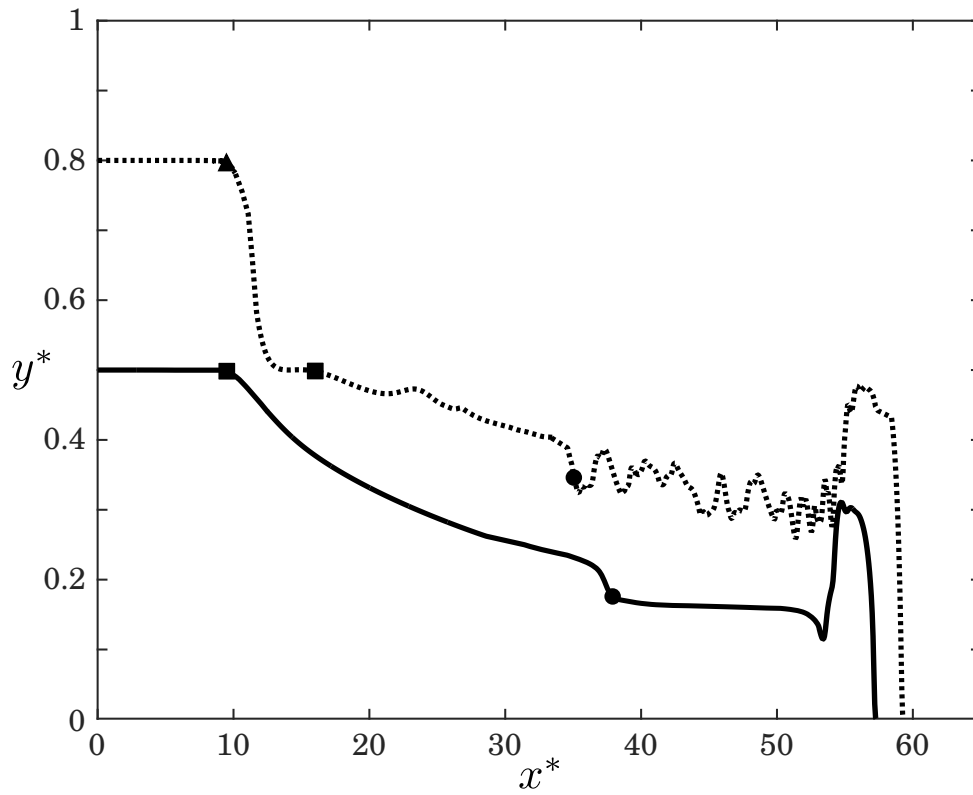
Figure 3.11: DNS results for the local interface height at $t^* = 50$, for $H_{lock}^* = 0.5$ (solid line) and 0.8 (dotted line). The circles, squares and the triangle represent the locations of the right and left edges of the rarefaction wave, as well as the left edge of the bore.

the leftmost point for which $|\eta^* - H_{lock}^*| > 0.01$. For $H_{lock}^* > 0.5$, when the flow gives rise to the left-propagating bore, this procedure yields the horizontal location of the left edge of the bore, denoted by x_b^*. In the presence of a bore, the left edge of the expansion fan x_l^* is found as follows. Coming from the bore, we look for the first location where $|\partial\eta^*/\partial x^*| < 0.01$, to make sure we have exited the bore region. We refer to this point as x_e^*. We then identify the left edge of the rarefaction wave x_l^* as the first location to the right of x_e^* at which $|\partial\eta^*/\partial x^*|$ exceeds 0.01. The interface height right after the hydraulic drop can then be calculated in the same fashion as the gravity current height, i.e. by averaging the local interface height η^* from x_e^* to x_l^*

$$h_l'^* = \frac{\int_{x_e^*}^{x_l^*} \eta^*(x^*, t_s^*)\ \mathrm{d}x^*}{x_l^* - x_e^*}\ . \tag{3.53}$$

Again, we select $t_s^* = 50$, which yields a quasisteady result.

Figures 3.9b and 3.10b represent the temporal variation of x_l^* and x_b^* for $H_{lock}^* = 0.5$ and 0.8, respectively. Note that the case $H_{lock}^* = 0.5$ is just at the limit of the regime where a left-propagating bore begins to form. After a brief initial transient, x_l^* and x_b^* vary linearly with time, indicating that the bore and the left edge of the expansion wave travel with constant velocities. The bore velocity is seen to be very close to 0.5, which is consistent with the analysis in section 3.1.1. Additionally, in agreement with the findings of section 3.1.1, Fig. 3.10b confirms that the left edge of the rarefaction wave travels more slowly than the bore, so that the distance between the bore and the expansion fan grows with time.

3.2.1 Comparisons

Figure 3.12 compares the predictions by the differential vorticity model with DNS results, as well as with earlier model predictions and experimental data by other authors
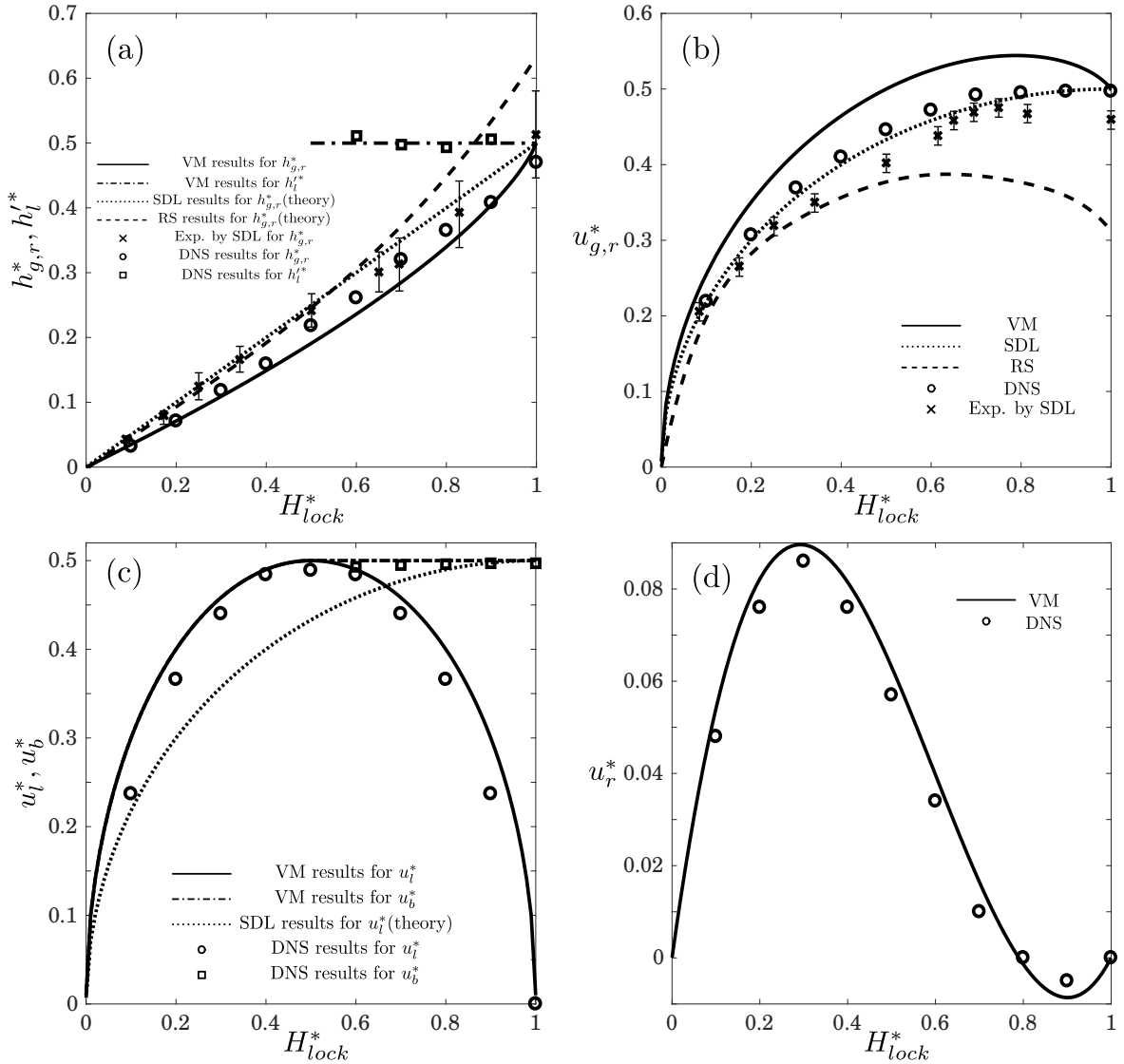
Figure 3.12: Variation as function of the lock height H^*_{lock}: (a) the height $h^*_{g,r}$ of the gravity current and the interface height h'^*_l after the hydraulic drop, (b) the velocity $u^*_{g,r}$ of the gravity current, (c) the velocity u^*_l of the left edge of the rarefaction wave and the velocity u^*_b of the bore, and (d) the velocity u^*_r of the right edge of the rarefaction wave. Here, VM refers to the current vorticity-based model, SDL to the results of [18], and RS to the results of [28], respectively.

where available. All existing models predict a continuous increase of the gravity current height with the lock height. The experimental and DNS results generally fall in between the various model predictions and indicate a gravity current height slightly less than half the lock height. Both the results of [18] and the vorticity model recover the classical full-depth lock-exchange result of [1] and [19]. Equations (3.19) and (3.24) of the present model also correctly predict that $u_l^* = u_r^* = 0$ in this limit, indicating that no expansion fan forms for a full-depth lock-release. The model of [28] does not converge to this limit, as it does not account for the left-propagating bore. Regarding the gravity current velocity, [18] predicts a continuous increase with lock height, whereas the vorticity model yields a maximum value of $u_{g,r}^*$ for $H_{lock}^* = 0.789$, which corresponds $h_{g,r}^* = 0.333$. This is consistent with the analysis of [19] and close to the results of [1], which display a maximum at $h_{g,r}^* = 0.347$. Although the gravity current speeds predicted by [18] agree more closely to the DNS and experimental results compared to those of the current study and [28], we should note that unlike other models, [18] cannot obtain $u_{g,r}^*$ for a gravity current with a given height, unless the height of the lock from which this gravity current has been produced is also prescribed, as can be realized from equation (3.1).

The DNS data for u_b^* are consistent with the finding by the vorticity model that a left-propagating bore emerges when the lock height exceeds half the tank depth, and that this bore travels with a velocity of 0.5, independent of H_{lock}^*. The current model also predicts that the interface height after this hydraulic drop $h_l'^*$ is always equal to 0.5, in very close agreement with DNS results. In addition the vorticity model predicts, and the DNS results confirm, that the dependence of the expansion fan's left edge velocity u_l^* on H_{lock}^* is symmetric with regard to $H_{lock}^* = 0.5$. The model of [18], on the other hand, predicts that the propagation speed of the fastest leftward disturbance, as represented by the left edge of the expansion fan before the formation of the bore and the bore otherwise, is always opposite and equal to the gravity current velocity, which is not confirmed by the

current DNS results. The vorticity model predictions for u_r^*, which are in close agreement with the DNS results, become negative beyond $H_{lock}^* = 0.789$, so that the rarefaction wave as a whole travels to the left.

3.3   Energy assessment

When deriving the set of governing equations, we did not invoke any assumptions about energy conservation or energy losses in the flow. Consequently, we can now assess the energetics of the flow *a posteriori*, by evaluating the headloss along the top wall of the tank from B to A in Fig. 3.1b and 3.1c. The pressure difference along this streamline can be calculated from the horizontal momentum balance for the control volume $ABDE$ in the laboratory reference frame. The flow is at rest at AE and BD, and the velocity along the top wall is taken from the preceding analysis. Due to the unsteadiness of the flow within $ABDE$, we need to employ the unsteady form of the streamwise momentum conservation equation and account for the rate $\dot{M}$ at which momentum changes within the control volume. Hence, we obtain

$$\dot{M} = \int_D^B p\mathrm{d}y - \int_E^A p\mathrm{d}y = (p_B - p_A)H - (\rho_g - \rho_a)g\frac{H_{lock}^2}{2}\,, \qquad (3.54)$$

where we assume that the pressure is hydrostatic at the boundaries. The rate at which momentum inside $ABDE$ changes with time is given by the sum of the rates at which momentum changes inside the gravity current, expansion wave and left-propagating bore regions

$$\dot{M} = \dot{M}_{gc} + \dot{M}_w + \dot{M}_{lb}\,. \qquad (3.55)$$

These individual rates can be calculated by multiplying the rate at which the area of the flow region under consideration increases, with the momentum per unit area. Con-

sequently

$$\dot{M}_{gc} \;=\; \rho_a(u_{g,r} - u_r)\big(u_{g,r}h_{g,r} - u_{a,r}(H - h_{g,r})\big)\,, \tag{3.56}$$

$$\dot{M}_w \;=\; \int_{h_{g,r}}^{H_{lock}} \rho_a \frac{\mathrm{d}u}{\mathrm{d}h}\big(u_g h - u_a(H - h)\big)\;\mathrm{d}h\,, \tag{3.57}$$

$$\dot{M}_{lb} \;=\; \rho_a(u_b - u_l)\big(u_{g,l}h'_l - u_{a,l}(H - h'_l)\big)\,. \tag{3.58}$$

Mass conservation gives $u_{g,r}h_{g,r} = u_{a,r}(H - h_{g,r})$ for the gravity current, $u_g h = u_a(H - h)$ in the expansion wave, and $u_{g,l}h'_l = u_{a,l}(H - h'_l)$ for the bore, so that the right-hand sides of equations (3.56)-(3.58) vanish in the Boussinesq limit. Hence we obtain $\dot{M} = 0$, so that equation (3.54) yields

$$p_B - p_A = (\rho_g - \rho_a)g\frac{H_{lock}^2}{2H}\,. \tag{3.59}$$

Once we determine the pressure difference $p_B - p_A$ along the top wall, the corresponding headloss Δ can then be obtained from the unsteady form of Bernoulli's equation along streamline BA

$$p_B + \frac{1}{2}\rho_a u_B^2 + \rho_a \frac{\partial \phi}{\partial t}\bigg|_B = p_A + \frac{1}{2}\rho_a u_A^2 + \rho_a \frac{\partial \phi}{\partial t}\bigg|_A + \Delta\,. \tag{3.60}$$

Here, ϕ denotes the velocity potential for the upper layer. u_A and u_B represent the flow velocities at A and B, which vanish as the fluid is at rest at these locations. Clearly, ϕ has to be continuous, and its x-derivative should recover the horizontal velocity in the

ambient. These conditions can be satisfied for $H_{lock} \leq H/2$ by

$$\phi = \begin{cases} 0 & \text{for } x_A \leq x < x_O \,, \\ -\int_{x_O}^{x} u_a \mathrm{d}s & \text{for } x_O \leq x < x_{O'} \,, \\ -u_{a,r}(x - x_{O'}) - \int_{x_O}^{x_{O'}} u_a \mathrm{d}s & \text{for } x_{O'} \leq x < x_F \,, \\ -u_{a,r}(x_F - x_{O'}) - \int_{x_O}^{x_{O'}} u_a \mathrm{d}s & \text{for } x_F \leq x \leq x_B \,, \end{cases}$$

(3.61)

and for $H_{lock} > H/2$ by

$$\phi = \begin{cases} 0 & \text{for } x_A \leq x < x_C \,, \\ -u_{a,l}(x - x_C) & \text{for } x_C \leq x < x_O \,, \\ -u_{a,l}(x_O - x_C) - \int_{x_O}^{x} u_a \mathrm{d}s & \text{for } x_O \leq x < x_{O'} \,, \\ -u_{a,r}(x - x_{O'}) - u_{a,l}(x_O - x_C) - \int_{x_O}^{x_{O'}} u_a \mathrm{d}s & \text{for } x_{O'} \leq x < x_F \,, \\ -u_{a,r}(x_F - x_{O'}) - u_{a,l}(x_O - x_C) - \int_{x_O}^{x_{O'}} u_a \mathrm{d}s & \text{for } x_F \leq x \leq x_B \,. \end{cases}$$

(3.62)

Relations (3.61) or (3.62) can be substituted into equation (3.60) to obtain Δ. We render the result dimensionless by scaling pressure and headloss with $p_{ref} = \Delta_{ref} = \rho_a g' H$. The other variables are nondimensionalized as described in section 3.1. We thus obtain for the dimensionless heaadloss Δ^*

$$\Delta^* = \begin{cases} {H_{lock}^*}^2/2 - u_{a,r}^* u_{g,r}^* + \int_{h_{g,r}^*}^{H_{lock}^*} \frac{\mathrm{d}u_a^*}{\mathrm{d}h^*} u^* \mathrm{d}h^* & \text{for } H_{lock}^* \leq 0.5 \,, \\ {H_{lock}^*}^2/2 - u_{a,r}^* u_{g,r}^* - u_{a,l}^* u_b^* + \int_{h_{g,r}^*}^{{h_l'}^*} \frac{\mathrm{d}u_a^*}{\mathrm{d}h^*} u^* \mathrm{d}h^* & \text{otherwise} \,. \end{cases}$$

(3.63)

Figure 3.13 displays the headloss along the top wall for the entire range of H_{lock}^*. Consistent with the analyses of [1] and [19], the flow is energy-conserving only for $H_{lock}^* = 1$, when the left- and right-propagating gravity currents occupy half the depth of the tank. For other values of H_{lock}^*, the flow dissipates energy in the region next to the gravity current, since its height is less than 0.5, as well as in the rarefaction wave, and
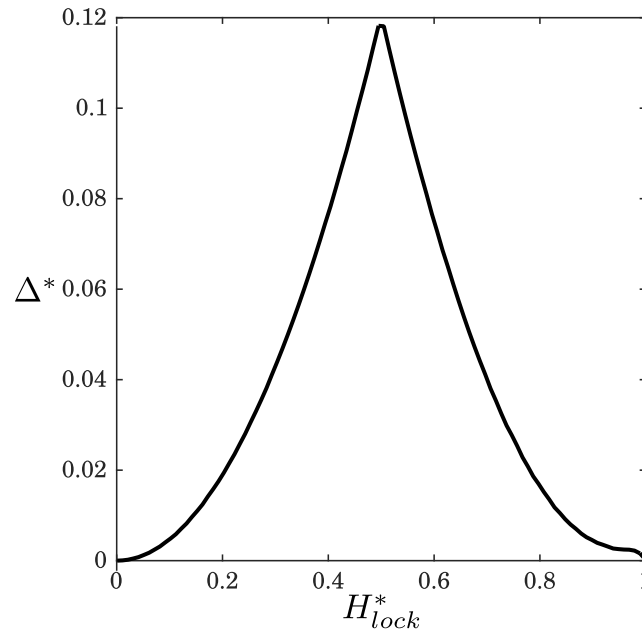
Figure 3.13: Headloss Δ^* along the top wall of the tank, computed from B to A , as a function of the lock height H^*_{lock}.

in the the left-propagating bore when $H^*_{lock} > 0.5$. Note that, on the other hand, the analysis of [18] had assumed nondissipative flow along the top wall. The headloss Δ^* has a maximum for $H_{lock} = H/2$, when the left-propagating bore begins to form.

3.4   Summary

The vorticity-based modeling concept for stratified flows was initially introduced by [19] and [25] for quasisteady conditions. In this chapter, we have further extended this approach to flows that are fully unsteady at least in some regions, so that they cannot be rendered quasisteady by a change of reference frames. In order to accomplish this, we shifted from the integral control volume balance employed in those earlier investigations to a differential control volume balance for the fully unsteady parts of the flow. Evaluation of the conservation equations for mass and vorticity then required the additional assumptions of locally uniform parallel flow within each layer. With these additional

assumptions, we showed that the unsteady vorticity modeling approach reproduces the two-layer shallow water equations for the unsteady sections of the flow.

In order to test this unsteady modeling approach, we applied it to the case of partial-depth lock-release flows, for which we can compare with model-based predictions as well as experimental data of other authors, and with DNS simulations conducted as part of the present investigation. Consistent with the shallow water analysis of [28], the vorticity model demonstrates the formation of a quasisteady gravity current front, a fully unsteady expansion wave, and (for $H^*_{lock} > 0.5$) a quasisteady propagating bore. When a bore forms, it travels with velocity 0.5, and the interface behind it always is at half the channel depth, independent of the lock height. We demonstrate analytically that such bores are energy-conserving. The differential vorticity model furthermore gives predictions for the height and velocity of the gravity current and the bore, as well as for the propagation velocities of the edges of the expansion fan, as functions of the lock height. All of these predictions are seen to be in good agreement with the DNS data and, where available, with experimental results. Since it does not require any energy-based closure assumptions, the vorticity model can be employed for an *a posteriori* analysis of the energetics of the flow. Such an analysis shows lock-release flows to be energy-conserving only for the case of a full lock, whereas they are always dissipative for partial-depth locks.

The current extension enables the vorticity-based approach to formulate simplified models for a range of stratified flow fields with at least some fully unsteady regions.

Chapter 4

Gravity currents propagating into two-layer stratified fluids

Frequently atmospheric or oceanic gravity currents propagate into stratified ambients, rather than into constant density environments. Density stratification due to gradients in temperature, moisture, salinity or sediment concentration, for example, may potentially result in significantly more complex dynamics of the flow, due to the formation of internal waves, with implications for the transport of nutrients or pollution [29–32]. Within the current investigation, we will focus on the specific situation of a two-layer stratified ambient, with a density jump $\Delta\rho$ between the lower and upper layers. For such flows we will formulate a group of models based on vorticity conservation arguments. Two-dimensional direct numerical simulation results will then be compared to predictions by these models, as well as to previous models developed by other authors.

Figure 4.1 presents a schematic of gravity currents propagating into two-layer stratified ambients. In the laboratory reference frame, the gravity current travels with a constant velocity U_g from right to left, into quiescent fluid. For the sake of formulating simplified theoretical models, we shift into the reference frame of the gravity current. In this reference frame the gravity current is at rest, and the ambient fluid approaches from the left inflow boundary with U_g. The gravity current density is denoted by ρ_1,
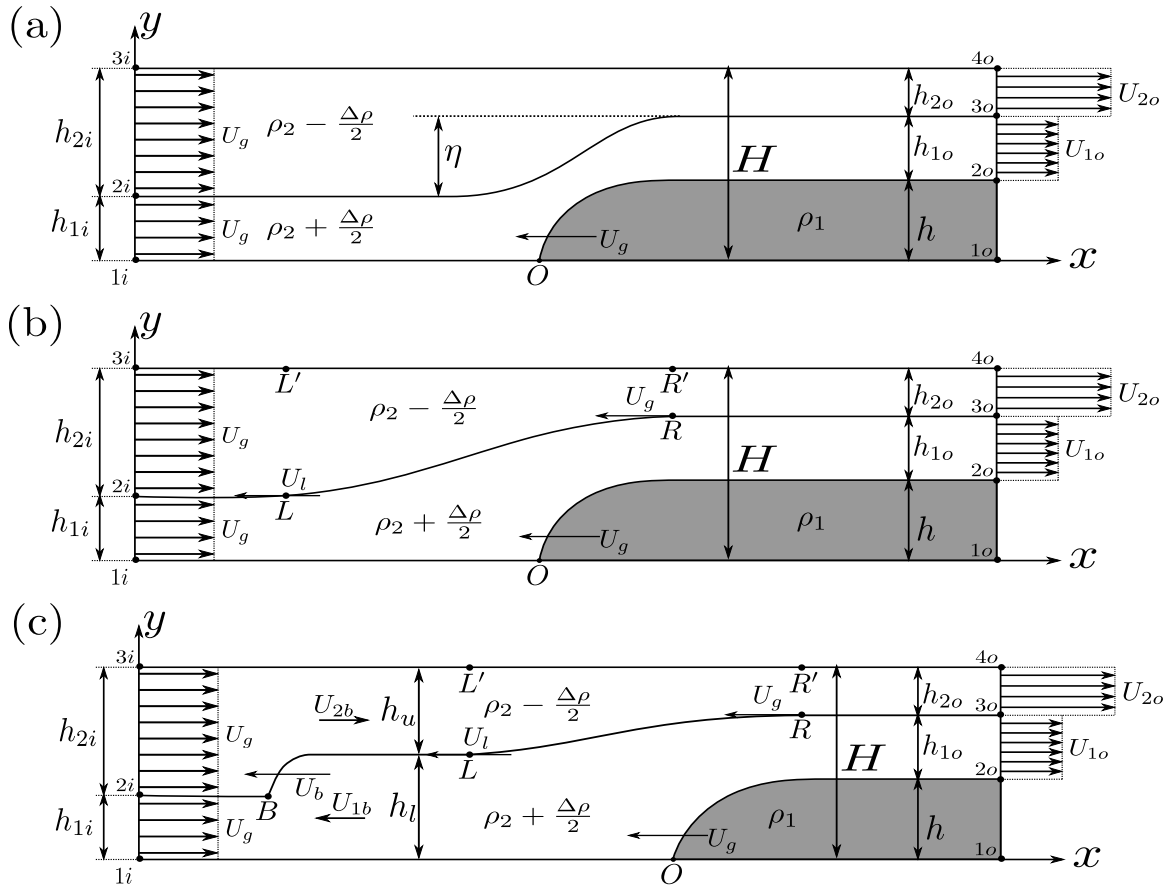
Figure 4.1: Schematic of a gravity current (shaded) propagating into a two-layer stratified ambient: (a) an upstream propagating expansion wave does not form, (b) an upstream wave is generated that travels faster than the gravity current ($U_l > U_g$), and, (c) a hydraulic jump forms that propagates faster than both the upstream traveling wave and the gravity current ($U_b > U_l > U_g$). The gravity current density ρ_1, the average ambient density ρ_2, the density jump $\Delta\rho$, the current height h, and the height h_{1i} of the ambient interface at the inflow boundary are prescribed. Hereafter, configurations a, b and c will be referred to as C1, C2 and C3, respectively.

while the two ambient layers have an average density of ρ_2, so that the densities of the upper and lower layers are $\rho_2 - \Delta\rho/2$ and $\rho_2 + \Delta\rho/2$, respectively. We consider only bottom currents, so that $\rho_1 > \rho_2 + \Delta\rho/2 > \rho_2 - \Delta\rho/2$. Other flow parameters include the depths h_{1i} and h_{2i} of the ambient layers at the inlet, the gravity current height h, and the channel height H.

The development of simplified theoretical models for configuration C1 in Fig. 4.1a dates back to the classical work by [8], who considered inviscid non-Boussineq flows. They solve for both the height and the velocity of the gravity current, as functions of prescribed inflow layer depths and densities. The authors enforce mass conservation in each ambient layer, as well as the conservation of horizontal momentum for the entire channel. To obtain the pressure jump across the front, they assume hydrostatic pressure distributions in the uniform parallel flow regions far up- and downstream. They subsequently close their system of equations by employing Bernoulli's equation along the stagnation point streamline $1i - O$ in Fig. 4.1a, as well as along streamlines $O - 2o$ and $2i - 3o$. Consequently, their model does not allow for energy dissipation in the ambient layers. As they observe multiple solutions for the gravity current height, the authors argue that nature prefers the solution that maximizes the volumetric inflow rate, which always corresponds to the largest gravity current height. The authors then extend their analysis to dissipative flows, by allowing for headlosses in their respective Bernoulli equations. They proceed to calculate the rate of energy dissipation $\dot{E}_d$ for the entire flow, and accept the solution that maximizes $\dot{E}_d$ for a constant volumetric inflow rate. This model was subsequently modified by [33], who considers nondissipative flows in the Boussinesq limit with an upstream propagating bore. The author assumes an infinitely deep channel, so that the velocity in the upper ambient layer is the same everywhere.

Similar to [8], the modeling approach by [34] employs the continuity equation for each ambient layer, along with the conservation of horizontal momentum for the entire

control volume, and Bernoulli's equation upstream of the stagnation point. The authors allow for dissipative effects by enforcing energy-conserving flow in only one of the ambient layers. Consequently, they suggest two different models: in the first model, they invoke Bernoulli's equation within the dense ambient fluid and along the gravity current interface ($O-2o$ in Fig. 4.1a), whereas in the second one, they employ Bernoulli's principle within the light ambient fluid and along the interface between the two ambient fluids ($2i-3o$ in Fig. 4.1a). In order to close both models, [34] assume that the change η in the ambient interface height from far upstream to far downstream is related to the channel height H and the ambient interface height h_{1i} at the inflow boundary as

$$\eta = \frac{1}{2}(H - h_{1i}), \qquad (4.1)$$

which leads to $h_{2o} = h_{2i}/2$. They base this empirical assumption on the examination of two limiting cases: (a) $h_{1i} \to 0$, for which [1] predicts $h/H \to 0.5$, so that $\eta/H \to 0.5$; and (b) $h_{1i} \to H$, for which the upper layer vanishes, i.e. $\eta \to 0$. Assuming that η varies linearly between these two limits, they arrive at equation (4.1). The authors compare their model predictions to experimental and numerical results, and observe good agreement for various flow properties and moderate values of $\Delta\rho$. For large values of $\Delta\rho$ the agreement deteriorates, as will be discussed further in section 4.5.

[35] further extend the above modeling approaches by allowing for equal headlosses in both layers. In order to incorporate potential upstream disturbances, they propose a flow configuration that includes a left-propagating internal bore, as shown in Fig. 4.2. In contrast to C2 or C3 in Fig. 4.1, they do not consider the formation of an expansion wave. To calculate the properties of the upstream bore, they utilize the model of [36] which conserves energy in the lower (expanding) layer. [35] find that the largest, fastest propagating bore forms when $h_l = H/2$, which is consistent with the observations of
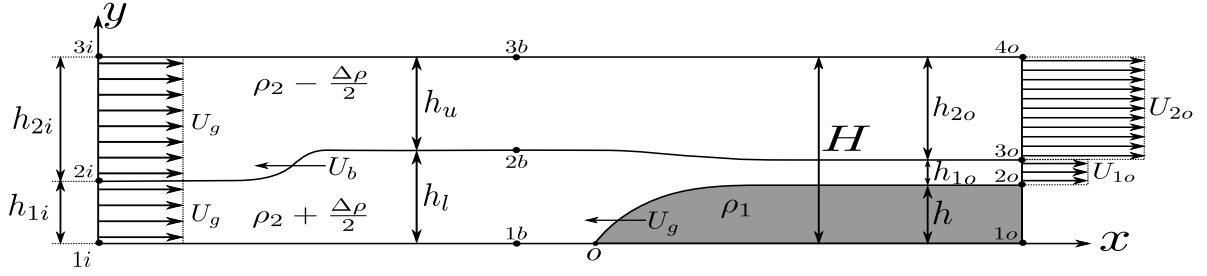
Figure 4.2: Schematic of the model by [35], adapted from their paper. An upstream bore is assumed to exist, with $h_l = H/2$.

[36] and [37]. An energy analysis of this bore in isolation shows the flow to be energy-conserving under these conditions. Thus, in order to close their system of equations, they either set the headloss along the gravity current interface to zero, or they assume the formation of an energy-conserving bore.

The situation of two-layer stratified flows over topography is closely related to gravity currents propagating into a two-layer stratified ambients. Pioneering experiments in this field are described in [38], including the existence of sub- and supercritical flow regimes, as well as upstream propagating expansion waves and internal bores. [38] furthermore discusses an analytical model based on the shallow-water equations that captures the dynamics of a subcritical-supercritical flow with an upstream wave, and he assesses the energy dissipation of the flow. Related investigations were carried out by [39], who categorize all possible flow regimes by defining two dimensionless parameters in the form of $D_o = h/h_{1i}$ and the Froude number $F_o = U/\sqrt{h_{1i}g\Delta\rho/\rho_2}$, where U and h_{1i} indicate the obstacle velocity and the upstream ambient interface height, respectively. Note that the obstacle velocity is related to the gravity current velocity in our study. Both [39] and [29] identify four different flow regimes, *viz.* supercritical, subcritical, partially blocked and completely blocked flows, shown as a, b, c and d in Fig. 4.3, respectively. Supercritical flows, in which an upstream propagating wave does not appear, correspond to configuration C1 in Fig. 4.1a. They can arise only for $F_o > 1$. Partially and completely blocked
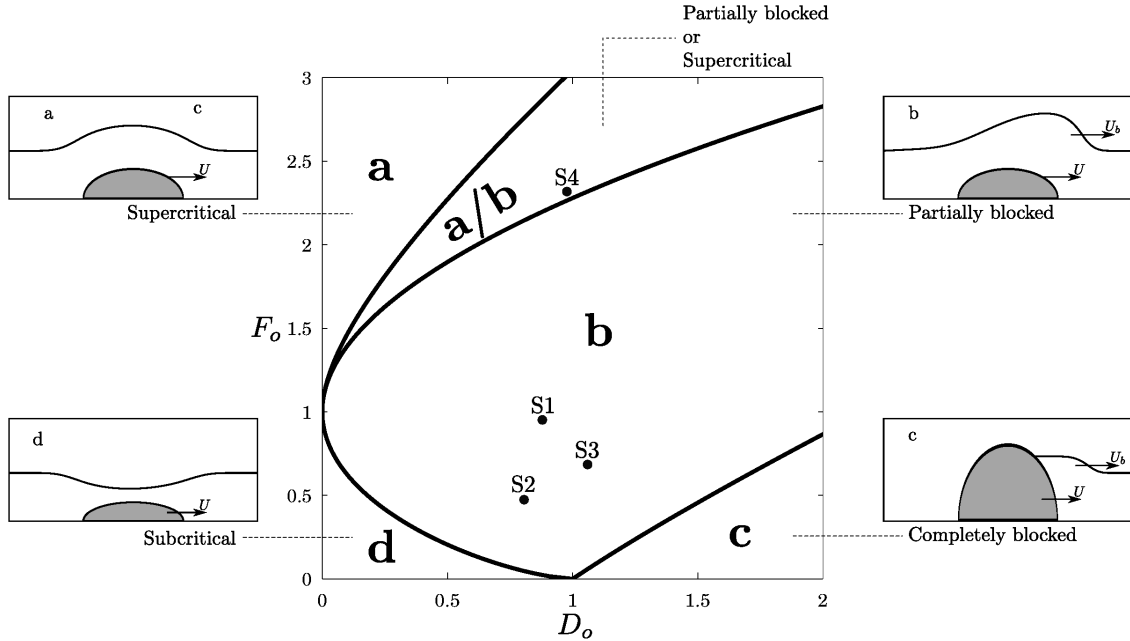
Figure 4.3: Flow regimes for two-layer stratified flows over a streamlined obstacle, with the upper layer being infinitely deep, adapted from [29]. S1 to S4 denote direct numerical simulations to be discussed in the next section.

flows give rise to waves that propagate upstream with velocity U_b, as shown in Fig. 4.3. The dynamics of partially blocked flows is analogous to that of C2- and C3-type flows, shown in Figs. 4.1b and c, respectively. Figure 4.3 illustrates the regions corresponding to each of these regimes for two-layer stratified flows over solid obstacles, along with a schematic of their behavior. The authors also compare their experimental results to the analytical model of [33], as well as to the numerical investigations of [40] and [41], and they observe good qualitative and quantitative agreement.

[35] employ a slightly different classification scheme for gravity currents entering two-layer stratified ambients, by defining the two dimensionless parameters $F_o = U_g/c_o$, and $D_o = h/h_{1i}$. Here $c_o = \sqrt{g\Delta\rho/\rho_2 h_{1i}(1 - h_{1i}/H)}$ represents the linear long wave speed, so that the resulting Froude number is different from that defined by [29]. [35] identify five different flow regimes, including subcritical gravity currents with a depression wave propagating along the ambient interface, gravity currents leading to the formation of an

internal bore traveling along the ambient interface that is followed by an expansion wave (their flow regime III), as well as supercritical gravity currents without upstream propagating disturbances. Their flow regime III corresponds to the partially blocked flows of [29], and to configuration C3 sketched in Fig. 4.1c. Similarly, their sub- and supercritical flow regimes correspond to those of [29]. [35] compare their model predictions to simulation results based on the Euler equations in the Boussinesq limit. They observe good agreement for sub- and supercritical gravity currents, while for flows with an upstream internal bore and/or expansion wave the discrepancy becomes more substantial.

In the following, we extend the vorticity-based modeling approach originally introduced by [19] and [25] for gravity currents and internal bores, to the flow configurations shown in Fig. 4.1. This approach incorporates the momentum conservation principle in its vorticity form along the individual interfaces, thereby reducing the need for empirical closure assumptions based on energy considerations. The resulting models enable us to predict the propagation velocities of the gravity current and any upstream propagating disturbances, as well as the ambient layer velocities and depths at the outflow boundary. Section 4.1 discusses DNS simulations for the different flow regimes. In section 4.2, we present the development of vorticity-based models for these regimes, and we discuss their energetics. Section 4.3 provides predictions based on the vorticity models, which are subsequently compared to the DNS simulation results in section 4.4, and to earlier models by other authors in section 4.5. Section 4.6 summarizes the findings of the current work and gives some concluding remarks.

4.1   DNS simulations

To demonstrate the distinct features that characterize the different flow regimes, and to obtain quantitative information that can subsequently be compared to model

predictions, we now proceed to discuss representative two-dimensional DNS simulation results for Boussinesq flows, based on the equations

$$\boldsymbol{\nabla}\cdot\mathbf{u}^* \quad = \quad 0\,, \tag{4.2}$$

$$\frac{\partial \rho^*}{\partial t^*} + \quad \mathbf{u}^* \quad \cdot\boldsymbol{\nabla}\rho^* = \frac{1}{Pe}\nabla^2\rho^*\,, \tag{4.3}$$

$$\frac{\partial \mathbf{u}^*}{\partial t^*} + \quad \mathbf{u}^* \quad \cdot\boldsymbol{\nabla}\mathbf{u}^* = -\boldsymbol{\nabla}p^* + \frac{1}{Re}\nabla^2\mathbf{u}^* + \rho^*\mathbf{e}^g\,. \tag{4.4}$$

The above system has been rendered dimensionless by introducing the characteristic scales

$$\mathbf{x}^* = \frac{\mathbf{x}}{H}\,, \qquad \mathbf{u}^* = \frac{\mathbf{u}}{\sqrt{g'H}}\,, \tag{4.5}$$

$$t^* = \frac{t}{\sqrt{H/g'}}\,, \qquad \rho^* = \frac{\rho - \rho_2}{\rho_1 - \rho_2}\,, \tag{4.6}$$

$$\Delta\rho^* = \frac{\Delta\rho}{\rho_1 - \rho_2}\,, \qquad p^* = \frac{p}{\rho_2 g'H}\,, \tag{4.7}$$

with the *-symbol indicating dimensionless quantities and $\mathbf{e}^g$ representing the unit vector in the direction of gravity. As dimensionless parameters we obtain $Re = \sqrt{g'H}H/\nu$ and $Pe = \sqrt{g'H}H/D$, where $g' = g(\rho_1 - \rho_2)/\rho_2$. ν and D denote the kinematic viscosity and the diffusivity of the density field, respectively. The simulations are conducted in a reference frame that is moving with velocity U_g^*, which is close to the gravity current front velocity. We impose no-flux conditions for the density field along with free-slip conditions for the velocity field at the upper and lower walls. At the inflow boundary we specify Dirichlet conditions that prescribe the ambient layer heights, velocities and densities. The outflow boundary is handled by a convective condition of the form

$$\frac{\partial q^*}{\partial t^*} + \bar{U}^* \frac{\partial q^*}{\partial x^*} = 0\,, \tag{4.8}$$

Table 4.1: Parameters of the DNS simulations to be discussed in this section.

Sim.	Fig.	Config.	h_{1i}^*	h^*	$\Delta\rho^*$	Re	Pe	L_x	L_y
S1	Fig. 4.4	C1	0.5	0.474	0.6	5,000	20,000	4	1
S2	Fig. 4.6	C2	0.5	0.405	1.4	5,000	20,000	15	1
S3	Fig. 4.7	C3	0.35	0.371	1.4	5,000	20,000	15	1
S4	Fig. 4.9a	C1	0.05	0.0049	1.89	6,000	60,000	4	1
S5	Fig. 4.9b	C1	0.05	0.427	1.89	5,500	30,000	4	1

where q^* can be any flow quantity, and $\bar{U}^*$ is taken as the maximum velocity in the domain. Initial conditions for the gravity current height and the ambient layer thicknesses above the gravity current, as well as the velocity U_g^* of the moving reference frame, are specified based on the simplified models to be derived in section 4.2, as exemplified by Fig. 4.4a. The domain size $L_x \times L_y$ is selected according to whether or not an upstream propagating expansion wave is expected to form. The uniform grid spacing of $\Delta x^* = 0.004$ and $\Delta y^* = 0.003$ is identical for all simulations, and the time step Δt^* is taken according to the CFL stability criterion. Table 4.1 summarizes the parameters of five simulations that will be discussed in some detail.

4.1.1   Partially blocked flows

Figure 4.4 illustrates the temporal evolution of the density field for simulation S1. Transient, convectively unstable Kelvin-Helmholtz waves along the gravity current interface are soon washed out of the control volume, and a quasisteady state evolves. We remark that for some simulations involving larger values of Re (not shown) the KH instabilities remained within the computational domain, so that a strictly quasisteady state did not emerge.

In order to compute the gravity current thickness, we mark the gravity current fluid initially by a passive dye of concentration $c_d^* = 1$. This dye has the same diffusivity as the density field. The local dimensionless height d^* of the gravity current is then obtained
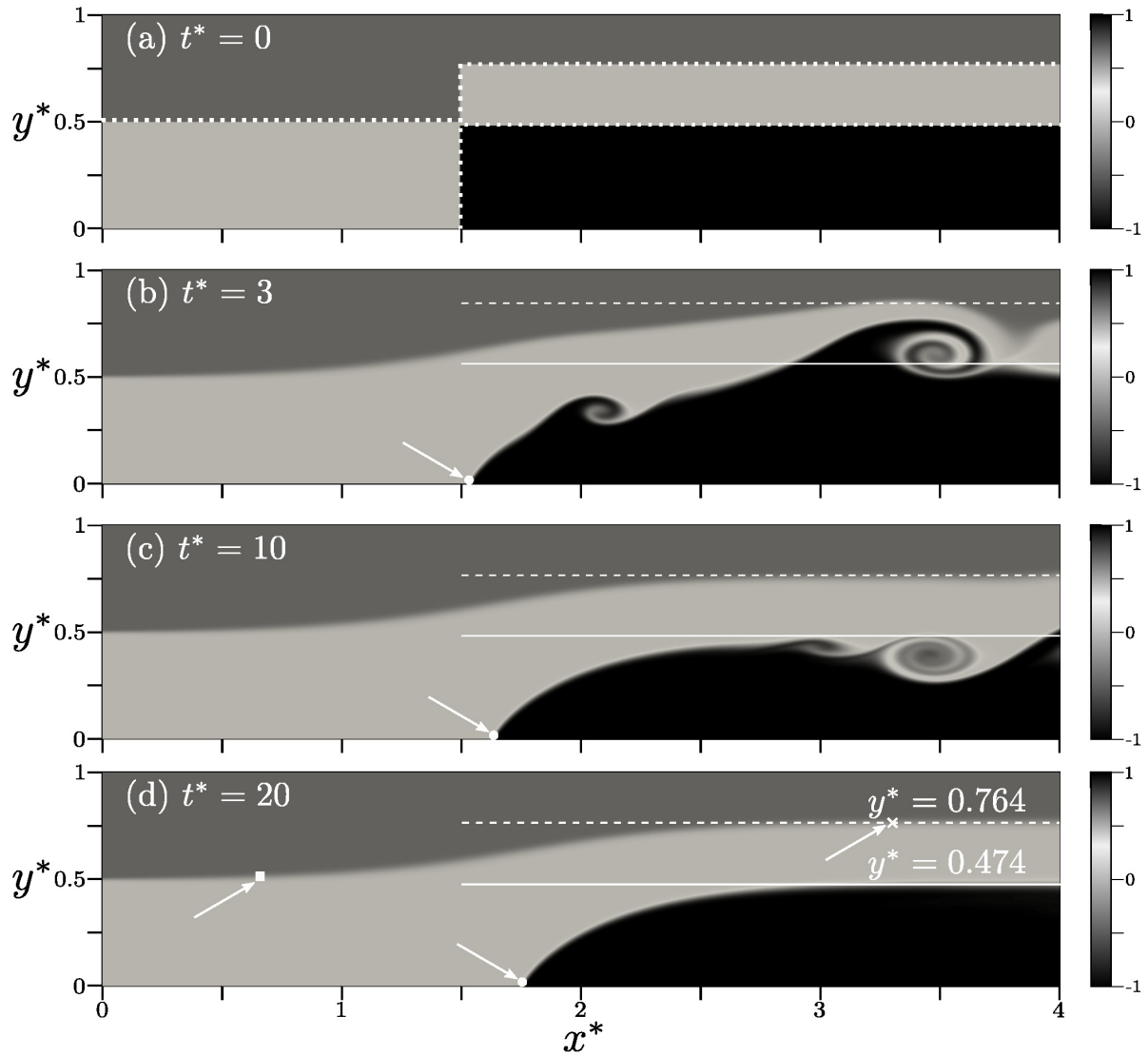
Figure 4.4: Temporal evolution of the density field for simulation S1, at $t^* = 0$ (a), 3 (b), 10 (c), and 20 (d). The simulation parameters are $h_{1i}^* = 0.5$, $\Delta\rho^* = 0.6$, $Re = 5,000$ and $Pe = 20,000$. The initial conditions are prescribed according to the simplified model for configuration C1 derived in section 4.2. The simulation shows the evolution of a steady flow field without upstream propagating disturbances. The transient Kelvin-Helmholtz vortices forming at the interface are swept outside the computational domain, reflecting their convectively unstable nature. The white horizontal solid and dashed lines represent the quasisteady gravity current height and the interface location between the ambient layers at the outflow, respectively. The white circle, square and cross indicate x_f^*, x_l^* and x_r^*, cf. the discussion in the text.

as

$$d^*(x^*, t^*) = \int_0^1 c_d^*(x^*, y^*, t^*) \, \mathrm{d}y^* . \tag{4.9}$$

The gravity current front location x_f^* is defined as the leftmost point at which d^* exceeds 0.01. The local thicknesses d_1^* and d_2^* of the ambient layers can be obtained analogously from corresponding passive dye fields. We furthermore identify the right and left edges of the ambient interfacial wave, x_r^* and x_l^*, in the following fashion: to obtain x_r^* as a function of time, we sweep the ambient interface from the current tip towards the outflow boundary and evaluate x_r^* as the first point at which $|\partial(d^* + d_1^*)/\partial x^*| < 0.01$. x_l^* is taken as the location of the leftmost point of the ambient interface where $d_1^* - h_{1i}^* > 0.01$. For those cases in which the flow gives rise to an internal bore propagating ahead of the expansion fan, this procedure yields the front location x_b^* of the bore. In the presence of a bore, the location x_l^* of the left edge of the expansion wave is then defined as the first point to the right of the bore at which $\partial d_1^*/\partial x^*\big|_{x^*} - \partial d_1^*/\partial x^*\big|_{x^*-\Delta x^*} < 0$. This definition is based on the rapid fall of the ambient interface slope as it transitions from the bore to the expansion fan region. In some cases this decrease occurs only very close to the gravity current tip, so that the disturbance takes the form of an expansion fan without a leading bore.

Within the moving reference frame of the simulation, Fig. 4.5a depicts the displacement with time of the gravity current tip x_f^*, relative to its initial location $x_{f,i}^*$, for all simulations of table 1. In all cases the front velocity $\mathrm{d}x_f^*/\mathrm{d}t^*$ initially varies with time, but eventually settles down to a constant value u_f^*. The front velocity in the laboratory frame is then obtained as

$$U_{g,lab}^* = U_g^* - u_f^* . \tag{4.10}$$

Figure 4.5b displays the displacement of the left edge of the expansion wave x_l^* with respect to the gravity current front location x_f^* as a function of time, for all simulations.
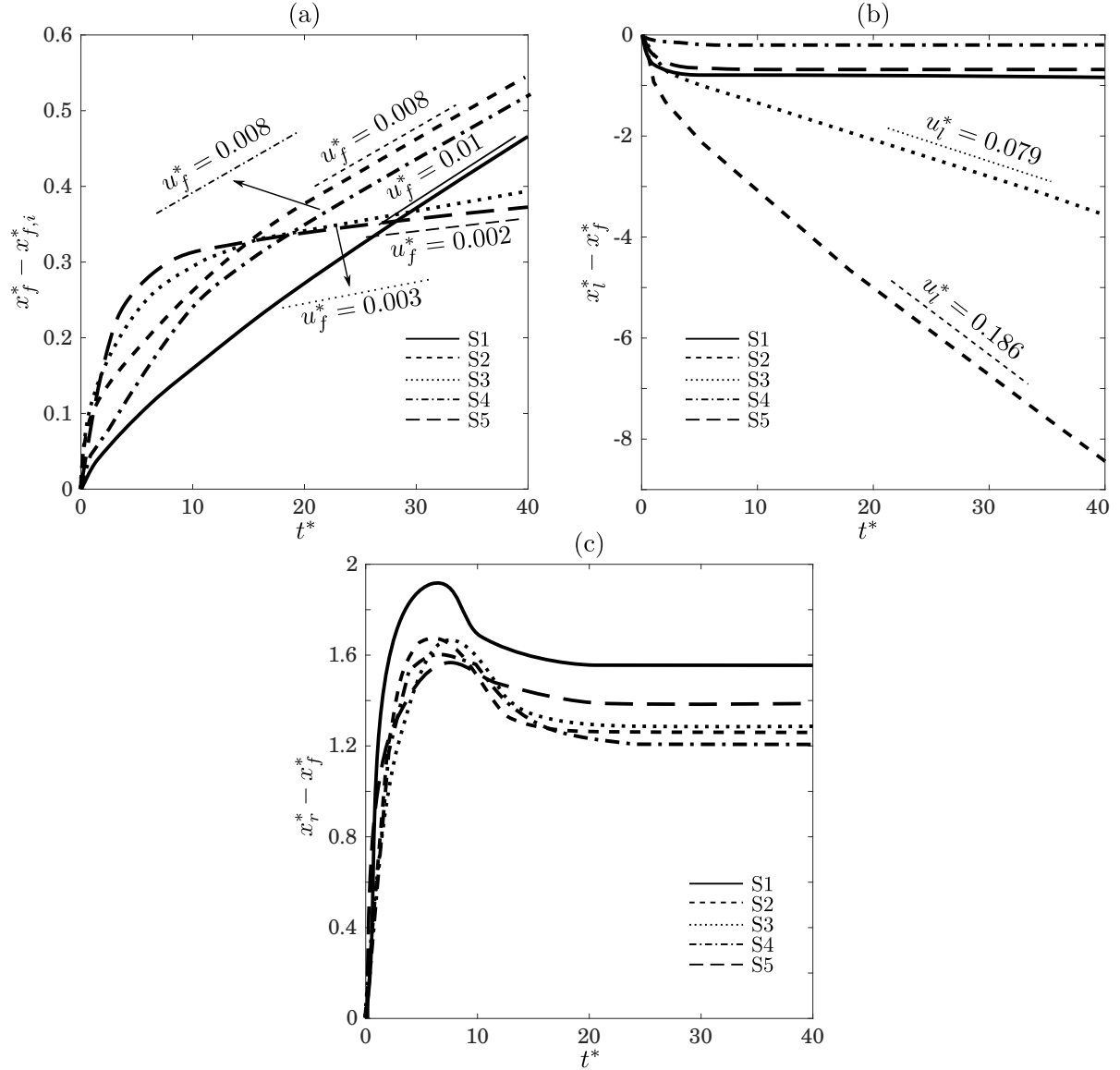
Figure 4.5: DNS results for the temporal evolution of: (a) the displacement of the gravity current tip x_f^* with respect to its initial location $x_{f,i}^*$, (b) the displacement of the expansion wave's left edge x_l^* relative to the gravity current front location x_f^*, and (c) the distance of the right edge x_r^* of the expansion fan from the current tip, evaluated for the simulations of table 1. The straight line segments indicate the quasisteady velocities of the corresponding features in the moving reference frame, which have been obtained by linear fits of the DNS results between $t^* = 20$ and $t^* = 40$, when the flow properties have become nearly independent of time. Note that the quasisteady velocities vanish for simulations S1, S4 and S5 in frame (b), and for all simulations in frame (c).

After a brief transitional phase, $x_l^* - x_f^*$ remains nearly constant with time for S1, S4 and S5, indicating that the left edge of the wave moves at the same speed as the current tip. On the other hand, for cases S2 and S3 the left edge of the wave travels faster than the current tip, so that a quasisteady flow configuration is not achieved, as will be discussed in the context of Figs. 4.6 and 4.7. Here the relative velocity of the left edge of the wave with respect to the front approaches a constant value u_l^* for long times. In the laboratory frame, the left edge of the wave thus travels with velocity

$$U_{l,lab}^* = U_{g,lab}^* + u_l^* . \qquad (4.11)$$

If the flow gives rise to a bore, as will be discussed in the following, the bore speed u_b^* in the moving reference frame can be determined analogously, by tracking the temporal evolution of $x_b^* - x_f^*$. The bore velocity in the laboratory frame is then obtained as

$$U_{b,lab}^* = U_{g,lab}^* + u_b^* . \qquad (4.12)$$

The interface height h_l^* at the left edge of the wave is evaluated as

$$h_l^* = d_1^*(x_l^*, t_s^*) , \qquad (4.13)$$

where we take $t_s^* = 35$, which falls into the quasisteady range.

The distance of the expansion wave's right edge from the gravity current tip $x_r^* - x_f^*$ is shown in Fig. 4.5c for all simulations. In all cases, this distance acquires a quasisteady value for sufficiently large times, which indicates that the right edge of the wave is anchored to the gravity current front.

In order to avoid any potential contamination from the outflow boundary, we evaluate the downstream values of the layer thicknesses some distance upstream of this boundary

as

$$h^* \;=\; d^*(0.9L_x, t_s^*), \tag{4.14}$$

$$h_{1o}^* \;=\; d_1^*(0.9L_x, t_s^*), \tag{4.15}$$

$$h_{2o}^* \;=\; d_2^*(0.9L_x, t_s^*), \tag{4.16}$$

at $t_s^* = 35$. The downstream velocities of the ambient fluid layers are obtained as the average horizontal velocity across the corresponding layer

$$U_{1o}^* \;=\; \frac{\int_{h^*}^{h^*+h_{1o}^*} u^*(0.9L_x, y^*, t_s^*) \,\mathrm{d}y^*}{h_{1o}^*}, \tag{4.17}$$

$$U_{2o}^* \;=\; \frac{\int_{h^*+h_{1o}^*}^{1} u^*(0.9L_x, y^*, t_s^*) \,\mathrm{d}y^*}{h_{2o}^*}, \tag{4.18}$$

for $t_s^* = 35$. The DNS results from this section will be compared to predictions by the vorticity model in section 4.4.

We now proceed to discuss simulations S2, which gives rise to an expansion fan, and S3, which results in the formation of an expansion fan and a bore. These observations are consistent with the findings of [34] and [35]. As shown for simulation S2 in Fig. 4.6c, in the absence of a bore the interfacial slope remains approximately constant over much of the wave region. If a bore is present, on the other hand, the slope of this interface undergoes a noticeable change at some intermediate location, as indicated by the white square in Fig. 4.7. For h_{1i}^* close to one half, the bore becomes weak and increasingly difficult to observe. This is in line with the observations of [28], who noticed that the bore emerging ahead of the expansion wave in their partial lock-release experiments becomes difficult to identify when the ratio of the lock height to the tank depth is below 0.7. Similarly, the simulations of [37] exhibit a more distinct bore when this ratio is 0.8 or
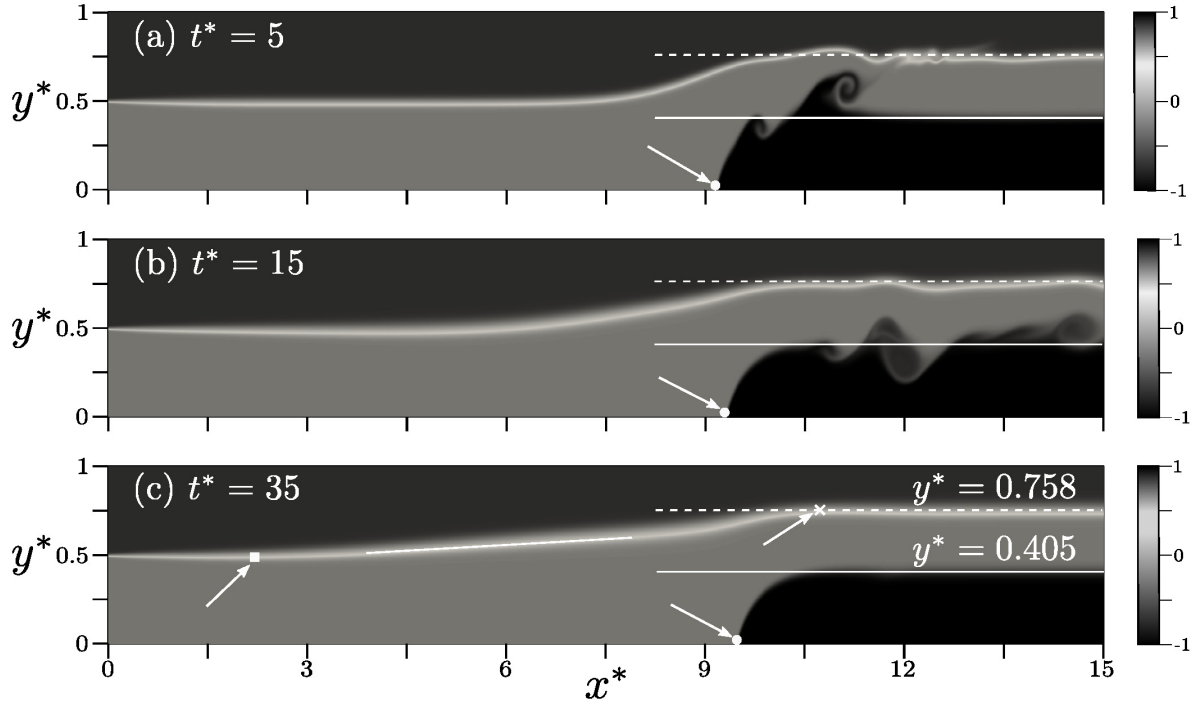
Figure 4.6: Temporal evolution of the density field for simulation S2, at $t^* = 5$ (a), 15 (b), and 35 (c). The simulation parameters are $h_{1i}^* = 0.5$, $\Delta\rho^* = 1.4$, $Re = 5,000$ and $Pe = 20,000$. The initial conditions are prescribed according to the simplified model for configuration C2 derived in section 4.2. The simulation gives rise to an upstream propagating disturbance in the form of an expansion wave. The white horizontal solid and dashed lines represent the quasisteady gravity current height and the interface location between the ambient layers at the outflow, respectively. The white solid line tangent to the ambient interface shows that the interface height varies approximately linearly along the expansion wave. The white circle, square and cross indicate x_f^*, x_l^* and x_r^*, respectively.
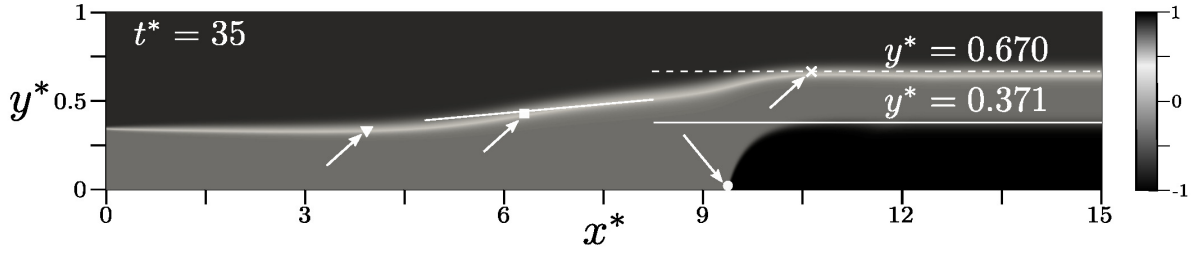
Figure 4.7: Snapshot of the density field for simulation S3 at $t^* = 35$. The simulation parameters are $h_{1i}^* = 0.35$, $\Delta\rho^* = 1.4$, $Re = 5,000$ and $Pe = 20,000$. The initial conditions are prescribed according to the simplified model for configuration C3 derived in section 4.2. The simulation gives rise to an upstream propagating disturbance in the form of a bore, followed by an expansion wave. The white horizontal solid and dashed lines represent the quasisteady gravity current height and the interface location between the ambient layers at the outflow, respectively. The white solid line tangent to the ambient interface is intended to show that the bore region has a larger slope than the expansion fan region. The white circle, triangle, square and cross indicate x_f^*, x_b^*, x_l^* and x_r^*, respectively.

greater.

We now analyze the variation of the ambient layer properties within the wave region, in preparation for developing simplified models in section 4.2. Frames a to d of Fig. 4.8 display the ambient interface height $d^* + d_1^*$, the horizontal flow velocities within the lower and upper ambient layers u_1^* and u_2^*, and the vortex sheet strength $\gamma^* = u_2^* - u_1^*$, within the expansion wave region as functions of the scaled horizontal location $x_s^* = (x^* - x_l^*)/(x_r^* - x_l^*)$, for simulation S2. Here, u_1^* and u_2^* are defined as

$$u_1^*(x^*, t^*) = \frac{\int_{d^*}^{d^* + d_1^*} u^*(x^*, y^*, t^*) \, \mathrm{d}y^*}{d_1^*}, \tag{4.19}$$

$$u_2^*(x^*, t^*) = \frac{\int_{d^* + d_1^*}^{1} u^*(x^*, y^*, t^*) \, \mathrm{d}y^*}{d_2^*}. \tag{4.20}$$

The results are shown for the three times $t^* = 25$, 30 and 35, when the Kelvin-Helmholtz instabilities have left the domain and the flow variables far up- and downstream have become time-independent. While the ambient interface height, as well as u_1^*, u_2^* and γ^*,

111

vary approximately linearly along much of the wave region, they experience more abrupt changes in the vicinity of the gravity current front (vertical dotted lines in Fig. 4.8), due to the strong upward acceleration of the ambient fluid caused by the current nose.

We note that in terms of their dimensionless parameters, all three of the above simulations fall into the partially blocked regime identified by [29] for two-layer stratified flows over solid obstables, cf. Fig. 4.3. The fact that only S2 and S3, but not S1, give rise to upstream propagating waves, reflects subtle differences between the solid obstacle case studied by [29] and the present case of a gravity current. We will return to this point later on.

4.1.2   Supercritical flow

In addition to the partially blocked flows with $U_{g,lab}^* > U_{l,lab}^*$ (or $u_l^* = 0$), there is another flow regime that does not give rise to upstream waves and can be modelled by C1. This supercritical region was introduced by [39] and is sketched in Fig. 4.3. Figure 4.9a, which corresponds to S4 in table 1, reflects this flow regime.

Consistent with Fig. 4.3, in order to achieve supercritical behaviour we take the ratio $D_o = h^*/h_{1i}^* \approx 1$, while the Froude number $F_o = U_g^*/\sqrt{h_{1i}^* \Delta \rho^*}$ needs to be sufficiently large. To increase F_o we select a small value for h_{1i}^* and focus on cases that yield large gravity current front velocities. According to the analytical model to be discussed in section 4.2, and corresponding results of section 4.3, for very small values of h_{1i}^*, U_g^* becomes largest when $\Delta \rho^* \approx 2$. Additionally, because $D_o \approx 1$, the gravity current height needs to be small as well. For these reasons, in case S4 we choose $h_{1i}^* = h^* = 0.05$. Simulating flows of very thin gravity currents whose density is close to that of the lower ambient fluid layer, requires large values of Re and Pe.

For moderate values of $h_{1i}^* \gtrsim 0.15$ the simulations typically yielded only a single
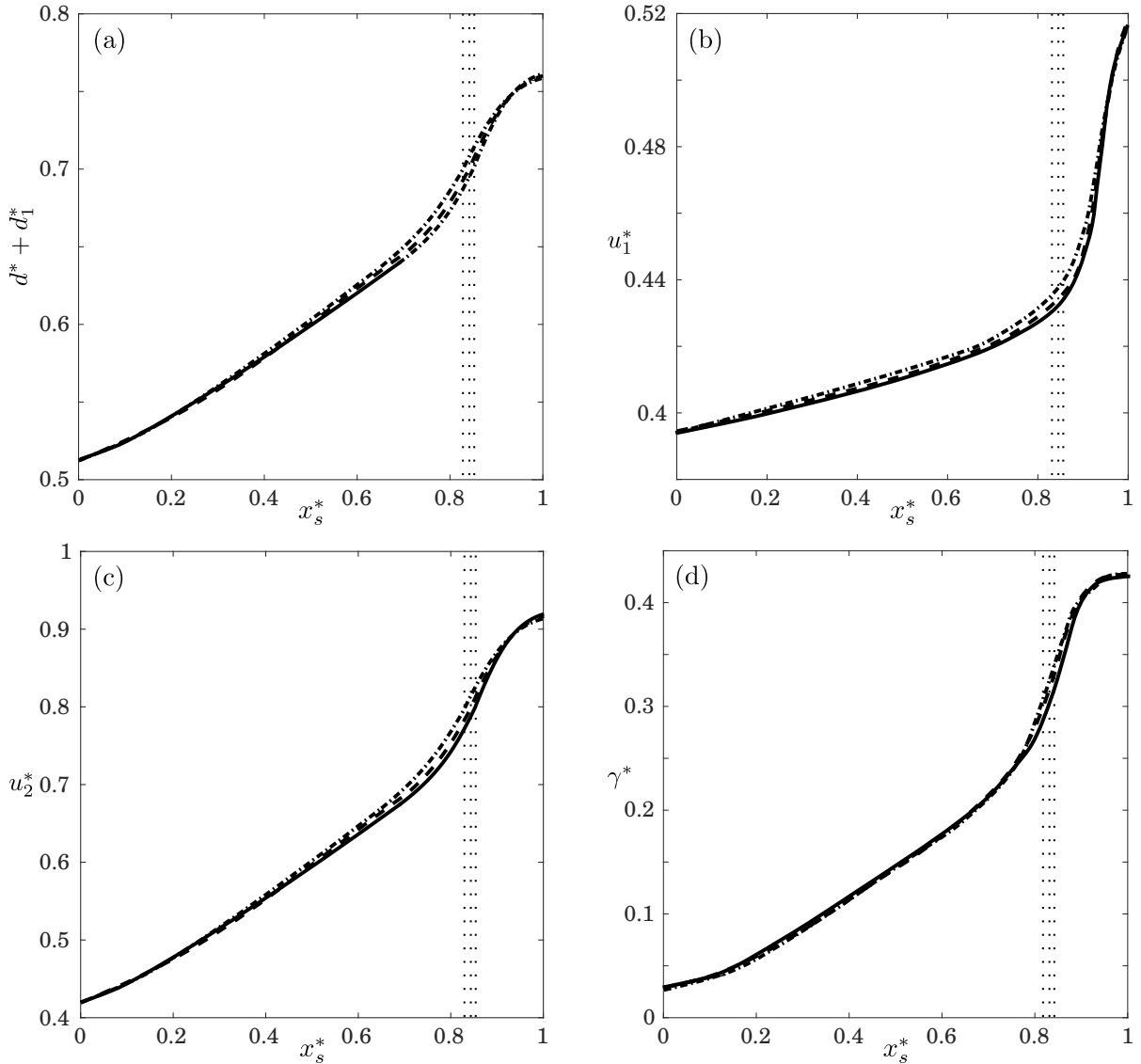
112

Figure 4.8: Simulation S2: DNS results for the spatial variation of various flow properties inside the wave region. (a) interface height $d^* + d_1^*$, (b) velocity u_1^* of the lower ambient layer, (c) velocity u_2^* of the upper ambient layer, and (d) the interfacial vortex sheet strength $\gamma^* = u_2^* - u_1^*$. The results have been obtained for $t^* = 25, 30$ and 35, indicated by the dash-dotted, dashed and solid lines, respectively. The vertical dotted lines denote the location of the gravity current tip, with the leftmost line corresponding to $t^* = 25$ and the rightmost one corresponding to $t^* = 35$. Over much of the expansion wave region, the respective flow properties are seen to vary approximately linearly.
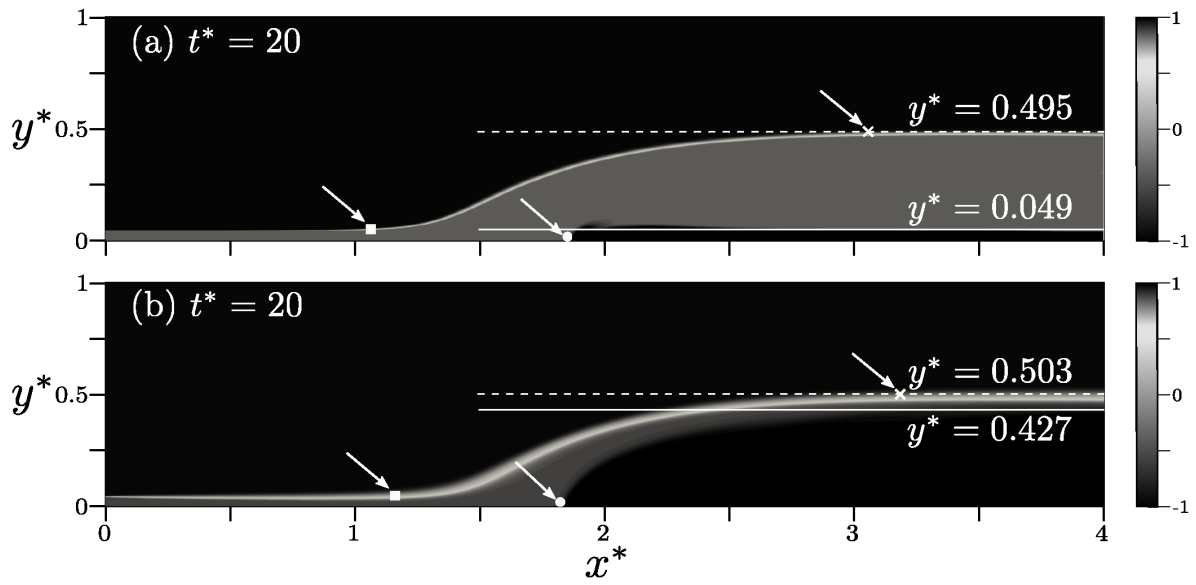
Figure 4.9: Snapshots of the quasisteady density fields for simulations S4 (a) and S5 (b), at $t^* = 20$. The simulation parameters are $h_{1i}^* = 0.05$ and $\Delta\rho^* = 1.89$, and slightly different values of Re and Pe, cf. table 1. S4 and S5, while both corresponding to configuration C1, are classified as supercritical and partially blocked flows, respectively, by [29]. The white horizontal solid and dashed lines represent the quasisteady gravity current height and the ambient interface location at the outflow. The white circles, squares and crosses indicate x_f^*, x_l^* and x_r^*, respectively.

possible gravity current thickness for each $\Delta\rho^*$. On the other hand, for very small values of h_{1i}^* we observed that gravity currents with two different heights might form for the same ambient density difference. Simulations S4 and S5, shown in Fig. 4.9a and b, represent an example in this regard. These simulations have the same values for h_{1i}^* and $\Delta\rho^*$, and slightly different values of Re and Pe, resulting in very different gravity current heights. According to [29], S5 would fall into the completely blocked flow regime for a two-layer flow over a solid obstacle. On the other hand, in our DNS simulations for gravity currents propagating into two-layer stratified ambients we never observed a completely blocked flow, i.e., a flow for which the ambient interface does not pass over the gravity current, even for very small lower ambient inflow thicknesses. Again, this indicates certain differences between the solid obstacle and gravity current cases.

4.2   Vorticity-based modeling

In the following we apply the vorticity-based modeling approach by [19] and [37] to gravity currents propagating into two-layer stratified ambients, for each of the configurations shown in Fig. 4.1.

4.2.1   Flows without upstream propagating disturbance

The most basic flow configuration C1, as sketched in Fig. 4.1a, is characterized by a smooth, steady ambient interface without upstream wave propagation. For a given gravity current height h^*, and prescribed ambient densities and upstream layer thicknesses, we have five unkowns: the velocity U_g^* of the gravity current, as well as the ambient velocities (U_{1o}^*, U_{2o}^*) and layer thicknesses (h_{1o}^*, h_{2o}^*) at the outflow boundary. In the reference frame moving with the gravity current front, the dimensionless mass conservation

equations for the ambient layers read

$$U_g^* h_{1i}^* \;=\; U_{1o}^* h_{1o}^* \,, \tag{4.21}$$

$$U_g^* h_{2i}^* \;=\; U_{2o}^* h_{2o}^* \,. \tag{4.22}$$

Vorticity conservation along the top of the gravity current $O - 2o$ and the interface between the ambient fluid layers $2i - 3o$ results in

$$\frac{1}{2} U_{1o}^{*\,2} \;=\; \frac{g_1'}{g'} h^* \,, \tag{4.23}$$

$$\frac{U_{1o}^* + U_{2o}^*}{2}(U_{2o}^* - U_{1o}^*) \;=\; \frac{g_2'}{g'}(h_{1o}^* + h^* - h_{1i}^*) \,, \tag{4.24}$$

where

$$\frac{g_1'}{g'} \;=\; \frac{\rho_1 - (\rho_2 + \frac{\Delta\rho}{2})}{\rho_1 - \rho_2} \,, \tag{4.25}$$

$$\frac{g_2'}{g'} \;=\; \frac{(\rho_2 + \frac{\Delta\rho}{2}) - (\rho_2 - \frac{\Delta\rho}{2})}{\rho_1 - \rho_2} \;=\; \frac{\Delta\rho}{\rho_1 - \rho_2} \,. \tag{4.26}$$

A fifth equation is obtained from the geometrical constraint at the outflow boundary

$$h^* + h_{1o}^* + h_{2o}^* = 1 \,. \tag{4.27}$$

The above equations (4.21)-(4.24) and (4.27) represent a closed algebraic system for the five unknowns U_g^*, U_{1o}^*, U_{2o}^*, h_{1o}^* and h_{2o}^*, so that empirical closure assumptions are not needed.

As an aside, we insert here a brief comment on the relationship between the headlosses in the upper and lower layers, for the quasisteady flow of C1 in the moving reference frame. Within each layer, the headloss is of course constant along all streamlines, since the flow

is irrotational. We write Bernoulli's equation with a headloss in dimensionless form, for fluid elements immediately below and above the streamline $2i - 3o$

$$p_{2i}^* + \frac{1}{2}U_g^{*2} + \frac{(\rho_2 + \frac{\Delta\rho}{2})g}{\rho_2 g'}h_{1i}^* = p_{3o}^* + \frac{1}{2}U_{1o}^{*\,2} + \frac{(\rho_2 + \frac{\Delta\rho}{2})g}{\rho_2 g'}(h^* + h_{1o}^*) + \Delta_1^*, \quad (4.28)$$

$$p_{2i}^* + \frac{1}{2}U_g^{*2} + \frac{(\rho_2 - \frac{\Delta\rho}{2})g}{\rho_2 g'}h_{1i}^* = p_{3o}^* + \frac{1}{2}U_{2o}^{*\,2} + \frac{(\rho_2 - \frac{\Delta\rho}{2})g}{\rho_2 g'}(h^* + h_{1o}^*) + \Delta_2^*. \quad (4.29)$$

Here Δ_1^* and Δ_2^* represent the dimensionless headlosses within the lower and upper ambient layers, respectively, scaled by $\Delta_{ref} = \rho_2 g' H$. Subtracting equation (4.29) from equation (4.28) yields

$$\Delta_1^* - \Delta_2^* = \frac{1}{2}(U_{2o}^{*\,2} - U_{1o}^{*\,2}) - \frac{g_2'}{g'}(h^* + h_{1o}^* - h_{1i}^*). \quad (4.30)$$

The right-hand side of this equation vanishes according to equation (4.24), and we conclude that vorticity conservation immediately implies that both ambient layers have the same headloss. We will return to this point when discussing the assumptions underlying previous models of earlier investigators in section 4.5.

4.2.2   Propagation of a rarefaction wave towards the inflow boundary

Figure 4.1b displays configuration C2, a flow with a rarefaction wave traveling towards the inflow boundary, which causes the steady state assumption to be invalid, even in the reference frame moving with the gravity current tip. The DNS results of section 4.1 show that the right edge R of the wave remains stationary in the reference frame of the gravity current. The speed U_l of the left edge L of the wave is merely a function of the inflow

conditions

$$U_l^* = \sqrt{\Delta\rho^* h_{1i}^* h_{2i}^*}\,, \tag{4.31}$$

cf. [37]. We then need five additional equations to determine the remaining unknowns U_g^*, U_{1o}^*, U_{2o}^*, h_{1o}^* and h_{2o}^*. These can again be obtained from the mass balances of the two ambient layers, the vorticity balances along the two interfaces, and the geometrical constraint provided by equation (4.27), although the unsteadiness renders the equations slightly more complex. While the vorticity balance along the steady upper boundary of the gravity current is still given by equation (4.23), the unsteady evolution of the rarefaction wave modifies the other three equations.

In order to quantify the temporal changes of the ambient layer volumes, and of the circulation along the boundary separating these layers, we assume that the ambient interface height as well as the vortex sheet strength vary linearly within the wave region from L to R. The DNS results of section 4.1 above showed that this approximation holds to a good degree over much of the wave region, although it becomes questionable in the region immediately above the gravity current front, cf. Fig. 4.8a. Hence it will be interesting to compare the predictions obtained on the basis of this approximation with the actual DNS results further below. Consequently, in the reference frame of the gravity current the mass balance for the deforming upper layer within control volume $L - 3o - 4o - L'$ yields

$$(U_l^* - U_g^*)\frac{h_{2i}^* + h_{2o}^*}{2} = U_l^* h_{2i}^* - U_{2o}^* h_{2o}^*\,. \tag{4.32}$$

Mass conservation for the entire channel $1i - 1o - 4o - 3i$ results in

$$U_g^* \;=\; U_{1o}^* h_{1o}^* + U_{2o}^* h_{2o}^*\,. \tag{4.33}$$

118

To obtain an equation for the vorticity along the ambient interface $2i - 3o$, we start from the integral form of the inviscid vorticity conservation equation

$$\frac{\mathrm{d}}{\mathrm{d}t^*} \int_{CV(t^*)} \omega^* \, \mathrm{d}A^* + \oint_{CS(t^*)} \omega \mathbf{V_r^*} \cdot \mathbf{n} \, \mathrm{d}S^* = - \int_{CV(t^*)} \frac{g_2'}{g'} \frac{\partial \rho^*}{\partial x^*} \, \mathrm{d}A^*, \tag{4.34}$$

where $\omega^* = \omega/\sqrt{g'/H}$, and CS denotes the boundary of the control volume that contains the ambient interface. $\mathbf{V_r^*}$ represents the relative flow velocity at this boundary. The temporal rate of change of the circulation inside the control volume is due to the elongation of the wave region resulting from the rarefaction wave propagation. The rate at which the wave region lengthens is given by $U_l^* - U_g^*$. Based on the DNS results of section 4.1, cf. Fig. 4.8d, we assume that the vortex sheet strength varies linearly from L to R, so that its average value in the wave region is $(U_{2o}^* - U_{1o}^*)/2$. Hence we obtain

$$\frac{\mathrm{d}}{\mathrm{d}t^*} \int_{CV(t^*)} \omega^* \, \mathrm{d}A^* = -\frac{1}{2}(U_l^* - U_g^*)(U_{2o}^* - U_{1o}^*). \tag{4.35}$$

There is no influx of vorticity into the control volume, and the shear at the outflow boundary yields

$$\oint_{CS(t)} \omega^* \mathbf{V_r^*} \cdot \mathbf{n} \, \mathrm{d}S^* = -\frac{1}{2}(U_{2o}^* - U_{1o}^*)(U_{2o}^* + U_{1o}^*). \tag{4.36}$$

The baroclinic vorticity production term can be evaluated as

$$-\int_{CV(t^*)} \frac{g_2'}{g'} \frac{\partial \rho^*}{\partial x^*} \, \mathrm{d}A^* = -\Delta \rho^* (h_{1o}^* + h^* - h_{1i}^*). \tag{4.37}$$

By substituting equations (4.35)-(4.37) into equation (4.34), we obtain the vorticity equa-

tion in the form

$$\frac{1}{2}(U_l^* - U_g^*)(U_{2o}^* - U_{1o}^*) + \frac{U_{2o}^{*\,2} - U_{1o}^{*\,2}}{2} = \Delta\rho^*(h^* + h_{1o}^* - h_{1i}^*)\,. \tag{4.38}$$

The system of equations (4.23), (4.32), (4.33) and (4.38) is then fully closed by the geometrical constraint (4.27).

4.2.3   Rarefaction wave following an upstream bore

When the rarefaction wave gives rise to a leading internal bore, we model the flow based on configuration C3, as sketched in Fig. 4.1c. As shown by [37], the mass and vorticity conservation equations along the rarefaction wave and in the laboratory reference frame can be written as

$$\frac{\mathrm{d}u_1^*}{\mathrm{d}d_1^*} = -\frac{u^* + u_1^* - U_g^*}{d_1^*}, \tag{4.39}$$

$$\frac{\mathrm{d}u_2^*}{\mathrm{d}d_1^*} = \frac{u^* + u_2^* - U_g^*}{d_2^*}, \tag{4.40}$$

$$\frac{(u^* + u_1^* - U_g^*)^2}{d_1^*} + \frac{(u^* + u_2^* - U_g^*)^2}{d_2^*} = \Delta\rho^*\,. \tag{4.41}$$

We recall from section 4.1 that u_1^* and u_2^* represent the dimensionless horizontal velocities of the lower and upper layers, while d_1^* and d_2^* denote the local depths of the layers. u^* indicates the interfacial velocity along the wave in the laboratory frame, which is positive towards the inflow boundary. Consequently, $u^*(x_r^*) = U_g^*$ and $u^*(x_l^*) = U_l^*$. The above system of equations, which can be obtained by applying the mass and vorticity conservation principles to an infinitesimal control volume along the expansion fan, yields the flow field within the fan as a function of the interface height $d_1^*(x^*, t^*)$, without invoking any assumptions regarding the interfacial shape, cf. [37].

If $|u^*(x^*)|$ decreases monotonically from left to right, only the expansion wave forms. On the other hand, if $|u^*(x^*)|$ has a maximum somewhere between L and R, the interface steepens locally and a bore emerges as shown in Fig. 4.1c. To investigate the conditions under which a maximum appears, we take the derivative of equation (4.39)

$$\left[\frac{2(u^* + u_2^* - U_g^*)}{1 - d_1^*} + \frac{2(u^* + u_1^* - U_g^*)}{d_1^*}\right]\frac{\mathrm{d}u^*}{\mathrm{d}d_1^*}$$
$$-\frac{3(u^* + u_1^* - U_g^*)^2}{d_1^{*2}} + \frac{3(u^* + u_2^* - U_g^*)^2}{(1 - d_1^*)^2} = 0, \tag{4.42}$$

where $\mathrm{d}u_1^*/\mathrm{d}d_1^*$ and $\mathrm{d}u_2^*/\mathrm{d}d_1^*$ have been substituted from equations (4.39) and (4.40), respectively. By letting $\mathrm{d}u^*/\mathrm{d}d_1^*$ be zero, we arrive at

$$\frac{u^* + u_1^* - U_g^*}{d_1^*} = \frac{u^* + u_2^* - U_g^*}{1 - d_1^*}. \tag{4.43}$$

We expect that the local extremum first apears for the smallest interface height, i.e. at the left edge of the expansion wave, where $d_1^* = h_{1i}^*$ and $u_1^* - U_g^* = u_2^* - U_g^* = 0$. By substituting these values into equation (4.43), we find that a bore emerges only if $h_{1i}^* < 0.5$. [37] show that in the presence of a bore, the flow chooses $h_l^* = 0.5$, which results in a nondissipative flow across the bore. The equations for mass and vorticity conservation around the internal bore, and in the reference frame moving with the bore, yield

$$U_b^* h_{1i}^* = (U_b^* - U_{1b}^*)h_l^*, \tag{4.44}$$

$$U_b^* h_{2i}^* = (U_b^* + U_{2b}^*)(1 - h_l^*), \tag{4.45}$$

$$\frac{1}{2}(U_{2b}^* + U_{1b}^*)(U_{2b}^* - U_{1b}^* + 2U_b^*) = \Delta\rho^*(h_l^* - h_{1i}^*), \tag{4.46}$$

where U_b^* is the bore propagation speed, and U_{1b}^* and U_{2b}^* represent the velocities of

the lower and upper layers downstream of the bore in the laboratory reference frame. Equations (4.44)-(4.46) can be solved to obtain

$$U_b^* \;=\; 0.5\sqrt{\Delta\rho^*}, \tag{4.47}$$

$$U_{1b}^* = U_{2b}^* \;=\; \sqrt{\Delta\rho^*}\left(0.5 - h_{1i}^*\right). \tag{4.48}$$

U_{1b}^* and U_{2b}^* can then be substituted into the vorticity balance equation (4.41) to arrive at a relationship for the propagation velocity of the left edge of the rarefaction wave

$$U_l^* = \sqrt{\Delta\rho^* h_{1i}^* h_{2i}^*}, \tag{4.49}$$

which is identical to that found for C2 in equation (4.31).

After finding the bore speed as well as the velocities of the ambient layers downstream of the bore, the gravity current velocity and the heights and velocities of the ambient layers at the outflow boundary can then be obtained by an analysis corresponding to those of sections 4.2.1 and 4.2.2. We thus obtain

$$(U_l^* \;-\; U_g^*)\frac{1 - h_l^* + h_{2o}^*}{2} = (U_{2b}^* + U_l^*)(1 - h_l^*) - U_{2o}^* h_{2o}^*, \tag{4.50}$$

$$\frac{1}{2}(U_l^* \;-\; U_g^*)(U_{2o}^* - U_{1o}^* + U_{1b}^* + U_{2b}^*) + \frac{U_{2o}^{*\,2} - U_{1o}^{*\,2}}{2} -$$
$$\frac{1}{2}(U_{1b}^* \;+\; U_{2b}^*)(U_{2b}^* - U_{1b}^* + 2U_l^*) = \Delta\rho^*(h^* + h_{1o}^* - h_l^*), \tag{4.51}$$

where the vortex sheet strength again has been assumed to vary linearly. Equations (4.23), (4.27), (4.33), (4.50) and (4.51) can then be solved to obtain the flow quantities for configuration C3.

4.2.4 Physically possible solutions

Since no energy-based closure assumptions were employed while deriving the above analytical models, the energetics of the flow can be assessed *a posteriori*, i.e. after determining the flow field. Towards this end, we will now analyze the rate of energy loss for the entire flow in the reference frame of the gravity current. The most general form of the energy equation is

$$\dot{E}_i^* - \dot{E}_o^* - \dot{E}_d^* - \dot{E}_s^* = 0 \,. \tag{4.52}$$

Here $\dot{E}_d^*$ and $\dot{E}_s^*$ represent the dimensionless rates of dissipation and storage of energy inside the control volume, while $\dot{E}_i^*$ and $\dot{E}_o^*$ indicate the rates at which energy is convected into and out of the control volume. These rates have been rendered dimensionless by $\rho_2 g'^{3/2} H^{5/2}$.

We begin by discussing the steady configuration C1, for which the storage term vanishes. $\dot{E}_i^*$ and $\dot{E}_o^*$ can be calculated as

$$\dot{E}_i^* = \int_0^1 \left(p^*(y^*) + \frac{1}{2} U_i^{*2} + \frac{\rho g}{\rho_2 g'} y^* \right) U_i^* \; \mathrm{d}y^* \,, \tag{4.53}$$

$$\dot{E}_o^* = \int_0^1 \left(p^*(y^*) + \frac{1}{2} U_o^{*2} + \frac{\rho g}{\rho_2 g'} y^* \right) U_o^* \; \mathrm{d}y^* \,. \tag{4.54}$$

Since the flow direction at the in- and outflow boundaries is horizontal, we can assume the local pressure distribution to be hydrostatic

$$p_i^*(y^*) = \begin{cases} p_{3i}^* + \frac{(\rho_2 - \frac{\Delta\rho}{2})g}{\rho_2 g'}(1 - y^*) & y^* \geq h_{1i}^* \,, \\[2ex] p_{3i}^* + \frac{(\rho_2 - \frac{\Delta\rho}{2})g}{\rho_2 g'} h_{2i}^* + \frac{(\rho_2 + \frac{\Delta\rho}{2})g}{\rho_2 g'}(h_{1i}^* - y^*) & y^* < h_{1i}^* \,. \end{cases} \tag{4.55}$$

123

$$p_o^*(y^*) = \begin{cases} p_{4o}^* + \frac{(\rho_2 - \frac{\Delta\rho}{2})g}{\rho_2 g'}(1 - y^*) & y \geq h^* + h_{1o}^*, \\[2em] p_{4o}^* + \frac{(\rho_2 - \frac{\Delta\rho}{2})g}{\rho_2 g'}h_{2o}^* + \frac{(\rho_2 + \frac{\Delta\rho}{2})g}{\rho_2 g'}(h^* + h_{1o}^* - y^*) & h^* \leq y^* < h^* + h_{1o}^*, \\[2em] p_{4o}^* + \frac{(\rho_2 - \frac{\Delta\rho}{2})g}{\rho_2 g'}h_{2o}^* + \frac{(\rho_2 + \frac{\Delta\rho}{2})g}{\rho_2 g'}h_{1o}^* + \frac{\rho_1 g}{\rho_2 g'}(h^* - y^*) & y^* < h^*. \end{cases} \quad (4.56)$$

Here, $p_i^*(y^*)$ and $p_o^*(y^*)$ denote the dimensionless pressure at the in- and outflow boundaries, respectively. The pressure drop $p_{3i}^* - p_{4o}^*$ along the top wall of the channel can be computed in a straightforward fashion, by applying the integral horizontal momentum balance for the entire channel in the reference frame moving with the gravity current

$$\dot{M}^* = \int_0^1 (p_i^* + U_i^{*2}) \, \mathrm{d}y^* - \int_0^1 (p_o^* + U_o^{*2}) \, \mathrm{d}y^*. \quad (4.57)$$

Here $\dot{M}^*$ has been rendered dimensionless by $\rho_2 g' H^2$. We note that for C1, $\dot{M}^* = 0$, due to the steady nature of the flow. By substituting the velocities evaluated in sections 4.2.1-4.2.3, and the pressure functions of equations (4.55) and (4.56) into equation (4.57), we obtain the following expression for the pressure drop along the top wall

$$\begin{aligned} p_{3i}^* - p_{4o}^* &= \frac{\Delta\rho^*}{2}\left(\frac{h_{1o}^{*\,2} - h_{2o}^{*\,2}}{2}\right) - \frac{\Delta\rho^*}{2}h_{1o}^*h_{2o}^* - \frac{\Delta\rho^*}{2}h^*h_{2o}^* \\ &+ \frac{\Delta\rho^*}{2}h^*h_{1o}^* + \frac{\Delta\rho^*}{2}\left(\frac{h_{2i}^{*\,2} - h_{1i}^{*\,2}}{2}\right) + \frac{\Delta\rho^*}{2}h_{1i}^*h_{2i}^* \\ &+ \frac{h^{*2}}{2} + U_{1o}^{*\,2}h_{1o}^* + U_{2o}^{*\,2}h_{2o}^* - U_g^{*2} + \dot{M}^*. \end{aligned} \quad (4.58)$$

For C2 and C3 the unsteady rarefaction wave results in $\dot{M} = \dot{M}_1^* + \dot{M}_2^* \neq 0$, where $\dot{M}_1^*$ and $\dot{M}_2^*$ indicate the rates at which momentum accumulates in the lower and upper

layers, respectively. These rates can be obtained as

$$\dot{M}_1^* = \left[\frac{\mathrm{d}}{\mathrm{d}t^*} \int_{x_l^*}^{x_r^*} u_1^*(x^*) d_1^*(x^*) \ \mathrm{d}x^* \right] - (U_l^* - U_g^*)U_g^* h_{1i}^*, \tag{4.59}$$

$$\dot{M}_2^* = \left[\frac{\mathrm{d}}{\mathrm{d}t^*} \int_{x_l^*}^{x_r^*} u_2^*(x^*) d_2^*(x^*) \ \mathrm{d}x^* \right] - (U_l^* - U_g^*)U_g^* h_{2i}^*, \tag{4.60}$$

where x_l^* and x_r^* denote the horizontal locations of the left and right edges of the wave, as defined in section 4.1. In order to be able to evaluate the above integrals analytically, we assume that the horizontal velocities of the individual layers vary linearly as a function of x^* along the wave, which is supported by the DNS data of the previous section. The validity of this assumption in the context of evaluating the energy budget of the flow, will be further investigated in section 4.4. The summation of $\dot{M}_1^*$ and $\dot{M}_2^*$ then gives the net accumulation rate $\dot{M}^*$ of momentum within the entire channel. The pressure drop along the top wall can be evaluated by substituting $\dot{M}^*$ into equation (4.58).

$\dot{E}_s^*$ is the rate at which the energy within the channel changes with time, as the rarefaction wave travels to the left. To assess the rate at which the kinetic energy of the flow changes, it is again convenient to analyze each layer separately. The rate of change of the kinetic energy of the lower and upper layers can be calculated as

$$\dot{E}_{k,1}^* = \left[\frac{\mathrm{d}}{\mathrm{d}t^*} \int_{x_l^*}^{x_r^*} \frac{1}{2} u_1^{*2}(x^*) d_1^*(x^*) \ \mathrm{d}x^* \right] - \frac{1}{2}(U_l^* - U_g^*)U_g^{*2} h_{1i}^*, \tag{4.61}$$

$$\dot{E}_{k,2}^* = \left[\frac{\mathrm{d}}{\mathrm{d}t^*} \int_{x_l^*}^{x_r^*} \frac{1}{2} u_2^{*2}(x^*) d_2^*(x^*) \ \mathrm{d}x^* \right] - \frac{1}{2}(U_l^* - U_g^*)U_g^{*2} h_{2i}^*. \tag{4.62}$$

$\dot{E}_{k,1}^*$ and $\dot{E}_{k,2}^*$ can then be added to calculate the net rate of change of kinetic energy $\dot{E}_k^*$ within the channel.

The propagation of the expansion wave furthermore lifts up the denser fluid of the lower layer, thereby increasing the potential energy. To quantify the rate of growth of
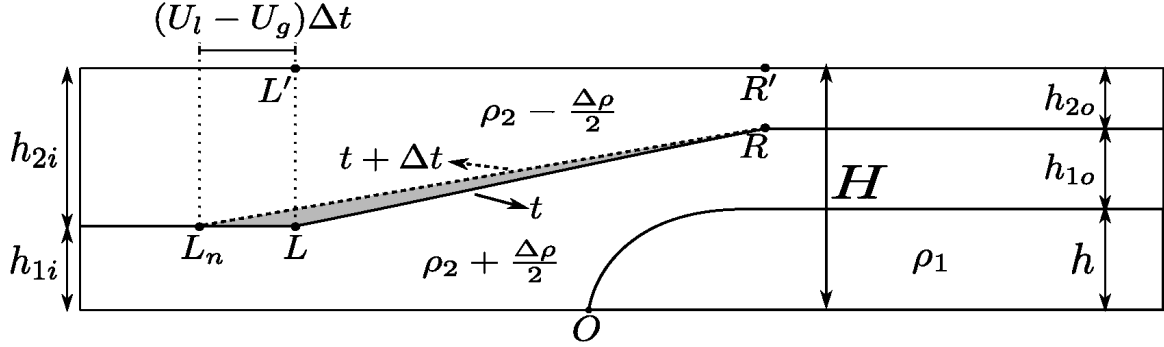
Figure 4.10: Sketch in support of evaluating the unsteady potential energy term, in the reference frame moving with the gravity current. Over a small time interval Δt, the left edge of the expansion wave travels from L to L_n with the constant velocity $U_l - U_g$, while the right edge R remains stationary. Within the expansion wave region, the interface is assumed to have a constant slope that changes with time. The shaded region indicates the volume of dense fluid of the lower layer that has replaced the light fluid of the upper layer during Δt.

potential energy, we analyze the evolution of the constant-slope interface over a small time interval Δt, due to the propagation of the rarefaction wave, as shown in Fig. 4.10. The shaded region indicates the volume of light, upper layer fluid replaced by dense, lower layer fluid during Δt. The rate at which the potential energy increases is then proportional to the rate at which the area of this triangle grows times the height of its center of gravity, which results in

$$\dot{E}_p^* = \frac{1}{2}\Delta\rho^*(U_l^* - U_g^*)(h^* + h_{1o}^* - h_{1i}^*)\left(\frac{h^* + h_{1o}^* + 2h_{1i}^*}{3}\right). \qquad (4.63)$$

The potential energy rate of growth can be added to the kinetic energy rate of growth to obtain $\dot{E}_s^*$. We then substitute $\dot{E}_s^*$ into equation (4.52) to compute the rate of energy dissipation $\dot{E}_d^*$.

A corresponding analysis can be conducted for configuration C3 in order to obtain the rate of energy dissipation. Towards this end, we first compute the pressure drop along the top wall from equation (4.58), where the rate of accumulation of momentum

$\dot{M}^*$ is now evaluated according to

$$
\begin{aligned}
\dot{M}_1^* &= \left[\frac{\mathrm{d}}{\mathrm{d}t^*} \int_{x_l^*}^{x_r^*} u_1^*(x^*) d_1^*(x^*) \, \mathrm{d}x^* \right] + (U_b^* - U_l^*)(U_g^* - U_{1b}^*) h_l^* \\
&\quad - (U_b^* - U_g^*) U_g^* h_{1i}^* ,
\end{aligned} \tag{4.64}
$$

$$
\begin{aligned}
\dot{M}_2^* &= \left[\frac{\mathrm{d}}{\mathrm{d}t^*} \int_{x_l^*}^{x_r^*} u_2^*(x^*) d_2^*(x^*) \, \mathrm{d}x^* \right] + (U_b^* - U_l^*)(U_g^* + U_{2b}^*)(1 - h_l^*) \\
&\quad - (U_b^* - U_g^*) U_g^* h_{2i}^* ,
\end{aligned} \tag{4.65}
$$

The results of the above integrals can then be added up to obtain $\dot{M}^*$ for C3, which then enables us to compute $p_{3i}^* - p_{4o}^*$ from equation (4.58). In a corresponding fashion, we obtain

$$
\begin{aligned}
\dot{E}_{k,1}^* &= \left[\frac{\mathrm{d}}{\mathrm{d}t^*} \int_{x_l^*}^{x_r^*} \frac{1}{2} u_1^{*2}(x^*) d_1^*(x^*) \, \mathrm{d}x^* \right] + \frac{1}{2}(U_b^* - U_l^*)(U_g^* - U_{1b}^*)^2 h_l^* \\
&\quad - \frac{1}{2}(U_b^* - U_g^*) U_g^{*2} h_{1i}^* ,
\end{aligned} \tag{4.66}
$$

$$
\begin{aligned}
\dot{E}_{k,2}^* &= \left[\frac{\mathrm{d}}{\mathrm{d}t^*} \int_{x_l^*}^{x_r^*} \frac{1}{2} u_2^{*2}(x^*) d_2^*(x^*) \, \mathrm{d}x^* \right] + \frac{1}{2}(U_b^* - U_l^*)(U_g^* + U_{2b}^*)^2 (1 - h_l^*) \\
&\quad - \frac{1}{2}(U_b^* - U_g^*) U_g^{*2} h_{2i}^* ,
\end{aligned} \tag{4.67}
$$

and

$$
\dot{E}_p^* = \frac{1}{2} \Delta \rho^* \left[(U_l^* - U_g^*)(h^* + h_{1o}^* - h_l^*) \frac{h^* + h_{1o}^* + 2h_l^*}{3} + (U_b^* - U_g^*) \frac{h_l^{*2} - h_{1i}^{*\,2}}{2} \right], \tag{4.68}
$$

so that we can evaluate the rate of energy dissipation $\dot{E}_d^*$ from equation (4.52).

4.3   Model predictions

In the following, we will discuss model predictions for the three configurations C1, C2 and C3. Towards this end, we solve the equations derived in section 4.2 via a MatLab-based bisection root finding technique.

Figure 4.11 displays contours of the gravity current velocity U_g^* for four different values of h_{1i}^*, in the $\Delta\rho^*, h^*$-plane. The shaded areas indicate the physically viable regions where the energy analysis of section 4.2.4 gives a positive energy dissipation rate $\dot{E_d}^* \geq 0$. The outer boundary of the shaded region, marked by a dashed line, corresponds to energy-conserving solutions. The dash-dotted lines separate steady C1-type solutions to the left $(U_g^* \geq U_l^*)$, from unsteady C2- and C3-type flows with upstream propagating waves $(U_g^* < U_l^*)$ to the right. The latter are based on the models of sections 4.2.2 or 4.2.3, depending on whether $h_{1i}^* \geq 0.5$ or $h_{1i}^* < 0.5$. We find that without stratification $(\Delta\rho^* = 0)$, all values of h_{1i}^* recover the classical result that half-depth gravity currents with $h^* = 0.5$ are energy-conserving and propagate with a velocity of 0.5 [1, 18, 19, 37]. We furthermore observe that for all inflow layer heights and stratification strengths, gravity currents with thickness greater than half the channel height cannot form without energy input.

Figure 4.12 shows the outflow velocity U_{1o}^* of the lower ambient layer, together with the shear across the ambient interface, as functions of the stratification parameter $\Delta\rho^*$, for several gravity current heights h^*. In the limit of $\Delta\rho^* \to 2$, the density difference between the lower ambient layer and the gravity current vanishes, so that no vorticity is being generated along their boundary, and the lower ambient outflow velocity tends to zero. In this limit, the gravity current becomes indistinguishable from the lower ambient layer, so that we effectively recover the situation of a bore propagating along the interface between the ambient layers [25]. Interestingly, for all density differences the shear across
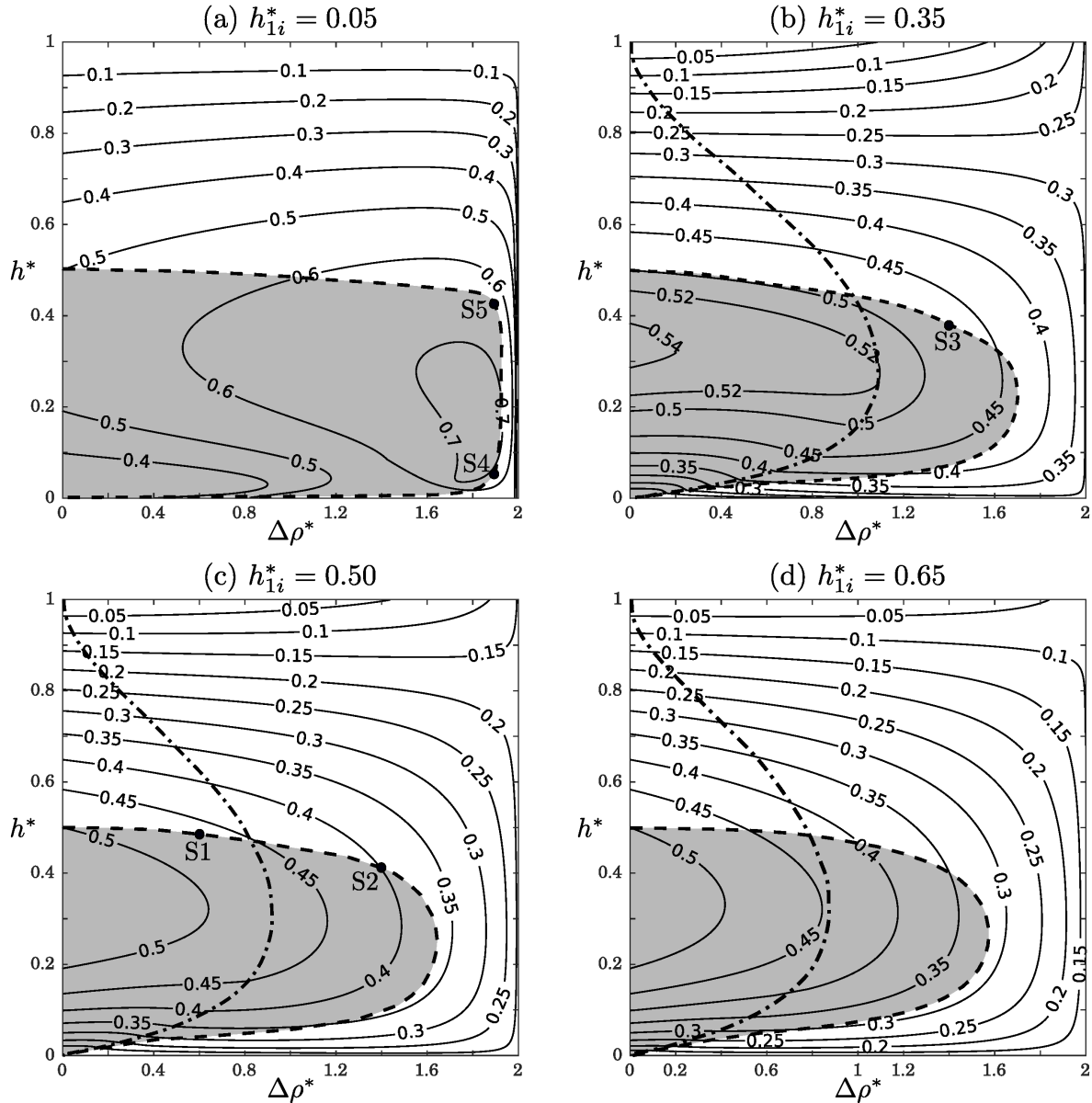
Figure 4.11: Phase-space diagrams for the gravity current velocity U_g^* as function of the gravity current height h^* and the stratification strength $\Delta\rho^*$. The interface heights at the inflow boundary are (a) $h_{1i}^* = 0.05$, (b) $h_{1i}^* = 0.35$, (c) $h_{1i}^* = 0.50$, and (d) $h_{1i}^* = 0.65$. The shaded regions indicate solutions that are energetically possible. The dash-dotted lines distinguish steady C1-type solutions to the left from unsteady C2- and C3-type solutions to the right.
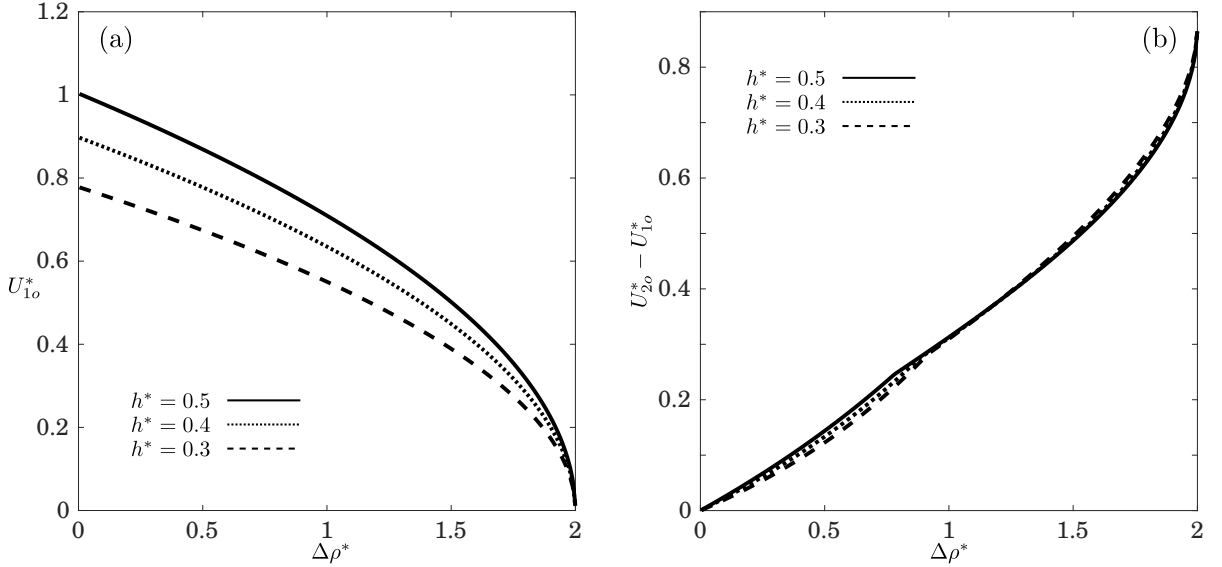
Figure 4.12: The lower ambient outflow velocity U_{1o}^* (a), and the outflow shear $U_{2o}^* - U_{1o}^*$ across the interface between the ambient layers (b), as functions of the stratification parameter $\Delta\rho^*$, for several gravity current heights h^*. In all cases $h_{1i}^* = h_{2i}^* = 0.5$. In the limit $\Delta\rho^* \to 2$ the flow reduces to a bore propagating along the interface between the ambient layers.

the interface between the ambient layers is nearly independent of the gravity current height.

Figure 4.13a demonstrates that h_{1o}^* grows with decreasing gravity current height, and that for a given gravity current height it increases monotonically with $\Delta\rho^*$. Figure 4.13b shows that the ratio h_{2o}^*/h_{1o}^* decays monotonically with $\Delta\rho^*$. For small values of $\Delta\rho^*$, the dependence of h_{2o}^*/h_{1o}^* on h^* is quite weak. For larger values of $\Delta\rho^*$, when upstream propagating disturbances emerge, the gravity current height has a substantial influence, so that smaller values of h^* result in considerably smaller h_{2o}^*/h_{1o}^*. We remark that in the limit of $\Delta\rho^* \to 0$, there will be no shear between the ambient layers at the outflow boundary, cf. equation (4.24) and Fig. 4.12b. Hence, since the ambient layers are equally thick at the inflow, continuity requires that they also have the same thickness at the outflow. This is confirmed by the figure, which shows that $h_{2o}^*/h_{1o}^* \to 1$ as $\Delta\rho^* \to 0$.

It is informative to relate the flow regimes considered in the present investigation
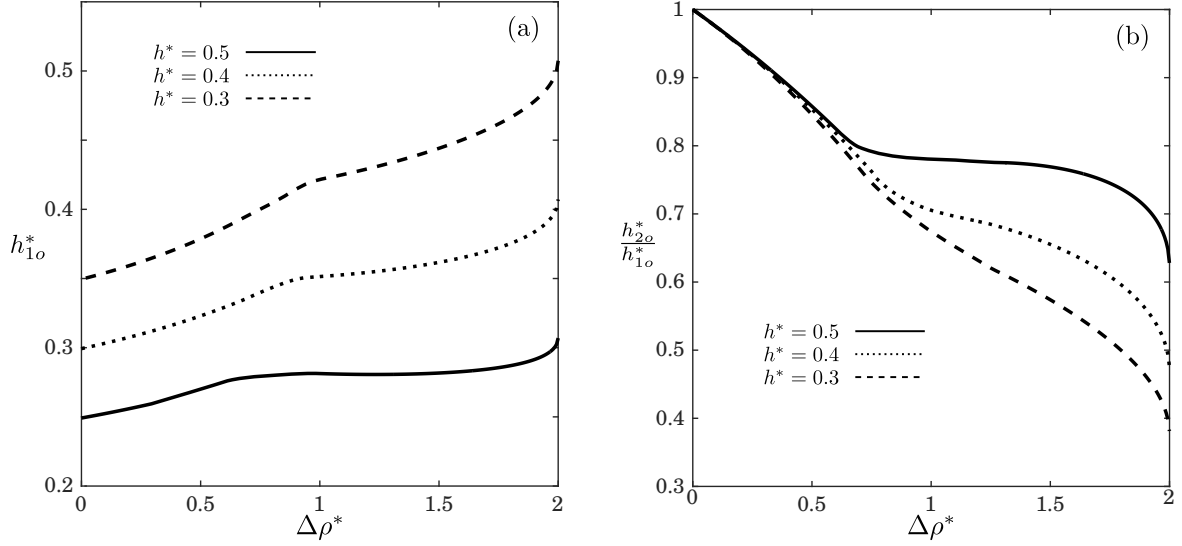
Figure 4.13: The outflow thickness h_{1o}^* of the lower ambient layer (a), and the ambient layer thickness ratio h_{2o}^*/h_{1o}^* (b), as functions of the stratification parameter $\Delta\rho^*$, for several gravity current heights h^*. In all cases $h_{1i}^* = h_{2i}^* = 0.5$.

of gravity currents propagating into two-layer stratified ambients, to those introduced by [29] for two-layer flows over solid topography. For four different values of h_{1i}^*, Fig. 4.14 indicates energetically feasible gravity current flows by shaded regions in the D_o, F_o-plane, based on the analysis of section 4.2.4. As stated at the beginning of this chapter, [29] define the Froude number $F_o = U_g^*/\sqrt{h_{1i}^*\Delta\rho^*}$, and the parameter $D_o = h^*/h_{1i}^*$. Since gravity currents with thicknesses above half the channel depth would require an external energy input, no physically possible solution exists to the right of $D_o = 0.5/h_{1i}^*$. The horizontal dotted lines separate flows allowing for unsteady upstream disturbances (below), from those which are quasisteady in the gravity current reference frame (above). The figure suggests that for intermediate values of h_{1i}^* partially blocked flows normally emerge, except when F_o is relatively large. This situation can occur in two scenarios: 1) the gravity current velocity becomes very large, which usually is not the case for these values of h_{1i}^*, since U_g^* always remains below 0.55, or 2) $\Delta\rho^* \to 0$. Alternatively, for small values of h_{1i}^* supercritical flows can also appear when $\Delta\rho^*$ is large, e.g. $\Delta\rho^* = 1.89$ in S4,
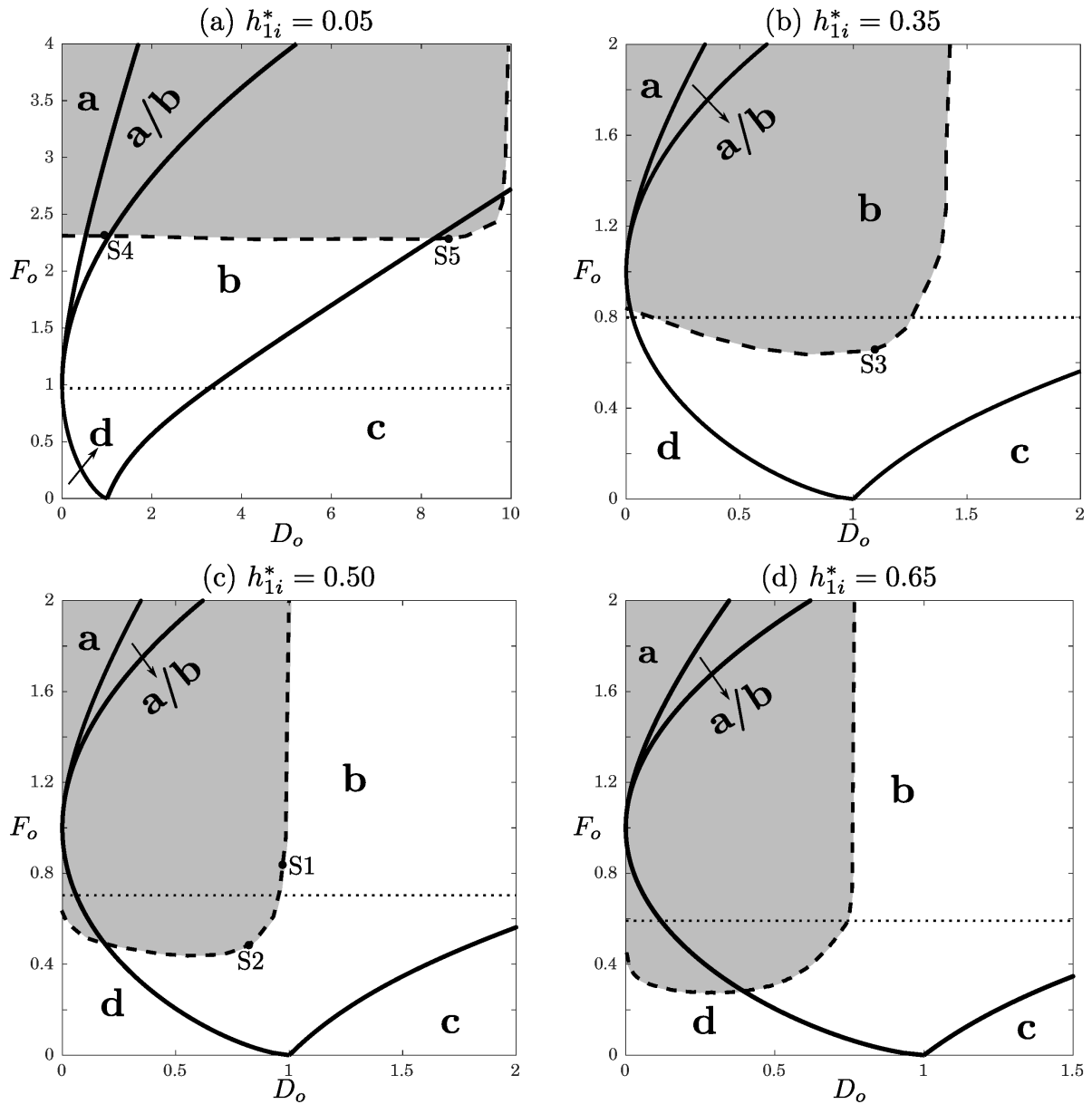
Figure 4.14: Relationship between the flow regimes considered here for gravity currents propagating into two-layer stratified ambients, and those investigated by [29] in the context of two-layer stratified flows over solid obstacles. Shaded areas indicate energetically possible flows. The interface heights at the inflow boundary are (a) $h_{1i}^* = 0.05$, (b) $h_{1i}^* = 0.35$, (c) $h_{1i}^* = 0.50$, and (d) $h_{1i}^* = 0.65$. Here, **a**, **b**, **c** and **d** represent supercritical, partially blocked, completely blocked and subcritical flow regimes, respectively, according to [29]. **a/b** indicates the region in which both supercritical and partially blocked flows are plausible, depending on how the flow has been initiated. The dotted horizontal lines distinguish gravity current flows with upstream interfacial waves (below) from those without (above).

132

since small values of h_{1i}^* result in large Froude numbers. Consequently, the simulations of section 4.1 with moderate values of h_{1i}^* all correspond to partially blocked flow. We note that partially blocked flows only result in upstream wave generation if the left edge of the wave travels faster than the gravity current head in the laboratory frame. The main distinction between supercritical and partially blocked flows is that the former never allow for the formation of upstream disturbances, whereas the latter may (S2 or S3) or may not (S1 and S5) lead to such disturbances, depending on whether $U_g^* < U_l^*$ or not, respectively. Those cases without upstream propagating waves are located above the dotted lines along which $U_g^* = U_l^*$, while those with upstream propagating waves fall below these lines.

4.4 Comparison of model predictions and DNS simulation results

Table 4.2 compares predictions by the vorticity models of section 4.2 to DNS simulation results, for the specific flows discussed in section 4.1. These comparisons were carried out in the following fashion: For a given stratification parameter $\Delta\rho^*$ and given ambient inflow layer heights, the DNS simulation was run until a quasisteady gravity current height h^* was achieved. The values of Re and Pe in these simulations were chosen sufficiently large so that viscous and diffusive effects can be assumed small. For these values of $\Delta\rho^*$ and h^*, the gravity current velocity U_g^*, the propagation speed U_l^* of the expansion fan's left edge (if applicable), and the outflow velocities and thicknesses of the ambient layers were then evaluated from the respective vorticity model, and compared to the corresponding DNS results. The subscript n in the table refers to the DNS results, whereas the model predictions do not have subscripts. The model predictions and DNS

results listed in the table are seen to agree with each other to within a few per cent. For simulation S3, the model predictions $h_l^* = 0.5$ and $U_b^* = 0.592$ for the internal bore properties (not listed in the table), while not quite as close, still agree reasonably well with the corresponding DNS results $h_{l,n}^* = 0.448$ and $U_{b,n}^* = 0.612$.

The slight differences between the model predictions and DNS results can be partly attributed to the assumption of inviscid flow without diffusion underlying the models. The DNS simulations, on the other hand, have to employ finite values for Re and Pe, so that all interfaces have finite thicknesses. Furthermore, the momentum transfer between the flow layers as a result of viscosity causes an effective head gain in the ambient lower layer and the gravity current, which reduces the gravity current velocity in the simulations as compared to the model prediction. The presence of viscosity also leads to some dissipation throughout the flow. The quantitative influence of Re and Pe on the flow variables will be further discussed below. Finally, some of the discrepancy is due to the assumption that the interface height and vortex sheet strength vary linearly within the expansion wave region.

In all simulations, the gravity current height converged to a value near the boundary of the shaded region in Fig. 4.11, indicating that the evolving flow field in the simulations was always close to energy-conserving for the given value of $\Delta\rho^*$ and the prescribed inflow layer thicknesses. Hence, the specific vorticity model solution that conserves the overall energy of the flow usually provides a good prediction of the flow properties observed in the DNS. For this reason, we will refer to this energy-conserving model solution as 'the vorticity model prediction' in the following.

As shown in Fig. 4.11, for a given value of $\Delta\rho^*$ there are generally two energy-conserving solutions for the gravity current height: one located on the upper branch, and other located on the lower branch of the boundary between the shaded and unshaded regions. Multiple energy-conserving solutions were also found by [8] and [35]. [8] state

that the current chooses the solution maximizing its volumetric inflow rate $U_g^* h^*$, which always corresponds to the one with the largest h^*-value. We observed a similar tendency in our DNS simulations, in that for moderate values of $h_{1i}^* \gtrsim 0.15$ the gravity current usually thickened and converged to the upper solution, even when initialized close to the lower branch. For very small values of h_{1i}^*, on the other hand, the DNS simulations converged to two different gravity current heights, depending on the initialization, as shown in Fig. 4.9.

4.4.1   Influence of dimensionless parameters

As stated earlier, in the analytical models presented in section 4.2, the fluids are assumed to be inviscid and the interfaces are considered sharp, so that no diffusive momentum or mass transfer can occur between the different flow layers. On the other hand, the DNS simulations of section 4.1 employ finite Reynolds and Péclet numbers, so that momentum and scalar interfaces have finite thicknesses. Here we investigate the quantitative influence of the Re- and Pe-values on the DNS results.

For simulation S1, Figs. 4.15 and 4.16 display the vertical density and velocity profiles far downstream of the gravity current front, at $x^* = 0.9 L_x$. Note that in all simulations of Fig. 4.15, $Pe = 20,000$, and in those of Fig. 4.16, $Re = 5,000$. While the model assumes that the velocity inside the gravity current vanishes in the reference frame moving with the gravity current front, the DNS simulations show that the gravity current fluid moves towards the front near the bottom wall, and away from it near the upper interface, as a result of the finite Re- and Pe-values. The agreement between the model predictions and DNS results improves for larger Re and Pe-values, as viscous and diffusive effects diminish. Similarly, the velocity gradients in the interfacial regions approach the step-like model profiles for larger Re and Pe. Corresponding observations can be made regarding

Table 4.2: Vorticity model predictions *vs.* DNS results for the flows discussed in section 4.1.

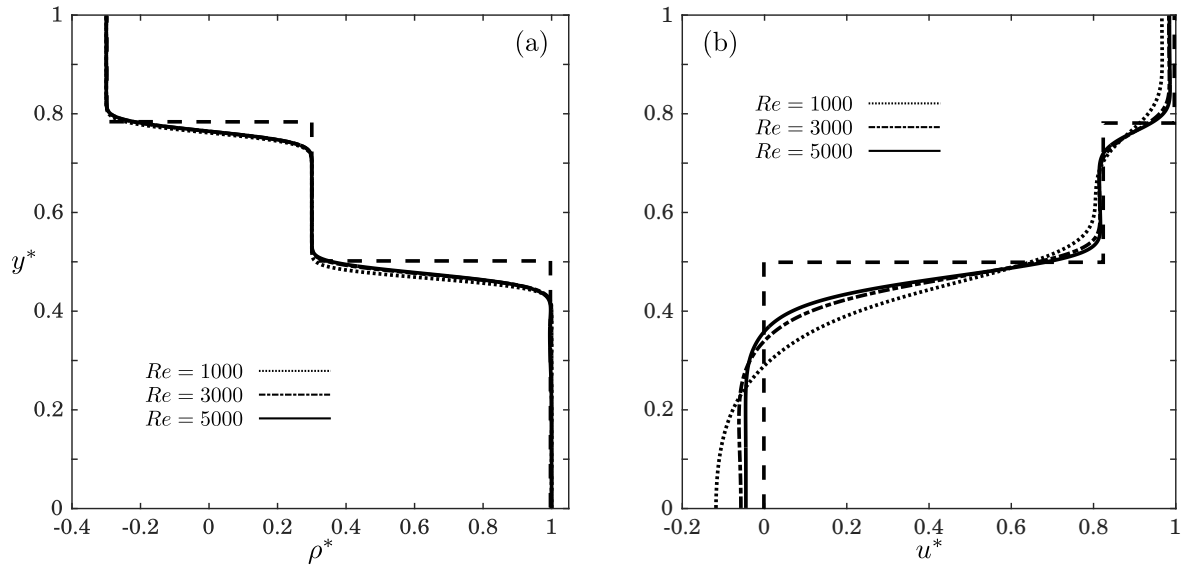| Sim.	U_g^*	$U_{g,n}^*$	U_l^*	$U_{l,n}^*$	h_{1o}^*	$h_{1o,n}^*$	U_{1o}^*	$U_{1o,n}^*$	h_{2o}^*	$h_{2o,n}^*$	U_{2o}^*	$U_{2o,n}^*$
S1	0.470	0.455	N/A	N/A	0.288	0.290	0.819	0.805	0.238	0.236	0.989	0.988
S2	0.401	0.392	0.592	0.578	0.356	0.353	0.493	0.505	0.239	0.241	0.942	0.922
S3	0.477	0.470	0.564	0.549	0.290	0.299	0.475	0.479	0.339	0.331	0.998	0.986
S4	0.680	0.673	N/A	N/A	0.463	0.446	0.073	0.072	0.488	0.505	1.324	1.276
S5	0.643	0.641	N/A	N/A	0.081	0.076	0.394	0.406	0.492	0.497	1.220	1.231

Figure 4.15: Influence of the Reynolds number on the downstream density (a), and velocity (b) profiles across the channel height, for simulation S1 shown in Fig. 4.4. Pe is held fixed at 20,000. The straight dashed lines represent the model predictions of section 4.2. As Re increases, the agreement between model predictions and simulation results generally improves.
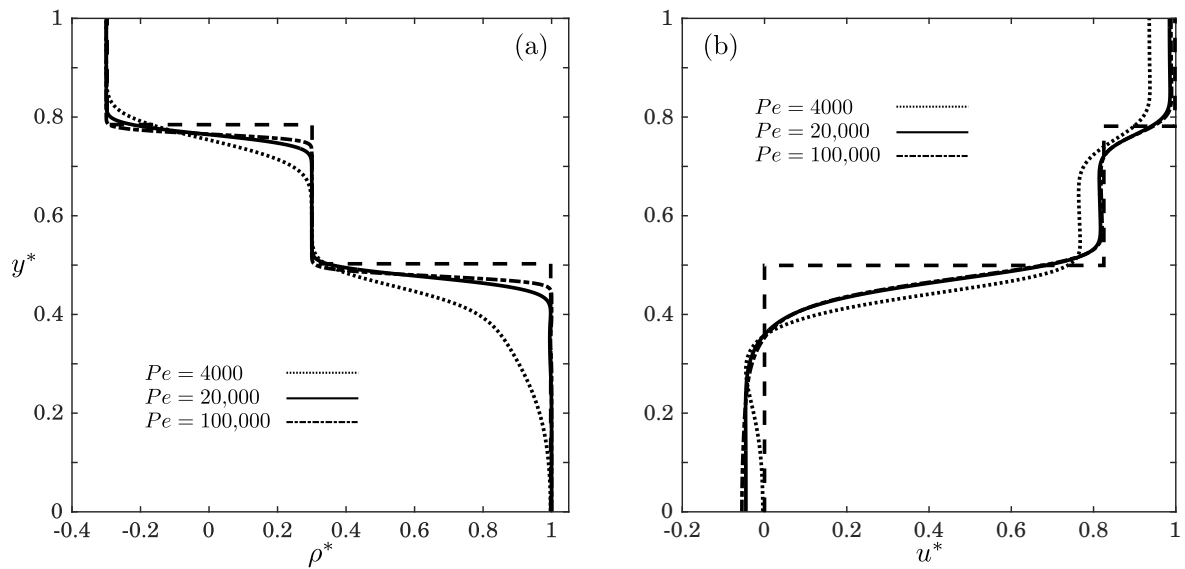

Figure 4.16: Influence of the Péclet number on the downstream density (a), and velocity (b) profiles across the channel height, for simulation S1 shown in Fig. 4.4. Re is held fixed at 5,000. The straight dashed lines represent the model predictions of section 4.2. As Pe increases, the agreement between model predictions and simulation results generally improves.

the density profiles, in that they become more step-like and closer to the model predictions as Re and Pe increase. The influence of Re on the density profiles is relatively small, however. We note that as Re is increased beyond approximately 6,000, the agreement between model predictions and DNS results will no longer improve, due to the appearance of unsteady Kelvin-Helmholtz vortices.

4.5 Comparison with earlier models

We now proceed to compare predictions by the current vorticity-based models to those of previous models by other authors. Figure 4.17 provides comparison data for the gravity current height h^* and velocity U_g^* as functions of the density jump $\Delta\rho^*$, for $h_{1i}^* = 0.5$. We note that the models of [8] and [34] solve for the gravity current height, while the model by [35] solves for the other flow parameters as a function of the gravity current height. Hence, for that models Fig. 4.17 shows the specific solution for which energy is conserved. Similarly, as discussed above, we take as the vorticity model prediction the energy-conserving solution. As shown in section 4.2.1, when the flow does not give rise to upstream waves and configuration C1 applies, vorticity conservation implies that the headloss in both ambient layers is identical, consistent with the assumption made by [35]. On the other hand, when upstream propagating disturbances in the form of an expansion wave or an internal bore followed by a rarefaction wave appear, overall energy conservation implies that an energy gain in one layer corresponds to an energy loss in the other one. According to Fig. 4.17, for $h_{1i}^* = 0.5$ the model of [35] predicts that no energy-conserving flows form for $\Delta\rho^* > 1.16$, while the corresponding value for the vorticity model is 1.64.

Figure 4.17 shows that all models reproduce the classical solution $h^* = 0.5$ and $U_g^* = 0.5$ of [1] for gavity currents without ambient stratification. Furthermore, for
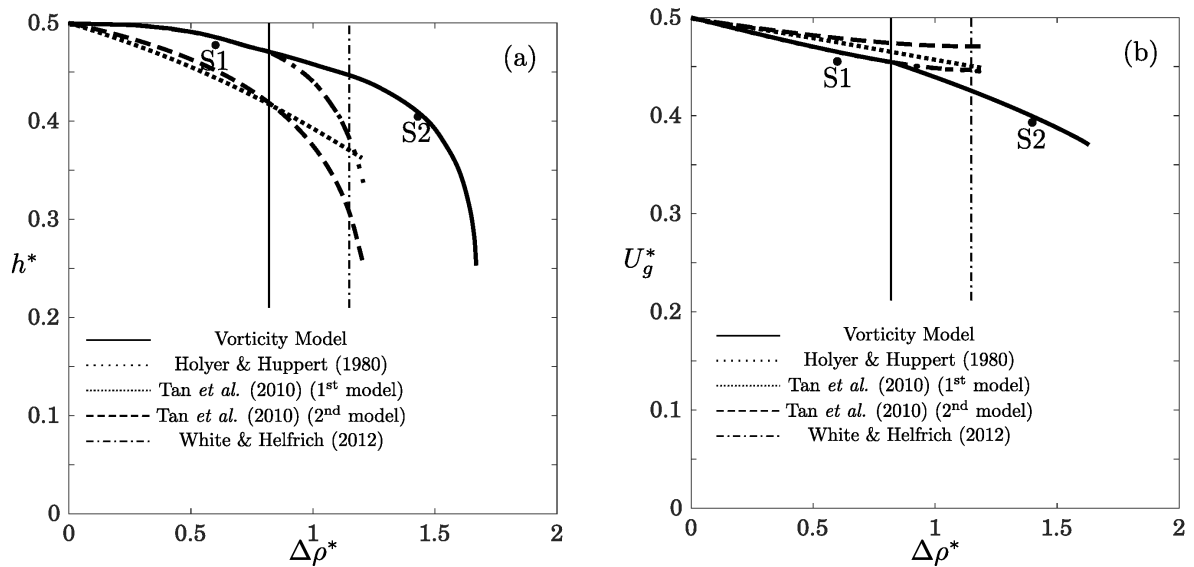
Figure 4.17: Comparison of current and previous model predictions for (a) the gravity current height, and (b) the gravity current velocity, as function of $\Delta\rho^*$ and for $h_{1i}^* = 0.5$. Here, those solutions from [35] and the current investigation are shown that conserve energy. The vertical solid line indicates the transition from C1 to C2 according to the vorticity model, while the vertical dash-dotted line represents the largest value of $\Delta\rho^*$ for which the conjuagte flow theory of [35] predicts an energy-conserving solution. The solution by [8] for configuration C1 is identical to the predictions of [35] and the vorticity model. The corresponding DNS results are indicated by S1 and S2.
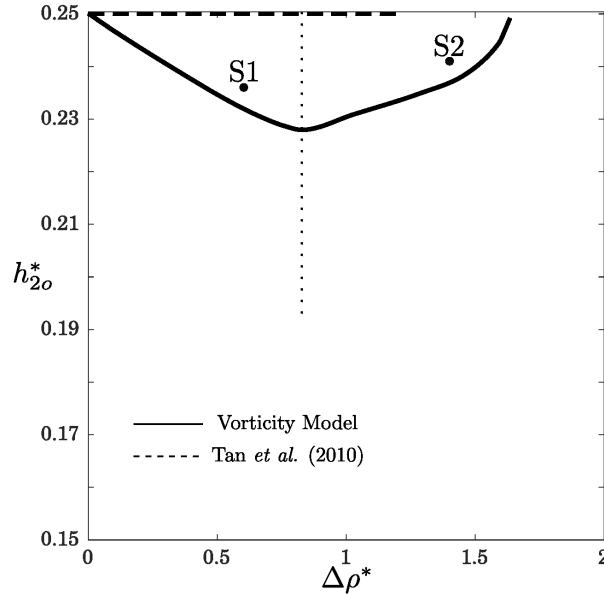
Figure 4.18: Predictions by the model of [34] and by the vorticity model for the outflow thickness of the upper ambient layer as a function of $\Delta\rho^*$, for $h_{1i}^* = 0.5$. The corresponding DNS results are indicated by S1 and S2. Configuration C1 exists to the left of the vertical dotted line.

configuration C1 the predictions by [8], [35] and the vorticity model are identical. When upstream propagating disturbances arise for $\Delta\rho^* > 0.83$, the predictions of the vorticity model devitate from those of [8] and [35], which do not account for this feature.

The two models of [34] invoke an empirical argument concerning the magnitude of the ambient interface deflection, as expressed by equation (4.1), and as a result their predictions for the height and velocity of the gravity current differ from the other models. Figure 4.18 compares this empirical assumption by [34] for the outflow thickness of the upper ambient layer with the corresponding prediction by the vorticity model, as well as with DNS results. While the predictions of the two models are clearly distinct, the quantitative difference is always less than ten per cent. The two DNS results are seen to agree more closely with the vorticity model prediction.

Interestingly, the models of [8] and [34] break down for $\Delta\rho^* > 1.2$, independent of the h_{1i}^*−value. [34] suggest that this degeneration may be due to the formation of upstream
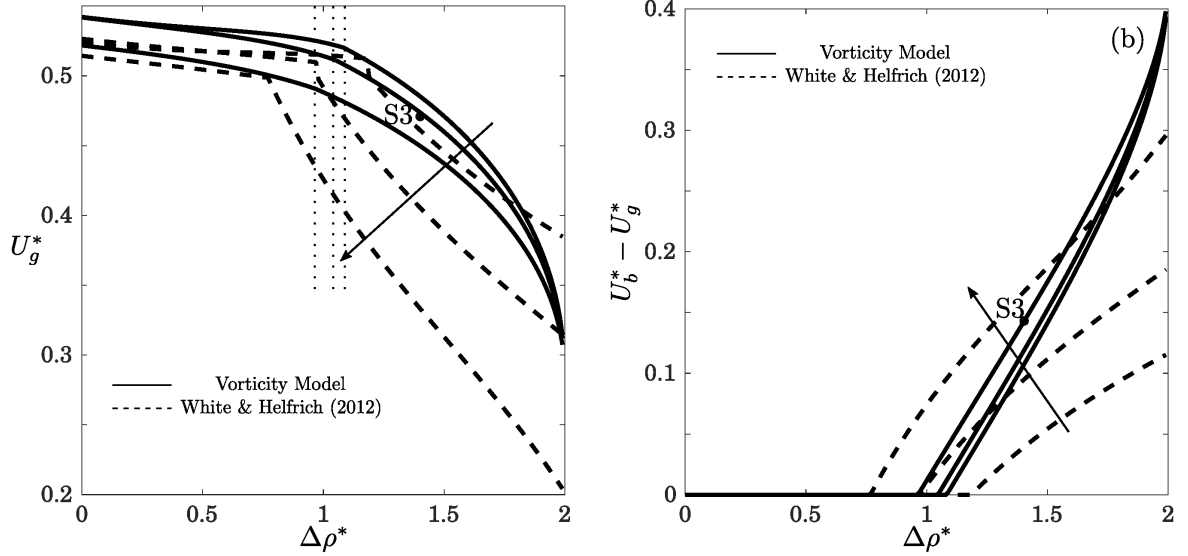
Figure 4.19: Comparison of the vorticity model and the bore-inclusive model of [35]: (a) gravity current velocity U_g^*, and (b) usptream bore speed in the reference frame moving with the gravity current $U_b^* - U_g^*$, as functions of $\Delta\rho^*$, for the three values $h^* = 0.30$, 0.371 and 0.45. The inflow height of the ambient interface is kept constant at $h_{1i}^* = 0.35$. The arrow indicates the direction of increasing gravity current height. According to the vorticity model, upstream propagating perturbations arise to the right of the dotted vertical lines, with the gravity current height decreasing from left to right. The corresponding DNS results for $h^* = 0.371$ (simulation S3) are indicated as well.

waves, which are neglected in both studies. As a possible alternative, they speculate that the headloss in the dissipative ambient layer becomes negative when $\Delta\rho^* > 1.2$. [34] furthermore suggest that the transition from the internal bore to the expansion fan occurs when $h_{1i}^* \gtrsim 0.3$. By comparison, the vorticity model predicts the transition from C2 to C3 to occur when $h_{1i}^* < 0.5$.

Figure 4.17 only shows the conjugate flow solution of [35], which does not account for upstream propagating waves. As mentioned in the introduction, [35] also propose an alternative model with an internal bore (but without an expansion fan), as sketched in Fig. 4.2. For this model, [35] close their system of equations in two different ways. In the first approach, they assume energy conservation downstream of the bore and within the gravity current region ($1b - 1o - 4o - 3b$), and in the second one, they allow for positive

headloss along $1b - O - 2o$ (or $2b - 3o$), while they assume energy-conserving flow within bore region ($1i - 1b - 3b - 3i$), which yields $h_l^* = 0.5$ and $U_b^* = 0.5\sqrt{\Delta\rho^*}$, consistent with the vorticity model. Figure 4.19 compares the results obtained with the second approach to those of the vorticity model. Both models obtain the same flow properties immediately downstream of the internal bore. Due to the presence of the expansion fan in the vorticity model, and its different treatment of the gravity current region, the two models yield different predictions. Figure 4.19a compares the gravity current velocities predicted by the vorticity model and the bore-inclusive model of [35] as a function of $\Delta\rho^*$, for three different gravity current heights. Both models predict that the current velocity increases with the decrease in current height. The discrepancies between the two predictions become more pronounced in the presence of upstream propagating waves. Figure 4.19b shows the difference between the bore and the gravity current velocities $U_b^* - U_g^*$ as a function of $\Delta\rho^*$. Both models predict the formation of an internal bore for smaller $\Delta\rho^*$-values as h^* increases. Furthermore, both models show a monotonic increase of the velocity difference with the ambient stratification.

4.6   Summary

We have extended the vorticty-based modeling approach originally introduced by [19] and [25] to gravity currents propagating into two-layer stratified ambients. Towards this end, we have developed vorticity-based models for three different flow configurations, *viz.* no upstream propagating wave (C1), an upstream propagating expansion wave only (C2), an upstream propagating expansion wave and a bore (C3). Configuration C1 is quasisteady in the reference frame moving with the gravity current, and it does not require any empirical closure assumptions. Configurations C2 and C3, on the other hand, are unsteady even in the moving reference frame, and in order to obtain a closed system

142

of equations we assume that certain flow properties vary linearly along the unsteady expansion fan. If we prescribe the gravity current height and the stratification strength along with the ambient inflow layer thicknesses and velocities, the models yield the gravity current velocity, the bore and expansion wave properties, as well as the ambient outflow layer thicknesses and velocities. Furthermore, the model equations provide information as to which of the three configurations will occur in a given parameter regime.

Since we do not require energy-related closure assumptions for any of the configurations, the energetics of the different flow fields can be analyzed *a posteriori*, after the full flow field has been determined. In this way, we can determine the dissipation associated with each gravity current height, for a given set of flow parameters. In order to determine which gravity current height will be selected in Navier-Stokes flows, we then conduct two-dimensional DNS simulations that can be compared to the model results. These simulations yield gravity current heights in close agreement with the vorticity model solutions for energy-conserving flows, so that we adopt this energy-conserving solution as the vorticity model prediction. For the quasisteady C1 configuration, the vorticity model predictions agree with the earlier models by [8] and [35], and with the DNS simulations. In the presence of an expansion fan, however, only the vorticity model predictions are close to the DNS results.

We furthermore discuss some of the differences between the present flow regimes for gravity currents propagating into two-layer stratified ambients, and earlier analyses of two-layer stratified flows over solid topography. Interestingly, the gravity current simulations do not indicate the presence of a completely blocked flow regime, whose existence is well established for flow over solid topography.

Chapter 5

Intrusive gravity currents in linearly stratified ambients

Intrusions can also penetrate into continuously stratified ambients, where the linear stratification has been frequently the interest of researchers [42–44]. The most typical way to generate such flows in the laboratory is by a lock-release experiment, which has been sketched in Fig. 5.1a. As can be seen, a large rectangular tank with the dimesnion $L \times H$ has been divided into two compartments through a solid vertical gate, so that the left compartment is filled by the intrusion fluid with the density ρ_c and the right one contains a stratified fluid whose density varies linearly from ρ_u at the top to ρ_l at the base of the stratification. The length of the left compartment L_{lock} should be selected adequetely large to capture the dynamics of the ambient return flow more precisely. Upon the instantaneous removal of the vertical wall, the fluid within the left compartment forms the right-propagating intrusion which travels at the velocity U_c. Concurrently, the ambient fluid travels above and beneath the intrusion and towards the left, which gives rise to two bottom- and top-propagating gravity currents with the respective front speeds U_l and U_u. Experimental and numerical findings of all earlier studies exhibit that these two left-propagating currents are fully symmetric with respect to the midplane of the tank, when $\rho_c = (\rho_l + \rho_u)/2$. The interface ahead of the intrusion also stays flat and unperturbed,

which indicates that no upstream disturbance emerges in these situations. Figure 5.1b displays the simplified configuration of these flows, referred to as symmetric or equilibrium intrusions by previous works [42–44]. On the contrary, when the intrusion density is not equal to the average of ambient fluid density, a nonsymmetric or nonequilibrium intrusion such that of configuration 5.1c will form in which left-propagating currents travel with significantly different velocities. Furthermore, the flow generates internal gravity waves traveling along all isopycnals and ahead of the intrusion, which can remarkably affect the flow dynamics upstream of it. [43] and [44] observe that however the wave amplitude varies across the tank height, so that the maximum amplitude appears near the isopycnal with the same density as the intrusion fluid (neutral buoyancy isopycnal), the waves of all isopycnals have the same propagation speed. Consistent with the observations of [16], the propagation of another internal wave is also expected located at the same streamwise location as the slower left-propagating current head, as will be shown in next sections.

Due to the complexity of analyzing the continuously stratified flows, only one previous study has proposed a theoretical model for the problem under consideration. This model developed by [42] is the extension of [14]'s model to the intrusions into linearly stratified medium in which, the authors have assumed all the Available Potential Energy (APE) prior to the removal of the gate can be converted to the kinetic energies of the gravity currents nondissipatively. They have also considered a quadratic expression for the square of intrusion front speed as a function of the level of asymmetry in the flow ϵ, given by

$$\epsilon = \left| \frac{\rho_c - 0.5(\rho_u + \rho_l)}{\rho_l - \rho_u} \right|. \tag{5.1}$$

To obtain the coefficients of this expression, [42] investigate the limit of symmetric intrusion, while their energy analysis shows that the intrusion speed attains a minimum
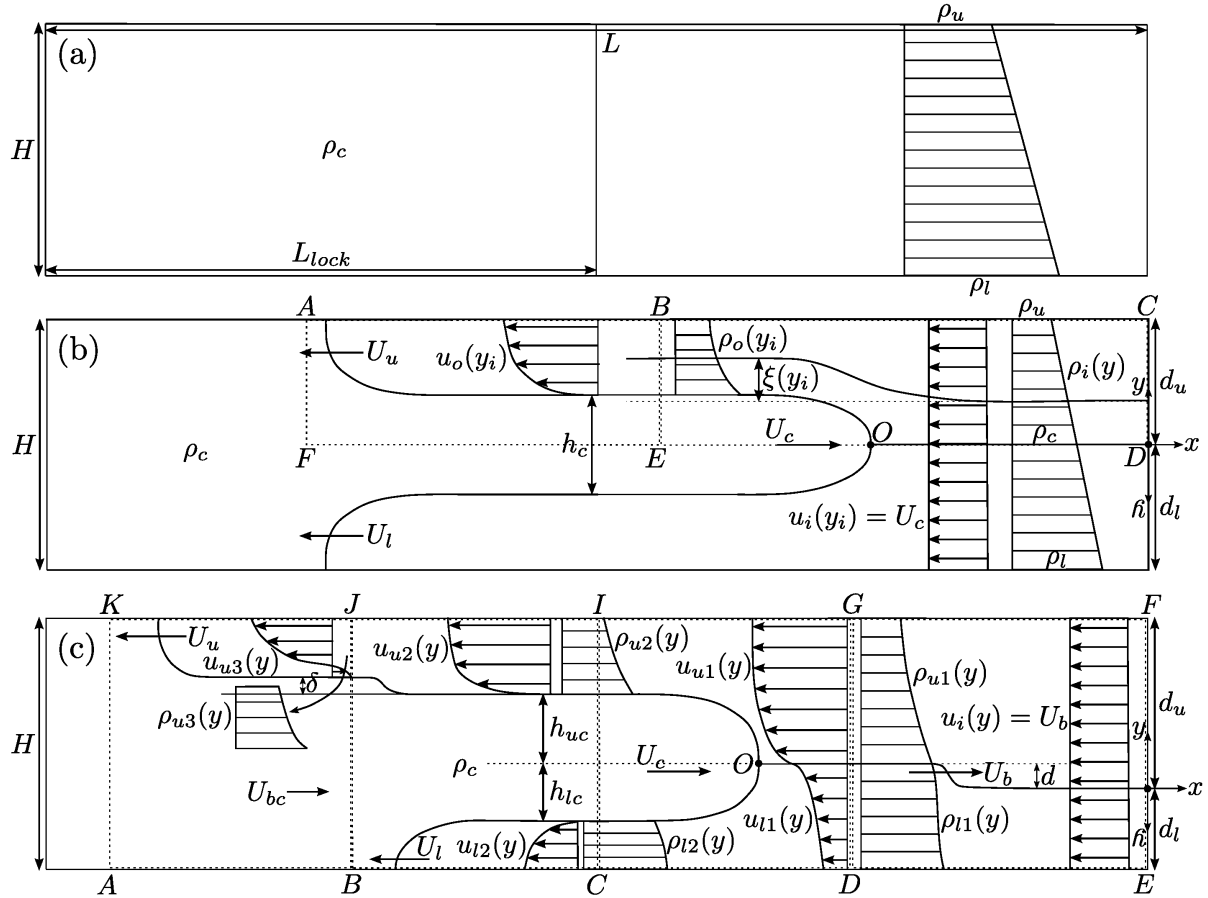
Figure 5.1: (a) Schematic of a lock-release process set up to examine the propagation of the intrusion into linear stratification. (b) Upon the removal of the vertical gate separating the intrusion fluid from the ambient, an equilibrium intrusion forms when $\epsilon = 0$. Concurrently, the return flow of the ambient produces two counterflowing gravity currents along the horizontal walls. As can be noted, the interface ahead of the intrusion remains flat, which indicates that internal gravity waves do no emerge in this case. We remark that U_c, U_l and U_u represent the front velocities of the intrusion and left-propagating currents in the lab-frame, whereas u_i and u_o are the flow velocities up- and downstream of the intrusion, respectively, and in the reference frame moving with its head. (c) On the other hand, when $\epsilon > 0$, the flow gives rise to internal gravity waves traveling ahead of the intrusion as well as a left-propagating internal bore always located at the same streamwise location as the slower counterflowing gravity current tip. In addition, the left-propagating currents travel with substantially different velocities in these situations. The arbitrary density and velocity profiles in various flow regions, compatible with general physical prerequisites such as the stability of the stratification, are also shown for all configurations. The dotted lines demonstrate the control volumes chosen for the derivation of conservation laws. As can be seen, $y = 0$ is shifted to the neutral buoyancy level for both types of intrusion.

in this limit. They furthermore argue that the speed of this case can be evaluated via employing the existing symmetry and modeling the top (or bottom) half of the intrusion as a gravity current with the thickness of half the tank depth which advances into a linear stratification. Consequently, they arrive at the following relation for the intrusion speed

$$\frac{U_c}{\hat{g}H} = \frac{F}{2}\sqrt{12\epsilon^2 + 1}\,, \tag{5.2}$$

where F equals 0.266 and 0.25, depending on whether they use the results of [30] or [45], for the calibration. $\hat{g}$ is also the reduced gravity defined as $g(\rho_l - \rho_u)/\rho_c$. The modified version of this model has been further employed by [46] to obtain the intrusion speed for when the intrusion fluid is also linearly stratified, rendering reasonably good predictions as well.

However [42] observe that the intrusion head becomes subcrtical with respect to the internal gravity waves of mode-1, as soon as the symmetry condition is broken, and with respect to those of mode-2, when $0 < \epsilon \lesssim 0.23$, but they do not incorporate it into their model, as they argue the energy associated with these waves is fairly small compared to APE. The authors acknowledged that the more accurate evaluation of intrusion velocity in these situations requires the in-depth assessment of the flow upstream of the intrusion, which has been left for further studies.

The investigation on the properties of the internal gravity waves associated with nonsymmetric intrusion as well as their contribution to the overall energy budget of the flow has been carried out by [43] and [44]. First of all, both studies observe the existence of two different modes for the internal waves which propagate with the speeds close to those predicted by [47] as

$$\frac{c_m}{\hat{g}H} = \frac{1}{m\pi}\,, \tag{5.3}$$

where c_m represents the speed of mode-m. The slight difference between the numerical or experimental wave speeds and those predicted by equation (5.2) has been related to the nonlinear interactions between the modes by both investigations. In agreement with [42], [43] and [44] observe that the intrusion speed finds its minimum when $\rho_c = (\rho_l + \rho_u)/2$ and no internal wave arises in these case. In addition, they both demonstrate that the amount of APE radiated into the gravity waves constantly grows, as we get farther from the equilibrium condition, such that away from this condition a considerable fraction of the initial APE can be transferred into the potential and kinetic energies of these waves. The maximum of this fraction has been reported to be around 20% and 30%, by [43] and [44], respectively. Both studies also note that in the vicinity of the equilibrium condition most of the wave energy is extracted by the mode-2 structure, while away from that, it is predominantly extracted by the mode-1. They however estimate the transition from mode-2 to mode-1, which is seen when the energy budget of mode-1 exceeds that of mode-2, occurs at fairly different values of ϵ. In fact [43] predicts this transition to begin when $\epsilon \approx 0.18$, whereas [44] anticipates it somewhat later when $\epsilon \approx 0.23$.

Within the present chapter, we extend the vorticity-based modeling of [48], proposed for the gravity currents enetering arbitrarily stratified and sheared ambients, to the intrusive gravity currents advancing into linearly stratified ambients. This enables us to find the velocity and thickness of the intrusion head as well as those of the counterflowing gravity currents. For the cases in which the internal gravity waves form, this approach also allows us to predict the propagation speed and the maximum amplitude of these waves. Thus, employing vorticity conservation principle in addition to the incorporation of right- or left-propagating waves eliminates the need for any empirical assumptions with regard to the energy budget of the flow, in contrast with the previous model. Section 5.1 discusses the analytical models for both equilibrium and nonequlibrium intrusions. In section 5.2, we describe the DNS simulations, and compare the predictions of the

vorticity model to the numerical predictions, as well as the theoretical and experimental findings, if available. Section 5.3 summarizes the findings and presents the main concluding remarks.

5.1   Theory

We now proceed to develop analytical vorticity-based models for the various types of intrusion, introduced previously in this chapter.

5.1.1   Symmetric intrusions

The simplified dynamics of an equilibrium intrusion is characterized by Fig. 5.1b. The symmetry with respect to $y = H/2$ as well as the existence of undisturbed interfaces enable us to calculate the intrusion front speed only via the assessment of the flow dynamics within the upper (or lower) half. Consequently, we can consider the upper half as a gravity current propagating into a linearly stratified ambient with the thickness of half the channel depth. Note also that the gravity current height is equal to half the intrusion thickness. To obtain a vorticity-based solution for the flow, we can then employ the thoery developed by [48] for the gravity currents advancing into arbitrarily stratified and sheared ambients, which suggests the following second-order ODE with respect to the upstream height y_i, in the reference frame moving with the gravity current

$$\xi'' u_i^2 + \xi'(1 + \xi')(2 + \xi')u_i u_i' - \xi(1 + \xi')^3 g \frac{\rho_i'}{\rho_c} = 0 \,, \qquad (5.4)$$

where ξ denotes the deflection of a certain streamline from upstream of the gravity current towards downstream and ρ_c has been selected as the reference density. u_i and ρ_i also show the horizontal velocity and density distributions at the inflow boundary,

respectively. Substituting the given upstream conditions into equation (5.4) leads to

$$\xi'' U_c^2 + \xi(1+\xi')^3 g \frac{\rho_l - \rho_u}{\rho_c H} = 0 \,. \tag{5.5}$$

The boundary values for the problem under consideration is however slightly more complicated than those suggested by [48], since the thickness h_c of the intrusion is an unknown as well. Using the vorticity balance equation along the upper interface of the intrusion gives

$$\frac{u_o(0)^2}{2} = g \frac{\rho_i(0) - \rho_c}{\rho_c} \frac{h_c}{2} \,, \tag{5.6}$$

where u_o is the horizontal velocity function at the outflow boundary of control volume $EDCB$. Note that in the case under investigation y_i varies from 0 to $H/2$, where $y_i = 0$ is located at the neutral buoyancy isopycnal (point D in Fig. 5.1b), which yields $\rho_i(0) = \rho_c$. We can thus conclude $u_o(0) = 0$. [48] arrives at the following relationship between the horizontal velocity profiles at the in- and ouflow bundaries by applying the mass conservation equation to a certain infinitesimal streamtube

$$u_o(y_i) = \frac{u_i(y_i)}{1+\xi'} \,. \tag{5.7}$$

Replacing $u_o(0) = 0$ into the above equation then yields $\xi'(0) = \infty$. It is also clear that the top wall of the tank is an undeflected streamline, i.e. $\xi(H/2) = 0$, and the deflection of the streamline at the neutral bouyancy level is given by $\xi(0) = h_c/2$. We still need an extra equation for the closure, since the intrusion thickness has to be found. To obtain this additional equation, applying the integral form of the inviscid vorticity conservation PDE to the flow within $FEBA$ control volume and in the reference frame of the upper

150

gravity current can be informative, which gives

$$\oint \omega \mathbf{u} \cdot \mathbf{n} \, \mathrm{d}S = -\iint \frac{g}{\rho_c} \frac{\partial \rho}{\partial x} \, \mathrm{d}A \,, \tag{5.8}$$

where ω and $\mathbf{u}$ represent the vorticity normal to the plane and the velocity vector, respectively. $\mathrm{d}A$, $\mathrm{d}S$ and $\mathbf{n}$ also indicate a differential area within the control volume, a differential length along the boundaries of the control volume, and the unit outer normal vector to the control volume boundaries. Equation (5.8) can be simplified to

$$\frac{1}{2}\left\{ (U_u + U_c)^2 - \left[U_u - (u_o(H/2) - U_c) \right]^2 \right\} = \int_{h_c/2}^{H/2} \frac{g}{\rho_c} [\rho_c - \rho_o(y)] \, \mathrm{d}y \,, \tag{5.9}$$

cf. [19] for the details. Note that $U_u - [u_o(H/2) - U_c]$ is the horizontal velocity along the top wall, at the inflow of $FEBA$ and in the reference frame moving with the upper gravity current. U_u can also be calculated as the average of horizontal flow velocity downstream of the intrusion and in the laboratory frame

$$U_u = \frac{\int_{h_c/2}^{H/2} [u_o(y) - U_c] \, \mathrm{d}y}{H/2 - h_c/2} \,. \tag{5.10}$$

We can then solve the vorticity model equations as follows: After making initial guesses for h_c and U_c, we integrate equation (5.5) subject to the boundary conditions $\xi(0) = h_c/2$ and $\xi'(0) = \infty$. The latter is implemented by setting $\xi'(0)$ to a large number. Tests show that for sufficiently large values $\xi'(0) > 10^3$, the numerical solution does not depend on the exact value chosen. Then we perform an inner iteration loop by updating our guess for h_c via a bisection shooting procedure until the condition $|\xi(H/2)| < 10^{-7}$ is satisfied. The final value for U_c is then found via an outer iteration loop, as follows: Since the density remains constant along a streamline, we can evaluate the outflow density $\rho_o(y)$ from $\rho_o(y_i + \xi(y_i)) = \rho_i(y_i)$, and the outflow velocity $u_o(y)$ is obtained from equation

(5.7). We then iterate on U_c until equation (5.9) is satisfied within the control volume $FEBA$ with an error less than 10^{-7}.

5.1.2   Nonsymmetric intrusions

Once the symmetry condition is violated, a nonequilibrium intrusion such that sketched in Fig. 5.1c forms, which also gives rise to right-propagating internal gravity waves. However these waves travel at the same speed along all isopycnals ahead of the intrusion [43, 44], their amplitude vary across the tank, so that it is zero along the bottom and top walls and becomes maximum close to the neutral buoyancy isopycnal, as stated earlier in this chapter. We notice that the linear stratification upstream of the intrusion gives the following relation for neutral buoyancy level y_N

$$y_N = 1 - \frac{\rho_c - \rho_u}{\rho_l - \rho_u} \, . \tag{5.11}$$

[43] suggests the following empirical expression for the maximum amplitude of the waves d_{max}

$$d_{max} = \alpha(0.5 + \epsilon) \, , \tag{5.12}$$

where $\alpha = 0.18 \pm 0.01$. Having the same propagation speed for the waves of all isopycnals as well as the existence of a maximum for their amplitude, incites us to treat these gravity waves as a hydraulic bore traveling along the neutral buoyancy isopycnal, at the speed U_b and with the amplitude d, as shown in Fig. 5.1b. The validity of this assumption will be further examined in section 5.2.1. To solve for the speed and the amplitude of this bore, we then employ a vorticity-based analysis similar to that of section 5.1.1, by applying equation (5.4) to both upper and lower regions of control volume $DEFG$ and

in the reference frame moving with the leading bore, which results in

$$\xi'' U_b^2 + \xi (1 + \xi')^3 g \frac{\rho_l - \rho_u}{\rho_c H} = 0 \,. \tag{5.13}$$

Note that $y-$axis is directed downward within the lower region, which makes the gradient of the density positive, but since the gravity is in the same direction as this vector, equation (5.13) retains its shape. The origin of the coordinate system for both regions is shifted to the neutral buoyancy isopycnal, in the same fashion as section 5.1.1. The boundary values of this equation for the regions below and above the wave can be written as

$$\xi_{u1}(0) = -\xi_{l1}(0) = d \,, \tag{5.14}$$

$$\xi_{u1}(d_u) = \xi_{l1}(d_l) = 0 \,. \tag{5.15}$$

Furthermore, the solution will be smooth at the interface, so that

$$\xi'_{u1}(0) = \xi'_{l1}(0) \,. \tag{5.16}$$

The procedure for solving the flow within the wave region is as follows: We make an initial guess for d and U_b. We then solve (5.13) for the upper and lower regions based on the boundary values of equations (5.14) and (5.15) and via a bisection shooting method, which renders the slopes of the deflection at the neutral buoyancy isopycnal $\xi'_{u1}(0)$ and $\xi'_{l1}(0)$. We then terminate the procedure and accept the solution if equation (5.16) holds, otherwise, we update our guess for U_b until it happens and the solution converges. We verify the validity of the initial guess for d later, and correct it, if needed.

The previous analysis of the leading bore also returns the density and velocity distributions upstream of the intrusion. Due to the propagation of the internal gravity waves,

the density stratifiction ahead of the intrusion will no longer be linear and the velocity distribution exhibits shear, i.e. the more sophisticated and general equation for ξ shown in (5.4) has to be employed to obtain the intrusion speed and thickness. Towards this end, we first investigate the flow within the slower left-propagating current, which is the lower one when $\rho_c > (\rho_l + \rho_u)/2$. Next, we guess a value for U_c and shift the reference frame from the leading bore to the intrusion by replacing u_i with $u_{l1} - U_b + U_c$ in equation (5.4). We then find the thicknesses of the lower gravity current and lower branch of the intrusion, h_l and h_{lc}, as well as the intrusion speed U_c by using the same numerical procedure as that described for a symmetric intrusion, except the closure equation should be modified as we apply the vorticity conservation equation (5.8) to the region below the stagnation point of the intrusion (O in Fig. 5.1c) and inside control volume $BCIJ$, while traveling with the bottom-propapgating current, which leads to

$$\frac{1}{2}\left\{(U_l + U_c)^2 - \left[U_l - (u_{l2}(d_l + d) - U_c)\right]^2\right\} = \int_{h_{lc}}^{d_l+d} \frac{g}{\rho_c}(\rho_{l2}(y) - \rho_c)\ \mathrm{d}y\,. \qquad (5.17)$$

U_l in above equation can be calculated in the same fashion as U_u in section 5.1.1

$$U_l = \frac{\int_{h_{lc}}^{d_l+d} \left[u_{l2}(y) - U_c\right]\ \mathrm{d}y}{h_l}\,. \qquad (5.18)$$

Computing U_c enables us to solve for the flow properties within the upper branch of the intrusion, when we substitute u_i and ρ_i with $u_{u1} - U_b + U_c$ and ρ_{u1}. We then guess a value for h_{uc} and correct our guess until integrating from ODE (5.4) yields $|\xi_{u2}(d_u - d)| < 10^{-7}$. The thickness h_c of the intrusion can then be computed as $h_{lc} + h_{uc}$.

Evaluation of the flow variables downstream of the intrusion then allows to study the left-propagating internal bore, which travels at the same speed as the slower left-propagating current (here U_l), as discussed earlier. Thus, we only need to find its ampli-

tude to obtain the flow condition downstream of the bore. Towards this end, we make a guess for the amplitude δ and solve the equation (5.4) in an iterative fashion, while we should also notice that the slope of deflection at the interface of the bore and the intrusion fluid is not infinity, since the flow velocity downstream of the bore and right above the interface is not zero in the reference frame moving with it. The slope $\xi'_{u3}(0)$ can then be reevaluated as the following

$$\xi'_{u3}(0) = \frac{U_c + U_l}{U_{bc} + U_l} - 1 \,. \tag{5.19}$$

This equation is achieved, when (5.7) is used along the interface of the bore. U_{bc} can also be calculated by using the continuity equation within the intrusion fluid and in the reference frame moving with the internal bore

$$(U_{bc} + U_l)(H - h_u) = (U_c + U_l)h_c \,. \tag{5.20}$$

As can be seen, the value of $\xi'_{u3}(0)$ is convoluted to the solution of ODE (5.5) for the left-propagating bore, i.e. this ODE has to be solved concurrently along with equations (5.19) and (5.20) to obtain the bore amplitude δ in addition to the flow properties downstream of the bore.

The analysis described above evaluates the properties of all flow components, while the amplitude d of the right-propagating bore was based on an initial guess. This guess can however be corrected by investigating the vorticity balance within the entire control volume $ABJK$ and in the reference frame moving with the top-propagating current, which yields

$$\frac{1}{2}\left\{(U_u + U_{bc})^2 - \left[U_u - (u_{u3}(H) + U_l)\right]^2\right\} = \int_{H-h_u}^{H} \frac{g}{\rho_c}\left[\rho_c - \rho_{u3}(y)\right]\,\mathrm{d}y\,, \tag{5.21}$$

where $h_u = H - h_c - h_l - \delta$. We then accept the solution entirely, if equation (5.21) holds with an error less than 10^{-7} or reiterate the whole procedure with an updated guess for d, if it did not.

5.2 DNS results vs. model predictions

In the following, we assess the validity and the predictive capability of the vorticity-based approach proposed in section 5.1, as we compare its findings with those of earlier investigations as well as the corresponding DNS results of our in-house software TURBINS, which solves the following conservation equations for mass, momentum and density, all in the dimensionless form

$$\boldsymbol{\nabla}\cdot\mathbf{u}^* \;=\; 0\,, \tag{5.22}$$

$$\frac{\partial\mathbf{u}^*}{\partial t^*}+ \;\mathbf{u}^* \;\cdot\boldsymbol{\nabla}\mathbf{u}^* = -\boldsymbol{\nabla}p^* + \frac{1}{Re}\nabla^2\mathbf{u}^* + \rho^*\mathbf{e}^g\,. \tag{5.23}$$

$$\frac{\partial\rho^*}{\partial t^*}+ \;\mathbf{u}^* \;\cdot\boldsymbol{\nabla}\rho^* = \frac{1}{Pe}\nabla^2\rho^*\,. \tag{5.24}$$

Here, $\mathbf{e}^g$ indicates the unit vector for the gravity, and Re and Pe are defined as $\sqrt{\hat{g}H}H/\nu$ and $\sqrt{\hat{g}H}H/D$, respectively. Furthermore, H, ν and D denote the channel height, kinematic viscosity and the diffusivity of the density field, respectively. The reference values for the lengths, velocities and the pressure have been chosen as H, $\sqrt{\hat{g}H}$ and $\rho_c\hat{g}H$, respectively, for nondimensionalizing. Dimesnsionless density has also been defined as $\rho^* = (\rho - \rho_u)/(\rho_l - \rho_u)$.

The free slip boundary conditions for the velocity, along with the vanishing normal flux conditions for the density field, have been enforced along all the solid boundaries. Figure 5.2a displays the initialization of the flow for an equilibrium intrusion, which can also be simply extended to the nonequilibrium cases. As shown in this figure, the density
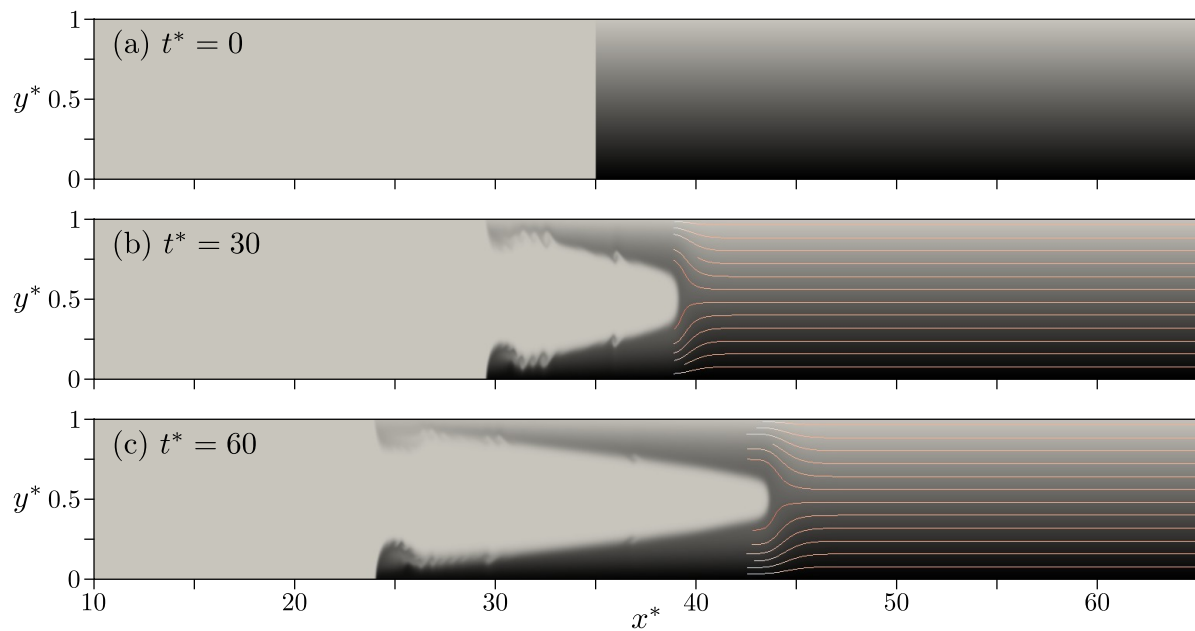
Figure 5.2: Temporal evolution of the density field for the symmetric intrusion ($\rho_c^* = 0.5$) starting from rest: (a) $t^* = 0$, (b) $t^* = 30$, and (c) $t^* = 60$. As can be seen, the streamlines ahead of the intrusion and in its own reference frame have been evaluated and visualized. Furthermore, the density field varies from $\rho^* = 0$ (light gray) to $\rho^* = 1$ (black), inside the ambient. Note that the intrusion fluid has been dyed in light gray (corresponding to $\rho^* = 0$) by using the passive marker technique, which enables us to distinguish between the intrusion and ambient more easily.
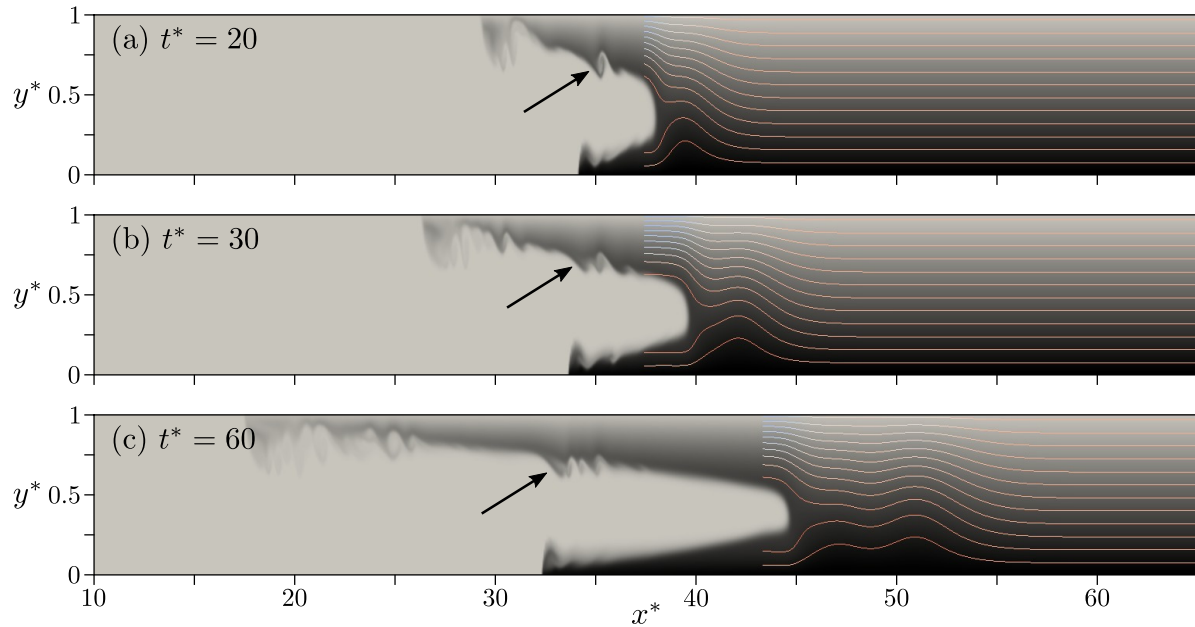
157

Figure 5.3: Various snapshots from the evolution of the density field for a nonsymmetric intrusion with $\rho_c^* = 0.7$ at: (a) $t^* = 20$, (b) $t^* = 30$, and (c) $t^* = 60$. As can be seen, the streamlines ahead of the intrusion and in its own reference frame have been evaluated and visualized. The arrows are also pointing towards the locations of the left-propagating bore. Furthermore, the density field varies from $\rho^* = 0$ (light gray) to $\rho^* = 1$ (black), inside the ambient. Note that the intrusion fluid has been dyed in light gray (corresponding to $\rho^* = 0$) by using the passive marker technique, which enables us to distinguish between the intrusion and ambient more easily.

has been set equal to ρ_c^* (dimensionless density of the intrusion fluid), everywhere to the left of the lock, while the density profile of $\rho^* = 1 - y^*$ has been applied to its right. The lock length has also been selected half the tank length, which avoids the intrusion and left-propagating currents hitting the vertical walls, unless sufficiently long after the flow variables have become time-independent. The fluids are also at rest at $t^* = 0$. We choose Re and Pe equal to 3×10^4 and 7.5×10^4, respectively, which are adequetely large to attenuate the diffusive effects for momentum and mass. We furthermore set the dimension of the computational grid equal to 70×1, and discretize it uniformly in both x^*- and y^*-directions, with the spacing of $\Delta x^* = 0.01$ and $\Delta y^* = 0.005$, which are sufficiently fine not to affect the simulation results.

Figure 5.2 and 5.3 represent the characteristics of the symmetric and nonsymmetric intrusions, respectively. The streamlines ahead of the intruison and its reference frame have also been evaluated and visualized for both flows. As can be seen, the streamlines remain flat and undisturbed, except in the vicinity of the intrusion head, for the symmetric intrusion, which indicates that no upstream wave emerges in this situation. On the other hand, for the nonsymmetric intrusion, these streamlines experience significant deflections, as the gravity waves arise ahead of the intrusion. Our numerical observations, obtained from running more than 100 simulations, show that when $\epsilon \lesssim 0.2$ the flow gives rise to both mode-1 and mode-2 structures, while the mode-1 waves travel nearly twice as fast as mode-2 waves. On the other hand, when $\epsilon \gtrsim 0.2$, only mode-1 waves can distincly be recognized. These observations are in very good agreement with those of [43] and [44]. In addition, all the studied simulations exhibit that the maximum deflection of the isopycnals occurs relatively close to the neutral buoyancy isopycnal and the disturbances (waves) of all isopycnals travel at exactly the same speed. Moreover, it is seen that all the flow variables including the front velocities and the thicknesses of the intrusion and the left-propagating graviy currents as well as the the propagation speed of the gravity waves and their maximum amplitude acquire quasisteady values, in all the simulations, fairly shortly after the release of the lock.

In order to obtain the accurate values for the front velocities of all currents, we employ a passive marker technique, i.e. we mark the fluids of the intrusion and ambient by separate dyes, implemented in the simulations by using different concentration fields for the intrusion and ambient, with the same Pe-value as the density field. The front location of the intrusive gravity current $x^*_{f,c}$ can then be defined as the rightmost point
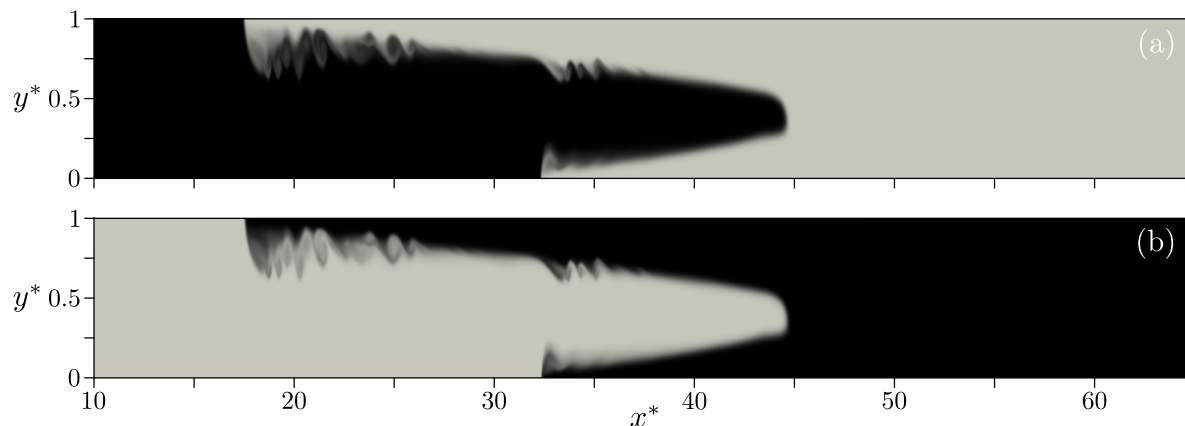
Figure 5.4: Marking the fluid of each current with dye enables us to calculate the current heights and velocities, as described in detail in the text. Here, $c_d^* = 1$ within the intrusion fluid and zero everywhere else for frame a, and vice versa for frame b.

at which the local dimensionless height $\eta^* > 0.01$, where η^* has been calculated as

$$\eta^*(x^*, t^*) \;\; = \;\; \int_0^1 c_d^*(x^*, y^*, t^*)\, \mathrm{d}y^* \,. \tag{5.25}$$

Here c_d^* denotes the dimensionless dye concentration, and above integration has been applied to the concentration field of Fig. 5.4a. In addition, we can apply the integral of equation (5.25) to the density field shown in Fig. 5.4b to evaluate the front locations of the lower and upper gravity currents, indicated by $x_{f,l}^*$ and $x_{f,u}^*$, respectively, while for the lower gravity current we take this integral for the lower half of the tank ($y^* = 0$ to 0.5) and for the upper gravity current, we compute it for the upper half ($y^* = 0.5$ to 1). Similarly, $x_{f,l}^*$ and $x_{f,u}^*$ are the first points from the left at which the respective η^* exceeds 0.01.

Figure 5.5a demonstrates the front locations of various gravity currents as functions of time, for the nonsymmetric intrusion of Fig. 5.3. As can be seen in Fig. 5.5a, after a very short transient time, all the currents travel with quasisteady speeds, in spite of the existence of nonvanishing mixing and turbulence along the interfaces. The straight line segments indicate the respective quasisteady front velocities, obtained by linear fits
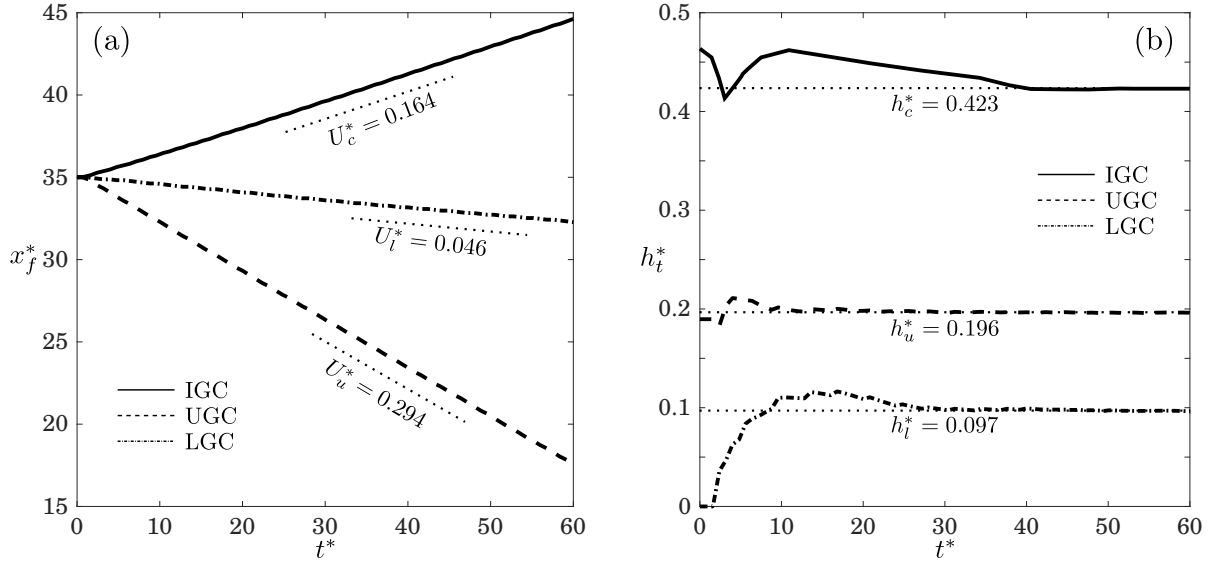
Figure 5.5: Simulation results for the a) front locations, and b) heights of various gravity currents, as functions of time, for the nonsymmetric case shown in Fig. 5.3. Here, IGC stands for Intrusive Gravity Current, while UGC and LGC denote Upper Gravity Current and Lower Gravity Current, respectively. The straight dotted line segments in frame a represent the quasisteady front velocities, obtained by linear fits of DNS results, and the horizontal dotted lines in frame b indicate the quasisteady heights, evaluated as described in the text.

of DNS results.

Evaluation of the front locations of various gravity currents enables us to calculate the effective gravity current heights as the following

$$h^*_{t,c}(t^*) = \frac{\int_{L^*_{lock}}^{x^*_{f,c}} \eta^*(x^*, t^*) \, \mathrm{d}x^*}{L^*_{lock} - x^*_{f,c}} \, , \tag{5.26}$$

$$h^*_{t,l}(t^*) = \frac{\int_{x^*_{f,l}}^{L^*_{lock}} \eta^*(x^*, t^*) \, \mathrm{d}x^*}{L^*_{lock} - x^*_{f,l}} \, , \tag{5.27}$$

$$h^*_{t,u}(t^*) = \frac{\int_{x^*_{f,u}}^{x^*_{f,l}} \eta^*(x^*, t^*) \, \mathrm{d}x^*}{x^*_{f,l} - x^*_{f,u}} \, , \tag{5.28}$$

where $h^*_{t,c}$, $h^*_{t,l}$ and $h^*_{t,u}$ denote the time-dependent heights for the intrusion and the boundary-propagating gravity currents, respectively. These heights can then be tempo-
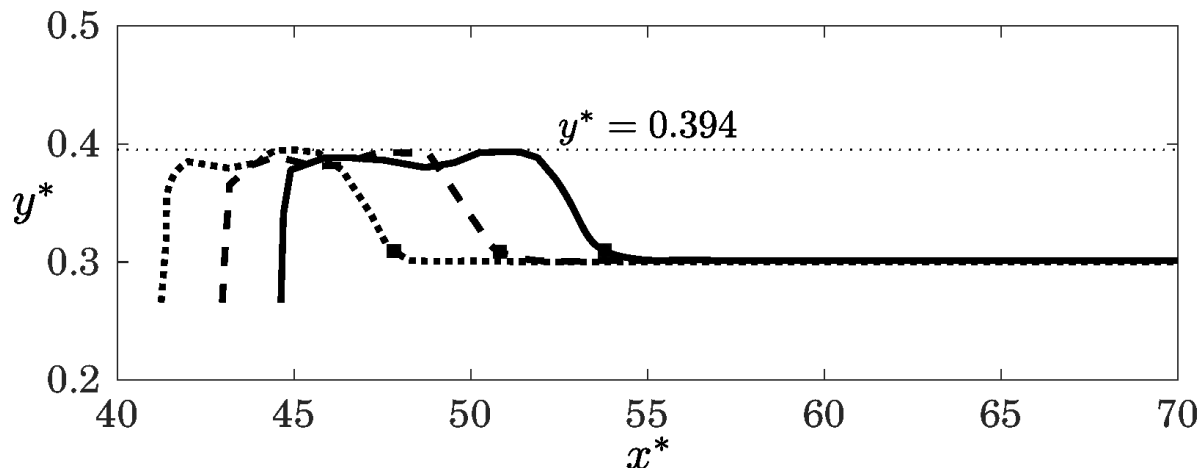
Figure 5.6: Temporal evolution of the neutral buoyancy isopycnal shown for three sufficiently large values of $t^* = 40$ (dotted line), $t^* = 50$ (dashed line) and $t^* = 60$ (solid line) at which the flow has become quasisteady. In addition, the black squares represent the front locations of the right-propagating bore at corresponding t^* and the horizontal dotted line indicates the quasisteady value of the maximum height h_b^* of the neutral buoyancy isopycnal.

rally averaged between two sufficinetly large times, at those the flow can be considered quasisteady, which yields the time-independent heights of the corresponding current

$$h^* = \frac{\int_{t_1^*}^{t_2^*} h_t^*(t^*) \, \mathrm{d}t^*}{t_2^* - t_1^*} \, . \tag{5.29}$$

Here, we take $t_1^* = 40$ and $t_2^* = 60$. As can be noted in Fig. 5.5b, the gravity current heights certainly converge to quasisteady values as their temporal variations become very insignificant for the fairly large values of t^*. However, we could also define the quasisteady heights as the effective heights at a relatively large time such as $t^* = 50$, we believe that the temporal average between two adequatly large times renders more accurate results, due to the slight change in the effective heights with time.

To measure the velocity U_b^* of the leading bore as well as its maximum height h_b^*, it is crucial to track the evolution of the neutral buoyancy isopycnal ahead of the intrusion with time, while we know the density of all the fluid particles along this line is ρ_c^*. Figure

5.6 represents the snapshots of this isopycnal at three sufficiently large values of t^*, when the flow can be considered quasisteady. We can thus define the front location $x_{f,b}^*$ of the leading bore (black squares in Fig. 5.6) as the rightmost point along the neutral buoyancy isopycnal at which $|y^* - y_N^*| > 0.01$, where y^* is the height of a certain point along this isopycnal. Figure 5.7a exhibits $x_{f,b}^*$ as a function of time, for the nonsymmetric intrusion shown in Fig. 5.3. Similar to the gravity currents, we observe that the propagation speed of the leading bore also achives a time-independent value, after a brief initial transition, as $\mathrm{d}x_{f,b}^*/\mathrm{d}t^*$ becomes constant fairly rapidly. The maximum height $h_{t,b}^*$ of the neutral buoyancy isopycnal can readily be evaluated as the maximum height y^* of this isopycnal, which can vary with time as well. $h_{t,b}^*$ can then be temporally averaged between $t_1^* = 40$ and $t_2^* = 60$ in the same fashion shown in equation 5.29 to obtain h_b^*. The horizontal dotted line in Fig. 5.6 indicates this value. Eventually, the amplitude d^* of the right-propagating bore can be calculated as

$$d^* = |h_b^* - y_N^*|. \tag{5.30}$$

Figure 5.7 demonstrates that both U_b^* and h_b^* (and thereby d^*) arrive at quasistady values, validating the assumption of treating the internal gravity waves as a single bore propagating with constant velocity and amplitude. By carrying out a corresponding analysis for other isopycnals, we confirm that all of them propagate with the same velocity. This procedure furthermore yields the displacement level as function of the isopycnal. We find that the largest displacement value d_{max}^* occurs close to the neutral buoyancy level. We refer to d_{max}^* as the maximum wave amplitude, consistent with [43] and [44].
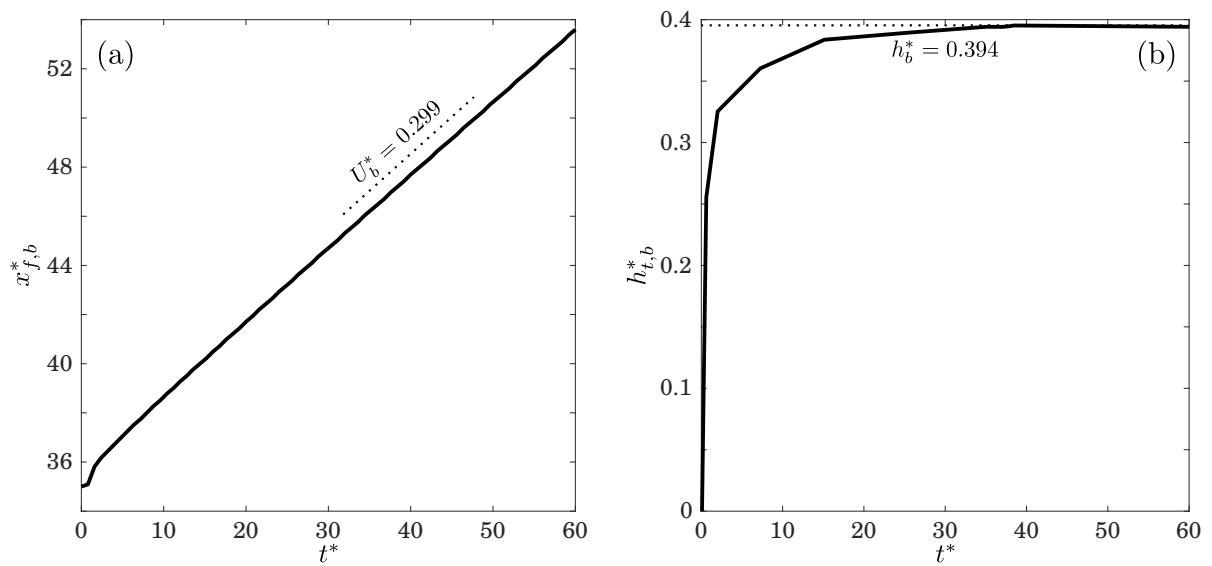
Figure 5.7: Variations of the a) front location of the leading bore, and b) the maximum height of the neutral buoyancy isopycnal, for the nonsymmetric case shown in Fig. 5.3. The straight dotted line segment in frame a represents the quasisteady propagation speed of the bore, obtained by linear fit of DNS results, and the horziontal dotted line in frame b indicates the quasisteady maximum height of the neutral bouyancy isopycnal, evaluated as described in the text.

5.2.1   Analytical results and comparisons

Figure 5.8 displays the propagation velocity U_b^* in addition to the amplitude d^* of the bore and the maximum deflection d_{max}^* of the isopycnals, as functions of the dimensionless intrusion density ρ_c^*. Shown are DNS results, vorticity model predictions, the estimates of [43], and the experimental data reported by [44]. The vorticity model predicts a constant bore propagation velocity $U_b^* \approx 1/\pi$, which is the theoretical propagation velocity of linear mode-1 waves [47]. Since nonsymmetric intrusions always give rise to mode-1 waves, and since these travel faster than any higher order modes, it is reasonable that the leading wave front travels with this velocity. The fact that mode-2 waves are symmetric with respect to the midplane of the tank, so that they result in smaller net displacements of the isopycnals [42], further supports this observation. The vorticity model predictions regarding U_b^* generally agree with the DNS results to within about 10%. Especially for near-symmetric intrusions, this is somewhat closer than the empirical formula of [43]. For $\epsilon \to 0.5$ (or $\rho_c^* \to 0, 1$) the vorticity model predictions agree with this empirical formula. Figure 5.8b indicates that $d^* \approx d_{max}^*$ for near-equilibrium intrusions, while they increasingly differ from each other as ϵ grows. Interestingly, for strongly nonsymmetric intrusions the vorticity model predictions for d^* are very close to the d_{max}^*-estimates of [43]. The vorticity model predictions for both d^* and d_{max}^* generally agree well with corresponding DNS results; although there is a noticeable discrepancy with the experimental data of [44].

Figure 5.9 shows model predictions, experimental data and DNS results for the propagation velocities and thicknesses of all three fronts, as functions of ρ_c^*. Figure 5.9a demonstrates good agreement among all data sets regarding the intrusion velocity. Both the vorticity model and the DNS data show that for intermediate intrusion densities the intrusion thickness attains a local minimum at $\rho_c^* = 0.5$, as seen in Fig. 5.9b. However,
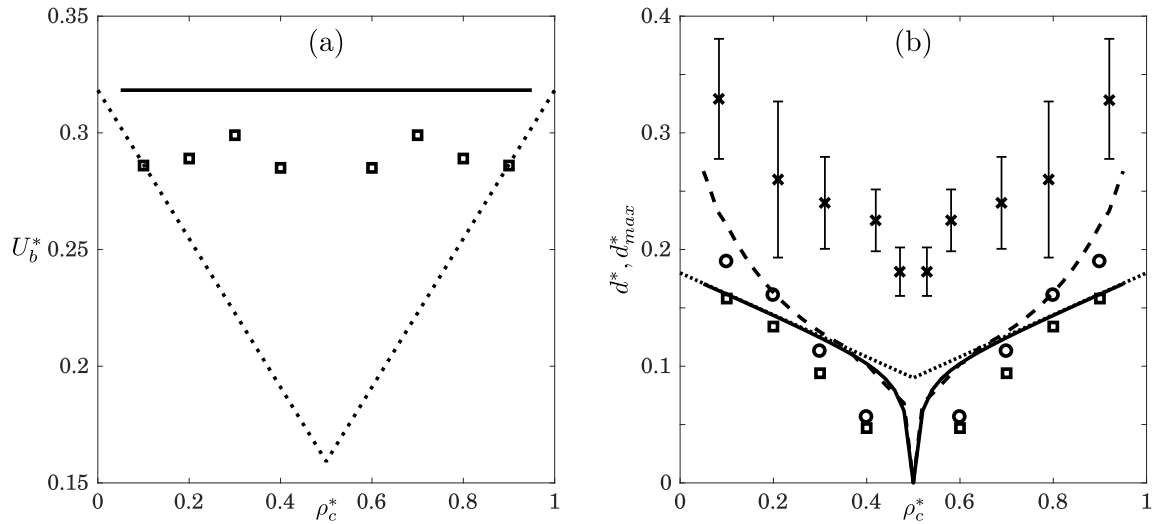
Figure 5.8: (a) Propagation speed of the internal gravity waves U_b^*, and (b) the maximum displacement d^* of the neutral bouyancy isopycnal as well as the maximum amplitude d_{max}^* of the waves, as functions of the dimensionless intrusion density ρ_c^*. In frame a, solid line represents the prediction of vorticity-based model of section 5.1, dotted line exhibits empirical approximation of [43], and discrete squares are DNS results. In frame b, the solid and dashed lines demonstrate the theoretical findings of the present study for d^* and d_{max}^*, respectively, the dotted line and discrete crosses indictate the estimate of [43] and experimental data of [44] with regard to d_{max}^*, and discrete squares and circles are the respective DNS results regarding d^* and d_{max}^*.
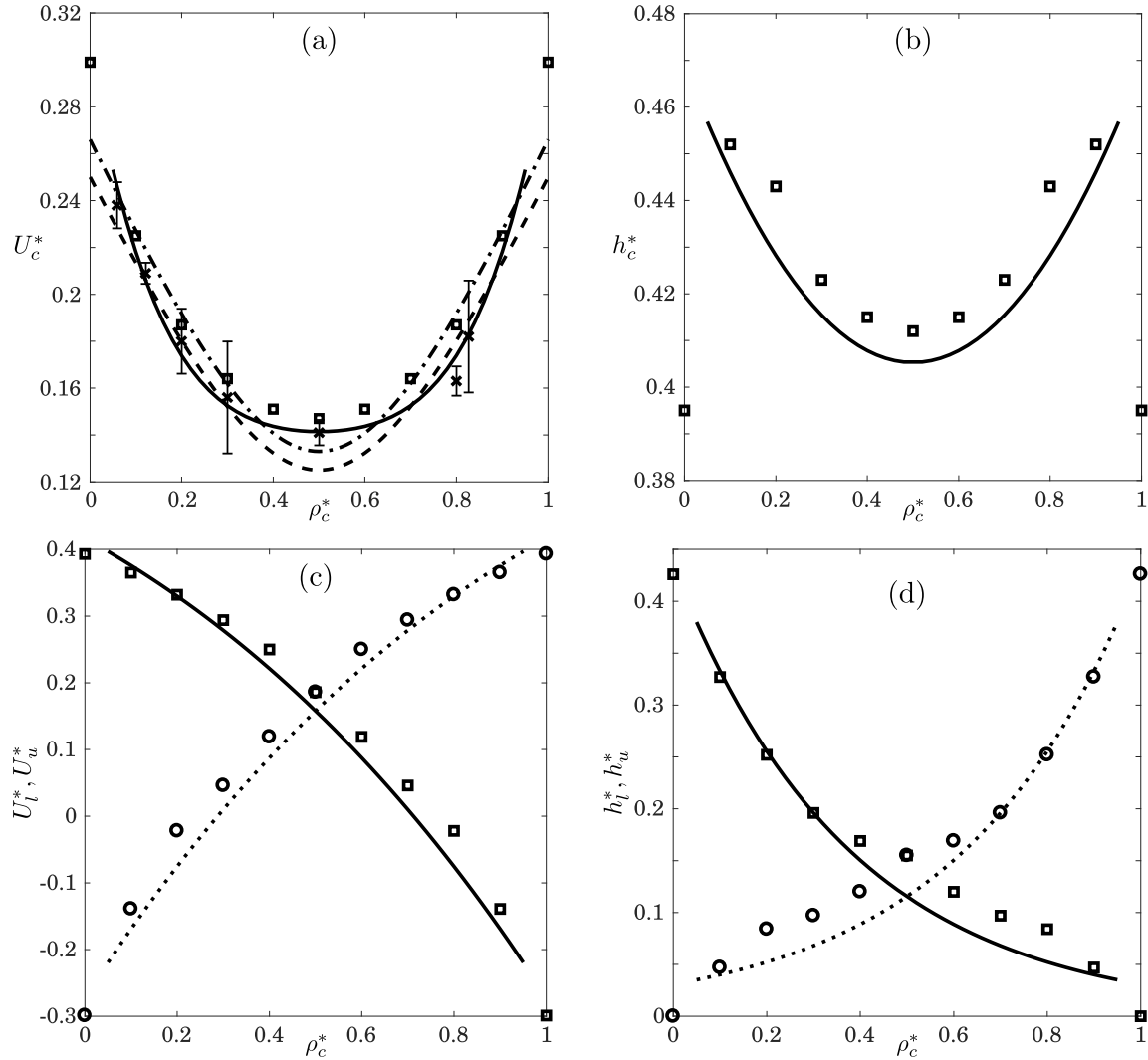
Figure 5.9: Variation as function of the dimensionless intrusion density ρ_c^*: (a) the intrusion front speed U_c^*, (b) the intrusion thickness h_c^*, (c) the front velocities of the bottom- and top-propagating gravity currents, U_l^* and U_u^*, and (d) the thicknesses of the bottom- and top-propagating gravity currents, h_l^* and h_u^*. Solid lines represent the predictions of the vorticity-based model of section 5.1 with regard to the intrusion and lower gravirty current properties and dotted lines show the properties of the upper gravity current obtained by this model. Furthermore, dashed and dash-dotted lines demonstrate the results of [42] for the intrusion speed, when $F = 0.25$ and 0.266, respectively. The discrete circles and squares also indicate the present DNS results, while the discrete crosses exhibit the experimental data of [42].

in the limits of $\rho_c^* = 0$ and 1 the DNS data indicate an even smaller intrusion thickness than for the symmetric case. In this context, we note that the vorticity model breaks down for $\rho_c^* > 0.95$ and $\rho_c^* < 0.05$, so that it does not yield meaningful predictions. This degeneration of the model indicates that these limits are singular, which is also reflected by the fact that the bore amplitude does not smoothly approach zero as $\rho_c^* \to 0$ or 1, cf. Fig. 5.8b, so that the flow does not smoothly transition to the full-depth lock-release case. The discussions provided by [15] and [16] provide additional insight into this issue.

Consistent with the findings of [16], the front speed and thickness of the lower gravity current decrease monotonically with increasing ρ_c^*, as shown in Figs. 5.9c and d. Beyond a certain value of the intrusion density, U_l^* becomes negative, so that the front of the lower current travels towards the right. Vorticity model predictions and DNS results are seen to be in close agreement.

5.3   Summary

We have extended the vorticity-based model of [48] developed for the gravity currents in ambients with arbitrary shear and density stratification to the intrusive gravity currents advancing into linearly stratified media. Towards this objective, we have applied ODE (5.4) to the several fronts in the flow field, by appropriate shifts in the reference frame to render each flow quasisteady. This enables us to obtain the intrusion front speed and other flow variables without invoking any energy-related arguments and assess the energy budget of the flow *a posteriori*. The present model predicts the existence of equilibrium intrusions when the density of the intrusion fluid equals the mean density of the ambient and nonequilibrium intrusions, when otherwise. Consistent with all previously reported observations, our model also shows that the equilibrium intrusions have the minimum propagation velocity. As confirmed by our DNS simulations, the main

difference between the equilibrium and nonequilibrium intrusions is that in the latter the intrusion head becomes subcritical to the leading gravity waves of mode-1 for all the values of ϵ and to those of mode-2, when $\epsilon \lesssim 0.2$, whereas in the former no right- or left-traveling wave emerges. These findings are in very good agreement with those of [43] and [44], as well. The formation of these two group speeds can substantially affect the flow conditions ahead of the intrusion, even though their influence on the energetics of the flow might be moderate. [30] and [49] demonstrate the significance of the internal gravity waves, as they interact with the head of the gravity current or intrusion.

As can be noted in the results displayed in section 5.2.1, the analytical model of the current investigation breaks down when $\epsilon > 0.45$. This can be attributed to the singularity of the limits $\rho_c^* \to 0, 1$, in the sense that the amplitude of the leading bore as well as the maximum amplitude of isopycnals do not smoothly tend to zero in these limits, as shown in Fig. 5.8b. As a result, the solution of the current model degenerates and does not lead to that for the boundary-traveling gravity currents into linear stratifications. [15] and [16] describe the behaviour of the leading wave in those limits in more detail.

Furthermore, we compared the analytical results of the current study to those of the present two-dimensional DNS simulations as well as earlier theoretical and experimental predictions, if available, and very close agreement was seen with regard to all flow variables, including the front speeds of the intrusion and the left-propagating gravity currents, their thicknesses, the propagation velocity and amplitude of the leading bore and the maximum amplitude of the isopycnals. Specifically, near the equilibrium condition, our model renders the intrusion speeds much closer to the experimental and numerical data, compared to those given by [42].

Chapter 6

Conclusions and outlook

Within this investigation, we utilized the vorticity modeling concept initially introduced by [19] and [25], to develop a set of analytical models for various stratified flows, *viz.* intrusive gravity currents into two-layer stratified ambients, partial-depth lock-release flows, gravity currents propagating into two-layer fluids and intusions into linear stratifications. These models enable us to capture the dynamics of complex stratified flows which consist of multiple fronts or interfacial disturbances such as internal bores and expansion waves, without relying on energy-related arguments made by previous authors. This allows for *a posteriori* analysis of the flow energy budget and the continuous energy transfer between different flow compartments. To assess the validity and the predictive capabilities of the proposed vorticty-based models, we compared their findings to the corresponding results of our DNS simulations, as well as the theoretical and experimental predictions of earlier investigations, while very good agreement was seen for all flow properties.

While we demonstrated the advantage of vorticity-based models over already existing models for several common stratified flows in this study, we believe that the capability of this approach is not restrained to these examples. One possible future path is to apply this model to intrusions and intrusion-generated waves with more complicated backround ambients, e.g. when the ambient fluid has shear or nonlinear density profile. These

waves can also be recognized independent from the intrusion, and might be undular (e.g. undular bores) or may reveal a periodic nature (e.g. solitary waves). The corresponding problems for boundary-propagating gravity currents have been investigated in detail by [48], while they consider the propagation of currents in any arbitrarily sheared and/or stratified ambients. Another area of exploration is to extend the planar models of [19] and [25] to three-dimensional stratified flows, which requires the integration from the three-dimensional vorticity conservation PDE. Such models have specific utility for the spatially-evolving wakes behind 3D objects like wind turbines and spheres. Since the more general form of the vorticity conservation law includes the term associated with vortex stretching ($\boldsymbol{\omega} \cdot \boldsymbol{\nabla} \mathbf{u}$), the development of three-dimensional vorticity-based models is expected to be more complex. Finally, vorticity models can be utilized to study flows with entrainment and turbulent effects, while the vanishingly thin interfaces between the fluids should be replaced by finite mixing (and shear) layers.

Bibliography

[1] T. B. Benjamin, *Gravity currents and related phenomena*, J. Fluid Mech. **31** (1968), no. 2 209–248.

[2] J. E. Simpson, *Gravity Currents in the Environment and Laboratory*. Cambridge University Press, 1997.

[3] M. Ungarish, *An Introduction to Gravity Currents and Intrusions*. CRC Press, 2010.

[4] E. Meiburg and B. Kneller, *Turbidity currents and their deposits*, Annu. Rev. Fluid Mech. **41** (2010), no. 2 135–156.

[5] M. W. Moncrieff, *The dynamical structure of two-dimensional steady convection in constant vertical shear*, Q. J. R. Meteorol. Soc. **104** (1978), no. 441 543–567.

[6] E. J. Hopfinger, *Snow avalanche motion and related phenomena*, Annu. Rev. Fluid Mech. **15** (1983), no. 1 47–76.

[7] P. F. Linden, *Gravity currents theory and laboratory experiments. In Buoyancy-Driven Flows (ed. E. Chassignet, C. Cenedese and J. Verron)*. Cambridge University Press, 2012.

[8] J. Y. Holyer and H. E. Huppert, *Gravity currents entering a two-layer fluid*, J. Fluid Mech. **100** (1980) 739–767.

[9] R. E. Britter and J. E. Simpson, *A note on the structure of the head of an intrusive gravity currents*, J. Fluid Mech. **112** (1981) 459–466.

[10] F. de Rooij, P. F. Linden, and S. B. Dalziel, *Saline and particle-driven interfacial intrusions*, J. Fluid Mech. **389** (1999) 303–334.

[11] R. J. Lowe, P. F. Linden, and J. W. Rottman, *A laboratory study of the velocity structure in an intrusive gravity current*, J. Fluid Mech. **456** (2002) 33–48.

[12] A. Mehta, B. R. Sutherland, and B. J. Kybia, *Interfacial gravity currents: Part ii - wave excitation*, Phys. Fluids. **14** (2002) 3558–3569.

[13] B. R. Sutherland, P. J. Kyba, and M. R. Flynn, *The front speed of intrusive gravity currents*, J. Fluid Mech. **514** (2004) 327–353.

[14] H.-B. Cheong, J. J. P. Kuenen, and P. F. Linden, *The front speed of intrusive gravity currents*, J. Fluid Mech. **552** (2006) 1–11.

[15] M. R. Flynn and P. F. Linden, *Intrusive gravity currents*, J. Fluid Mech. **568** (2006) 193–202.

[16] M. A. Khodkar, M. M. Nasr-Azadani, and E. Meiburg, *Intrusive gravity currents propagating into two-layer stratified ambients: Vorticity modeling*, Phys. Rev. Fluids **1** (2016), no. 4 044302.

[17] T. von Kármán, *The engineer grapples with non-linear problems*, Bull. Am. Math. Soc. **46** (1940) 615–683.

[18] J. O. Shin, S. B. Dalziel, and P. F. Linden, *Gravity currents produced by lock exchange*, J. Fluid Mech. **521** (2004) 1–34.

[19] Z. Borden and E. Meiburg, *Circulation-based models for Boussinesq gravity currents*, Phys. Fluids **25** (2013*a*), no. 10 101301.

[20] C. Pozrikidis, *Introduction to Theoretical and Computational Fluid Dynamics*. Oxford University Press, 1996.

[21] C. Härtel, E. Meiburg, and F. Necker, *Analysis and direct numerical simulation of the flow at a gravity-current head. part 1. flow topology and front speed for slip and no-slip boundaries*, J. Fluid Mech. **418** (2000) 189–212.

[22] M. M. Nasr-Azadani and E. Meiburg, *Gravity currents propagating into shear*, J. Fluid Mech. **778** (2015) 552–585.

[23] B. R. Sutherland, *Interfacial gravity currents. I. mixing and entrainment*, Phys. Fluids. **14** (2002) 2244–2254.

[24] S. K. Ooi, G. Constantinescu, and L. Weber, *2d large-eddy simulation of lock-exchange gravity current flows at high grashof numbers*, J. Hydraul. Eng. **133** (2007) 1037–1047.

[25] Z. Borden and E. Meiburg, *Circulation-based models for Boussinesq internal bores*, J. Fluid Mech. **726** (2013*b*) R1.

[26] M. M. Nasr-Azadani and E. Meiburg, *TURBINS: An immersed boundary, Navier-Stokes code for simulation of gravity and turbidity currents interacting with complex topographies*, J. Comput. Fluids **45** (2011), no. 1 14–28.

173

[27] M. M. Nasr-Azadani, B. Hall, and E. Meiburg, *Polydisperse turbidity currents propagating over complex topography: Comparison of experimental and depth-resolved simulation results*, Comput. Geosci. **53** (2013) 141–153.

[28] J. W. Rottman and J. E. Simpson, *Gravity currents produced by instantaneous releases of a heavy fluid in a rectangular channel*, J. Fluid Mech. **135** (1983) 95–110.

[29] J. W. Rottman and J. E. Simpson, *The formation of internal bores in the atmosphere: A laboratory model*, Q. J. R. Meteorol. Soc. **115** (1989) 941–963.

[30] T. Maxworthy, J. Leilich, J. E. Simpson, and E. H. Meiburg, *The propagation of a gravity current into a linearly stratified fluid*, J. Fluid Mech. **453** (2002) 371–394.

[31] J. D. Nash and J. M. Moum, *River plumes as a source of large-amplitude internal waves in the coastal ocean*, Nature **437** (2005) 400–403.

[32] J. D. Kilcher and J. D. Nash, *Structure and dynamics of the Columbia river tidal plume front*, J. Geophys. Res.-Oceans **115** (2010) C00B12.

[33] N. A. Crook, *The formation of the morning glory*, in *Mesoscale meteorology - theories, observations and models*, pp. 349–353, Springer, 1983.

[34] A. W. Tan, D. S. Nobes, B. A. Fleck, and M. R. Flynn, *Gravity currents in two-layer stratified media*, Environ. Fluid Mech. **11** (2010), no. 2 203–223.

[35] B. L. White and K. R. Helfrich, *A general description of a gravity current front propagating in a two-layer stratified fluid*, J. Fluid Mech. **711** (2012) 545–575.

[36] J. B. Klemp, R. Rotunno, and W. C. Skamarock, *On the propagation of internal bores*, J. Fluid Mech. **331** (1997) 81–106.

[37] M. A. Khodkar, M. M. Nasr-Azadani, and E. Meiburg, *Partial-depth lock-release flows*, Phys. Rev. Fluids **2** (2017), no. 6 064802.

[38] P. G. Baines, *A unified description of two-layer flow over a topography*, J. Fluid Mech. **146** (1984) 127–167.

[39] P. G. Baines and P. A. Davies, *Laboratory studies of topographic effects in rotating and/or stratified fluids*, in *Orographic effects in stratified fluids*, no. 23, pp. 233–299, GARP Publ., 1980.

[40] N. A. Crook, *A numerical and analytical study of atmospheric undular bores*. PhD thesis, University of London, 1984.

[41] N. A. Crook and M. J. Miller, *A numerical and analytical study of atmospheric undular bores*, Q. J. R. Meteorol. Soc. **111** (1985) 225–242.

[42] D. T. Bolster, A. Hang, and P. F. Linden, *The front speed of intrusions into a continuously stratified medium*, J. Fluid Mech. **594** (2008) 369–377.

[43] J. R. Munroe, C. Voegeli, V. Birman, B. R. Sutherland, and E. H. Meiburg, *The front speed of intrusions into a continuously stratified medium*, J. Fluid Mech. **635** (2009) 245–273.

[44] B. D. Maurer and P. F. Linden, *Intrusion-generated waves in a linearly stratified fluid*, J. Fluid Mech. **752** (2014) 282–295.

[45] M. Ungarish, *On gravity currents in a linearly stratified ambient: a generalization of Benjamin's steady-state propagation results*, J. Fluid Mech. **548** (2006) 49–68.

[46] B. D. Maurer, D. T. Bolster, and P. F. Linden, *Intrusive gravity currents between two stably stratified fluids*, J. Fluid Mech. **647** (2010) 53–69.

[47] A. D. McEwan and P. G. Baines, *Shear fronts and an experimental stratifed shear flow*, J. Fluid Mech. **63** (1974) 257–272.

[48] M. M. Nasr-Azadani and E. Meiburg, *Gravity currents propagating into ambients with arbitrary shear and density stratification: vorticity-based modelling*, Q. J. R. Meteorol. Soc. **778** (2016) 1359–1370.

[49] B. R. Sutherland and J. T. Nault, *Intrusive gravity currents propagating along thin and thick interfaces*, J. Fluid Mech. **586** (2007) 109–118.